Understanding the mechanisms and parameters affecting the structural corrosion of sheet gauge 7xxx alloys

A Dissertation
Presented to
The Academic Faculty

by

Ganesh Bhaskaran

In Partial Fulfillment
of the Requirements for the Degree
Doctor of Philosophy in the
School of Materials Science and Engineering

Georgia Institute of Technology
May 2023

Understanding the mechanisms and parameters affecting the structural corrosion of sheet gauge 7xxx alloys

Approved by:

Dr. Preet Singh, Advisor
School of Material science and Engineering
Georgia Institute of Technology

Dr. Richard Neu
School of Materials Science and Engineering,
The George W. Woodruff school of Mechanical engineering

Dr. Josh Kacher,
School of Materials Science and Engineering
Georgia Institute of Technology

Dr. Naresh Thadani
School of Materials Science and Engineering
Georgia Institute of Technology

Dr. Matthew McDowell
School of Materials Science and Engineering,
The George W. Woodruff school of Mechanical engineering
Georgia Institute of Technology

Dr. Yudie Yuan
Principal Scientist and Manager of R&D center, Zhenjiang Plant
Novelis Inc.

Date Approved: April 24, 2023

To Aarabhi, Rithvik, Madhu and

my beloved members of my family

ACKNOWLEDGEMENTS

I extend my deepest gratitude to Prof. Preet Singh for giving me this great opportunity to pursue a doctoral degree under his supervision. The last five years have been an exciting journey and I would like to acknowledge Prof. Singh's patience and unwavering guidance during this period of time. I have learned the importance of patience and how to critically evaluate research from his mentorship. I would like to express my deepest appreciation to my committee for their valuable input and for taking the time to peer review my work.

I cannot begin to express my gratitude to Dr. John Hunter (retd. Senior manager, Novelis Inc), Dr. Yudie Yuan (Principal Scientist, Novelis Inc), and Dr. Rajeev Kamat (Senior Principal Scientist, Novelis Inc), who championed the case for my Ph.D. at Novelis Inc. They have been great mentors and provided a strong platform for my future career. I extend my sincere thanks to the Novelis R&D leadership team Mr. Phillip Meyer (SVP & Chief Technical Officer), Dr. James Fekete (RTD, NNA & NSA), and Dr. Dewei Zhu (Senior Manager) for their continued support. I must also thank the past and present Novelis Inc leaders, Mr. Todd Summe, Dr. Graeme Marshall, Dr. Rashmi Mohanty, Dr. Luis Vega, Dr. Devesh Mathur, Dr. Lasitha Cumaranatunge, Dr. Venky Sundaram, Mr. Duane Bendinski, Dr. Alp Manavbasi, Dr. Peter Redmond, Mr. Xavier Varone, and Mr. Rahul Kulkarni for their unwavering support. Many thanks to the scientific and lab members of Novelis Global Research and Technical Center, Kennesaw, for providing much-needed support in executing the experiments. Special thanks to Mr. Paul Nolan and Mr. Jason Leszczewicz for SEM and STEM training.

I would like to acknowledge the support that I received from members of the corrosion materials research laboratory (CMRL) Garret, Liang, Krishna, Rupesh, and Jamshad. I cannot leave Georgia Tech without thanking my fellow Ph.D. cohorts, Dr. Jahnavi Desai, Dr. Sahitya Movva, Ms. Pragna Bhaskar and, others for the memorable times while taking the course work.

I would like to express my heartfelt gratitude to my master's degree supervisor, Prof. Roger Newman (University of Toronto, Canada), and my undergraduate degree supervisors, Dr. Kalpana Giridharan and Dr. N. G. Ranganathan (Central Electrochemical Research Institute (CECRI), India), whose inspiration and encouragement laid the foundation for my research pursuits in electrochemistry of materials. Additionally, I would like to thank my high school teachers, Mr. Rajagopalan, Mr. Sundarajan, and others for sparking my interest in the STEM field

I am deeply indebted to my family members, starting from my daughter Aarabhi, my son Rithvik, and most importantly my loving wife Madhu, for their unconditional love and unparalleled support. They have been the pillar of my strength and the source of my motivation throughout this doctoral journey. I also would like to express my deepest gratitude to my parents, Mr. Bhaskaran and Mrs. Uma, for their countless sacrifices in shaping my life. The completion of this dissertation and research work would not have been possible without my in-laws, Mr. Thiagarajan, Mrs. Revathi, Mrs. Lakshmi Gurusamy, Sriram, Mathura, and Samarth, for their patience that cannot be underestimated.

TABLE OF CONTENTS

LIST OF TABLES

LIST OF FIGURES

LIST OF SYMBOLS AND ABBREVIATIONS

DFT	Density functional theory
EBSD	Electron backscattered diffraction
EDS	Energy dispersive spectroscopy
HEDE	Hydrogen enhanced de-cohesion
ICP-OES	Inductively coupled plasma – optical emission spectroscopy
IGC	Intergranular corrosion
OEM	Original equipment manufacturer
RSW	Resistance spot welding
SCC	Stress corrosion cracking
SEM	Scanning electron microscope
SPR	Self-pierce rivet
SSRT	Slow strain rate test
STEM	Scanning transmission electron microscope
SVET	Scanning vibratory electrode technique
T6	Peak age temper

SUMMARY

The light weighting of automotive structures has been an effective method of increasing vehicle fuel efficiency. In the past, the use of aluminum alloys was limited to hang-on parts and outer skin applications to reduce weight. However, due to the high strength-to-weight ratio of 7xxx series alloys, exciting alternative options for replacing high-strength steels in load bearing or structural applications have emerged. These alloys derive their strength through the precipitation hardening mechanism, which involves the formation of nanosized precipitates after a specific heat treatment sequence. However, one of the main roadblocks to the penetration of 7xxx alloys in structural applications like rockers and bumpers is concerns regarding structural forms of corrosion, such as intergranular corrosion (IGC) and stress corrosion cracking (SCC). These can be attributed to the microstructure features of the grain boundary, specifically the precipitate and adjoining precipitate-free zone. Most published structural corrosion work on 7xxx alloys has been associated with plate gauge applications with thicknesses greater than 10mm. However, for automotive applications, sheet type with thicknesses of 1.5 to 2.8mm is desired, as it enables weight reduction without loss of dent resistance while meeting stiffness requirements. Moreover, the difference in the manufacturing process between sheet and plate leads to a distinct microstructure.

The objective of this study is to examine the impact of processing sequence, alloy composition, and joining methods on grain boundary microstructure, as well as to understand their potential impact on the structural forms of corrosion in sheet gauge 7xxx alloys. Due to the complex grain boundary microstructure and corrosion property

relationship, an efficient research scheme was needed to minimize or isolate the secondary effects. The research scheme was designed in such a manner that when one of the variables of interest was changed, the rest of the processing parameters were kept constant.

The research is divided into three sections. In the first part, two different processing sequences were utilized to alter the grain size of the material. They were recovery anneal of final gauge material and reduction of the percentage of cold work on hot-rolled material. The grain boundaries were characterized using scanning transmission electron microscopy (STEM) to determine the width of the precipitate-free zone, the size and continuity of grain boundary precipitates between the finer and coarser grain materials. The samples were then subjected to IGC and SCC tests to determine the impact of microstructure on the corrosion mechanism. In the second part, the effect of Cu and Zn/Mg ratio on the resulting microstructure of high-solute 7xxx alloys and their impact on corrosion resistance was evaluated, with a specific focus on the effect of testing environment and constituent particles on localized corrosion resistance. In the third part, the microstructure changes, and their impact on the corrosion properties of commonly used automotive joining methods, such as resistance spot welding (RSW) and self-pierce rivet (SPR), were evaluated for the dissimilar aluminum alloy joint of 7075-T6 to 5182-O. The gradient microstructure of the joint sections was characterized and evaluated for corrosion resistance.

The study revealed that the three factors (processing, composition, joining) uniquely influenced the size, continuity, and composition of the grain boundary precipitates and adjoining precipitate-free zone, which in turn affected the IGC and SCC performance of

the materials. The results also showed that the grain boundary features that control the corrosion mechanism vary uniquely, depending on the environment.

The findings of this research have significant implications for the development of 7xxx sheet gauges, particularly in the areas of alloy design, manufacturing process selection, and end application. The study will provide valuable insights into improving the corrosion resistance of these alloys, which will enable them to compete more effectively with ultra-high strength press-hardened steel in automotive structural applications. Ultimately, this research has the potential to contribute to the development of the next generation of high-performance aluminum alloys.

CHAPTER 1: INTRODUCTION

In the automotive industry, sustainability and emission regulations are becoming increasingly important. Therefore, the industry is shifting away from traditional materials that are difficult to recycle and have high density, towards sustainable and lightweight alternatives. [1]. Although electrification of powertrains is one way to help decarbonize the life cycle of a vehicle, the materials that go into a car also matter. According to the McKinsey report, close to 60% from the emissions of the automotive industry by 2040 will come from materials used in production [2]. As a result, original equipment manufacturers (OEM) are actively looking for lighter, high performance, and recyclable materials to be used in automotive applications [3] [4].

This market pull provides an exciting opportunity in the field of material science and engineering to develop new materials with properties and/or create new products with existing materials to meet the OEM requirement. The key tenets of material science are process structure and property relationship. To obtain desired properties, the materials must be fine-tuned to obtain the appropriate microstructure.

1.1 Materials in auto industry

The automotive industry is one of the largest consumers of construction materials in the world. Increasing the durability and reliability of car parts of cars is a relevant and important problem in materials science [5]. The key requirements for materials to be selected for automotive applications are improved crashworthiness, noise and vibration, overall cost, and fuel economy. The key design philosophy is based on the right material

at the right place. **Figure 1-1** shows the breakdown of the current use of materials by parts on an automobile chassis [6].

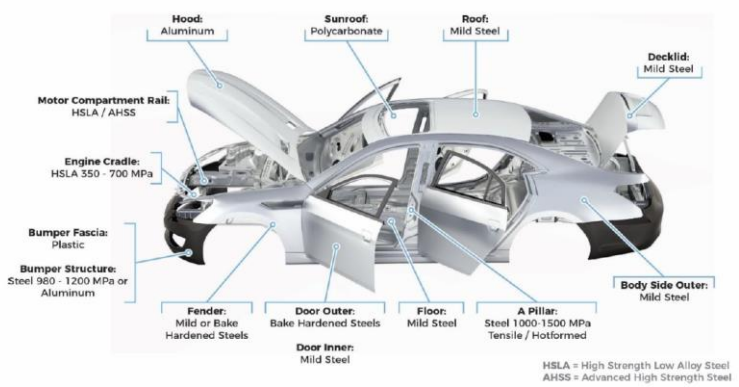

Figure 1-1: Materials commonly used for major vehicle structure components in the current fleet [6].

The categories into which the current raw materials, considering both interior and exterior, are divided are: metals and their alloys (ferrous and nonferrous), polymers, glass, textiles, coatings, fluids, and lubricants, etc. [7]. **Figure 1-2** shows that steel and aluminum alloys are key engineering metals that dominate vehicle architecture in current and future projections [6].

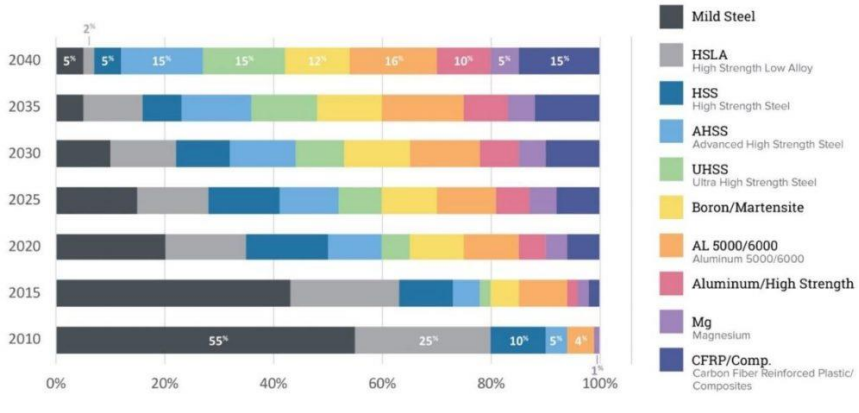

Figure 1-2: Trend in volume of engineering metals used in the automobile industry [6].

1.1.1 Steel

Since the advent of automobile manufacturing, steel has been the main material used in the industry. Over the years, steel manufacturers have been agile in adapting to changing industrial needs. As a result, the steel product portfolio has evolved continuously (**Figure 1-3**) [8]. For example, in the 1970s, low carbon steel began to be developed for automotive industry, followed in the 1980s by dual-phase (DP) and baked hardened steel, in the 1990s by transformation-induced plasticity steel (TRIP) and its microalloying concept [9]. Similarly, in the mid-1990s, a consortium of sheet steel manufacturers, composed of 35 companies from 18 countries, launched the Ultralight Steel Automobile Body (ULSAB) to explore the possibility of reducing weight in automotive components. Engineering research has resulted in the development of 90 per cent HSS steel car bodies. The new body weight was 25% lower than the standard four-door sedan and the cost was 14% lower. Additionally, torsion stiffness increased by 80% and bending stiffness by 52%. [10].

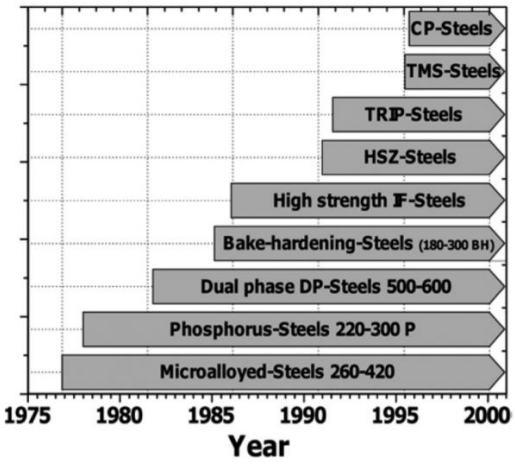

Figure 1-3: Evolution of high-strength steel from the mid-1970s [8].

The typical distribution of the steel in a vehicle based on the total curb mass is as follows. Nearly 40% is used in the body structure such as panels, doors, and trunk closures for high-strength and energy absorption in case of a crash. While 23% is used in drive train areas consisting of cast iron for the engine block and machinable carbon steel for wear resistant gears. Approximately 12% is used in the suspension, using high-strength rolled steel strip.

One of the commonly used parameters for classifying steel is yield strength. Steel having a yield strength less than 210 MPa is considered conventional steel. High-Strength Steels (HSS) have yield strengths of 210 to 550 MPa, while Ultra / Advanced High-Strength Steels (UHSS or AHSS) steels have yield strengths greater than 550 MPa. The difference in yield strength is due to the presence of complex microstructure phases. In the case of conventional steel, ferrite is the main phase, while AHSS has a combination of ferrite and other phases such as martensite, bainite, austenite, and/or retained austenite in quantities sufficient to produce unique mechanical properties [11]. Just like other engineering metals, strength and ductility have inverse relationship (**Figure 1-4**). However, advances in steel research have led to classes of steel such as Twinning-induced plasticity steel (TWIP) that not only has high strength but also have high elongation. In this class of steel, multiple slip activations mechanisms are enabled when the material is subjected to applied stress. These mechanisms include dislocation glide, $\alpha_{bcc}/\varepsilon_{hcp}$ martensite formation and/or mechanical twinning [12].

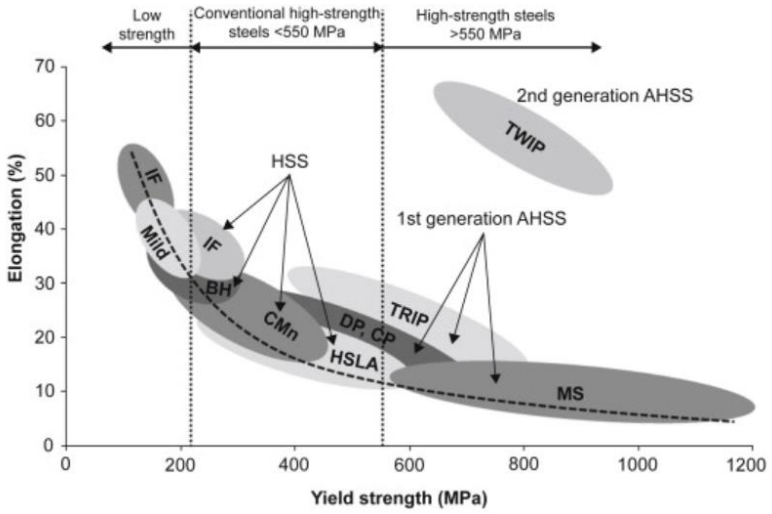

Figure 1-4: Elongation vs. tensile strength of different classes of steel [13].

The following are the key types of conventional and AHSS steels that are commonly used in automotive applications.

1.1.1.1 Conventional steel

Mild steel

Mild steels are hugely affordable and can be engineered in many different ways to meet both crash safety and performance requirements. They have a ferritic microstructure that provides good drawing quality. One of the major issues associated with this material is a surface quality defect called a stretcher-strain pattern (St-St). This defect is caused by local yielding during press forming followed by locking of the mobile dislocations by carbon (C) or nitrogen (N) atoms in solid solution. This led to the development of interstitial free steel by reducing the amount of C in solid solution before cold rolling and annealing, leading to robust deep drawability [1]. Mild steels were once the dominant material in car

bodies, but now their use is limited to rigidity-related components and cosmetic parts with complex bending and drawing. Some examples include clutch housings, suspension parts, control arms, brackets, etc. Its decorative uses can also range from wheel rims, covers, screws, washers, bolts, nuts, and fasteners.

Bake-hardenable steel (BH)

BH steels have a basic ferritic microstructure and derive strength by strengthening solid solution. A unique feature of these steels is the chemistry and processing designed to keep carbon in solution during steelmaking and then allow this carbon to come out of solution during paint baking. This results in the an increase in yield strength of the component for increased dent resistance without a reduction in formability. The strengthening mechanism is attributed to the diffusion of carbon atoms to form the so-called Cottrell atmosphere around dislocations that will result in pinning of dislocations and, in turn, increase the strength. Bake hardening steels can be produced from interstitial free chemistries by adjusting the composition during steelmaking to leave carbon in solution, or by annealing at high temperature to take carbides formed during processing into solid solution [14]. They are typically used in vehicle body panels with high formability requirement without loss of dent resistance [15].

High-Strength, Low-Alloy (HSLA) Steels

HSLA steels increase strength primarily by microalloying elements contributing to fine carbide precipitation, substitutional and interstitial strengthening, and grain size refinement. The microstructure of HSLA steel is mostly precipitation-strengthened ferrite, with small amounts of pearlite and bainite added depending on the required strength levels.

HSLA steels are used in body-in-white components and increase the in-service load application components. Hot-rolled HSLA steels can be used for applications such as suspension systems, wheels, chassis, and seat mechanisms, while cold-rolled HSLA can be used in seat brackets and reinforcements [16].

1.1.1.2 Advanced High-Strength Steel

Dual phase (DP) steel

DP steels consist of a ferritic matrix with a hard martensitic phase in the form of islands. They typically have high ultimate tensile strength (UTS) (enabled by martensite) combined with low initial yielding stress (enabled by the ferrite). The delta between the yield and UTS results in high early-stage strain hardening and homogeneous plastic flow. These features make DP steels ideal alloy systems for automotive-related sheet-forming operations [17]. It is produced by controlled cooling from the austenite phase (in hot-rolled products) or from the two-phase ferrite plus austenite phase (for continuously annealed cold-rolled and hot-dip coated products) to transform some austenite into ferrite before a rapid cooling transforms the remaining austenite into martensite. The fraction of the hard martensite phase embedded in the softer ferrite phase ranges anywhere from 10 to >50 vol.% [18]. Application includes wide areas such as roof outer, door outer, body side outer, package tray, floor panel, hood outer, body side outer, cowl, fender, floor reinforcements, body side inner, quarter panel inner, rear rails, rear shock reinforcements, Safety cage components (B-pillar, floor panel tunnel, engine cradle, front subframe package tray, shotgun, seat), roof rails, B-pillar upper, etc.

Transformation-induced plasticity (TRIP) steels

TRIP steels exhibit a unique combination of high strength combined with ductility. The microstructure typically contains allotriomorphic ferrite as a matrix, blocky retained austenite, and a mixture of bainitic ferrite and lath-retained austenite in the microstructure. The key reason for the ductility is the martensitic transformation of retained austenite induced by mechanical deformation [19]. TRIP steels use higher amounts of carbon than DP steels to obtain sufficient carbon content to stabilize the retained austenite phase to below ambient temperature. This steel is used for frame rails, rail reinforcements, side rail, crash box, dash panel, roof rails, upper B pillar, roof rail, engine cradle, front and rear rails.

Hot-Formed (HF) Steel:

Hot-formed steel contains 1.2% Mn and a small amount of B boron steels (upto 0.001%), they have a martensitic structure and tensile strengths ranging up to 1,500 MPa. The unique feature of this material is the transformation of martensite in situ during the hot forming operation which involves heating the steel in the pre martensitic form to 930°C. The tensile strength of boron steels increases from approximately 400 MPa before hot formation to 1,500 MPa after hot formation [20]. They are used in applications such as A-pillar, B-pillar, cross beam, etc.

1.1.1.3 Challenges for Steel Technology

Climate change and air pollution have become the main concerns of the 21st century, and governments around the world have begun to implement legislation to improve fuel economy and reduce emissions. These regulations are geared towards addressing problems

that, among other things, the sustainability of the material manufacturing process. In 2019, the iron and steel industry represented 22% of industrial energy consumption and 28% of industrial carbon emissions [21]. One of the strategies to improve fuel economy is to reduce the weight of the vehicle. On average, the fuel economy improves by 6%, for every 10% reduction in vehicle mass. During the past 30 years, the industry has reduced the weight of its vehicles by approximately 30% [22]. Engineering metals such as aluminum, titanium, and magnesium are increasingly being considered to replace steel counterparts. The key attribute towards light weighting is to achieve a high strength-to-weight ratio.

1.1.2 Aluminum

Aluminum is considered an ideal lightweight material due to its low density of 2.7 g/cm^3. It allows for a mass saving of up to 50% compared to competing materials without compromising safety [23]. Since the oil crisis in the 1970s, lightweight vehicles became a major fuel efficiency driver, and many aluminum-intensive vehicles were built. Aluminium alloys are widely used in automobile and aircraft body structures due to their low density, high strength-to-weight ratio, corrosion resistance, and relatively low cost compared to composites [24, 25]. For automotive applications, aluminum alloys are typically used in semi-finished forms (**Figure 1-5**) such as engine blocks, power train parts, space frames, sheet structures, or as closures, hang-on parts, and other structural components [23]. From a sustainability perspective, the recyclability of aluminum components offers substantial reduction in energy and CO_2 emissions compared to steel counterparts [26]. The principal methods for transforming extracted aluminum are castings, extrusions, and rolling. Casting makes it possible to manufacture near-net parts with complex geometry. Although traditional casting applications were largely restricted to engine blocks, the advent of

technologies such as high-pressure die casting has potential to make a large portion of the structural part of the vehicle [27]. Extrusion is a process by which the material is pulled

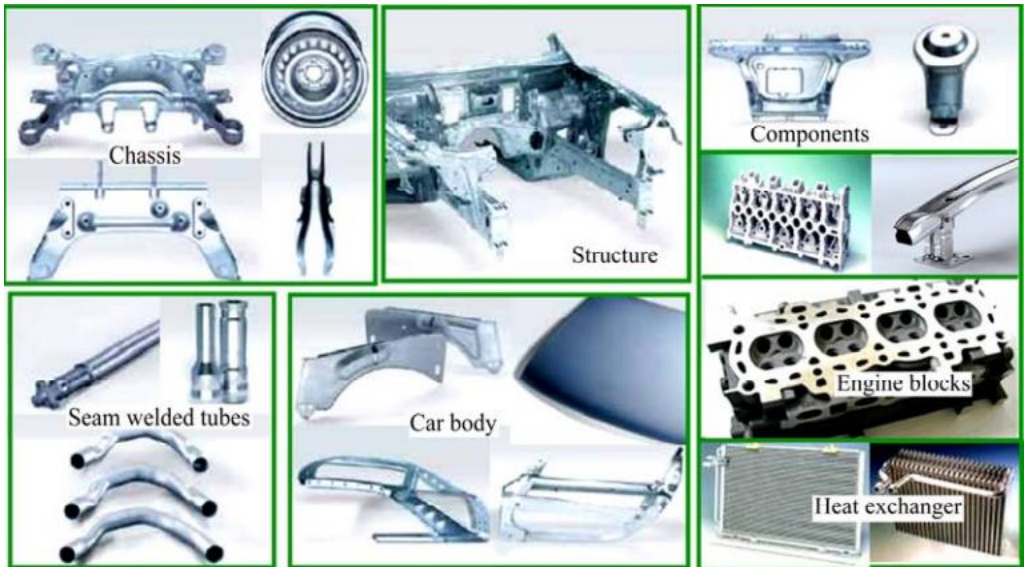

Figure 1-5: Typical automotive components made of aluminum alloys [23].

through the die to change the cross section or harden the materials, which makes it feasible to produce part profiles with a very wide range of shapes and dimensions [28]. Some of the common applications in automotive structures include bumper systems, door beam, and vehicle body frame member [29].

The final category is the wrought alloys that are typically manufactured through the rolling process. It starts with casting of the aluminum alloy into large ingots that are several inches thick and then they are subjected to thickness reduction by the rolling process. Traditionally, wrought alloys are designated into two categories, namely strain-hardenable and age-hardenable alloys, due to the usage of a distinct metallurgical processing route.

1.1.2.1 Strain-hardenable alloys

These are the class of wrought alloys that are strengthened by work hardening mechanisms. As the dislocation density in the metal increases, there is strong resistance to movement of the dislocation due to the strong repulsive force of the dislocation – dislocation strain interaction [30]. Although these class materials can be strengthened by other methods such as grain size engineering or solid solution strengthening, they cannot be age hardened. Al – Mg alloys (5xxx) are a very good example of this type of materials used in the automotive industry. Typical applications include inner body panels, reinforcement members, brackets, etc. [31]. They have very good formability but low strength in the range of 125 MPa, as a result, they are not used in strength driven applications.

1.1.2.2 Age-hardenable alloys

For applications demanding strength, such as bumper reinforcements and body panels, aluminum alloys with higher yield strength (250 to 300 MPa) such as Al-Mg-Si (6xxx) are used [32]. These classes of alloys derive their strength through precipitation hardening mechanisms. After a specific sequence of heat treatment steps, called artificial aging, fine nanosized second-phase particles precipitate out of the matrix. The lattice deformations established at the precipitate–matrix interface resist dislocation motion during deformation, making the alloy harder and stronger [30]. Al-Cu (2xxx) and Al-Mg-Zn (7xxx) alloys belong to this class, and they typically have significantly higher strength than 6xxx alloys.

1.2 7xxx series alloys

The use of aluminum alloys (5xxx and 6xxx) has been restricted to hang on parts and outer skin applications. For structural applications such as rocker, bumper, and B-pillar, there is a need to increase the strength of aluminum alloys to compete with high-strength steels. Due to their high Strength (Yield strength 500 MPa) to weight ratio, 7xxx series alloys offer exciting alternative options for replacing high-strength steels in automotive load bearing or structural applications [6]. Historically, these alloys have been used in the aerospace applications. The 7xxx series also alloys derive their strength via the precipitation hardening mechanism. The nano sized precipitates are formed after the heat treatment of the alloy at the super saturated solid solution state. Factors such as alloy composition, rolling practices, and heat treatment parameters (time, temperature, quench rate) affect the size and distribution. The precipitation sequence usually entails the formation of vacancy-rich solute clusters during quenching of the alloys from above the solvus temperature. Then these clusters aid in the formation of coherent layers of Zn and Mg/Al in <100> direction called the Guinier-Preston-I (GP-I) zone. In some instances, there have been reports of the presence of plate-like features along 111 Al planes called Guinier-Preston-II (GP-II) zone. Artificial ageing results in the formation of plate-shaped precipitates called η' on the {111} Al planes, they are typically made of $MgZn_2$ or Mg (Zn, Al, $Cu)_2$ with a hexagonal close-packed structure. Since they have a well-defined crystallographic relationship with the Al matrix, they are coherent in nature. As a result, they are very effective in impeding the movement of dislocations due to the widespread disruption of the lattice [33]. This results in higher strength, and the condition in which the alloy attains its highest strength is called the T6 (peak aged) temper. Further ageing results

in the formation of the cigar-shaped precipitate called η phase and is typically observed in T7 (overaged temper). They are incoherent with the Al matrix and result in a decrease in the strength. [34]

1.3 Key Issues

Unfortunately, this class of alloys is sensitive to several forms of localized corrosion, which, in turn, affects the mechanical performance of these materials. As shown in **Figure 1-6**, the corrosion severity of 7xxx alloys increases at the peak ageing temper. Although several heat treatment options are available, which increase localized corrosion resistance, they typically reduce the strength [35]. Several factors, from alloy composition to processing parameters, affect the corrosion performance of this class of alloys [3].

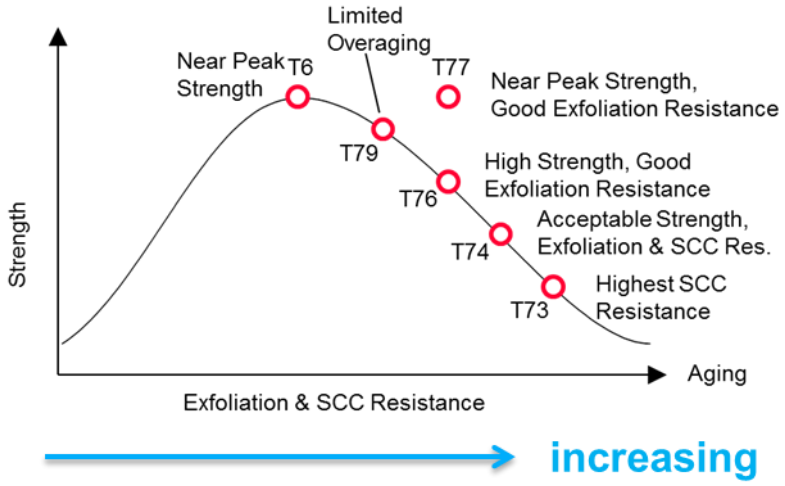

Figure 1-6: Effect of aging on the SCC performance of alloys of the 7xxx series.

Previous work [4] has shown that these strengthening $MgZn_2$ precipitates are anodic (-960 mV_{SCE}) to the aluminum matrix, and as a result these particles are preferentially attacked

in corrosive environment. The size, composition, and distribution of these precipitates affect the corrosion path. In some cases, corrosion affects all metallurgical constituents in the matrix and results in transgranular mode. In others, the corrosion front may propagate preferentially along the grain boundary, thus resulting in intergranular mode. The latter form of corrosion will occur only if three of the conditions are met; first, the presence of corrosive medium, second, the potential difference between the precipitate and the adjoining zone should be of the order of mV, and finally, the presence of continuous precipitates along the boundary [36].

7xxx alloys also exhibit another type of selective grain boundary corrosion called exfoliation attack. In this case, the corrosion proceeds laterally from the initiation sites along planes parallel to the surface, generally at the grain boundaries. The resulting corrosion product forces the unattacked metal away from the body of the material, resulting in a layered appearance [37].

These high-strength heat-treatable alloys also susceptible to stress corrosion cracking (SCC). This type of failure is typically observed due to the synergistic action of the mechanical stress (tensile) and corrosion reactions. Anodic dissolution-assisted cracking and hydrogen-induced cracking are the two key types of mechanisms reported for high-strength aluminum alloys [38]. According to the anodic dissolution model, selective dissolution of the grain boundary or the adjoining region results in the propagation of the crack in the presence of tensile stress [39, 40]. In case of hydrogen-induced cracking, the initiation of SCC requires a certain threshold concentration of hydrogen build-up in the cracking sites [41, 42]. Since corrosion reactions at the grain boundaries can result in the formation of adsorbed hydrogen, both mechanisms can play a synergistic role [43].

1.4 Motivation

Applications using 7xxx alloy series have been limited to the aerospace industry due to the high variable cost associated with forming and joining these materials. Therefore, most of the data reported in the 7xxx series corrosion literature are associated with the plate gauge (> 10mm) used in the aerospace industry [44-46]. Recently, there has been growing interest in the use of these alloys in automotive sheet gauge applications (1.5 to 2.8mm), as it allows weight reduction without loss of resistance to dent, while maintaining the stiffness requirements [23]. The metallurgical process for sheet gauge production is completely different from that of plate gauge. Furthermore, the upstream manufacturing process affects the corrosion performance of the aluminum alloys in its final working temper. This includes factors such as alloy composition, rolling practices, and final heat treatment steps (time, temperature, quench rate). Additionally, in automotive structural applications, such as pillars and door entry beams, long-term durability of the joints is essential to avoid premature component failure [47, 48] [49]. One of the most popular joining methods in the automotive industry is resistance spot welding. This is a type of fusion welding that results in a gradient microstructure near the joint area [50]. Such microstructures are very vulnerable to corrosion and can seriously compromise the mechanical properties of joints. The objective of this work is to understand the effect of alloy composition, processing sequence, and joining methods on the grain boundary microstructure and its subsequent effect on structural forms of corrosion (IGC, SCC) in the 7xxx class of sheet gauge alloys.

CHAPTER 2: LITERATURE REVIEW

2.1 Grain size effect

The 7xxx class of alloys are known to have low formability at room temperature, making hot forming a commercially viable process for forming these alloys [51]. Grain size plays an important role in the hot forming operations window, with coarser grains resulting in a wider operational window compared to fine grain materials. Therefore, it is important to study the effect of grain size on other material properties, such as corrosion.

K.D. Ralston et al. [52] surveyed the effect of grain size on the corrosion resistance of various engineering alloys. This study noted that factors such as texture, impurity segregation, and residual stress could act as pitfalls while studying the effects of grain size on corrosion resistance. These factors typically co-exist with the changes in the grain size resulting from the usage of various thermomechanical processing sequences to achieve the desired microstructure. This work showed a clear correlation with the reduction in grain size and improved corrosion resistance in the case of Mg and Ti alloys. However, in the case of Al alloys the grain size appears to have both an increased and a decreased corrosion susceptibility depending on the processing and the environment.

E. Sikora et al. [53] compared the localized corrosion resistance of the conventional 5083 alloy with the nanocrystalline version. The conventional alloy had a grain size of 40 um, while that for the nanocrystalline variant was in between 0.2 to 0.5 um. The potentiodynamic polarization data showed that the nanocrystalline variant did not show any improvement in terms of the breakdown potential and passivation current density in

comparison to the conventional alloy. However, due to the smaller size of the second phase constituent particles, the nanocrystalline material had a better degree of protection against pit nucleation. Interestingly, the severity of intergranular corrosion increased with decrease in the grain size. The authors did not provide any mechanistic explanation behind this behavior. The alloys used for the intergranular corrosion testing had a higher amount of Mg (7.5 to 8.5%) compared to conventional 5083 (4 to 4.5%). The observed drop in the intergranular corrosion resistance could be due to the effect of Mg rather than the grain size. The increase in the bulk Mg concentration, is generally associated with a higher sensitivity to intergranular corrosion. Furthermore, polycrystalline alloys were fabricated by cryomilling and hot isostatic pressing, while the coarse grain 5083 was fabricated via a conventional rolling process with the H111 temper designation. The inherent difference in the manufacturing sequence could have made the nanocrystalline alloy more susceptible to intergranular corrosion attack.

The effect of grain size on the SCC performance on 2mm thick 7475 was reported by Tsai et al. [54]. They compared the material with grain sizes of 10 um and 100 um. These samples were solutionized at 515 ° C for 1.5 h followed by a water quench. Subsequently, these samples were aged to T6 (120^{o}C for 24h), T73 (107 ° C for 6h + 163^{o}C for 24h) and RRA (T6 + 220 ° C for 5min + water quench + T6) tempers. The SCC tests were carried out in 3.5% NaCl + 0.3% H_2O_2 with a strain rate of 4 x 10^{-6} s^{-1}. To determine the susceptibility of hydrogen embrittlement, the samples were preloaded to 70% yield strength followed by application of -1500 mV_{SCE} in HCl solution adjusted to pH 1. The samples were strained to 2% at a strain rate of 4 x 10^{-6} s^{-1}. Subsequently, the solution was removed and the samples were broken in the air at a stain rate of 3.3 x 10^{-4} s^{-1}. The

susceptibility was assessed on the performance of the uncharged specimens. They noticed that in the T6 temper, the finer grain size material had lower SCC resistance compared to coarser grain size material. However, in T73 temper the reverse was observed. The hydrogen embrittlement susceptibility test showed a trend similar to that of the SCC tests. They did not observe any significant differences in terms of the precipitate size and width of the precipitate-free zone between the grain sizes. However, the size of the grain boundary precipitate of the finer grain material was consistently smaller than the coarser grain materials, especially at T6 temper. They also noticed that the slip behavior was influenced by grain size as well. A reduction in the coarseness of an slip band and the increase in the homogeneity of the slip character were observed in finer grain size material. The fractionographs revealed the presence of equiaxed and pancake-type morphology confirming the intergranular fracture. The enhanced resistance to SCC of the coarser grain materials was associated with the size of the grain boundary precipitates (GBP). They reported that most of GBP in coarser grain size material was larger than 20 nm, the critical value for precipitate to form hydrogen bubbles based on L. Christodoulou et al. [55] work, resulting in improved resistance.

W. Tian et al. [56] studied the effect of bimodal 7075 aviation aluminum alloys and their corrosion properties by spark plasma sintering. They noticed a difference in the dissolution behavior between the coarse (100 um) and finer grains (10 um), the former having a higher rate of dissolution. The cathodic (Cu and Fe rich) particles in the coarse grains contained more heavy alloying elements. This in turn accelerated the formation and thickening kinetics of the oxide film on the metal matrix surrounding them. Once the oxide film ruptured in a low pH solution, the reduction of hydrogen ions was easily carried out on

cathodic (Cu and Fe) particles resulting in a higher dissolution of the matrix. However, this paper did not study the effect of grain size on intergranular corrosion attack.

K. Gopala Krishna et al. [57] reported that the finer grains from cryorolling of the Cu free Al-2Mg-4Zn alloy reduced the susceptibility to intergranular corrosion. The samples were solutionized at 480 ° C for 1 h before cryorolling at -170^{o}C. The rolled strips were then annealed at 150 ° C for 3 min to facilitate partial recovery and recrystallization. Two-step maximum aging practice was carried out at 100 ° C for 5 h followed by 150 ° C for 6 h. The performance of the cryorolled alloy with a grain size of 98 ± 28 nm was compared to the 90% cold worked material with a grain size of 80 ± 13 µm. Transmission electron microscopy (TEM) examination revealed the presence of coarse $MgZn_2$ precipitates along the grain boundaries and a precipitate free zone 50 nm wide, while no such features observed for fine-grain materials. As a result, a clear sign of intergranular attack was observed in the coarse grain material, while a uniform dissolution of the matrix occurred in fine grain material.

2.2 Alloy composition

In the 7xxx alloy family, Zn and Mg are key elements that are added to the matrix for the formation of nano-sized $MgZn_2$ strengthening precipitates. The addition of copper to high-strength A1–Zn–Mg alloys has been developed to increase the volume fraction of strengthening precipitates [58, 59]. Similarly, Zr was added as a minor alloying element for the formation of Al_3Zr dispersoids. These dispersoids are very effective in inhibiting recrystallization. Therefore, the resulting alloy has higher strength as a result of the unrecrystallized microstructure. Recently there has been growing interest in combining

these two approaches to design next-generation 7xxx alloys with yield strength close to 600 MPa [60, 61]. These next generation alloys can compete directly with the ultra-high-strength press-hardened steel for automotive structural applications. Therefore, it is need for understanding the corrosion mechanisms of such alloys.

2.2.1 Effect of Cu

Sarkar et al. [46] studied the effect of Cu content on the SCC resistance of 6.5 mm thick 7xxx plates. The Cu content varied from 0, 1, 1.6 and 2.1 wt% in the Zr containing alloy. Samples were solutionized at 477 ° C followed by water quench. The subsequent ageing was carried out at 120^{o}C for 48, 68, 100 and 300h. The SCC test was carried out by measuring the crack propagation rate of pre-cracked double cantilever beam specimen in 3.5% NaCl. Then the crack velocity (v) is plotted as a function of stress intensity factor (K) (Error! Reference source not found.**)**. The v-K curve consists of three distinct regions, the i nitial linear segment (region I) followed by a plateau region (region –II) and a linear region (region III) at high K values. The linear region I is controlled by mechanical and environmental factor, while the plateau region-II is mainly controlled by environmental factors, i.e. corrosion reaction. In the v-K curve, it was shown that an increase in the copper content decreases the region II plateau velocity by several orders of magnitude. For Cu-free alloys the plateau velocity was about 1.2 x 10^{-8} m/s and for alloys containing 2.1 wt% Cu the plateau velocity decreased to 4.1 x 10^{-10} m/s. Similar trends were also observed in overage conditions as well, increase in Cu content consistently decreased the plateau velocity. TEM images of the 1% plastic strained samples showed inhomogeneous planar deformation in low Cu-containing alloys and homogeneous lopping (wavy) deformation in higher copper alloys. This change in dislocation microstructure resulted in the shifting of

the region I line to the right in the v-K curve of higher Cu alloys. The reduction in the region II velocity attributed to the shift in electrochemical activity of the grain boundary precipitates as a function of Cu content. This study claimed that fast quench is beneficial as they retain Cu in solid solution, resulting in higher Cu containing precipitates during subsequent ageing process. In Cu lean alloys, slow quenching improved the SCC resistance. This was due to the formation of incoherent precipitates that led to homogenous deformation. These statements were based on the assumptions that in peak age temper, the Cu added in solid solution is fully incorporated in the precipitate. This work did not show any experimental data for phase composition to show an increase in Cu content for precipitates with an increase in the bulk Cu content.

Ramagopal et al. [62] experimentally showed the effect of the addition of Cu on the electrochemical activity of the $MgZn_2$ thin films prepared by flash evaporation. The open circuit potential (OCP) of the 7150 alloy was measured and recorded as a function of time. Later, this potential transient was applied to the thin film analog samples and the corresponding current responses of the thin films were measured (OCP play back). Copper additions, up to about 8 at %, did not have much influence on the breakdown potential; however, with a further increase in Cu concentration, the breakdown potential was ennobled. The OCP playback experiments showed that the low Cu-containing precipitates would completely dissolve during exposure at OCP in a deaerated chloride solution. However, in the case of high Cu-containing alloys, the particles did not completely dissolve at OCP. They proposed that these precipitate (at higher Cu concentrations) could de-alloy leading to the enrichment of Cu, which can in turn affect the corrosion behavior of the 7xxx alloys. In high pH solutions, these thin film analogs are susceptible to localized breakdown

due to the protection offered by the stability of $Mg(OH)_2$. Therefore, in terms of relevance to IGC of 7xxx alloys, the authors suggested that the grain boundary precipitate phases will undergo preferential dissolution at potentials well below the critical potentials associated with intergranular corrosion.

Gupta et al. [45] studied the effects of Cu addition on the metastable pitting rate (MPR) of the 7xxx aluminum alloy. They used 7079 (low Cu) and 7150 (high Cu) in the T651 temper to correlating precipitate size, shape and composition with the MPR and the pit density after exposure. TEM analysis of grain boundary precipitates confirmed a higher Cu content (16 at%) in 7150 compared to (1 at%) in 7079. They reported that the breakdown potential in deaerated 0.01M NaCl did not differentiate the electrochemical activity as a function of microstructural changes (ageing). However, the MPR had a clear correlation with stable pitting. In 7079, the MPR increased with increasing precipitate size of the bulk alloy, but 7150-showed inverse relationship for a larger precipitate size. This transition in MPR was associated with the compositional changes that occurred during precipitate evolution. With a longer aging time, the Cu content of the precipitate also increased in 7150 and as a result, the dissolution kinetics of the precipitates were altered. The enrichment of Cu in precipitates is dependent on the total Cu content of the alloy. The MPR also correlated well with the region II velocity of the v-k curve in 0.1M NaCl.

Xu et al. [63] reported the beneficial effect of high temperature dissolution of the S-phase (Al_2MgCu) on the SCC performance of 7150. The addition of Cu led to the presence of a significant part of Cu in the form of S phase and Al_7Cu_2Fe after casting, resulting in the degradation of the tensile properties, fracture toughness, and the resistance to environment-assisted cracking (EAC) of the final product. They compared the SCC performance of

single step solution heat treatment (475^{o}C for 8h), to multi step treatment (475^{o}C for 8h + 485^{o}C for 4h + 495^{o}C for 2h) or the RRA temper (120^{o}C/24h + 185^{o}C/1.5h + 120^{o}C/24h). The TEM analysis showed that the Cu content in multistep treatment (MSS) samples grain boundary precipitate is 8.1 at% compared to 4.2 at% for the single step precipitates. Electrochemical measurements showed that the multistep samples (MSS) samples had noble E_{corr} and higher polarization resistance values than single step samples. Interestingly, in both cases, the Al_7Cu_2Fe/matrix interface remained relatively unattacked. The MSS samples also reported to have higher threshold stress intensity value than single-step samples. The improved corrosion resistance in MSS is associated with the high solubility of the s-phase during high-temperature solution heat treatment. The dissolved S particles can also release Mg and Cu atoms during stepped solution treatment. Extra Cu tends to be contained in the relatively higher volume fraction of precipitates after RRA treatment. The decrease in the crack velocity was attributed to the reduced rate of dissolution of the more noble precipitates or reduced rate of hydrogen ion reduction and hydrogen absorption at the crack tip at the more noble potential.

Wang et al. [64] studied the effect of Cu content on the susceptibility of the commercial 7xxx alloys in the salt spray environment. In Cu-containing alloys, they reported Al_7Cu_2Fe as primary intermetallic particles, while in Cu free alloy it was Al_3Fe. A double break down potential was observed for Cu containing 7055 while a single break down potential was observed for the Cu lean alloy in polarization experiments in 3.5% NaCl. The effect of changes in the matrix Zn content dominated the effect of changes in the matrix Cu content for underaged samples, while the opposite trend was reported for overaged samples. For the Cu-free Al alloy, the break-down potential increased with aging. This was attributed to

the depletion of the matrix Zn content resulting from the nucleation and growth of precipitates. The pitting corrosion depth changed with ageing practice in Cu containing alloys, the overaged temper had deepest pit and peak aged temper had shallowest pits. In Cu-free alloys no such trend was observed and the pit depth was significantly lower than 7055. In 7055 the pits were observed around Al_7Cu_2Fe and the depletion of the Cu content had a larger impact on localized pitting corrosion than the matrix Zn content. In Cu-free alloys, pits were observed around Al_3Fe but these particles sustained lower cathodic current than Al_7Cu_2Fe.

Meng et al. [65] reported the detrimental effect of Cu addition to the pitting and polarization resistance behavior of 7xxx alloys. The samples were solution heat treated at 475 ° C for 30 min followed by quenching in water, then artificially aged to T6 temper (120 ° C for 24h). Energy dispersive spectrum (EDS) analysis of the precipitate indicated that with increasing bulk Cu content the Cu content of the precipitates also increased. Polarization curves in acidified 0.5M NaCl solution showed two breakdown potentials. The first breakdown potential was associated with transient dissolution at the surface, while sustained dissolution occurred above the second breakdown potential. They also reported semi-continuous shallow attack on grain boundaries in the low Cu content alloys, while continuous and relatively deep intergranular attack was reported in high Cu alloys. Under free-corrosion potential conditions, the polarization resistance of high-Cu alloys were consistently lower than that of Cu-free alloys. X-ray photoelectron spectroscopy (XPS) analysis of the corroded products clearly indicated the presence of Cu rich clusters in the high Cu-containing alloys. Such Cu enrichment on the surface facilitates the oxygen

reduction reaction. Due to this effect, the overall influence of Cu on the corrosion behavior is detrimental, despite the increase in the breakdown potentials with Cu content.

2.2.2 Effect of Zn/Mg ratio

The work of Gruhl [44] work provided SCC data for low- and high-copper-containing Al-Zn-Mg-Cu alloys. In this study alloys with a Zn / Mg alloy ratio was between 2.7 and 3 had a high SCC resistance. In the peak age (T6) temper, addition of 1% Cu to alloys with varying Zn:Mg ratios increases the 'duration of life" or EAC resistance by an order of magnitude.

Holroyd et al. [66] summarized the data of SCC of 7xxx in saline solutions. For the 7xxx alloys, containing Cu less than 0.2 wt% or greater than 0.8 wt% both the Zn/Mg ratio and the excess Mg had an effect. The crack velocities decreased with increasing Zn / Mg ratio and reached a minimum for a ratio value between 2 and 3. A further increase in the ratio increased the crack velocities. Similarly, for this Cu range, the increase in excess Mg decreased the crack velocities up to a value of 2 and a further increase in excess Mg increased the crack velocity again. However, for alloys with Cu levels in between 0.2 and 0.8 wt%, such a trend in crack velocities was observed only with excess Mg content. They also predicted that only 0.8 wt% copper is required for over-aging to be beneficial for SCC resistance rather than the widely accepted level of 1 wt% copper.

Recently, Wang et al. [67] reported the effect of the Zn / Mg ratio (2, 2.5, 3, 3.6 and 4) on microstructure and stress corrosion cracking of low Cu (0.09 wt%) 7005 alloy. After hot rolling, the samples were solutionized at 475 ° C for 1.5 hr followed by quenching in water at room temperature and aging at 120 ° C. They noticed that when the Zn/Mg ratio is

relatively low, an increase in Zn content delays the time that the alloy reaches the peak hardness point. Two age peaks were observed when the Zn / Mg ratio is greater than 3. The first peak was associated with the GPII and the second with η'. An increase in the Zn/Mg ratio increased the electrical conductivity of the alloys. TEM data indicated that as the Zn/Mg ratio increased, the grain boundary precipitate phase of the alloy gradually became larger and shifted from a continuous precipitation to discontinuous precipitates at the grain boundaries. The SCC test in 3.5% NaCl + 0.5% H_2O_2 showed that the resistance to SCC increases with increasing Zn / Mg ratio. They also postulated that smaller η' precipitates and GP I zones undergo faster dissolution in the chloride-containing environment. This results in the formation of Mg-H corrosion channels that would accelerate the expansion of micro cracks. With increasing Zn / Mg ratio, the coarser and discontinuous η' precipitates at the grain boundary improves the resistance of SCC.

Wu et al. [68] reported the effects of the Cu / Mg ratio (0.67, 1.0, 1.06, 1.6) on the microstructure, mechanical properties and corrosion behavior of the AA7085. After hot extrusion at 420 ° C, the samples were solutionized at 475 ° C for 2 h followed by water quench and T6 aging at 120 ° C for 24 h. They reported that the degrees of recrystallization increased with a decrease in the Cu/Mg ratio. They predicted that when the Cu/Mg ratio is equal to 1, the trend for the formation of Al-Cu-Zn phases will be strong. For lower ratio values, when the Mg content increases, the trend of forming intermetallic compounds, such as the phases S (Al_2CuMg), T ($Al_2Mg_3Zn_3$) and η (MgZn2) increases. They also mentioned that the amount of S phase would be lower for alloys of lower ratio than that of the alloys with a Cu / Mg ratio of 1. Therefore, with an increase in the Cu/Mg ratio, the volume fraction of other tiny phases increases, resulting in higher Zener pinning. In other words,

the dispersion of these particles will exert a retarding force or pressure on the moving grain boundaries. The mechanical properties of the alloy have a close relationship with the degree of recrystallization. The fully recrystallized alloy exhibited low fracture toughness due to the higher density of the grain boundary precipitates. However, partially recrystallized alloys exhibited higher fracture toughness with ductile transgranular fracture. Similarly, in fully recrystallized grain materials, precipitates with higher density formed at the high-angle grain boundaries and were preferentially attacked at the beginning of intergranular corrosion. In partially recrystallized materials with fine sub-grain boundaries the precipitates were fine and discontinuous at the grain boundary. This partially recrystallized appears to have increased resistance to intergranular corrosion and exfoliation corrosion.

2.2.3 Effect of minor alloying elements (Zr, Yb, Cr, Er)

When the F-temper samples are subjected to solution heat treatment, the deformed grains due to the prior rolling practice undergo a phenomenon called recrystallization. This is defined as the process of removing defects in the microstructure by nucleation and migration of high-angle grain boundaries. At the end of the recrystallization process, the deformed grains are completely replaced by equiaxed grains with a mis-orientation angle greater than 15^{o} [69]. These high angle grain boundaries tend to be energetically favorable for precipitate nucleation during the aging sequence. The resulting grain boundary microstructure consists of a continuous presence of precipitate, and they are highly susceptible to intergranular attack [70]. Elements such as Zr, Cr, Er, Sc are added to the aluminum alloys to form nanometer-sized dispersoids in order to inhibit the recrystallization. The coherent and cubic L12 Al_3Zr dispersoids more efficiently exert a

Zener drag on migrating subgrain boundaries during high-temperature processing (e.g., extrusion or hot rolling) and annealing of the alloy [71]. Zener drag is the phenomenon of the dispersed second-phase particle exerting a drag force on the migrating grain boundary [72]. Inhibition of recrystallization during the thermal treatment process results in the preservation of the unrecrytallized microstructure from the prior rolling process. The unrecrystallized microstructure contains subgrain boundaries with a lower misoreintation angle. These grain boundaries are not energetically favorable for precipitate nucleation during ageing treatment and as a result, they are not susceptible to intergranular corrosion [70].

Chen et al. [73] studied the effect of micro alloying elements such as the addition of Yb, Cr and Zr on microstructure, mechanical properties and corrosion behavior. The extruded samples were heated to solution at 480^{o}C for 2h followed by water quench and aged to T6 at 130 ° C for 24h. XRD measurements showed the presence of $YbCr_2Al_{20}$ dispersoids in alloys containing Yb. The crystal structures of these dispersoids are of the type cubic $CeCr_2Al_{20}$. These dispersoids stabilized the deformation–recovery microstructure with low angle subgrain or grain boundaries by pinning the subgrain boundaries and retarding the transformation of subgrain boundaries to high angle grain boundaries. The η phase particles were distributed discontinuously at the grain boundaries of the non-recrystallized alloy with high proportion of low angle grain boundaries. This, in turn, appears to have improved exfoliation and intergranular corrosion resistance. In general, complex additions of Yb, Cr and Zr to the Al-Zn-Mg-Cu alloy resulted in increased resistance to stress corrosion cracking and increased the threshold or critical stress intensity factor (K_{ISCC}) from 9.8 to 17.0MPa $m^{1/2}$.

Fang et al. [74] followed up on Chen et al [73] work to probe into the localized corrosion of Al–Zn–Mg–Cu alloy with micro additions of Yb, Cr, and Zr. Electrochemical polarization in IGC test solution (30 g/L NaCl + 10 g/L HCl) showed that Yb additions pushed the free corrosion potential in a noble direction and decreased the corrosion current.

Work on other rare earth elements such as the Al-Zn-Mg-Cu-Zr alloy had been reported as well [75]. TEM and selected area electron diffraction (SAED) patterns confirmed the presence of coherent Zn, Mg, Cu, and Cr-containing Al_3(Zr, Er) dispersoids. These dispersoids inhibited recrystallization more than those of the Yb, Cr--containing alloys. This resulted in higher resistance to exfoliation corrosion (EXCO) (Rank EA, based on ASTM G34 [76]) than the alloys containing recrystallized microstructure (rank EB+, based on ASTM G34 [76]). The critical stress intensity factor of the stress corrosion cracking K_{ISCC} in the v-K plot increased from 9.2 to 22 MPa $m^{1/2}$ in the Er-containing alloy. Even U-bend samples didn't fail after 149 h exposure in 3.5% NaCl solution, while the recrystallized material failed into two independent pieces after 10 min of exposure. The addition of rare earth stabilized the $L1_2$ – structured coarsening resistant and coherent Al_3(Zr,RE) type dispersoids. These dispersoids significantly inhibited recrystallization by pining the grain boundary and stabilized the deformation–recovery microstructure with numerous fine subgrain boundaries. Finer and scattered $MgZn_2$ phases precipitated along the unrecrystallized subgrain boundaries having a lower energy, which led to decreasing the percentages of intergranular fracture, delaying the propagation of SCC crack, and increasing the fracture toughness and localized corrosion resistance of the Al-Zn-Mg-Cu alloy.

S. Chen et al. [77] investigated the effect of recrystallization related to the grain boundary and its influence on the size and distribution of grain boundary precipitate. They controlled the degree of recrystallization for a 20mm thick forged 7085 (7.5Zn, 1.5Cu, 1.6Mg, 0.12Zr, 0.06Fe, 0.02Si and balance Al, wt.%), by subjecting them to solution heat treatment for 1h. These samples were further aged to T6 (120 ° C @ 24h) and T74 (110 ° C @ 6 h + 160 ° C @ 10 h). The fracture surface after mechanical testing indicated that with an increase in the volume fraction of recrystallization, the morphology changed from transgranular to intergranular. The SCC test indicated that the cracking susceptibility decreased with decreasing recrystallization fraction. TEM images showed that fine grain boundary precipitate increased with a decrease in the volume fraction of recrystallized grains. The improved resistance was associated with the ability of unrecrystallized boundaries to act as hydrogen trapping sites and decrease hydrogen concentration in grain boundaries. In addition, the large number of subgrains was benefited to homogeneous slip. In the improved SCC resistance was associated with coarsening of grain boundary precipitate and enrichment of Cu concentration.

M.B.Kannan et al. [78] reported the improved resistance to SCC of the Al–Zn–Mg–Cu–Zr with addition of scandium, Sc. The samples were heat treated to 465^{o}C followed by water quench and two-step peak aging conditions (100 ° C @ 8h + 120^{o}C @ 8h). The scandium-containing alloy showed elongated fibrous unrecrystallized grains, whereas the base alloy revealed large pancake-shaped grains as well as equiaxed recrystallized grains. TEM images of the grain boundary showed that the base alloy had a continuous presence of precipitates along the grain boundary while the scandium-containing alloy showed discontinuity in the arrangement of precipitates along the grain boundary. No differences

were observed in the chemical composition between the grain boundary precipitates of the two alloys. The slow strain test showed that the scandium-containing alloy had a higher strain ratio than the base alloy. Similarly, the U-bend samples of the base alloy failed after 20 h of exposure, while the Sc-containing alloy didn't fail even after four months of exposure. The improved SCC resistance of the scandium-containing alloy was associated with the discontinuity in the grain boundary precipitate, resulting in a lower rate of dissolution.

2.3 Joining of 7xxx

Thermal dissipation during the joining process induces localized isothermal sections. This thermal gradient is detrimental to the microstructure and affects the mechanical properties of the welded joint [50]. During fusion welding of heat treatable aluminum alloys (2xxx, 6xxx, 7xxx), the region close to the base metal (heat affected zone) experiences a relatively lower temperature; this results in the coarsening of the precipitates similar to the overaging process. The zone next to this region called the fusion zone experiences a temperature above the solvus limit and the precipitates in this zone are completely dissolved into the matrix. Finally, the zone adjacent to the fusion zone is called a partially melted zone. The grain boundaries in the partially melted zone are rich in the solute. [79, 80]

The resistance spot welding (RSW) process is based on the joules law of heating, and the resistance (R) between the faying surfaces increases the heat output (J) when a constant current (I) is applied on them ($J = I^2R$). The heat generated during this process results in fusion welding of the surfaces. After the current flow is stopped, the electrode force is maintained for another short duration (forging step) to allow the workpiece to rapidly cool

and solidify. Generally, the microstructure of Al alloy resistance spot welds can be divided into three distinct zones: the base metal (BM), the heat-affected zone (HAZ), the fusion zone (FZ) or the nugget zone. Furthermore, the Al alloys have shown that the FZ contained two different microstructures, ie, a columnar grain structure at the edge of the nugget and an equiaxed grain structure at the center of the nugget (Error! Reference source not found.). T he reason for the two different microstructures was associated with the variation in cooling rate within the nugget zone.

F.Hayat [81] studied the effect of ageing treatment on the similar and dissimilar resistance spot welds of 6061-T6 to 7075-T651. They noticed that the HAZ is formed in different grain sizes and widths at 6061 and 7075 alloy portions of dissimilar RSW joints. Similarly, the fusion zone was narrower for 7075 compared to 6061. A higher degree of incipient melting was observed on the 7075 near the transition zone between fusion and HAZ. This was attributed to the wide solidification range of the alloy. The porosity in the fusion zone was associated with hydrogen, as it can dissolve in a greater amount in liquid aluminum. XRD and electron probe micro analysis (EPMA) analysis confirmed the presence of various intermetallics such as AlZn, AlMg and MgO and $Mg_2AlSi_4O_{12}$ at the interface of weld joints. The decrease in microhardness was attributed to the dissolution of strengthening precipitates in welds of the Al alloy. The largest reduction in microhardness was observed in the nugget of the welds, where the melting of the base materials promoted the total dissolution of the strengthening precipitates. The fracture mode during the tensile testing was the button mode in the dissimilar weld joint. The 7075 fractographs showed a clear sign of brittle failure, while the 6061 side showed ductile failure. The distinct

difference in the fracture surface was associated with the presence of brittle intermetallic phases.

S.Wu et al. [82] recently reported the presence of a thermo-mechanically affected zone (TMAZ) in AA6111 spot welded samples. The region between the base metal (BM) and the weld nugget, which experienced both heat and indentation deformation during the welding process, was defined as TMAZ. The reported width of the TMAZ was 1.5 to 2.0 mm. They further classified this region in to three parts TMAZ – I, II and III based on the location from the fusion zone. Region I was close to the partially melted zone and located at the nugget boundary. It was harder than the nugget, but softer than the BM. Region II was a cylindrical shell around the nugget and was harder than region BM. TEM examination of the FIB liftoff in this region showed a clear presence of dislocation cells and a few GP zones. Therefore, the increase in hardness was attributed to the hardening of the strain. Finally, region III is between the nugget and the outer sheet surfaces at the electrode imprint, and the hardness value is comparable to that of BM. The fracture mode was interfacial fracture during tensile testing. The metallography cross section of the fractured surface showed that the fracture began at the sharp weld notch, then propagated through the soft nugget. It provides the least resistance to fracture. The relatively large difference in the hardness profile of the nugget and the hardened TMAZ constitute a metallurgical notch that impacts load transference throughout the joint. This is very critical in cyclic load situations where fatigue crack often starts at this combined metallurgical and geometrical notch on the faying surface.

Recently Maddela et al. [83] compared the corrosion performance of the RSW and self-pierce rivet joints of 6061-T4 and low-carbon steel. After 50 cycles of exposure to

GMW17026, they noticed that RSW joints exhibited higher galvanic corrosion resistance compared to the riveted joint. However, the addition of structural adhesive improved the galvanic corrosion performance of the riveted joints. The residual strength of the joints after corrosion testing showed a similar trend. The RSW joints did not exhibit a statistically significant drop in strength; of the strength however, the riveted joints dropped by 48% compared to unexposed samples. Interestingly, both adhesive RSW and riveted joints showed a 55% drop in strength, which was attributed to the degradation of adhesive at the interface resulting from the cyclic corrosion testing.

Although the microstructure of the spot-welded joints have been characterized in detail, the corrosion aspect of this microstructure remains largely unexplored.

2.4 Problem definition

Data from the literature on 7xxx effect of grain size on the corrosion appears to be inconclusive. Tsai et al. [54] work was carried out on two commercially available products with different grain sizes. It did not focus on the effect of specific processing sequence impacting grain size and subsequent effect on stress corrosion cracking susceptibility. Few factors such as the degree of cold work reduction, recovery annealing temperature, and duration of solution heat treatment play dominant role in affecting the grain size of the material during sheet metal manufacturing. In the case of precipitate hardening alloys such as 7xxx, the grain size variation could affect the precipitate microstructure at the grain boundary (size and, composition) and in turn affects the corrosion performance. Therefore, there is a need to *understand the effect of grain size on the corrosion performance of 7xxx alloys.*

In the area of the 7xxx alloy composition, the role of Cu is under constant scrutiny. However, none of the reported works varied Cu with the same upstream processing parameters, such as the homogenization step, the reduction of hot and cold work. In most of the work, the final solution heat treatment and ageing steps were kept the same but the upstream processing sequences of the alloys were unknown. The majority of the reported literature work shows that the addition of Cu improves intergranular corrosion due to the incorporation of Cu in $MgZn_2$ particles [46, 62, 84]. In precracked specimens, the increase in Cu content increases the threshold stress intensity factor and decreases the region II plateau velocity. However, the increase in the number of Al7Cu2Fe-type particles in high Cu alloys remains a concern due to its higher cathodic activity relative to the matrix [85]. Zr is added to the 7xxx matrix to inhibit recrystallization, due to the formation of Al_3Zr dispersoids. Such an unrecrystallized microstructure affects the misorientation angle and subsequent grain-boundary corrosion resistance. Alloys with combination of unrecrystallized microstructure and Cu addition have resulted in the high strength in new class of 7xxx alloys [60, 61]. However, *there is limited understanding of the effect of Cu and Zr on the corrosion performance of such alloys.*

When it comes to 7xxx joint corrosion, the data in the literature mainly focuses on the solid-state welding process such as the friction stir welding process but the data on the RSW process are very scant. Interestingly, the RSW is one of the commonly used joining technique by automotive original equipment manufacturer (OEM). A typical automotive body structure has 3000 – 5000 spot welds, yet very limited corrosion data is available [86]. The RSW process results in gradient microstructures that are very susceptible to

localized corrosion. Therefore, a need for *characterizing the 7xxx RSW microstructure and its impact on the corrosion resistance of the joints is needed.*

2.5 Hypothesis

1. The microstructure of the grain boundary and composition of features such as the grain boundary precipitate (size and distribution) and the adjacent precipitate freezone is affected by changing the grain size of the material. This in turn affects the corrosion morphology and the SCC resistance.
2. The addition of Cu in Zr-containing alloys appears to increase Al_7Cu_2Fe and S phase particles. The increase in Al_7Cu_2Fe particles will result in increased pitting susceptibility and decreased resistance to SCC. The increase in S phase particles has an effect on the Al_3Zr number densities. This in turn will affect the misorientation angle resulting in intergranular attack morphology.
3. Zn/Mg ratio in the matrix affects the grain boundary composition (PFZ and GBP) and this in turn affects the SCC performance in humid environment due to interaction with the adsorbed hydrogen.
4. The sensitized grain boundary in the heat affected zone controls the corrosion performance and durability of the 7xxx RSW joints.

2.6 Research objectives

The overall objective of this work is to understand the effect of alloy composition, processing sequence, and joining methods on the structural forms of corrosion (IGC, SCC) in 7xxx class of sheet gauge alloys. The following subsections outline the specific aspects of the work that will be investigated to fill known gaps in existing research.

2.6.1 Effect of grain size on the SCC of 7075-T6

The aim of this work is to establish a link between grain size and its effect on grain boundary microstructure and its subsequent effect on corrosion resistance. The features of grain boundary microstructure that are of interest in this work are size, continuity, and composition of grain boundary precipitate and the adjoining precipitate free zone.

In this work, we will explore two distinct methods namely the cold work reduction and recovery anneal, to control the grain size. The grain boundary features will be characterized by scanning transmission electron microscopy (STEM). The samples will then be subjected to IGC, SCC, and hydrogen penetration tests to determine the underlying mechanism of stress corrosion cracking.

2.6.2 Effect of Cu addition on the SCC of Zr containing 7xxx-T6

The purpose of this work is to understand the effect of major (Cu) and minor (Zr) alloying elements on the corrosion performance of Al-Mg-Zn alloys. This would unravel the link between the alloy composition and corrosion property relationship of 7xxx alloys.

Alloys with controlled addition of Cu (0.3, 1.17, 1.35 wt%) and Zr (0.1 wt%) to the 7xxx matrix will be obtained by the direct chill casting method. The samples will be then subjected to similar homogenization, hot and cold roll sequence to obtain 2mm thick material. The resulting microstructure will be characterized and evaluated for its corrosion resistance. The specific focus will be on the effect of the testing environment and second phase particles (constituents and precipitates) on the localized corrosion resistance of these alloys.

2.6.3 Effect of Zn/Mg ratio on the SCC of high solute 7xxx-T6 in humid environment

Recent publication in the European Aviation Safety Agency (EASA) safety information bulletin (SIB No: 2018-04) indicated that the high solute level of the next generation of the 7xxx alloys may be susceptible to cracking in a humid environment. Zn and Mg ratio is one of the key parameter that is adjusted to increase the strength of the alloys. The objective of this work is to assess the effect of bulk Zn/Mg ratio on the SCC performance in humid environment.

2.6.4 Microstructure and corrosion characterization of the 7075-5182 dissimilar joints via resistance spot welding and self-pierce rivet.

The goal of this work is to understand the effect of the 7075 to 5182 RSW and SPR microstructure on its corrosion resistance. This work would also focus on the evaluation of the corrosion performance of different joints (7xxx to 5182) and the post-weld heat treatment. The weld microstructure will be characterized and the concepts of the localized electrochemical technique will be applied extensively.

CHAPTER 3: EXPERIMENTAL

In this dissertation, the following characterization methods were extensively used to understand the link between the grain boundary microstructure and the corrosion performance of the 7xxx alloys. The experimental methods are broadly classified into microstructure characterization, corrosion evaluation, and density functional theory simulation.

3.1 Microstructure Characterization

This section includes the basic principles and method details of the techniques that were used to determine the composition, imaging of the microstructure features, and local mechanical property evaluation.

3.1.1 Inductively coupled plasma - optical emission spectroscopy (ICP-OES)

To measure the alloy composition of the samples, inductively coupled plasma with optical emission spectroscopy (ICP-OES) was used. ICP-OES is an analytical technique that can be used to identify and measure the concentration of elements of interest. The ICP-OES uses an argon plasma to excite atoms of elements in the assay, and as they return to ground state, they emit light of specific wavelength. This characteristic wavelength is used to identify elements within the assay. The amount of light released at each wavelength is proportional to the number of atoms or ions making the transition, and from Beer-Lamberts law one could determine the concentration of the elements based on the light intensity. In this work, the Varian Vista Pro ICP-OES that was calibrated with the CPI international multielement custom standard containing Cu, Fe, Mg, Mn, and Zn Cr, Ni, Ti and V was

used. The aluminum samples were digested in orthophosphoric acid at 200^{o}C to prepare the assay.

3.1.2 Optical microscopy

Optical microscopy was extensively used to examine features such as the grain structure, the morphology of the corrosion attack, and the crack propagation path of the fractured samples. To analyze the grain structures the samples were mounted on the epoxy molds and progressively polished to 0.05 μm finish, followed by anodizing in Barker's solution (1.8% Fluoboric acid in water) at 25V DC for 2 minutes. The etched samples were imaged under plane polarized light with tint using the Ziess AxioImager.A1m metallurgical microscope. The corrosion morphology after immersion experiments was determined by imaging polished cross sections of the samples with the Keyence VHX 5000 digital optical microscope. A similar procedure was adopted to image the fractured samples after sectioning along the loading direction.

3.1.3 Electron microscopy

When an accelerated electron beam interacts with the material atoms, several phenomena could occur simultaneously depending on the thickness of the sample [87]. Some key examples include generation of secondary electrons, backscattering of primary electron beam, generation of characteristic X-rays, and elastically and inelastically scattered electrons. The application of each of these phenomena can offer value insights into the microstructure of the material at different length scales. These include information on grain boundary misorientation angle, texture, imaging of fractured surface, particle analysis,

grain boundary features characterization, etc. [88]. The following is a summary of the key methods that were used in this work.

3.1.4 Scanning electron microscopy (SEM)

Secondary electrons (SE) are generated when an accelerated electron beam ejects weakly bound conduction band electrons in metals. This process is an inelastic electron scattering event, and the SE suffers rapid energy loss with distance traveled, limiting the range of an SE to a few nanometers. As a result, only the electrons generated from the surface of the samples reach the detector, allowing for an accurate characterization of the surface features using this method. Fractured surface images were characterized under the secondary electron imaging mode in the FEI Versa Dual Beam SEM at an accelerated voltage of 20 kV. To prepare the fractured surfaces for imaging, the samples were cleaned with hexane and methanol to remove loose dirt and grease, followed by drying with compressed air. For samples with extensive corrosion product on the fractured surface, desmutting was performed using concentrated HNO_3.

3.1.5 Scanning Transmission Electron Microscopy (STEM).

When the thickness of a sample is in the order of a few nanometers, an accelerated electron beam can be transmitted through the material, resulting in elastic and inelastic scattering events. In a Scanning Transmission Electron Microscope (STEM), a bright field image is formed when the detector captures electrons scattered at low angles (< 10 mrad) [89]. The detector also collects electrons that pass through the sample with little or no scattering, creating a high-contrast image of the sample's atomic structure. In STEM, a fine electron

probe is scanned across the sample, allowing for the acquisition of a series of images that can be used to reconstruct a high-resolution image of the sample.

The grain boundary features, such as precipitates and adjoining precipitate-free zones, were imaged in bright field mode using FEI Versa Dual Beam SEM equipped with a STEM 3+ detector at an accelerated voltage of 30 kV or a Tecnai G2 F30 S-TWIN FEG transmission electron microscope in STEM mode at 300 kV. STEM lamellae were prepared by sequential grinding down the samples to a thickness of 100 µm, followed by jet polishing in a mixture of 30% HNO_3 and CH_3OH at -25°C. A DC voltage of 15.5 V was used in the Struers twin jet electropolisher machine to make the perforated specimen.

3.1.6 Energy dispersive spectroscopy (EDS)

The characteristics of X-rays are generated as a result of the interaction between the incoming electron beam and the electrons in the inner core shell of a metal atom [88]. When the kinetic energy of the electron beam is greater than the ionization energy of the electron in the inner shell, such as the K-shell, a vacancy is created due to removal of this inner-shell electron. Electrons from an outer shell, such as the L-shell, make a transition to fill this hole, releasing energy in the form of X-rays during this K-L intershell transition. As the electron shell energy levels are highly discretized, the energy of the generated X-ray is unique to the transition and can be used to identify the element. To determine the composition of the grain boundary precipitates and adjoining precipitate free zone, the Tecnai G2 F30 S-TWIN FEG transmission electron microscope equipped with the PentaFET Precision Xplore - 80mm^2 SDD from Oxford instruments was used at an

accelerated voltage of 300 kV or FEI Apreo equipped with Oxford's XmaxN - 150 mm^2 SDD and STEM 3+ detector at an accelerating voltage of 30kV.

3.1.7 Electron backscattered diffraction (EBSD)

When the primary electron interacts with the crystalline materials, the backscattered electrons that are generated through the elastic scattering events can be diffracted by the atomic arrangements in crystalline materials. These diffracted electrons when captured on a phosphor screen exhibit line patterns called Kikuchi bands or electron backscattered patterns (EBSP). These data serve the purpose of identifying the phase, indexing the pattern, and determining the orientation of the crystal from which the pattern originated [90]. In addition, the local average misorientation (LAM) maps give information on the plastic strain within the grain or crystal [91]. This is a pixel-based measurement that calculates the average misorientation between a point on the 3x3 measurement grid and its neighbors. In this work, FEI Versa Dual Beam SEM equipped with the NordlysMax detector from Oxford instruments was used for the EBSD measurements. The samples were polished to 0.05 µm colloidal silica finish and placed at an angle 70^o to the primary electron beam. The accelerating voltage was set at 20kV with a EBSD scan step size of 1um was used. The data were analyzed in the Aztec crystal software.

3.1.8 Microhardness

Vickers hardness is commonly used to determine the ability of the materials to resist indentation. The microstructure changes brought about by the various joining methods can be characterized with the help of a hardness map. The Vickers microhardness distribution maps were measured on the cross-section of the resistance spot welded and self-pierce rivet

joints using the LECO 248AT tester under a load of 50 gf for 15 seconds. The spacing between the subsequent indentation was maintained at least 2.5 times the width of the indenter to conform with the ASTM E384-17 standard. The joint samples were sectioned and polished to a 0.05 µm finish.

3.2 Corrosion Testing

The following section briefly describes the methods that were used to assess the corrosion performance of the monolithic and joint samples. They are based on commonly used ASTM standards and automotive original equipment manufacturer (OEM) test cycles.

3.2.1 Immersion experiments

To determine the morphology of the corrosion, the samples were immersed in a solution containing NaCl and H_2O_2 according to ASTM G110. This standard is mainly used for heat treatable aluminum alloys such as 2xxx and 7xxx alloys. The samples were etched in HNO_3 and HF containing solution followed by exposure in NaCl and H_2O_2 over a period of 24h. After exposure, the samples were sectioned, polished, and examined under an optical microscope.

3.2.2 Slow strain rate test (SSRT)

The slow strain rate technique is an uniaxial tensile testing method performed at a strain rate of 10-6 s^{-1}. The samples are tested in an inert environment such as air or silicone oil, as well as in corrosive environments of interest. The ratio of the mechanical properties (yield strength, total elongation) in the corrosive to inert environment gives a measure of the susceptibility to stress corrosion cracking (SCC) [92]. A ratio close to 1 indicates that

the material has higher resistance to SCC in the tested conditions, while lower values indicate lower resistance. In this work, the samples were machined into a flat dog-bone geometry and the side sections were polished to remove machining marks. A nominal strain rate of 2 x 10^{-6} s^{-1} was used in both air and ASTM D1384 (165 ppm NaCl + 138 ppm $NaHCO_3$ + 148 ppm Na_2SO_4) containing 1% H_2O_2 peroxide. After the test, the fractured samples were subjected to metallography cross-section and SEM examination to determine fracture mode and morphology.

3.2.3 Constant displacement test

Constant displacement testing was carried out to assess the resistance to SCC of the 7xxx alloys in humid environment. Two types of constant displacement frames were used, namely uniaxial and four point bend fixtures. The uniaxial constant displacement frame was based on the ASTM G49-85 (2019) standard. The specimen is machined to a dog bone geometry and loaded to the predetermined stress level, and locked into the final position by moving the side beams. The stress level of the samples was monitored using the strain measurements from the digital image correlation (DIC). Four-point bending fixtures were based on the ASTM standard G39-99 (2021). The sample geometry is rectangular shape with dimension of 4" (rolling) by 1" and the sheared edges were polished to 240 grit finish. The samples were assembled in the four-point bend fixture and loaded to a predetermined stress level based on the deflection. The following equation relates the stress level at the midpoint of the samples to the deflection.

$$\sigma = \frac{12Ety}{3H^2 - 4A^2}$$

Where σ is the maximum tensile stress at the midpoint of the rectangular specimen, E is the modulus elasticity, t is the thickness of the specimen, y is the maximum deflection (between the outer supports), H is the distance between the outer supports and A is the distance between the inner and outer supports. The dimensions of the fixtures were chosen such that H = 4A.

3.2.4 Electrochemical Polarization

The samples were tested in the mill finish condition after degreasing with hexane and methanol to remove loose dirt and organics. Potentiodynamic tests were carried out in Gamry reference 600 electrochemical unit. The aluminum sample of interest was the working electrode while saturated calomel and graphite were used as the reference and counter electrode, respectively. Before the start of the polarization, the free corrosion potential (E_{corr}) was monitored over a period of 1h to allow the system to reach a stable equilibrium. For the anodic polarization the potential window was from -20mV_{Ecorr} to + 1000mV_{Ecorr} and for the cathodic polarization it was from +20mV_{Ecorr} to -1000mV_{Ecorr}. A scan rate of 10mV/min was used for both polarization types. For measuring galvanic current corrosion transients, the zero resistance ammeter (ZRA) mode was used. The samples were placed at the two ends of the flat electrochemical cell, one sample was connected to the working and working sense electrode, and the other sample connected to the counter and counter sense. The saturated calomel was used as the reference electrode. The transients were measured over a period of 24h.

3.2.5 Scanning Vibrating Electrode Technique (SVET)

The scanning vibrating electrode technique (SVET) measures the potential gradients developed in the electrolyte as a result of the flow of ionic currents between the anodic and cathodic zones [93]. As a result, this can be used to map variations in current densities at the microscale over a corroding metal. In this thesis, SVET was used to study the corrosion hot spots of the RSW and SPR joints. Joint samples were cross sectioned and polished to a 0.05 µm finish. The Verascan scanning electrochemical system was used to perform the SVET measurements in 0.5 wt% NaCl. The Pt/Ir microelectrode was placed at a distance of 100 µm from the sample surface. The following were experimental conditions; the gain of the electrometer was set at 1000, a time constant of 500 mS, amplitude of 30 µm, frequency of 80 Hz and the scan area was 3.5mm by 16mm. The joint section corrosion activity was monitored over a period of 24h with a scan carried out at every one hour. To convert the measured potential value to current densities, we used the following calibration procedure [94].

$$\Delta V = -i\rho\Delta r$$

Where ΔV is the potential measured by SVET at any point, ρ is the solution resistivity, Δr is the distance between the two points where ΔV is measured and *the* current density i at a distance r from the point source. For a point source with a current value of I, the current density *i* is calculated from the following equation.

$$i = \frac{I}{4\pi r^2}$$

The quantity ρ. Δr is called the proportionality factor and is determined from the slope of *i vs* ΔV. In this work, the 3µm gold wire embedded in epoxy supplied by Verascan was used as a point source. For the calibration process, tap water with a conductivity of 108 µS was used as an electrolyte and the applied current was varied from 10uA to 70 µA. The proportionality factor was updated for 0.5 wt% NaCl solution conductivity to convert the measured local potential values to current densities.

3.2.6 ASTM G85-A2

It is a cyclic acidified salt spray test that is generally applicable to ferrous and non-ferrous metals and also organic and inorganic coatings [95]. This test cycle was used to assess the effect of residual stress on the SCC performance of the RSW and SPR joints. The qfog CCT 1100 chamber was programmed to run the test cycle at constant temperature of 49 ° C. It consists of 45 min of salt spray (5% NaCl, acidified to pH 3 with acetic acid) followed by 2 hours of dry air purge and 3 hours of 15 minutes of soak at high relative humidity (> 95% RH). This 6 h cycle was repeated over the course of 28 days. At the end of the test cycles, the samples were subjected to metallography cross section and residual strength measurements.

3.2.7 ASTM G44

This is an alternate immersion test cycle that is used to assess SCC resistance, but is often used for other forms of corrosion, such as uniform, pitting, intergranular, and galvanic corrosion of aluminum alloys [96]. This test cycle was used to assess the impact of environmental exposure in the elongation to fracture of unstressed 7xxx alloys. The test cycle consists of immersion for 10 min in 3.5% NaCl followed by 50 min period of the

solution, during which the samples are allowed to dry. The experiments were carried out at room temperature of 27^{o}C and a relative humidity of 45%. The test duration was 40 days, and at the end of the testing period, the samples were subjected to metallography examination and assessment of residual tensile properties.

3.2.8 OEM cyclic corrosion test.

This OEM test cycle was carried out to assess the effect of applied stress on the SCC performance of the RSW and SPR joints. Joint samples were stressed to 50% of their maximum strength using a spring-loaded tube. The Qfog CRH 1100 chamber was programmed with a test cycle consisting of 0.5% NaCl spray at room temperature followed by 6 h exposure at 60% relative humidity at 20 ° C, followed by 15 h exposure at 85% relative humidity at 50 ° C and finally 3 h exposure at 30% relative humidity at 50 ° C. The duration was about 100 days and at the end of it, the joint samples were subjected to a metallography examination and a determination of residual tensile properties.

3.3 Density Functional Theory (DFT) calculations

The fundamental principle of density functional theory states that the electronic charge or density is functional for electronic energy. In other words, there exists one-to-one mapping between electronic density to electronic energy. To determine the energy of a particle from first-principles calculations methods the Schrodinger wave equation must be solved. For a system with multiple particles or atoms, the complexity in solving the wave functions increases rapidly. DFT offers approximations to determine the energy of the system without the need for explicit calculations of wave functions [97].

It involves the following steps.

1. Specification of the geometry of the system under study, including the positions of the Al atoms and solute atoms such as H, Zn, Mg, etc.
2. Choosing a suitable exchange-correlation functional to describe the electronic interactions in the system.
3. Select a basis set to represent the electronic wavefunction, such as plane waves.
4. Solve the Kohn-Sham equations, which describe the electronic structure of the system, to obtain the electronic density and the electronic energy.

In this work, the DFT calculations are used to calculate the grain boundary segregation energy of the solute atoms in the aluminum matrix and its subsequent effect on the grain boundary embrittlement energy. The calculations were performed according to the Vienna Ab-initio simulation package (VASP) with the exchange and correlation terms described by the generalized gradient approximation (GGA) proposed by Perdew, Burke, and Ernzerhof (PBE). A plane-wave cut-off of 500 eV was taken for all calculations. The convergence tolerance of the atomic forces was 0.01 eV / and of total energies is 10^{-6} eV. The k-point sampling number was set large enough so that the convergence of the total energies was within 2 meV per atom. Brillouin zone integration was made using Methfessel–Paxton smearing. Ionic relaxations were allowed in all calculations while the shape and volume fixed. The calculated values of $\sum 5$ grain boundary energy (587 mJ/m^2) and free surface energy (1059 mJ/m^2) of pure Al were found to be within the convergence criteria, which is consistent with previous DFT-GGA calculations [97, 98].

CHAPTER 4: EFFECT OF GRAIN SIZE ON THE IGC AND SCC RESISTANCE OF 7075 ALLOY.

4.1 Background

From the literature review it is evident that the grain size effect on the corrosion performance is still subject of debate. The primary reason behind the confounding effect is due to changes in the microstructure such as texture or grain boundary misorientation angle etc, whenever there is a change in grain size. Similarly, the effect of grain size on the grain boundary features is still not clearly established. The objective of this chapter is to systematically establish the link between the grain size and the corrosion resistance of the 7075 alloy in T6 temper.

4.2 Approach

The composition of the 7075 is listed in **Table 4-1**. Grain size of the samples were changed either by controlling the degree of cold work of hot rolled gauge (CR) or by recovery annealing (RA) of final gauge F-temper material. Schematic version of the fabrication step is shown in **Figure 4-1**. In cold work route, a 10mm thick hot rolled 7075 was scalped down to 4 mm using the computer numerical control (CNC) milling machine. Equal amount of material was removed from the top and bottom during the milling process. Then the material was cold rolled down to 2 mm (50% CR). For comparison purpose, the 10mm thick hot band was directly cold rolled to 2mm (80% CR). Then samples were subjected to solutionizing and T6 ageing treatment. In recovery annealing (RA) route, a final gauge 2mm thick F-temper material was annealed either to 250^{o}C, 350^{o}C or 450^{o}C for 2h.

Table 4-1: Alloy composition of 7075-T6

Elements	Zn	Cu	Mg	Fe	Si	Mn	Cr
Composition in wt%	5.68 – 5.88	1.58 – 1.78	2.43 – 2.26	0.25 – 0.35	0.04 – 0.14	0.05 – 0.15	0.20 – 0.30

A heat ramp of 50°C/h and the cooling ramp of 10°C/h was used to produce the samples. Then these samples were subjected to solutionizing and T6 ageing treatment. The following heat treatment sequence was used in achieving the T6 temper. Solutionizing samples at 480°C for 5 min followed by water quench at a rate of 350°C/s. Subsequent T6 ageing was carried out at 125°C for 24h.

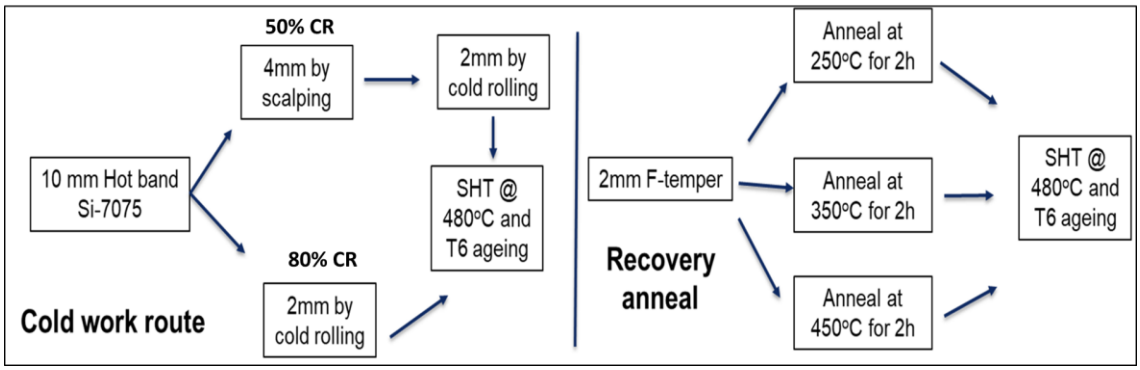

Figure 4-1: Schematic of two independent (cold work and recovery anneal) thermomechanical treatment used for generating samples with different grain size.

4.3 Results

Effect of Cold Work (CR)***Error! Reference source not found.*** shows the plane view images of the Barkers-etched samples under plane polarized light. We could observe that the 80% cold-worked material (80% CR) has coarser grains compared to the 50% cold-work material. The grain size from the intercept method showed that 80% CR had an average grain size of 27 µm, while the 50% CR had a grain

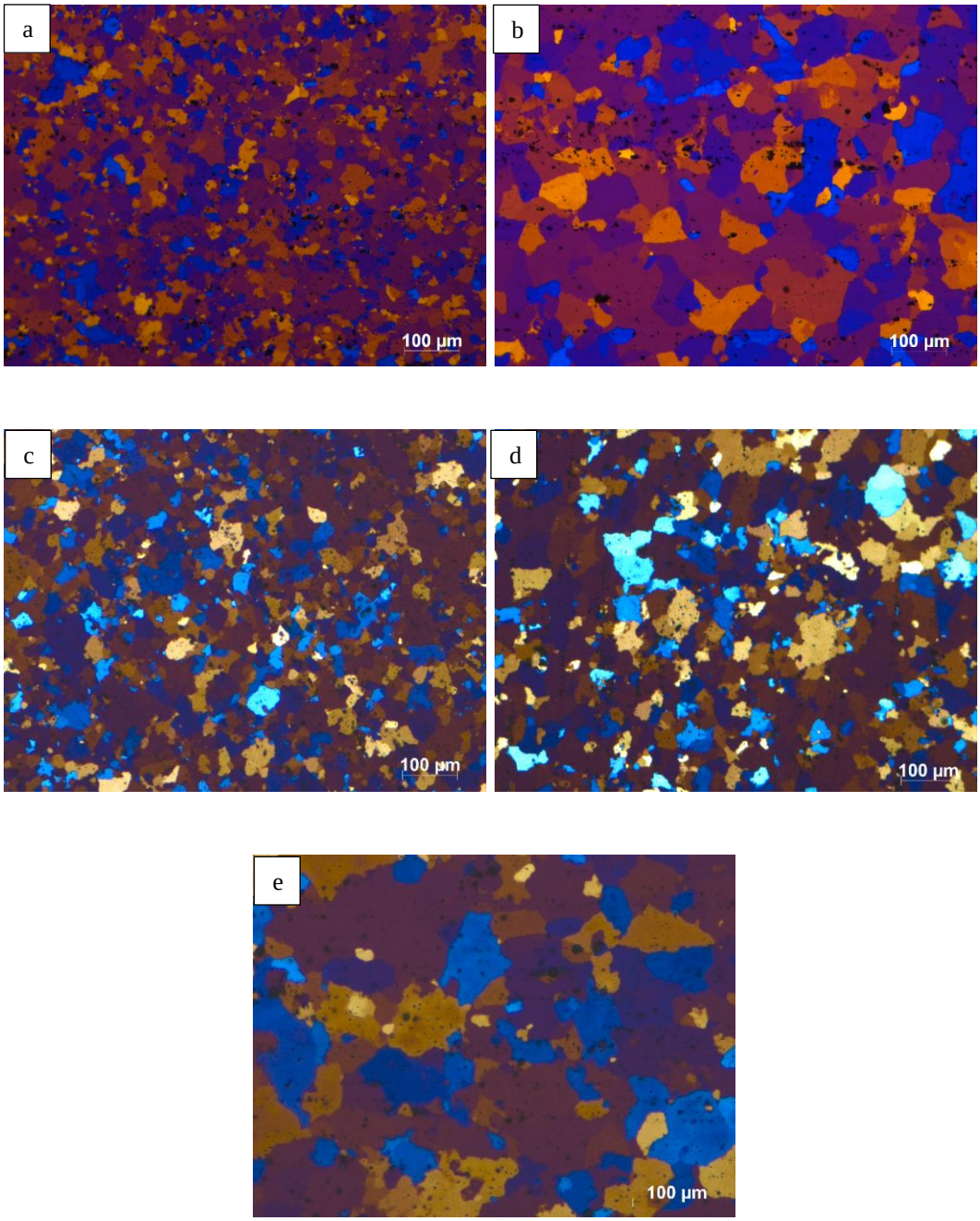

Figure 4-2: Plan view optical microscope images of the (a) 80% CR (b) 50% CR (c) 250°C RA (d) 350°C RA (e) 450°C RA respectively.

size of 51 µm in plane view. Error! Reference source not found. shows the inverse pole f igure map from EBSD analysis, apart from the grain size, qualitatively the crystallographic orientation was comparable between the 80% and 50% CR samples.

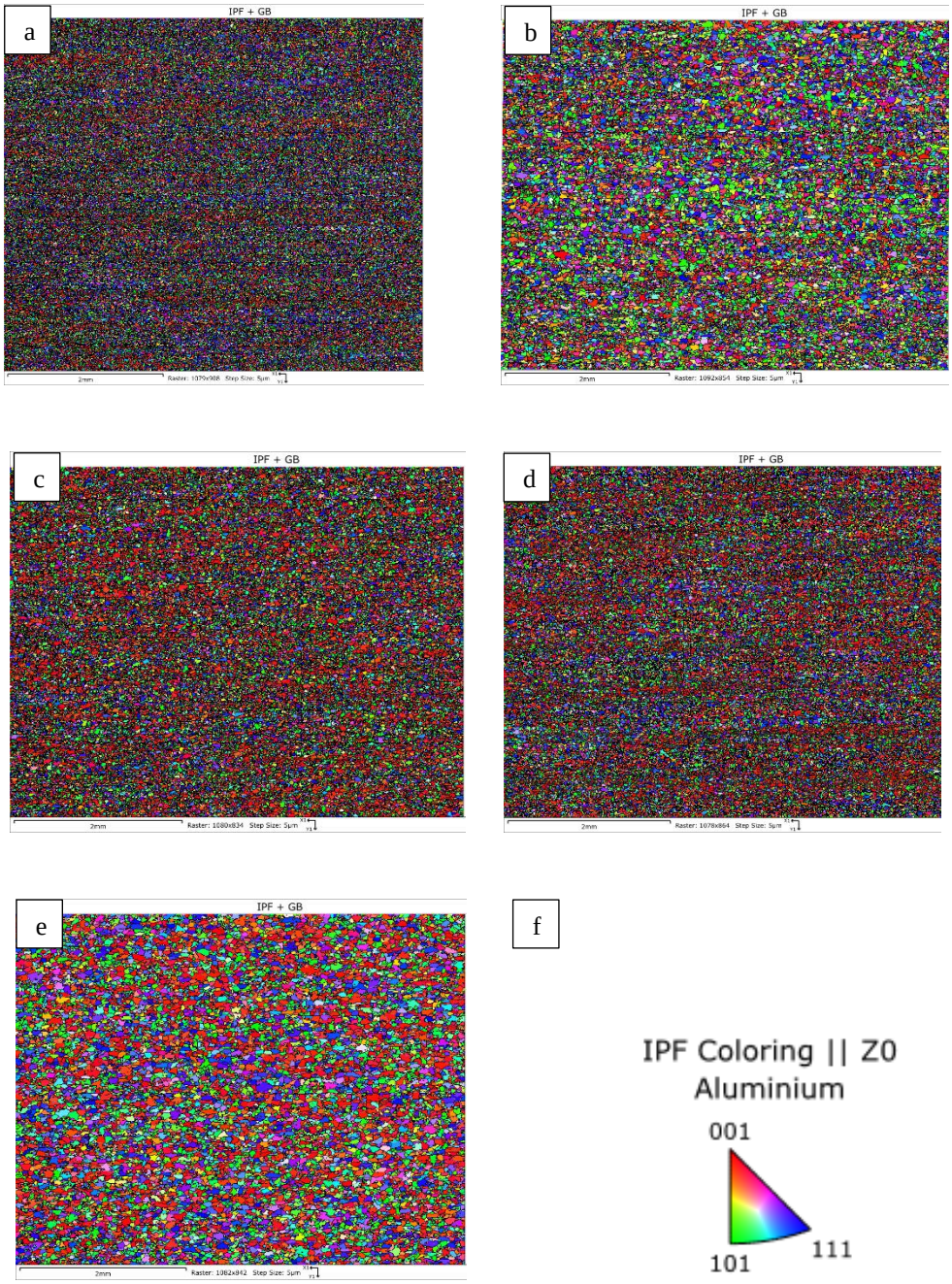

Figure 4-3: Inverse pole figure (IPF) map from EBSD analysis of (a) 80% CR (b) 50% CR (c) 250ºC RA (d) 350ºC RA (e) 450ºC RA (f) IPF coloring chart respectively

Table 4-2 shows the breakdown of the key texture components of the two cold work reduction paths. The rolling texture components constituted roughly 11% while the recrystallization texture components were about 5% in both scenarios. The rest of the texture components were classified as random texture. The **Table 4-2** also shows the difference in high and low angle grain boundaries between the 80% and 50% CR materials. In both cases, the high angle grain boundaries were of the majority type accounting for nearly 95% while the remaining 5% belong to the low angle grain boundaries category.

Table 4-2: Effect of grain size on the mis-orientation angle and texture components.

Sample	Grain mis-orientation angle (%)		Key texture components (%)		
	5-15º	>15º	Random	Recrystallization	Rolling
80% cold work	6.37	92.99	81.85	6.28	11.87
50% cold work	4.72	94.67	84.01	4.59	11.4
250ºC recovery anneal	5.82	93.67	88.97	4.04	6.99
350ºC recovery anneal	6.28	92.96	87.48	5.49	7.03
450ºC recovery anneal	5.79	93.44	78.37	7.9	13.73

Figure 4-4 shows the SSRT data for 80% CR and 50% CR samples in ASTM D1384 with 1% H_2O_2. The elongation to the fracture was higher in air compared to the corrosive environment in both samples.

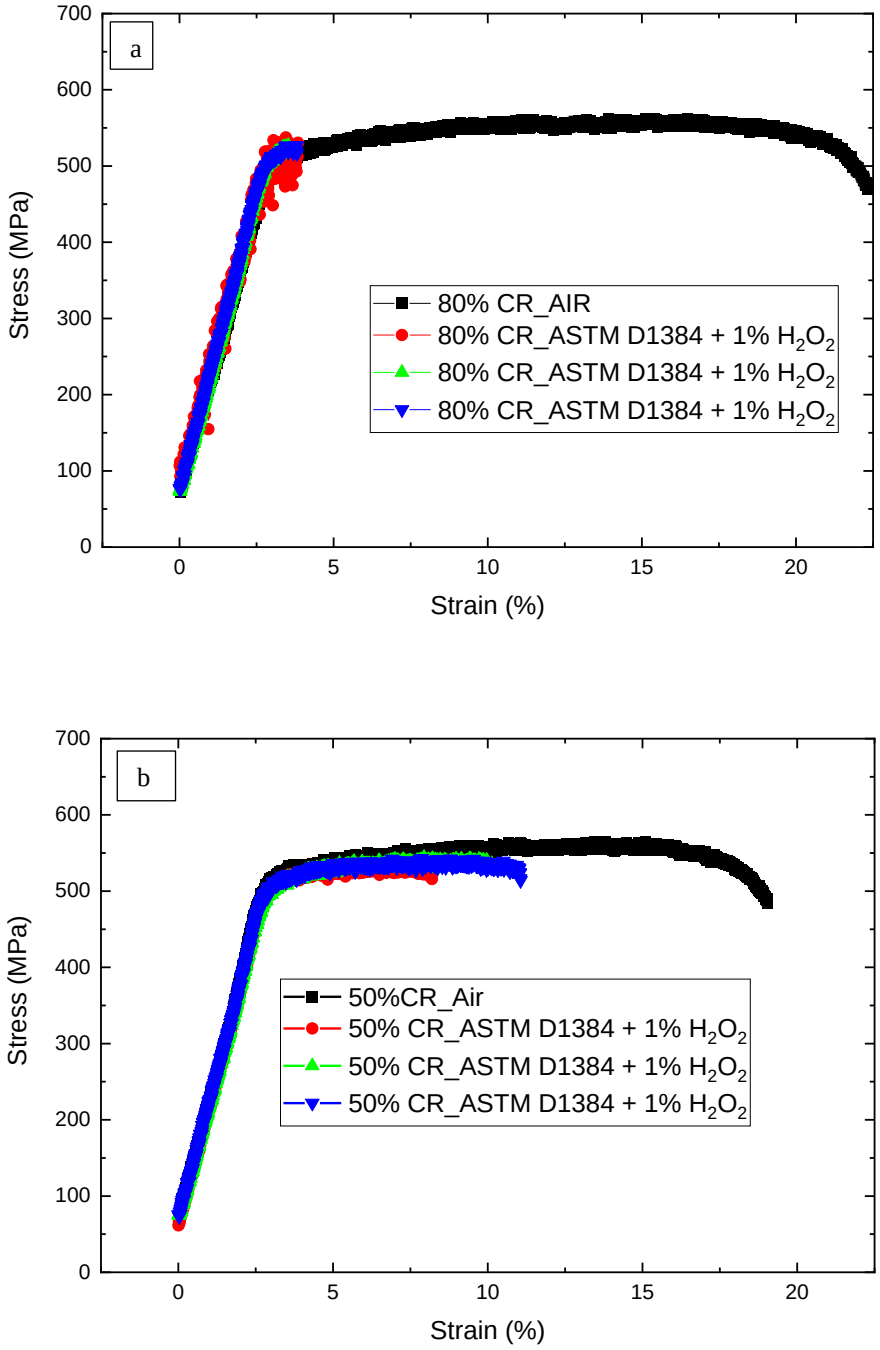

Figure 4-4: SSRT of (a) 80% CR + T6 and (b)50% CR + T6 in Air and ASTM D1384 solution + 1% H_2O_2

Interestingly, there were also differences in the ability to reach the maximum strength values in the corrosive environment. The material that underwent 80% cold rolling

fractured when it was close to reaching the yield strength value. In contrast, the 50% cold rolling samples broke when they were nearing the maximum tensile strength. A significant difference in the grain size effect was observed in the strain ratio. As shown in **Figure 4-5**, the strain ratio value for the fine-grain 80% CR samples was 0.2, while the coarse-grain 50% CR samples exhibited a higher strain ratio of 0.5.

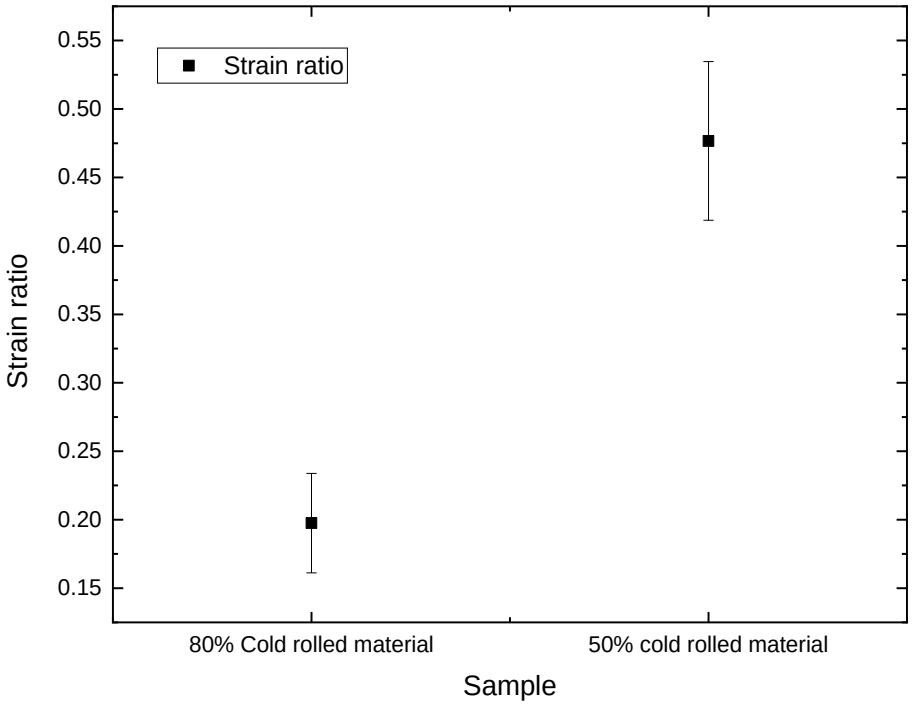

Figure 4-5: Effect of cold work on strain ratio in ASTM D1384 solution + 1% H_2O_2

Error! Reference source not found. shows the metallographic section of the fractured s amples from the SSRT. Cracks were observed near the fractured region in both types of samples. The higher magnification cross-section images showed the distinct presence of intergranular corrosion sites in 80% CR sample, while the 50% CR samples exhibited pitting type of corrosion morphology.

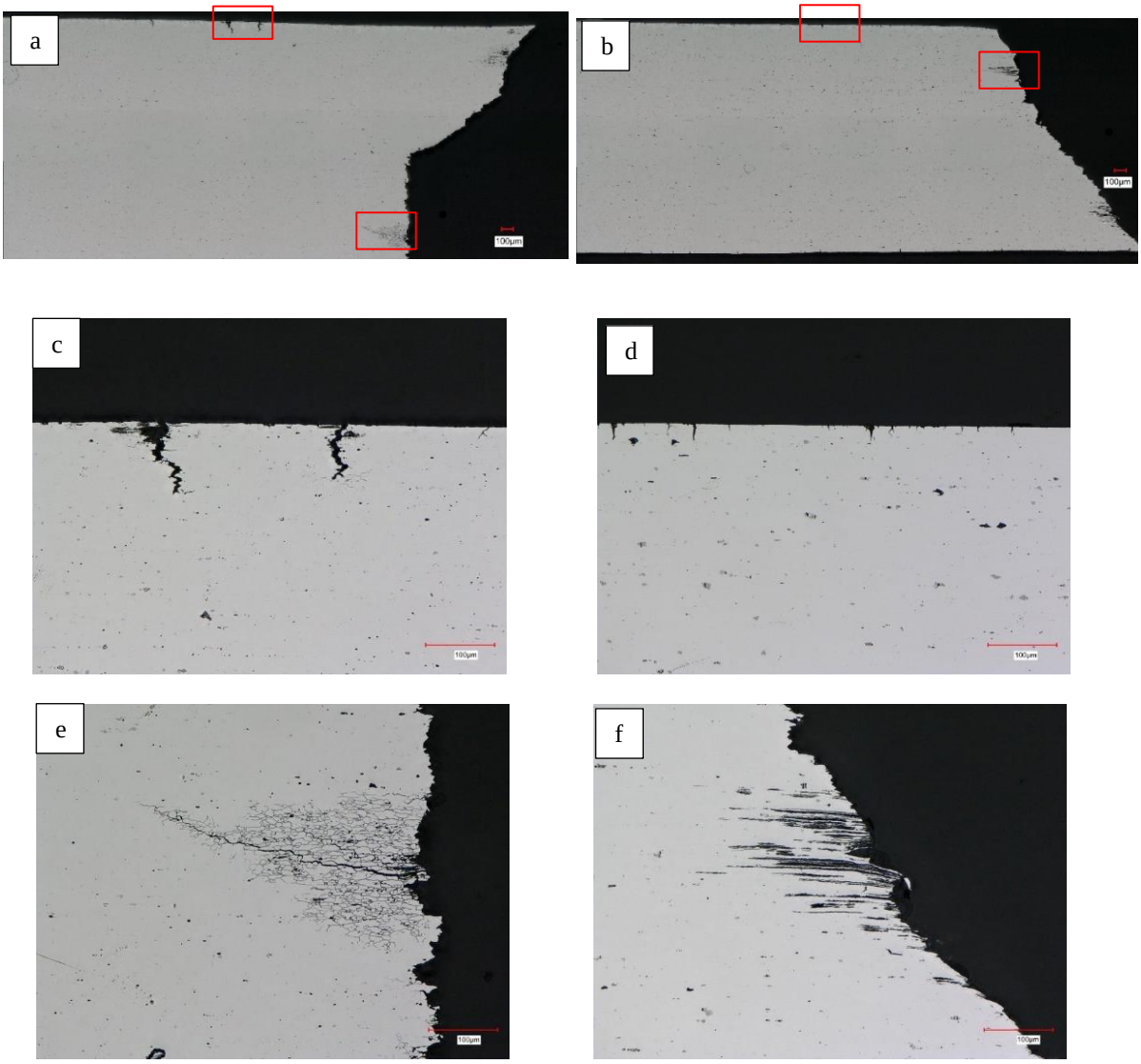

Figure 4-6: Metallography section images of the fractured samples (a,c,e) 80% CR + T6 and (b,d,f) 50% CR + T6.

Error! Reference source not found.**Table 4-3** indicates that there were notable differences between the fine-grain 80% CR samples and the coarser-grain 50% CR samples in terms crack depth. The maximum crack depth of the 80% CR samples was 187 µm while the maximum depth of 50% CR was at least eight times smaller. A similar difference was observed in the average depth values as well. Despite the higher standard deviation in the 80% CR crack depth values, there was a statistically significant difference between the two samples. An independent sample t-test was conducted to compare effect of grain size on average crack depth. There was a significant difference in the crack depth for 80% CR (mean = 88µm, standard deviation = 56µm) and 50% CR (mean = 18µm, standard deviation = 3.6µm) conditions; t (15) = 4.52, p = 0.0004.

Table 4-3: Average and maxim crack depth values measured from optical microscope images.

Sample	**Crack depth (µm)**	
	Average	**Maximum**
80% cold work	88.82 ± 56	187
50% cold work	18.04 ± 3.66	23.56
250°C recovery anneal	116.95 ± 75	254.43
350°C recovery anneal	83 ± 24.69	122.52
450°C recovery anneal	43.87 ± 26.9	87

Error! Reference source not found. shows the fractography of the 80% CR samples, which e xhibits a unique morphology compared to the 50% CR samples. The grain faces are clearly visible and the crack appears to have propagated along the grain boundary, indicating a clear sign of brittle intergranular fracture. Additionally, the grain facets appear smooth with no sign of work hardening. On the 50% CR fractured samples exhibit a rough morphology, with a distinct presence of clustering of dimples or voids on the microscale, indicating a sign of ductile-dominant fracture morphology.

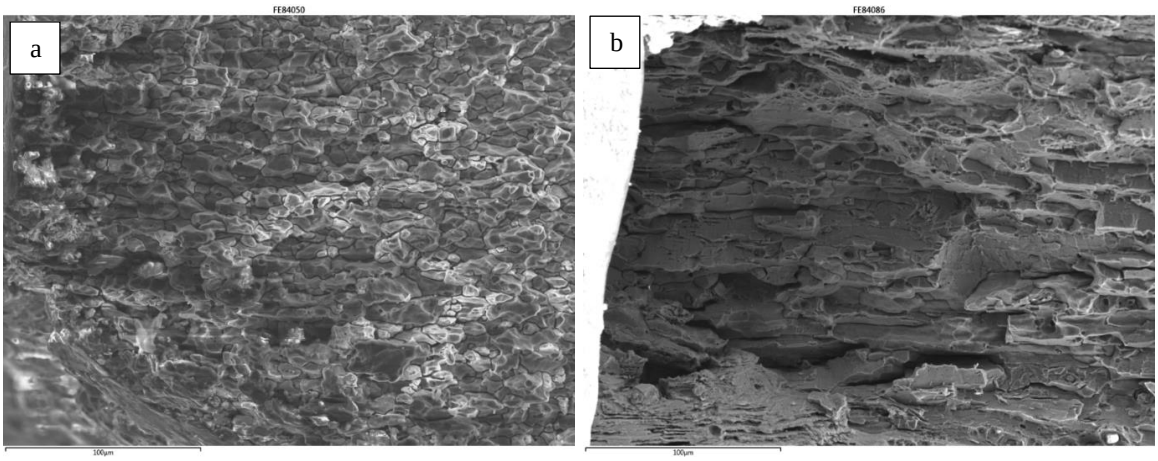

Figure 4-7: Effect of cold work (a) 80% CR + T6 (b) 50% CR + T6 on the fracture surface of 7075 in ASTM D1384 solution + 1% H_2O_2

To observe the initiation and propagation mode of cracks at the micron level, we performed focused ion beam (FIB) lift-out of the fractured samples. Scanning transmission electron microscope (STEM) bright- and dark-field images of the FIB lift-off samples in the 80% CR material are shown in **Figure 4-8**. The grain interiors appear to be intact, but there was selective attack on the grain boundaries. The high magnification image shows the presence of porous substance covering the walls of the grain boundary and a crack separating the two adjoining grains. In contrast, the 50% CR material, the low magnification image clearly showed that the crack was propagating through the grains and the grain boundaries were intact. The high magnification image showed that the crack originated in the region where there was a pitting type attack on surface of the grains (**Figure 4-9**).

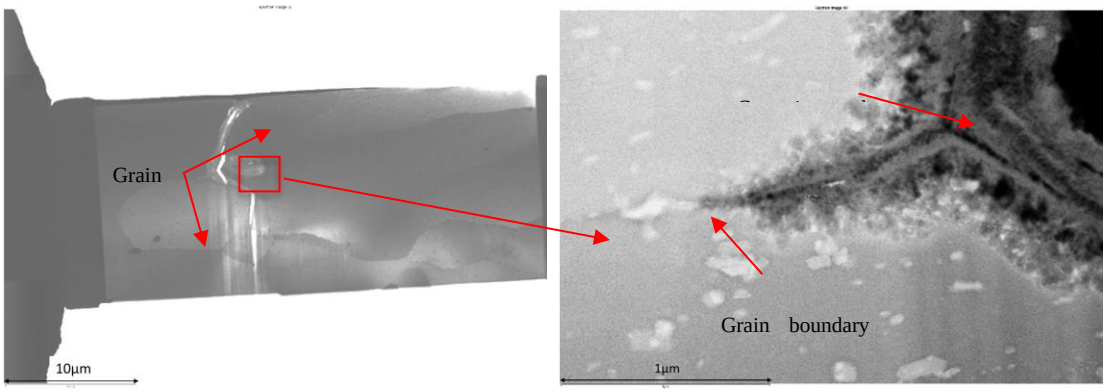

Figure 4-8: FIB liftout of crack tip of 80% CR samples bright field (left) and dark field (right).

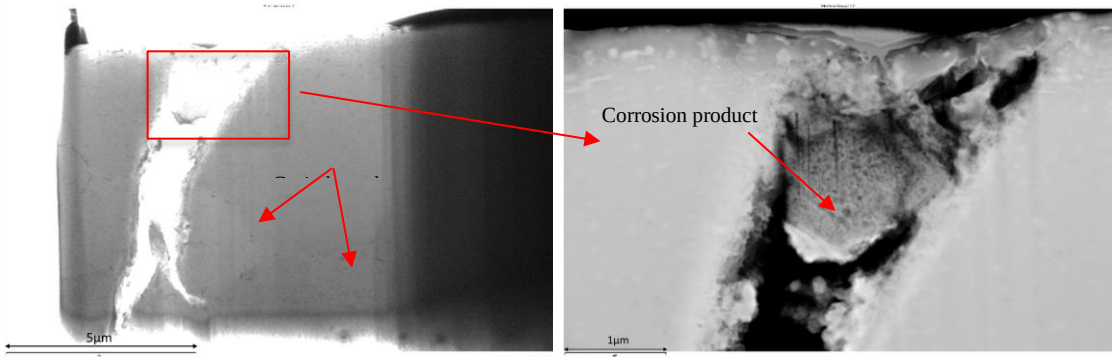

Figure 4-9: FIB lift-out of crack tip of 50% CR samples bright field (left) and dark field (right).

Figure 4-10 shows the metallography cross section after 24h immersion in ASTM D1384 with 1% H_2O_2. There were clear differences in the corrosion morphology for the two grain size materials even in the absence of applied stress. 80% CR material grain boundaries were selectively attacked indicating the intergranular corrosion features, while the 50% CR material exhibited only pitting corrosion.

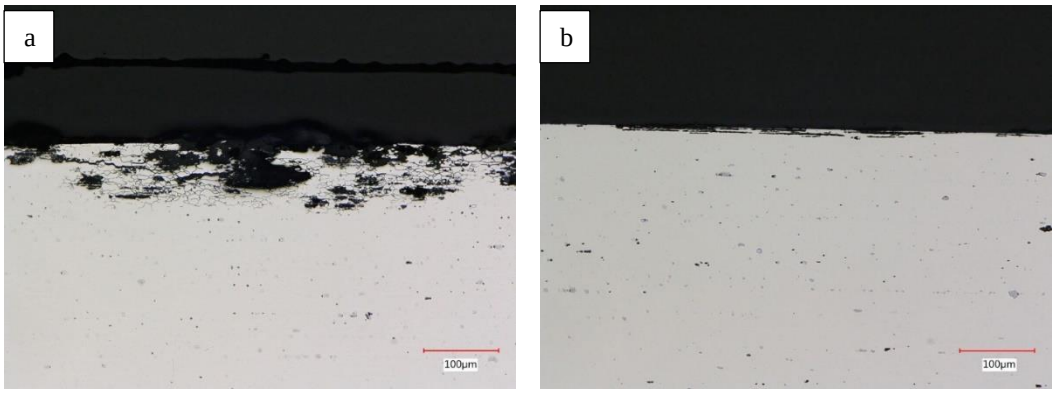

Figure 4-10: Metallography cross section of (a) 80% CR (b) 50% CR samples after 24h exposure in ASTM D1324 solution containing 1% H_2O_2.

Figure 4-11 a and b show the STEM images of the grain boundary microstructure of 80% CR and 50% CR, respectively. The images clearly show the presence of grain boundary precipitates (GBP) and adjacent precipitate-free zones (PFZ). In the 80% CR sample, the grain boundary precipitates were fine and continuous, while in the 50% CR sample, they were largely coarse and discontinuous.

Table 4-4: Composition of the grain boundary features from EDS measurements.

Sample	EDS composition PFZ (wt%)			EDS composition GBP (wt%)		
	Cu	Zn	Mg	Cu	Zn	Mg
80% cold work	2.11 ± 0.24	2.23 ± 0.99	1.1 ± 0.21	2.51 ± 0.79	9.9 ± 3.5	2.64 ± 0.4
50% cold work	1.7 ± 0.65	2.09 ± 0.32	0.9 ± 0.22	3.07 ± 0.99	9.6 ± 3.6	2.63 ± 1
250ºC recovery anneal	2.47 ± 0.44	1.83 ± 1	0.94 ± 0.38	3.4 ± 0.9	9.5 ± 2.8	2.59 ± 0.79
350ºC recovery anneal	2.55 ± 0.4	2.86 ± 1.14	1.23 ± 0.4	3.03 ± 0.57	8.01 ± 2.1	2.31 ± 0.43
450ºC recovery anneal	2.9 ± 0.4	1.88 ± 0.43	0.97 ± 0.16	3.54 ± 0.58	13.1 ± 4.8	3.05 ± 0.91

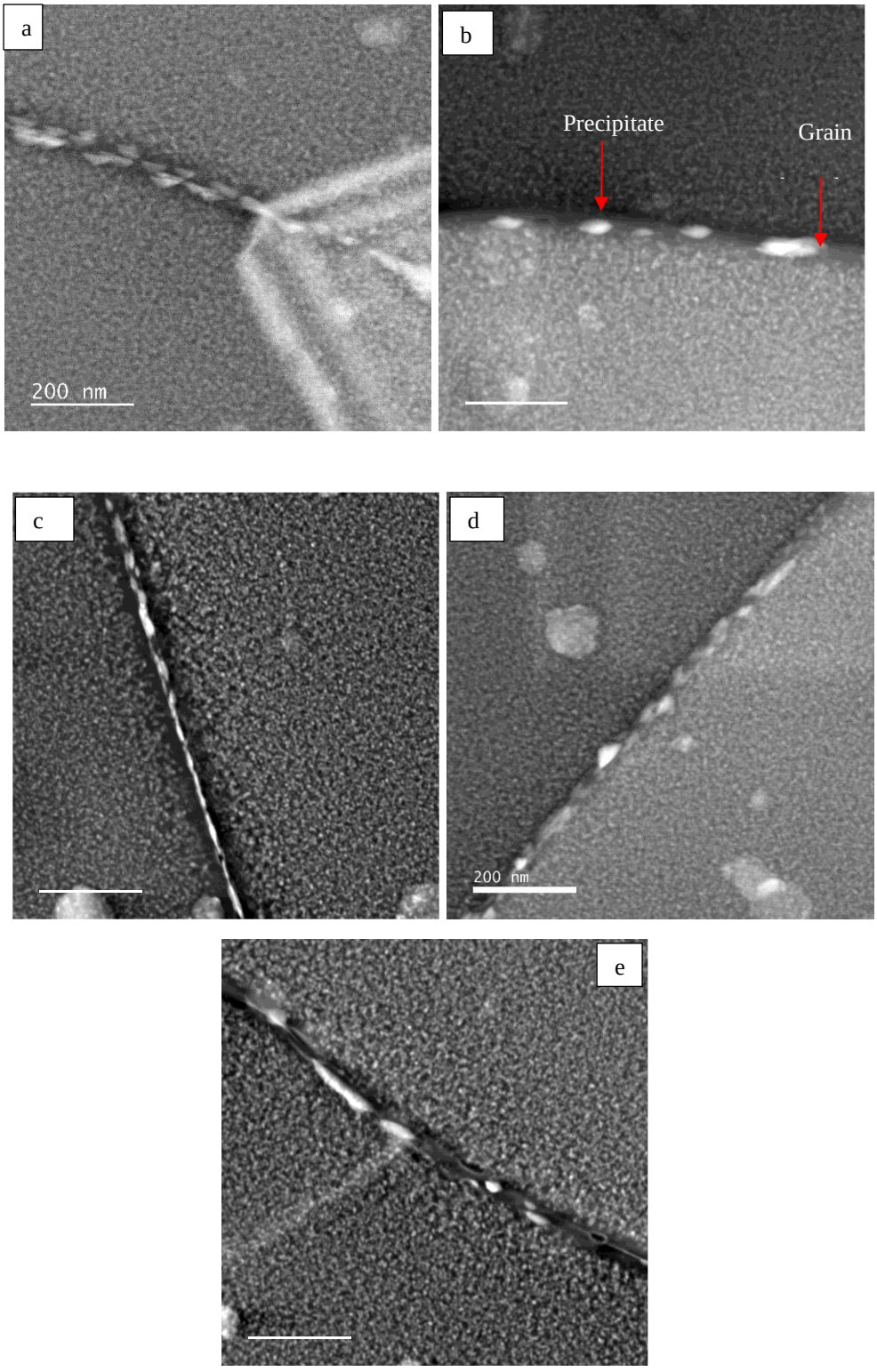

Figure 4-11: Bright field images of grain boundary microstructure of (a) 80% CR (b) 50% CR (c) 250ºC RA (d) 350ºC RA (e) 450ºC RA.

Table 4-4 contains the average composition of GBP and PFZ from EDS measurements of 20 randomly selected features for each sample. The results indicate that the GBP had higher levels of Zn and Mg compared to the PFZ. However, the difference in grain size between the 80% CR and 50% CR samples did not significantly affect the composition of the GBPs or the PFZs.

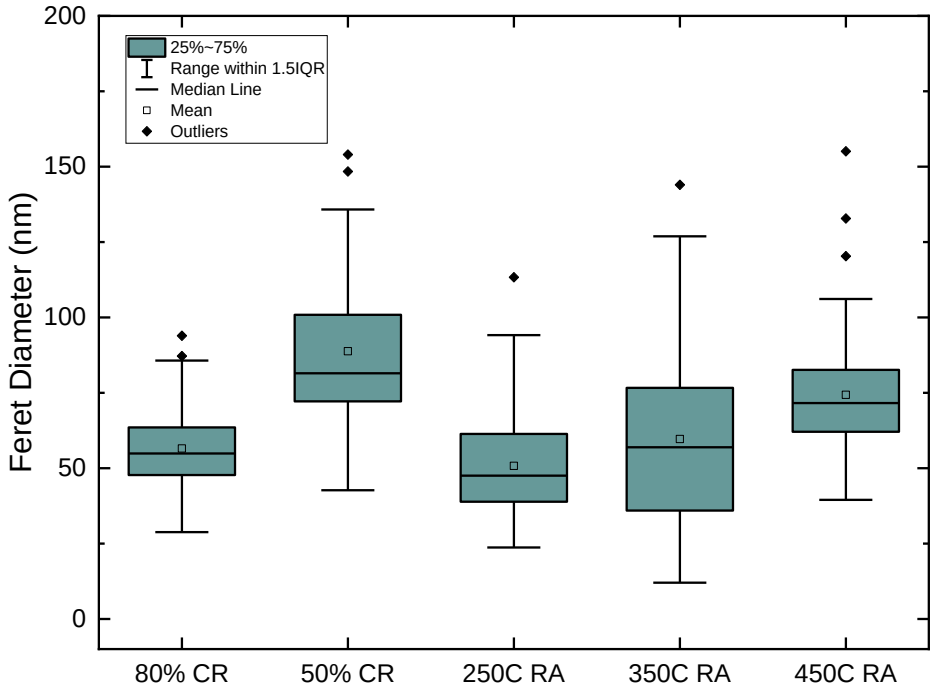

Figure 4-12: Feret diameter box plot as function of different thermomechanical treatments.

Error! Reference source not found. displays a box plot of the mean Feret diameter of the 5 0 randomly selected GBPs for each sample. The normality of the data set was confirmed using the Kolmogorov-Smirnov (KS) test. An independent sample t-test (**Table 4-5**) was conducted to compare the effect of grain size on the Feret diameter of GBP. The results indicate a significant difference in Feret diameter between the 80% CR and 50% CR at $p < 0.05$. This suggests that as the grain size increases, so does the Feret diameter of the

GBPs. Consequently, there was a clear discontinuity in the presence of precipitates along the grain boundary in the 80% CR samples. compared to the 50% CR samples.

Table 4-5: Statistical t-test analysis of effect of cold work on Feret diameter of the grain boundary precipitates.

Sample	Observations	Mean Feret diameter (nm)	Standard deviation	t-value	p-value
80% cold work	50	56.5	15	7.80	0.0001
50% cold work	50	88.7	25		

By plotting the Feret diameter as a function of grain size (**Figure 4-13)** a linear correlation was observed with an exponent of 0.43.

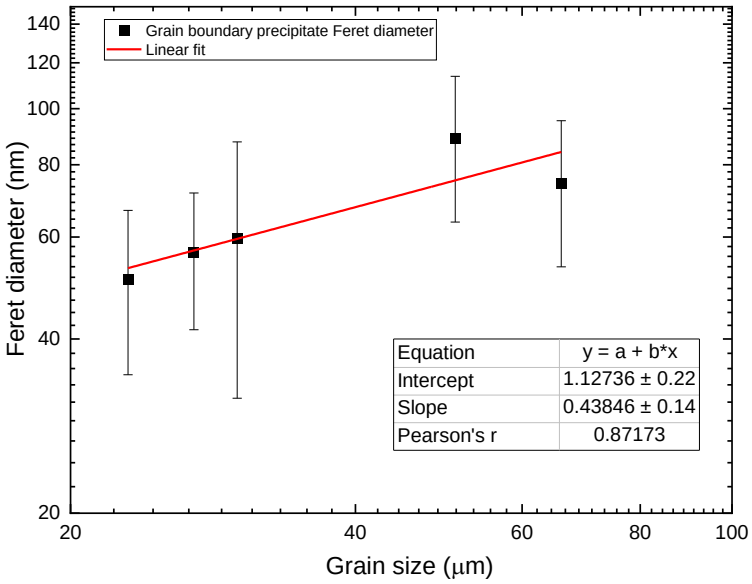

Figure 4-13: Relationship between the grain size and the Feret diameter of the grain boundary precipitate.

Similar linear trend was observed in **Figure 4-14** where a correlation between the Feret diameter and the strain ratio and the maximum crack depth.

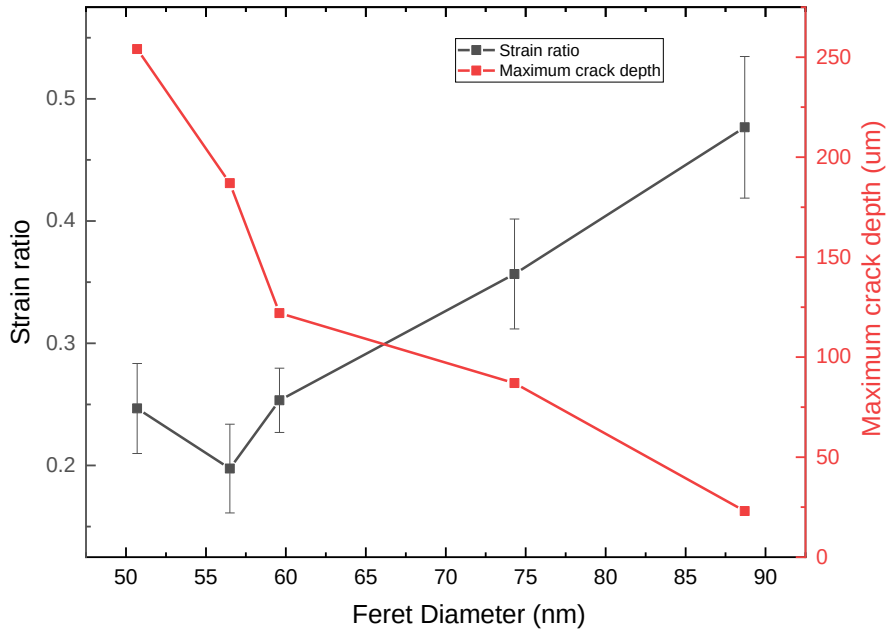

Figure 4-14: Effect of GBP size (Feret diameter) on strain ratio and maxim crack depth.

4.3.1 Effect of recovery anneal (RA)

The plane view optical microscopy images and in plane pole figures of the recovery anneal samples are shown in **Figure 4-2** and **Figure 4-3** respectively. From these figures, it could be seen that with an increase in recovery anneal temperature, the grain size also increased. The average grain sizes of the 250^{o}C RA, 350^{o}C RA, 450^{o}C RA samples were 23 µm, 30 µm and 66 µm respectively. For comparison purposes, the 80% CR sample was used as a control in recovery anneal studies. **Table 4-2** shows the breakdown of the texture components from the EBSD measurements. In all three samples, the recrystallization

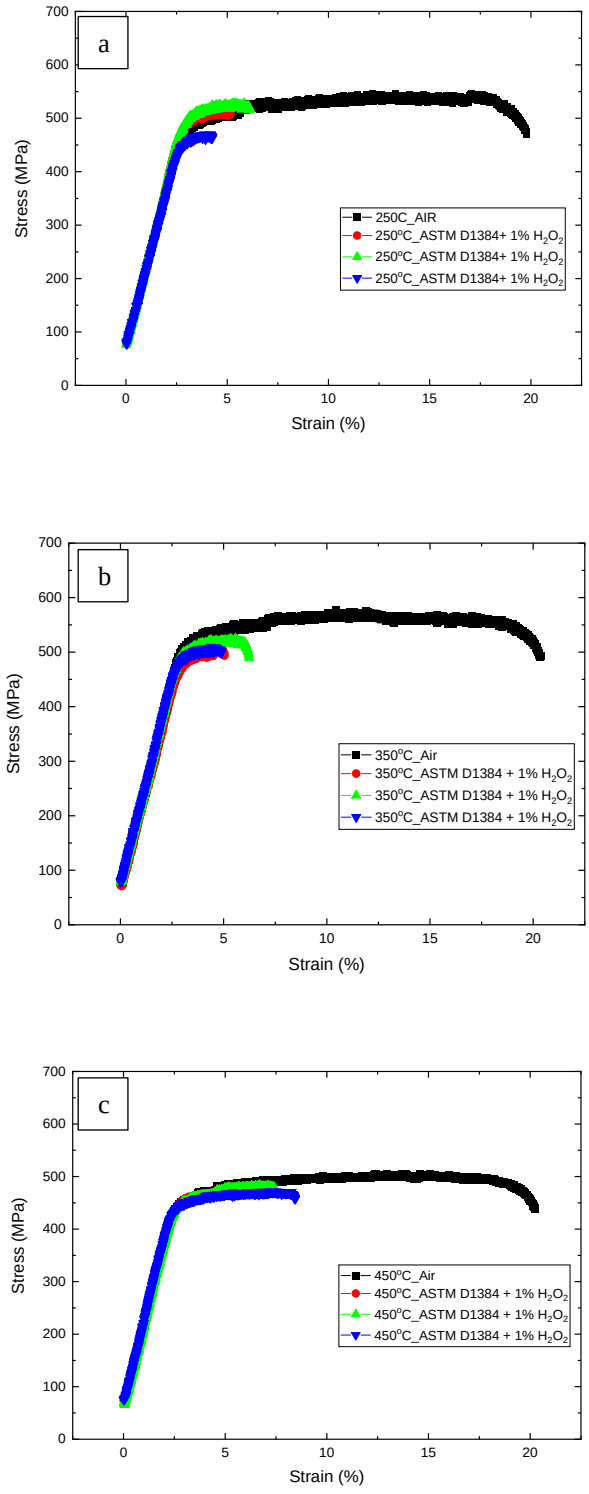

Figure 4-15: SSRT in ASTM D1384 solution + 1% H_2O_2 (a) 250°C recovery anneal + T6 (b) 350°C recovery anneal + T6 (c) 450°C recovery anneal + T6.

texture constituted 5%, while the deformation texture constituted 10%. The remaining texture components were classified as random texture.

Figure 4-15 contains the stress strain curve from the SSRT for the recovery annealed samples. Unlike the control 80% CR samples, the recovery annealed samples failed only after crossing the yield point. The strain to failure in the corrosive environment was lower than that of the stain to failure in the air. **Figure 4-16** shows the strain ratio of the recovery anneal samples and it could be seen that the 250 ° C RA samples had a strain ratio of 0.25, this was higher than the 80%CR samples whose strain ratio was 0.18. Increasing the recovery anneal temperature to 350 ^{o} C did not lead to a significant change in the strain ratio value. However, at 450 ^{o} C, there was a notable increase in the strain ratio value. The trend in recovery anneal grain size effect on the strain ratio was similar to the cold roll effect.

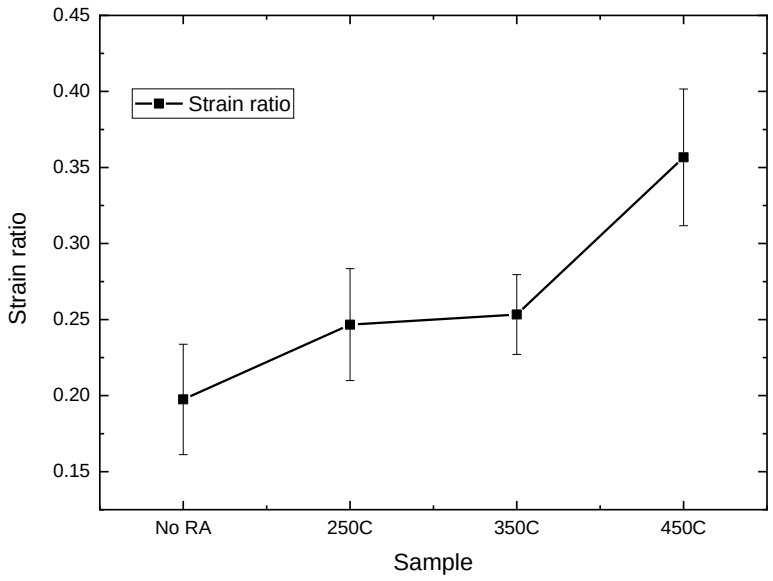

Figure 4-16: Effect of recovery anneal on the strain ratio of the 7075 T6

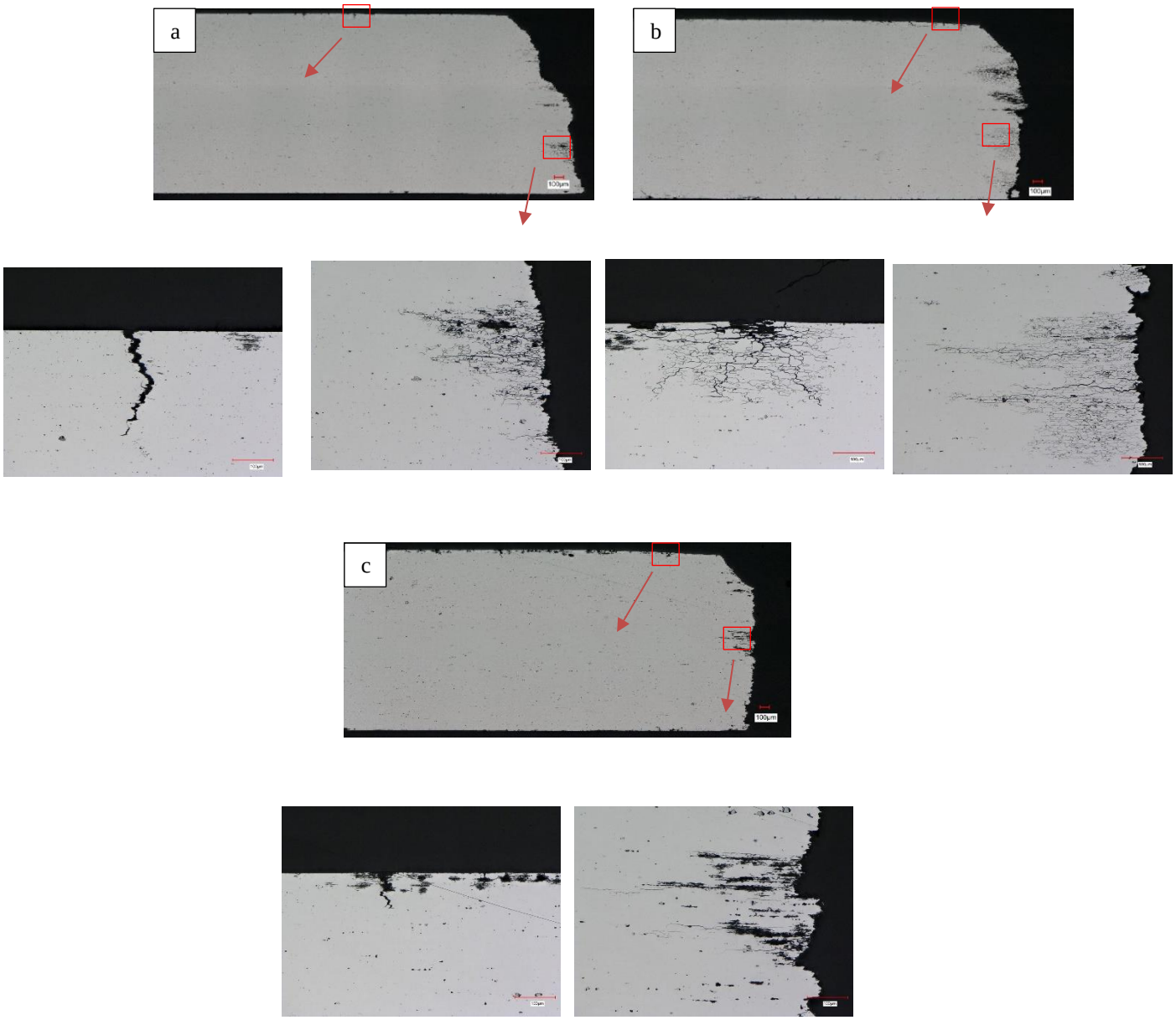

Figure 4-17: Metallography cross section of the fractured sample (a) 250ºC recovery anneal + T6 (b) 350ºC recovery anneal + T6 (c) 450ºC recovery anneal + T6.

The metallography cross section after SSRT (**Figure 4-17**) shows deeper cracks and a clear sign of intergranular corrosion attack in 250 ° C RA and 350 ° C RA. However, in 450ºC RA the degree of cracking was higher, but the cracks were shallower compared to the other two lower recovery temperatures studied. Similarly, no signs of intergranular corrosion attack were observed in 450ºC RA samples. Crack depth values (**Table 4-3**) decrease with an increase in recovery anneal temperature. The maximum crack depth value of the 250ºC RA samples was 254 µm, while the 450ºC RA was only 87 µm. The 350ºC RA samples had an intermediate value of 120 µm. A similar trend was also observed in the average crack depth values.

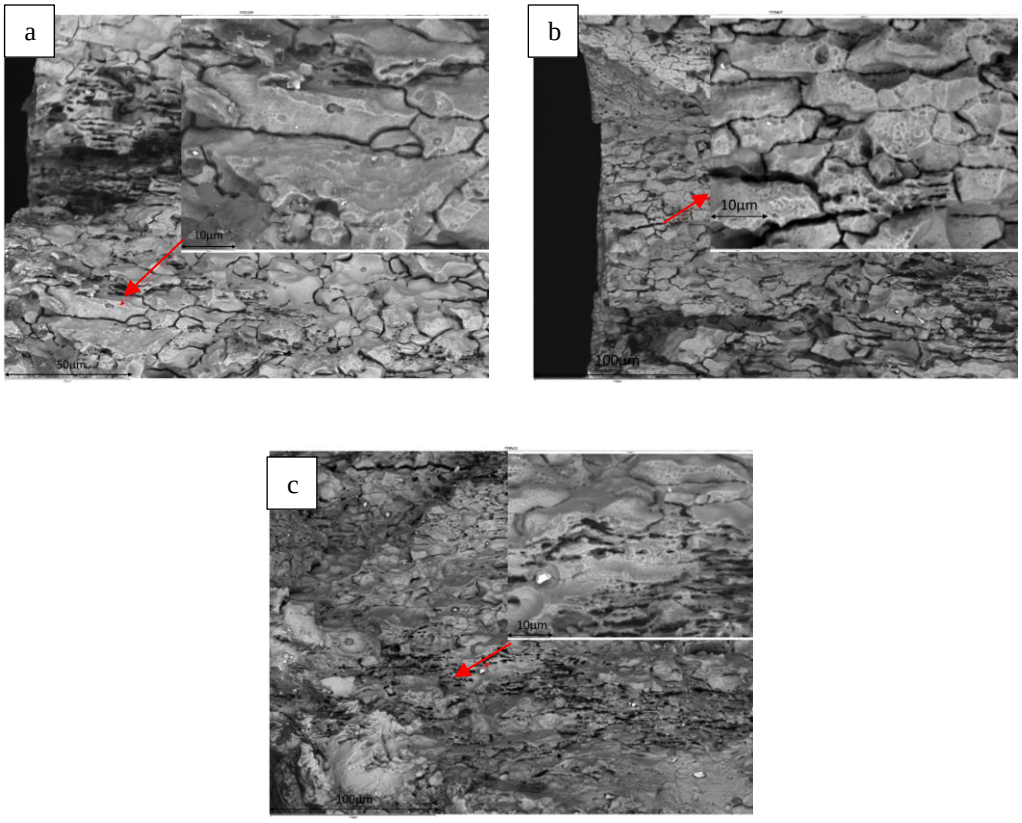

Figure 4-18: scanning electron microscope images of the fractured surface (a) 250ºC recovery anneal + T6 (b) 350ºC recovery anneal + T6 (c) 450ºC recovery anneal + T6.

SEM fractographs (**Figure 4-18**) of recovery anneal samples show distinct shift in morphology at higher temperatures. Both 250^{o}C RA and 350^{o}C RA had a similar fracture surface. The grain facets were clearly visible without any sign of deformation. In the higher magnification images, the crack propagation along the grain boundaries could clearly be seen. These features are a clear sign of a brittle intergranular fracture. However, the 450^{o}C RA samples show a distinct presence of a cluster of micro-voids or dimples in the fractured region, indicating dominant ductile features.

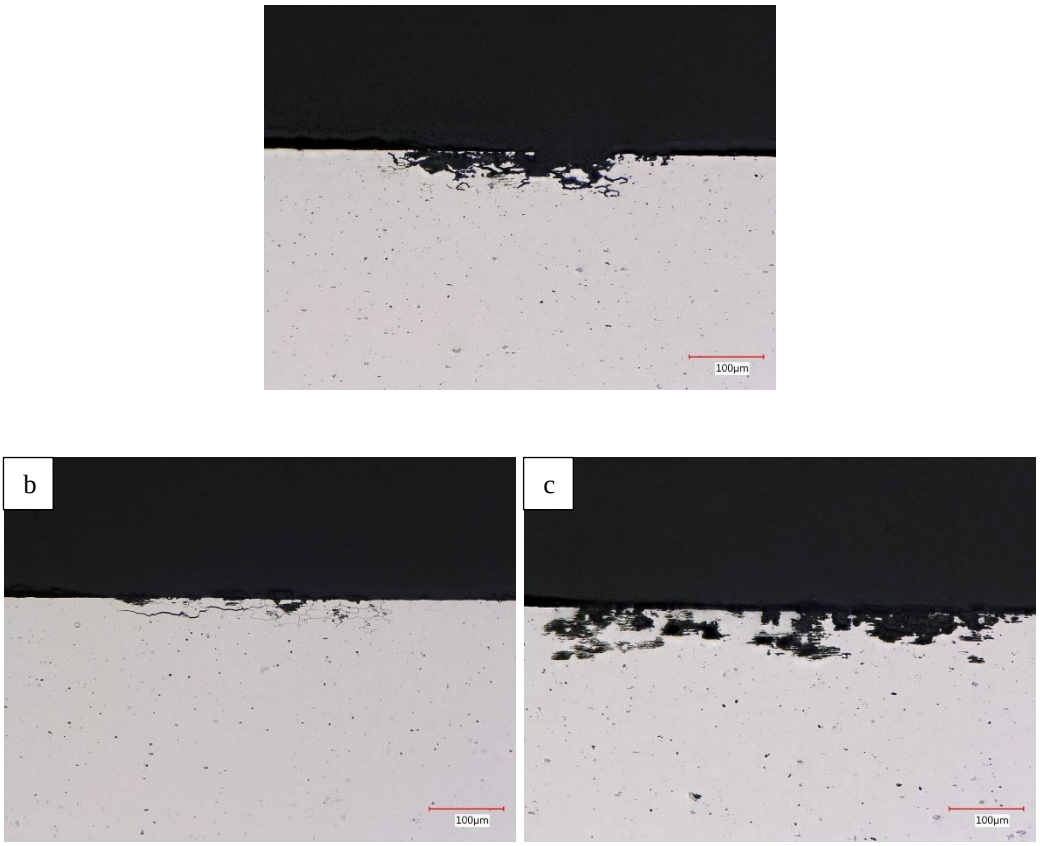

Figure 4-19: Metallography cross section of (a) 250^{o}C RA (b) 350^{o}C RA (c) 450^{o}C RA samples after 24h exposure in ASTM D1324 solution containing 1% H_2O_2.

Even in the absence of applied stress, (**Figure 4-19**) the corrosion morphology was different at higher recovery anneal temperatures. The 250 ° C RA and 350 ° C RA samples exhibited intergranular attack morphology, where the grain boundaries were selectively corroded. These characteristics were very similar to the corrosion attack morphology that was observed in the 80% CR material shown in **Figure 4-10**. The 450^{o}C RA samples, on the other hand, exhibited the same pitting corrosion morphology as the 50% CR samples.

Figure 4-11 shows the bright field STEM images of the grain boundary of the recovery anneal samples. Like the cold roll samples, the grain boundaries of the recovery anneal materials had precipitates and adjoining precipitate-free zone. The increase in recovery anneal temperature affected the size and continuity of the precipitates. The low temperature recovery anneal sample such as 250^{o}C and 350^{o}C had continuous presence of the fine precipitates along the boundary, while the higher temperature recovery anneal sample had discontinuous and coarse precipitates. The size of the precipitates was measured interms of the Feret diameter (**Figure 4-12**). The 250 ° C RA samples had the smallest Feret diameter of 50 µm while the 450 ° C RA samples had Feret diameter of 75 µm.

A one-way analysis of variance (ANOVA) was performed between recovery anneal samples to compare the effect of recovery anneal temperature on the size of the GBP (**Table 4-6**). There was a significant effect of recovery anneal temperature on GBP Feret diameter at the $p < 0.05$ level for the four conditions. Post hoc comparisons using the Tukey HSD test (**Table 4-7**) indicated that the mean GBP size for the small-grained samples (i.e., 80% CR, 250^{o}C RA and 350^{o}C RA) was significantly different from the larger grained 450^{o}C RA. However, the 80% CR, 250^{o}C RA did not differ significantly from the 350^{o}C RA. Taken together, these results suggest that recovery anneal temperatures do have an

effect on GBP size. However, it was observed that a high recovery anneal temperature (450°C RA) is needed in order to see a statistically significant effect on grain size and GBP size. Lower temperatures levels of 250°C RA and 350°C RA do not appear to increase the GBP size significantly.

Table 4-6: one-way ANOVA of effect of recovery anneal on Feret diameter of grain boundary precipitates.

Groups	df	F	p value
Between groups	3	11.09	0.0000
Within groups	196		

Similar to the samples produced by the cold-roll route, the GBP for the recovery-annealed samples also had higher levels of Zn and Mg compared to the PFZ (**Table 4-4**). Likewise, the grain size difference in 250°C RA, 350°C RA and 450°C RA samples did not significantly affect the composition neither between the GBPs nor between the PFZs.

Table 4-7: Post hoc comparisons using the Tukey HSD test of effect of recovery anneal on Feret diameter of grain boundary precipitates.

Sample	Observations	Mean Feret diameter (nm)	Standard deviation
80% cold work	50	56.5	15
250°C RA	50	50.7	16
350°C RA	50	59.6	28
450°C RA	50	74.3	21

Figure 4-14 shows the Feret diameter of the relationship between the recovery anneal samples and the SCC resistance. The strain ratio values increase with an increase in Feret diameter, while the maximum crack depth decreases with increase in the Feret diameter.

The results were consistent with the observations in the grain size effect of the cold-rolled samples.

4.4 Discussion

In this study, we observed a strong correlation between the microstructure of the grain boundary and SCC susceptibility. The two distinct thermomechanical treatment process (cold work and recovery anneal) changed the grain size as well as the size and continuity of the grain boundary precipitates. STEM images and particle analysis showed that smaller grain materials consistently had finer and continuous grain boundary precipitates. This appears to have made smaller grain materials more susceptible to intergranular corrosion compared to coarse grain materials. In the presence of stress, these smaller grain materials underwent a brittle intergranular fracture, while ductile fracture was dominant in coarse grain materials. The FIB lift off the cracked samples also confirmed the evidence of corrosion product along the grain boundary only in the smaller grained samples. EDS compositional data did not show any significant differences in the precipitate free zone as well as the grain boundary precipitate compositions between samples with different grain sizes.

In accordance with the concerns raised Ralston et al. [52], variables such as texture, mis-orientation angle, solutionizing temperature, quench rate, and aging conditions were held relatively constant, while the grain size of the material was altered. The two distinct thermo-mechanical processes used in this work appear to have changed the grain size, and the grain boundaries precipitate size and continuity. The SCC performance of the materials

in this work appears to have been impacted by the grain boundary microstructure more than by the grain size.

4.4.1 Grain Size Effect in microstructure

The inverse pole-figure map from EBSD, shown in **Figure 4-3**, confirmed the presence of fully recrystallized grains in both processing routes. The fine grains in the 80% CR samples could be associated with the strain energy from the cold roll reduction. This trend can be explained by the Johnson-Mehl transformation kinetics $DR_x = k(G/N)^{1/4}$, where DR_x is the grain size of the material, k is constant, G is the growth rate and N is the number density of the nucleation sites for recrystallization [99]. Dislocations act as a preferred nucleation site for the grain growth during solutionizing treatment and the cold rolling invariably increases the density [100]. This results in the formation of finer grains. In the case of 50% CR samples, the reduction in the dislocation density results in coarser grain size.

The coarsening of grain at higher recovery anneal temperature could be associated with the recovery and grain growth mechanism. Since there are no grain growth suppressing elements such as Zr, Sc, Yb, etc., the higher temperature facilitates coarsening of the grains [101, 102].

In the Al sheet, the major components of the texture are classified in three main categories recrystallization (cube, P, R), rolling (brass, copper, Goss, S, Dilamore or Taylor) and shear (rotated cube, inverse brass, E, F) [103]. The texture analysis (**Table 4-2**) showed that regardless of the processing route (cold work or recovery anneal), the random texture constitutes about 80%. This confirms the absence of any dominant texture after recrystallization. Similarly, the percentage of the high angle grain boundary was upwards

of 90% and there was no significant presence of the low angle grain boundaries (**Table 4-2**). This implies that except for the size difference, both smaller and coarser grain materials were fully recrystallized with random texture containing mostly high-angle grain boundaries irrespective of the processing route.

It appears that the change in grain size only affects the grain boundary features such as size and continuity of the precipitates along the grain boundary (**Figure 4-11** and **Figure 4-12**). From these results, it is clear that coarser grains lead to the formation of coarser grain boundary precipitate while smaller grains lead to finer grain boundary precipitates. The reason for these findings can be attributed to the fact that the presence of grain boundaries facilitates precipitation to occur, and as the size of matrix grains becomes finer, the number of such sites for precipitation nucleation increases. Saito et al. [104] reported similar results in their Monte Carlo simulations of the grain boundary precipitation. They reported a logarithmic relationship between the precipitate size at the grain boundary (d_p) and the grain size (Dm), as shown in the equation below.

$$d_p = C D_m^{0.37}$$

where C is a constant.

Figure 4-13 shows a similar relationship between grain size and the grain boundary precipitate size, with an exponent of 0.43. Zhang et al. [105] have recently reported that cryo-rolling of 5083 aluminum alloy results in the formation of fine grains that exhibit lower degrees of sensitization, mainly due to the discontinuity of precipitates present in the grain boundary. However, the apparent discrepancy between their findings and those of the current study could be attributed to the absence of an annealing step aimed at removing

dislocations generated by the cryorolling process, which subsequently act as nucleation sites for β-phase precipitation. These results imply that the discontinuity of the precipitates at the grain boundary can be achieved even in fully recrystallized material without the need of any complex processing conditions.

4.4.2 Grain Size Effect in SCC

The SCC improvement in coarse grain materials is in line with Tsai et al [54] work on the hydrogen embrittlement of 7475, however there are key differences when it comes to the grain boundary precipitate sizes. In their work, the improvement in the resistance to T6 of coarse grain material was attributed to the size of the precipitate at the grain boundary being above a critical precipitate size of 20 nm as it was necessary to nucleate hydrogen bubbles. In the present work, it has been observed that even in materials with smaller grain sizes, the Feret diameter of the precipitates was found to be 50 nm, which is well above the critical size. Despite this factor, the strain ratio of the smaller grain material was much lower compared to that of the coarse grain materials. We interpret this difference as a shift in the SCC mechanism from hydrogen embrittlement to anodic dissolution based on the following results.

Figure 4-10 and **Figure 4-19** indicate that even in the absence of stress, the smaller grain samples exhibited clear signs of intergranular corrosion. However, the coarser grain materials exhibited a pitting type of attack. This indicates that there is an inherent difference in the grain boundary microstructure between these materials.

Similar corrosion morphology differences were observed in the fractured samples during the SSRT in ASTM D1384 solution containing 1% H_2O_2. **Figure 4-8** shows the FIB cross-

section liftoff of the 80% cold rolled sample, where the crack propagated along the corroded grain boundary. The crack walls were covered with an oxide confirming the intergranular corrosion. The presence of continuous grain boundary precipitates at the tip of the crack could be observed. **Figure 4-9** shows the FIB cross-section liftoff of crack tip of 50% cold rolled material. Unlike finer grain material, the stress corrosion crack appears to have originated at the pitting corrosion site and propagated along a transgranular path. In addition, the presence of coarse and discontinuous precipitates along the grain boundaries can be observed in the case of a coarser grain sample.

The fractographs in **Figure 4-7** and **Figure 4-18** are in good agreement with the data from the cross sectioned samples. There appears to be a distinct difference in the fracture morphology between the small and the coarse grain materials. In large grain materials the morphology (**Figure 4-7b and Figure 4-18c**) resembled a transgranular dimple fracture due to overload. The presence of constituent particles within the dimple-like features can also be observed. However, in smaller grain materials, the equiaxed intergranular cleavage morphology (**Figure 4-7a and Figure 4-18a,b**) was observed. The higher magnification of the fractured surface (**Figure 4-18**) showed a speckled appearance on the facets of the fractured grains. This could be attributed to the anodic dissolution of the strengthening precipitates in the SSRT test solution. No signs of crack arresting marks were observed. Such features are generally associated with hydrogen-assisted cracking [106]. These data suggest that the anodic dissolution of the grain boundaries appears to play a dominant role in SCC of smaller grain materials under tested conditions.

In 7xxx alloys, strengthening precipitates ($MgZn_2$) nucleate and grow at both matrix and grain boundaries. The $MgZn_2$ precipitates are typically anodic to the matrix, so dissolution

of these grain boundary precipitates results in intergranular corrosion, especially when these precipitates are fine and continuous along grain boundaries [33, 107, 108]. Several researchers [75] [73] [74] have reported improvement in intergranular corrosion and subsequent resistance to SCC by engineering the grain boundary to aid in the formation of coarse discontinuous precipitates. This is generally achieved by suppressing recrystallization leading to formation of a low angle grain boundary that favors discontinuous precipitation. For example, Kannan et al. [78] reported the improved resistance to SCC of the Sc containing Al–Zn–Mg–Cu–Zr. The Sc addition resulted in recrystallization suppression leading to formation of low angle subgrain boundaries. This in turn led to formation of coarse and discontinuous grain boundary precipitates, leading to a lower rate of dissolution. **Figure 4-14** shows the relationship between the mean Feret diameter with the strain ratio and the maximum depth of the crack. It is evident that with an increase in the GBP size, the strain ratio increases while the maximum crack depth decreases.

These results are in line with observations of Andreatta et al. [109] work on 7075 grain boundary microstructure on intergranular corrosion resistance. They showed that susceptibility to intergranular attack in the T6 temper was due to continuous precipitation along the grain boundary. They correlated the improvement in intergranular corrosion resistance in T73 with the increase in size of the $MgZn_2$ particles at the grain boundaries and their distance between particles. Similarly, Chen et al. [77] showed that fine grain boundary precipitate size led to decrease in SCC resistance. The present study reports a similar improvement in the resistance of 7075-T6 alloy to IGC and SCC by increasing the grain size through standard thermomechanical treatments. This leads to the formation of

coarse and discontinuous grain boundary precipitates, which enhances the resistance of the alloy. Given the study design, between the coarseness and discontinuity it's not clear which factor has a pronounced on the SCC resistance. However, it is desirable to have the combination of these two factors for a good grain boundary corrosion resistance.

Alternatively, the composition of the grain boundary also affects the intergranular corrosion. Therefore, alloying elements such as Cu are added to the 7xxx alloys to improve the intergranular and SCC resistance. The improvement is associated with Cu incorporation into $MgZn_2$ leading to a lower dissolution of the grain boundary precipitates. Ramagopal et al. [62] experimentally showed that copper additions, up to approximately 8 % to $MgZn_2$ analogs did not have much influence on the breakdown potential. In their subsequent work Ramagopal et al. [110] compared the grain boundary microstructure compositions of 7075 alloy in the T6 and T73 temper. The composition of the solute-depleted zone (SDZ) was comparable between the tempers. However, the Cu content in the grain boundary precipitates of T6 was 8 at% while that of T73 was 30 at%. It was hypothesized that this difference in Cu concentration caused SDZ to either actively dissolve or repassivate in chloride solutions. This implies that under the standard T6 ageing conditions the Cu incorporation in grain boundary precipitates is limited and does not significantly affect the dissolution kinetics of the grain boundary precipitate. STEM EDS data (**Table 4-4**) of the GBP and PFZ clearly showed that grain size didn't affect the composition. Irrespective of the processing conditions and grain size, the compositions of the GBP are comparable and the small differences are not statistically significant. This is not surprising since the base alloy composition, solution heat treatment, quenching, and aging practices were all kept constant in our work. Knight et al. [36] showed that there is little or no correlation between

grain boundary microstructure and SCC, but the microchemistry of the precipitates is the only factor that determines the resistance to SCC. However, they were comparing the effect of over-aging but not the effect of same temper on the different upstream processing sequence.

One of the interesting outcomes of this work was that, between the two thermo-mechanical processes, the cold work reduction appears to have produced grain boundaries with the coarsest precipitates compared to recovery anneal. Similarly, the highest strain ratio and lowest crack depth were observed in 50% cold rolled material. The grain size aspect of the material alone did not appear to have made any difference when it comes to the propagation of stress corrosion cracks. In the smaller grain material, the fully recrystallized boundaries did not provide a more tortuous path for crack propagation. This aspect should be probed further by crack growth techniques as it can further deconvolute the grain size and grain boundary microstructure effects. Similarly, this study did not focus on understanding the relationship between grain size and the growth kinetics of grain boundary precipitates as it was beyond the scope of our work. From SCC mechanism perspective the current body of evidence strongly suggest that under the tested conditions, the anodic dissolution of the grain boundary precipitates plays a dominant role in SCC propagation, however the role of hydrogen is still not clear. Further work is needed to elucidate the role of the hydrogen in SCC under these conditions.

4.5 Summary

This work shows that the grain size affects the IGC and SCC performance of the 7075-T6. Finer grain materials tend to have fine and continuous anodic precipitates along the grain

boundary, whereas coarse grain materials tend to have coarse and discontinuous GBP. When such microstructures are exposed to corrosive environment, these grain boundary precipitates are preferentially attacked, resulting in IGC in finer grain materials. When stress is applied to these materials, cracks tend to propagate along the corroded grain boundary leading to a brittle intergranular fracture. By engineering the grain boundary through standard thermomechanical treatments, we could significantly improve the performance of structural corrosion (IGC, SCC) of 7075-T6.

Figure 4-1

CHAPTER 5: EFFECT OF COPPER ON THE SCC RESISTANCE OF HIGH SOLUTE ZIRCONIUM CONTAINING 7XXX ALLOYS.

5.1 Background

The literature review chapter indicates that the effect of Cu on corrosion performance is not entirely clear. Previous studies have used over-aging techniques to amplify the Cu effect, but these techniques are not feasible for real-world applications. Additionally, researchers who changed the alloy composition also changed the downstream processing, resulting in multi-factor effects on the final corrosion performance. The purpose of this work is to understand the effect of Cu additions on the corrosion performance of Zr containing high solute alloys 7xxx alloys in T6 temper.

5.2 Approach

A high solute Zr containing 7xxx alloys (**Table 5-1)** with different Cu levels (0.3, 1.17, 1.35 wt%) were made by the direct chill casting method. The samples were then subjected to similar homogenization, hot and cold roll sequence to obtain 2mm thick material. The samples were aged to standard T6 condition (125^{o}C for 24h) after solutionizing (480^{o}C, 5 min) and water quench (350^{o}C/s). The resulting microstructure was characterized and evaluated for its corrosion resistance in an oxidizing environment (ASTM D1384 + 1% H_2O_2).

Table 5-1: Composition of the alloys from the ICP-OES measurements.

Sample	Cr	Cu	Fe	Mg	Si	Zn	Zr
Alloy A	0.01 – 0.11	0.30	0.16 – 0.18	2.16 – 2.36	0.08 – 0.18	9.13 – 9.33	0.13 – 0.23
Alloy B	0.03 – 0.13	1.17	0.18 – 0.28	2.18 – 2.38	0.07 – 0.18	8.82 – 9.12	0.13 – 0.23
Alloy C	0.04 – 0.14	1.35	0.17 – 0.28	2.10 – 2.30	0.13 – 0.23	7.82 – 8.12	0.09 – 0.29
7075	0.19 – 0.29	1.59	0.17 -0.28	2.54 – 2.74	0.04 – 0.14	5.79 – 6.09	0.01 – 0.2

5.3 Results

5.3.1 Microstructure characterization:

The composition of the alloys from ICP measurements is listed in **Table 5-1**. Compared to conventional 7075, the alloy variants have higher amount of Zn and similarly, in terms of minor alloying elements, Cr was replaced with Zr in the high-solute alloys. The key difference between the high-solute variants (alloys A, B, C) was the amount of Cu. Alloy A was the low copper variant with 0.3% Cu, while alloys B and C had 1.17% and 1.35% Cu, respectively. As mentioned above, the downstream processing conditions were similar between the alloys. Therefore, the microstructure and the corresponding properties changes are mainly associated with the difference in Cu levels in the alloys. Cross-sectional view images of the grain structure after T6 aging are shown in **Figure 5-1**. 7075 showed fully recrystallized and equiaxed grains. However, the rest of high-solute alloys showed varying degree of recrystallization. Alloy A exhibited a fibrous grain structure without any sign of recrystallization after solution heat treatment and aging. Alloy B showed a mixture of fibrous and fully recrystallized grains, while alloy C predominantly showed fully recrystallized grains. Differences in the Cu level appears to be affecting the recrystallization resistance in the high-solute alloys.

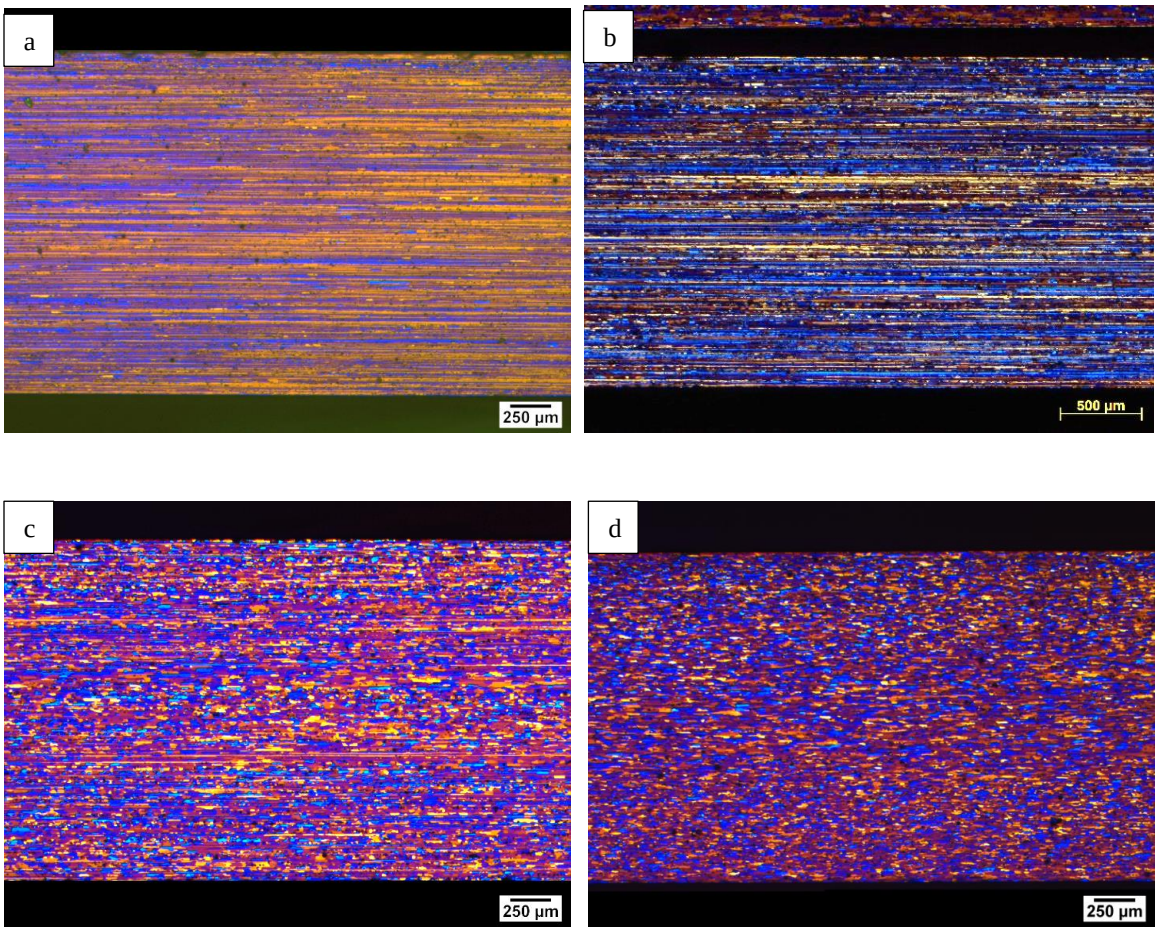

Figure 5-1: Cross section view optical microscope images of the (i) Alloy A (ii) Alloy B (iii) Alloy C (iv) 7075 in T6 temper.

Figure 5-2 shows the grain boundary misorientation data in plane view from the EBSD measurement. When the misorientation angle between adjacent grains was in the range of 5 – 15^{o}, the grain boundary was considered to be a low angle grain boundary, while the angle greater than 15^{o} was considered as the high angle grain boundary. The conventional 7075 alloy had only 6% of low angle grain boundaries, while the rest of the boundaries were high angle in character. In the low Cu variant Alloy A, the low angle grain boundaries (55%) are of a dominant type. However, Alloy B containing 1.17% Cu had significantly

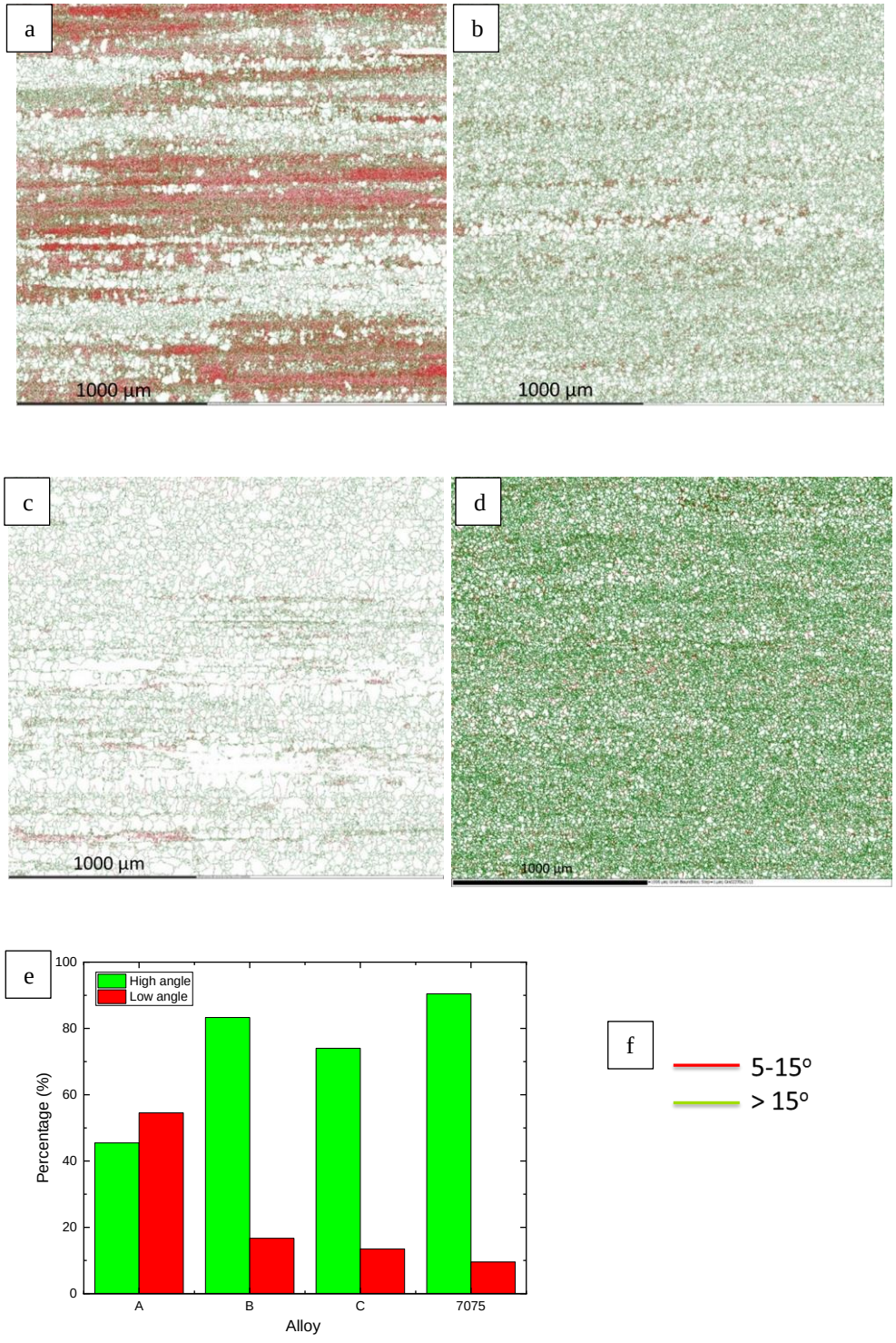

Figure 5-2: Grain boundary misorientation map for (a) Alloy A (b) Alloy B (c) Alloy C (d) 7075 in T6 temper (e) estimation of grain boundary as function of composition (f) legend for the misorientation maps.

fewer low angle grain boundaries (17%) compared to Alloy A. The high Cu variant Alloy C had a similar percentage of low (12%) and high (88%) angle grain boundaries to that of 7075. Consistent with the optical microscope images, the EBSD data also confirmed the impact of Cu addition on the recrystallization resistance of the high-solute alloys with misorientation angle parameter.

Table 5-2: Data from the particle analysis over 0.5mm^2 area.

Phase	Particle percentage (%)			
	Alloy A	**Alloy B**	**Alloy C**	**7075**
Al_7Cu_2Fe	32.82	55	55.72	73.61
Al_2MgCu	20.28	16.73	7.66	1.25
Mg_2Si	7.84	4.56	10.02	12.01
M Phase	39.04	23.69	26.58	13.13

Error! Reference source not found. contains the particle analysis data from the feature d etection and characterization technique. In the characterized area of 0.5 mm^2, Alloy A had 598 particles, of which 32% were characterized to be Al_7Cu_2Fe type particles. The other particles found in the analysis were MgZnCu (M) phase (39%), Al_2CuMg (20%) and Mg_2Si (7%). Alloy B and Alloy C had 702 and 718 particles over the measured area, respectively. In the case of Alloy B, the Al_7Cu_2Fe constituted to 55% of the particles followed by M phase (23%), Al_2CuMg (16%) and Mg_2Si (4%). Alloy C also had the phase distribution comparable to Alloy B with Al_7Cu_2Fe (55%), M phase (26%), Al_2CuMg (7%) and Mg_2Si (10%). Overall, the total number of particles increased in higher Cu-containing alloys. The percentage of Al_7Cu_2Fe particles were higher in Alloy B and C compared to Alloy A. However, Al_2CuMg decreased with increase in the Cu content, while Mg_2Si did not show any specific trend.

Table 5-3: Data from the particle size analysis.

Phase	Particle size ECD (um)			
	Alloy A	**Alloy B**	**Alloy C**	**7075**
Al_7Cu_2Fe	2.10	2.19	1.83	1.41
Al_2MgCu	0.76	0.75	1.65	1.23
Mg_2Si	1.89	1.28	1.67	1.5
M Phase	1.88	1.87	1.86	1.49

Table 5-3 shows the equivalent circle diameter (ECD) of the particles. The ECD of the particles was typically around 1.5 um and was comparable between the alloys. No clear trends were observed between the Cu levels and the size of the particles.

Figure 5-3 shows the bright-field STEM images of the grain boundaries of the high-solute 7xxx alloys. Irrespective of the composition, all alloys showed distinct presence of a narrow region adjoining the grain boundaries that was devoid of the precipitate. The width of this precipitate free zone (PFZ) was approximately 30 nm, and it was comparable between the alloys. Similarly, there were precipitates along the grain boundaries. In Alloy A, the grain boundaries were mostly free of precipitates and in the boundaries where precipitates were observed, they were largely discontinuous. On the other hand, Alloy B had discontinuous presence of coarse precipitates along the grain boundaries. The standard 7075 alloy exhibited a fine and continuous presence of precipitates along the grain boundaries.

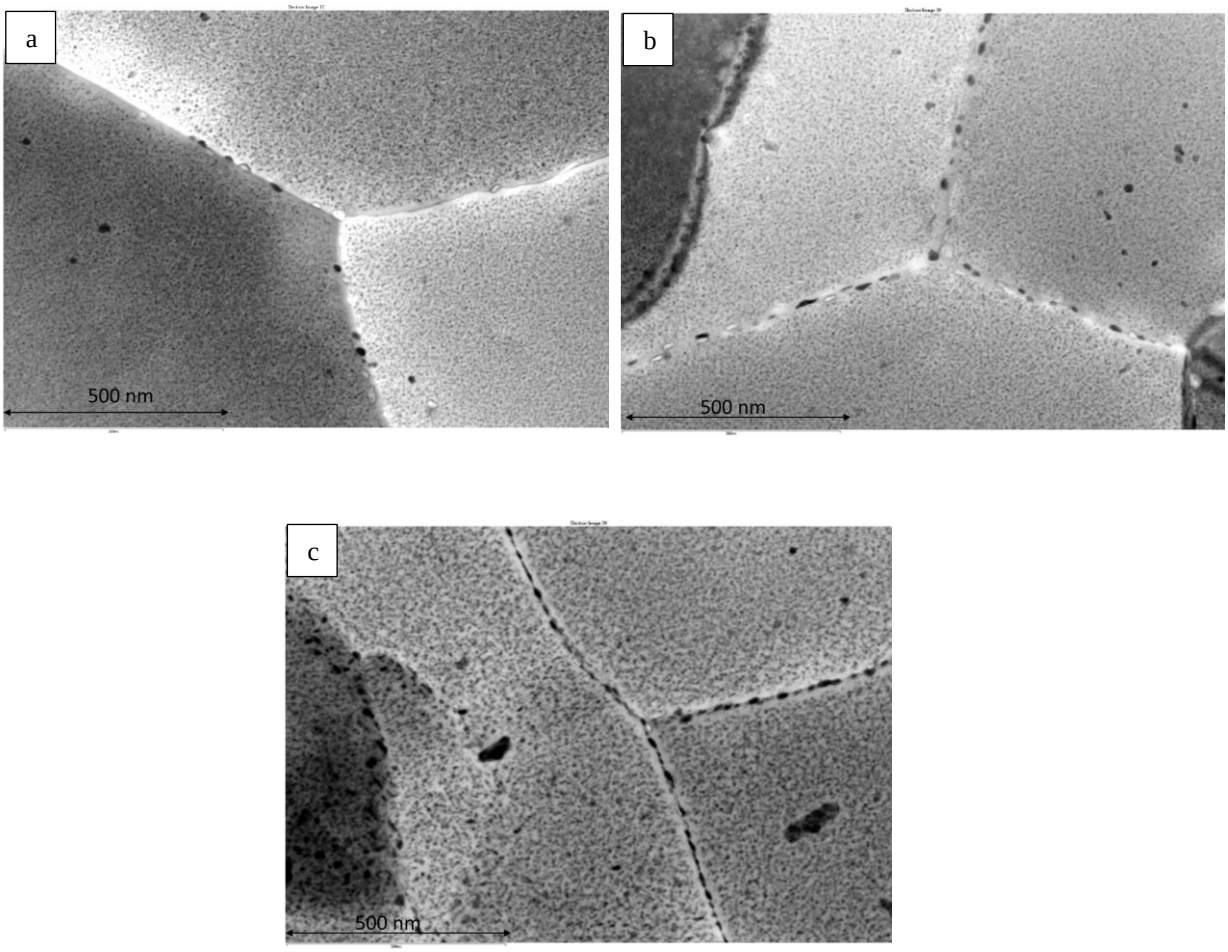

Figure 5-3: STEM bright field images for (a) Alloy A (b) Alloy B (c) 7075 in T6 temper.

To determine the impact of the alloy composition changes on the amount of the eutectic phases the differential scanning calorimetry (DSC) was carried out (**Figure 5-4)** in the as-cast conditions. Alloy A showed a sharp endothermic peak that started at 477 ° C and ended at 481 ° C. The delta H associated with this transition was -1.2J/g. Alloy B exhibited a stronger endothermic peak that started at 475 ° C and ended at 479 ° C with a delta H value of -7.18J/g. The endothermic transition of Alloy C was similar with a delta H of -8.65J/g. With an increase in the Cu content, the enthalpy of the endothermic reaction increased in

high-solute alloys. The standard 7075 had the endothermic peak at 490°C with an intermediate delta H of -3.73 J/g.

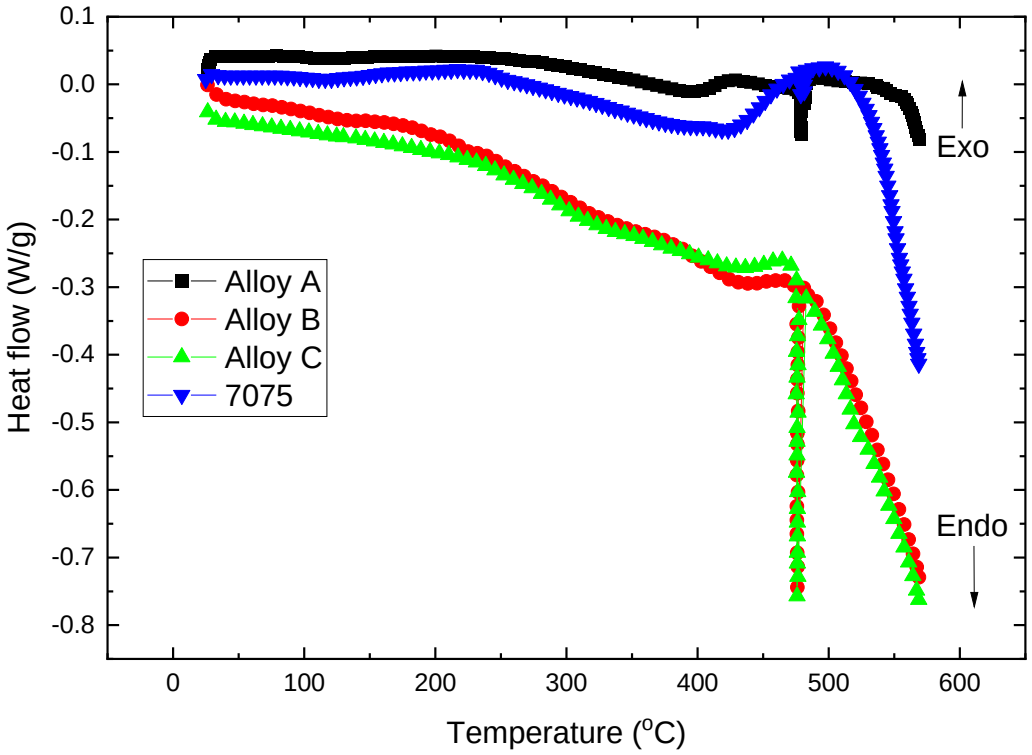

Figure 5-4: DSC curve for the alloys containing different Cu levels.

5.3.2 Corrosion testing.

Figure 5-5 shows the anodic and cathodic polarization behavior of the high solute alloys in the ASTMD 1384 test solution. The free corrosion potential of the low Cu Alloy A was approximately -904 mV_{SCE}, with an increase in Cu level the potential value started shifting in noble direction as in the case of Alloy B (-684 mV_{SCE}) and Alloy C (-600 mV_{SCE}). 7075 alloy had the most noble free corrosion potential of -570 mV_{SCE}. In the anodic polarization

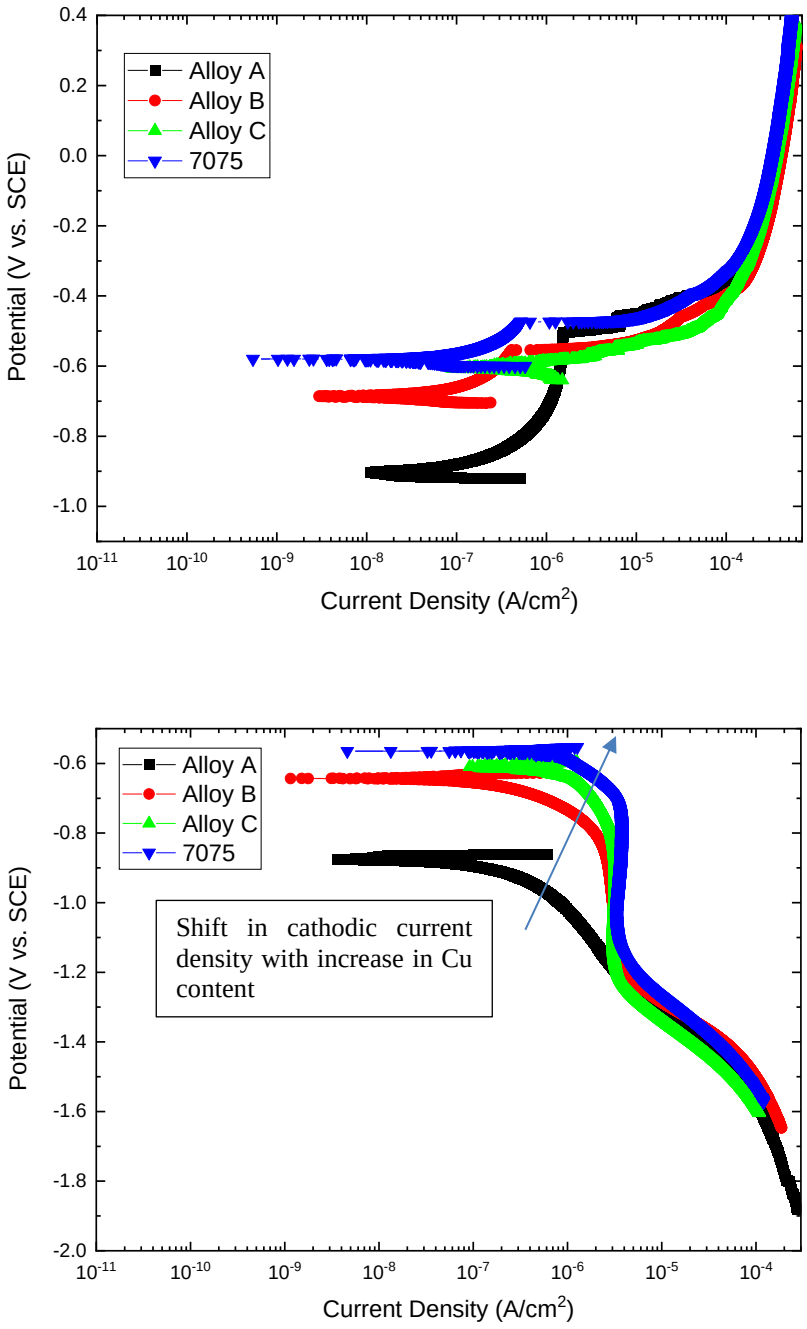

Figure 5-5: Electrochemical anodic (above) and cathodic (below) polarization testing in ASTM D1384 solution.

of alloy A and B, as the potential increased from the free corrosion potential point, the current initially increased but reached a steady-state limited value (passivation) and beyond an inflection point (breakdown potential) the current increased significantly with small change in the potential. However, the Alloy C did not exhibit strong passivation behavior; with the increase in the potential from the free corrosion potential point, the current also increased logarithmically. 7075 alloy exhibited a small passivation range and the breakdown potential were comparable to high-solute alloys. The Cu addition did not significantly affect the breakdown potential values. During cathodic polarization, as the potential was swept from the free corrosion potential point, the cathodic current quickly reaches a limiting value in all three alloys. However, the value of the limiting current is impacted by the Cu content. Alloy A had the lowest value, while 7075 had the highest limiting current value.

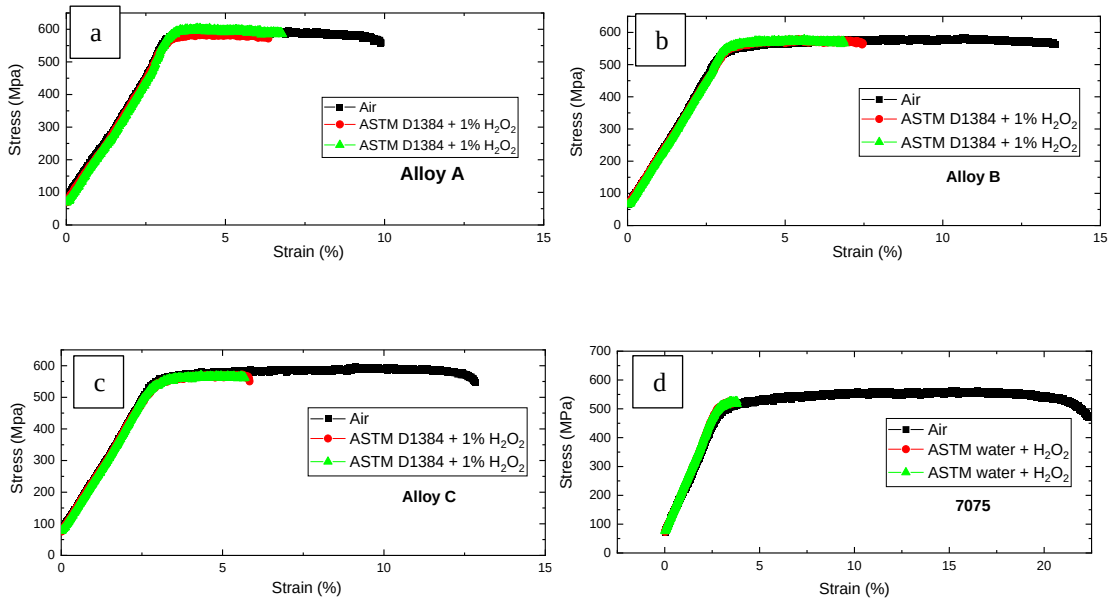

Figure 5-6: SSRT in ASTM D1384 solution + 1% H_2O_2 (a) Alloy A (b) Alloy B (c) Alloy C (d) 7075 in T6.

Figure 5-6 shows the stress strain curve from the slow strain rate test (SSRT) that was carried out in air and in ASTM D1384 + 1% H_2O_2. The strain at failure was higher in the materials tested in air compared to the corrosive environment. The ratio of strain at failure in corrosive environment to air was used to assess the susceptibility of the stress corrosion cracking. **Figure 5-7** shows the effect of alloy composition on the strain ratio. Alloy A had the highest strain ratio of 0.66, while 7075 had the lowest strain ratio of 0.18. Alloy B had a strain ratio of 0.55 while Alloy C had the strain ratio of 0.45. With an increase in the Cu content, the strain ratio decreased consistently.

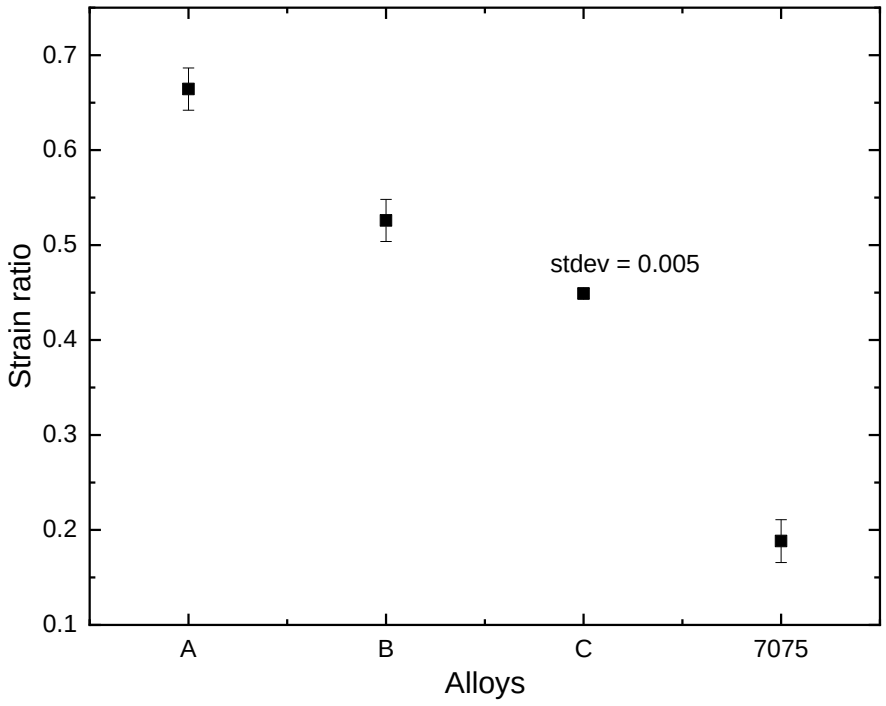

Figure 5-7: Effect of Cu content on the strain ratio of the alloys in ASTM D1384 + 1%H_2O_2

Figure 5-8 shows the cross section of the fractured samples after SSRT. All samples showed clear sign of stress corrosion cracking. In case of 7075 the cracks were propagating

along the corroded grain boundaries. In alloy A, the crack appears to have initiated from the pitting corrosion sites. There was no sign of intergranular crack propagation. Similar features were observed in Alloy B and C. Even with an increase in Cu content, the crack initiation and propagation modes were comparable.

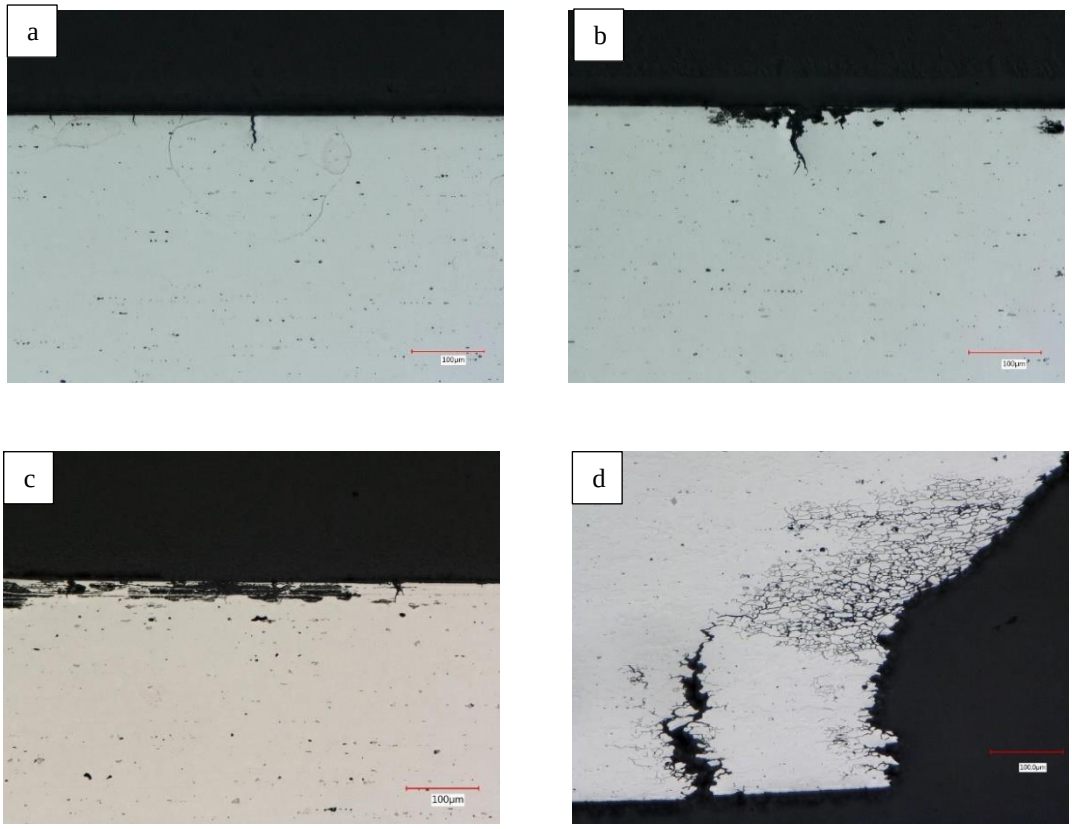

Figure 5-8: Metallographic cross section of the fractured samples after SSRT in ASTM D1384 + 1% H_2O_2 (a) Alloy A (b) Alloy B (c) Alloy C (d) 7075 in T6.

Figure 5-9 shows the SEM images of the fracture surface of the alloys. The high-solute alloys have morphology that resembles combination quasi-cleavage and ductile

dimple/microvoid features. Alloy B fracture surface additionally has a layered/foliated feature close to the edge, where the corrosion attack had happened. Alloy C exhibits both

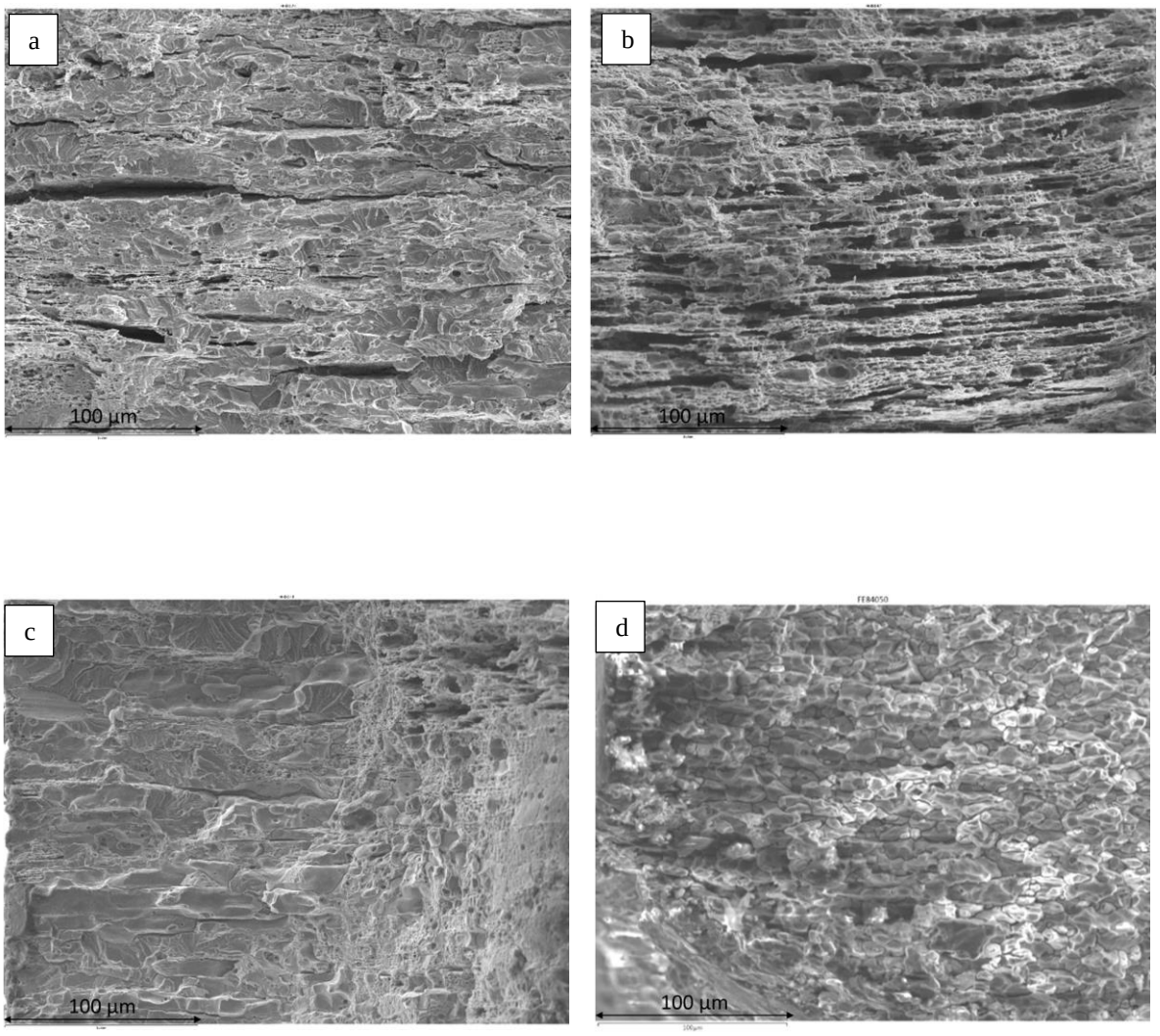

Figure 5-9: SEM images of the fractured samples after SSRT in ASTM D1384 + 1% H_2O_2 (a) Alloy A (b) Alloy B (c) Alloy C (d) 7075 in T6.

ductile and quasi-cleavage fracture features. In case of 7075 we can observe equiaxed intergranular cleavage morphology, with no sign of any micro void features.

Figure 5-10 shows the cross-section images of the samples after 24 hours of exposure in solution containing ASTMD1384 + 1% H_2O_2. All alloys have undergone localized corrosion attack. The corrosion attack morphology for the 7075 alloy was IGC. The corrosion had initiated as a pit but propagated along the grain boundaries.

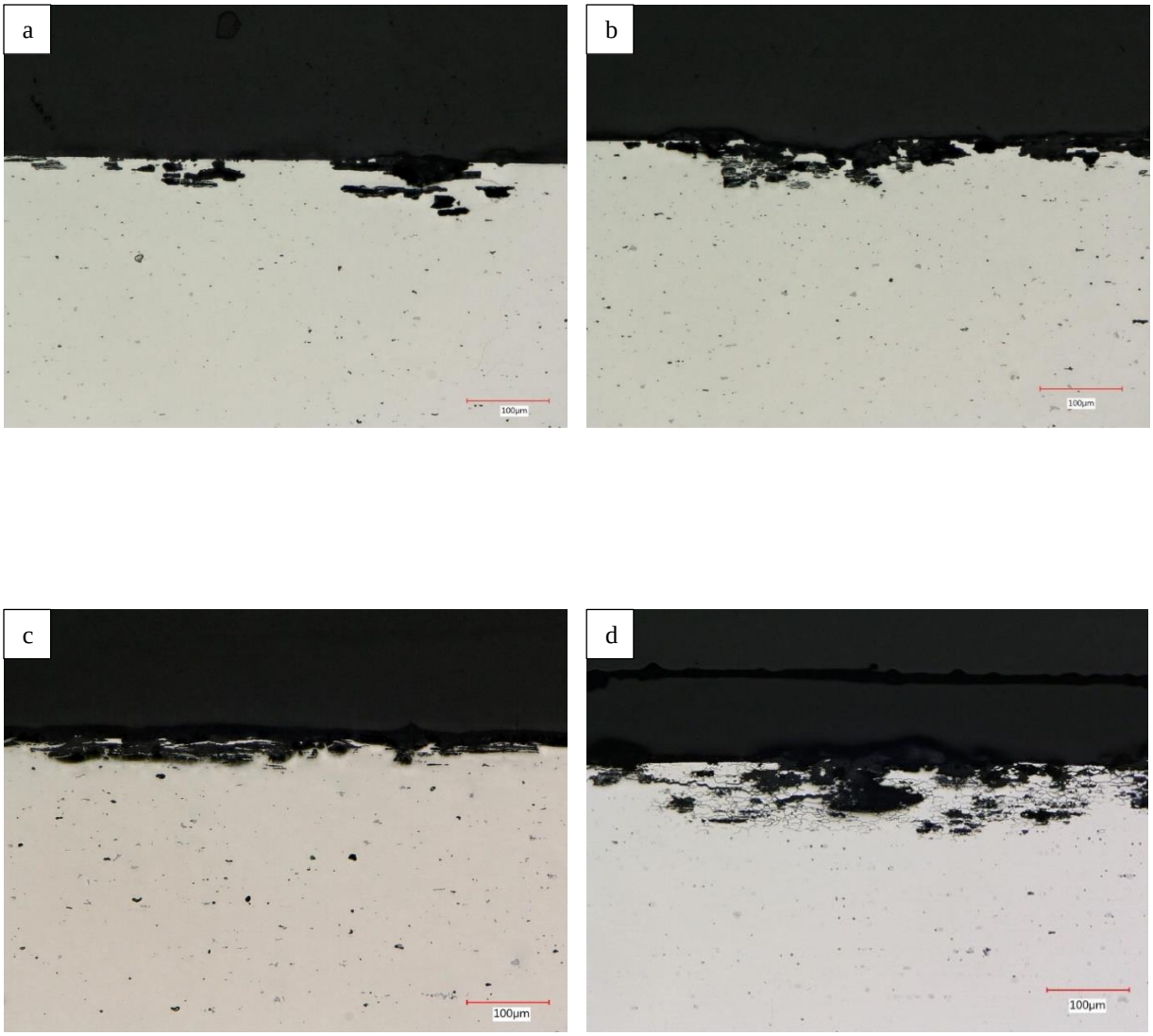

Figure 5-10: Metallography cross section images after 24h immersion in ASTM D1384 + 1% H_2O_2 (a) Alloy A (b) Alloy B (c) Alloy C (d) 7075 in T6.

The cross-section images showed that the boundaries of the equiaxed grains had been attacked selectively, while the grain interiors remained intact. The corrosion morphology of Alloy A was pitting, and no sign of intergranular corrosion was observed. The number of pitting sites was very limited. Alloy B also showed a pitting type of attack, but the number of corroded sites was higher compared to Alloy A. Similarly, Alloy C had a higher number of pitting corrosion sites than Alloy A and B but exhibited pitting type of corrosion morphology.

5.4 Discussion

The aim of this study was to investigate the effect of adding Cu to high-solute 7xxx alloys on their microstructure and corrosion resistance. The addition of Cu had two main effects on the microstructure, which, in turn, affected the corrosion performance. Firstly, the amount of Al_7Cu_2Fe particles increased with increasing Cu content, which caused a shift in the free corrosion potential towards the noble direction and increased the susceptibility to pitting as confirmed by electrochemical polarization and immersion testing. Secondly, Cu addition affected the recrystallization resistance of the alloys. An increase in Cu content resulted in a higher fraction of fully recrystallized grains and an increase in the percentage of high-angle grain boundaries. Despite the increase in high-angle grain boundaries, the high-solute alloys did not undergo intergranular corrosion, unlike standard 7075. STEM images revealed that the grain boundaries in the high-solute alloys were relatively free of precipitates, whereas those in 7075 had a continuous layer of precipitates. These two key microstructure characteristics made the high-solute alloys more resistant to stress corrosion cracking compared to standard 7075.

5.4.1 Effect of Cu on Al_7Cu_2Fe

Various iron-containing intermetallics such as Al_7Cu_2Fe and $(Al,Cu)_6(Fe,Cu)$ are formed during the casting of the 7xxx alloy series [111, 112]. Formation depends mainly on the Fe and other binding solute elements in the melt. Once these intermetallics are formed, it is difficult to re-dissolve them in the matrix, even during high temperature homogenization and solutionizing treatment. Generally, they do not undergo any further phase transformation but are broken down into smaller sizes during the subsequent rolling operations. The localized corrosion resistance, such as pitting, is strongly dependent on the number density and chemistry of these intermetallics. Fe-containing particles are generally cathodic to the matrix, so a strong galvanic coupling between the matrix and particles is widely reported to have detrimental effects on the resistance to pitting [113]. N Birbilis et al. [85] reported that the 7075-T651 corrodes at the periphery of Al_7Cu_2Fe particles. This was attributed to the higher free corrosion potential of Al_7Cu_2Fe than that of the matrix 7075-T651 alloy. Similarly, from the cathodic polarization experiments, they showed that the particles were able to sustain higher rates of oxygen reduction reaction.

The particle analysis (**Table 5-2, Table 5-3**) of Alloy A containing 0.3 wt% Cu showed that 32% of the measured particles were Al_7Cu_2Fe. With increase in Cu content the percentage of Al_7Cu_2Fe increased. As mentioned above, due to the high melting temperature of Fe-bearing particles such as Al_7Cu_2Fe, Al_3Fe, α-AlFeSi, remain in the alloy even after the downstream high temperature thermal process such as homogenization and solution heat treatment. In our current work, we noticed that Al_7Cu_2Fe appears to be the only iron-containing constituent particle. This could be due to the presence of Cu in all of the alloys tested. One of the mechanisms proposed in the literature for the formation

Al_7Cu_2Fe particles is the incorporation of Cu in Al_3Fe [114] . Higher Cu level in the melt accelerates the atomic diffusion leading to the Al_7Cu_2Fe nucleation and growth on the phase boundary. Interestingly, even in the case of Alloy A (0.3 wt% Cu), no sign of Al_3Fe was observed. This indicates that even a smaller amount of Cu can easily favor the formation of Al_7Cu_2Fe during casting or during the high-temperature homogenization treatment. Cu diffuses in Al_3Fe, resulting into full transformation of Al_7Cu_2Fe particles. Wang et al. [115] also reported a similar trend in Cu containing 7055 which had predominantly Al_7Cu_2Fe while the Cu-free Al-Zn-Mg alloy contained Al_3Fe. A similar trend was observed by Qiao et al. [116] with the addition of 1.23% Cu to the 5052 alloy. They observed a significant increase in Al_7Cu_2Fe particles during casting and homogenization treatment, leading to a further increase in this particle due to the transformation of $Al_6(Fe,Cu)$ to Al_7Cu_2Fe.

In **Figure 5-5** the shapes of the polarization plots are comparable. This indicates that there is no large shift in the nature of the mechanisms in both the anodic and cathodic regions. However, we could clearly see a difference in the oxygen reduction current density region and the free corrosion potential. This could be due to an increase in the amount of particles such as Al_7Cu_2Fe. These Cu-containing particles are more noble to the matrix and are efficient in reducing dissolved oxygen in the electrolyte. This causes the particles to be more cathodic to the matrix. The galvanic coupling of the matrix and Al_7Cu_2Fe particles leads to anodic dissolution of the matrix [117]. As a result of the increased cathodic activity, the free corrosion potential is pushed in the noble direction. However, the addition of Cu does not seem to have an impact on the break-down potential of the metal. This could indicate that most of the Cu addition has gone into second-phase constituent particles such

as Al_7Cu_2Fe or to the strengthening M (MgZnCu) phase. If the substantial amount of Cu was in solid solution, it would have pushed the breakdown potential of aluminum in more positive direction [118]. We also notice that the addition of Cu also decreases the passivation range, i.e. the potential difference between free corrosion potential and the breakdown potential. This could indicate that the pitting susceptibility increases at the open circuit potential for high Cu containing alloys. Meng et al. [119] reported a different trend when it comes to the breakdown potential as a function of the Cu content. They observed a linear increase in the break-down potential as they increased Cu content of the Al-Mg-Cu-Zn alloys in a deaerated solution. However, the high Cu-containing alloys showed lower polarization resistance during EIS measurements in aerated solution.

Figure 5-10 shows the cross section after the immersion experiment. With an increase in Cu, the number of pitting corrosion sites on the surface increased significantly. The test solution contains hydrogen peroxide which strongly increases the oxygen reduction activity on the surface of Al_7Cu_2Fe particles. This would naturally increase the free corrosion potential to the metastable pitting potential region. As a result, alloys containing a higher amount of Al_7Cu_2Fe would have a higher amount of pitting corrosion sites. The observed trend is consistent with literature reports where higher and deeper pitting corrosion sites were found in Cu-containing 7xxx alloys compared to Cu-lean alloys [115, 120]. These reports have demonstrated the galvanic coupling between the 7xxx matrix and Al_7Cu_2Fe particles, with the local pH increase during oxygen reduction reactions attributed to the dissolution of the matrix. In one study, it was reported that during the early stages of pitting, selective dissolution of Al from Al_7Cu_2Fe resulted in the formation of Fe and Cu-

rich clusters on the particle surface, which increased cathodic activity and resulted in a stronger galvanic coupling with the matrix, leading to pitting [122].

The results from the current work build on existing knowledge about the formation and characteristics of the Al_7Cu_2Fe particles in 7xxx alloys. Although the current work did not identify the critical Cu concentration limit for the formation of Al_7Cu_2Fe particles, nonetheless the current results clearly show that even at 0.3wt% Cu, Al_7Cu_2Fe formation cannot be avoided.

5.4.2 Effect of Cu on recrystallization resistance

Several minor alloying elements, such as Zr, Sc, Yb, Er, are added to inhibit recrystallization in 7xxx alloys [74, 75, 77]. Unrecrystallized grain boundaries offers better quench sensitivity leading to improved grain boundary corrosion resistance compared to fully recrystallized materials. This is due to the presence of low angle sub grain boundaries in unrecrystallized materials that are energetically less favorable for precipitation [70]. In Zr-containing alloys, fine Al_3Zr dispersoids are formed during processing [121]. They exhibit superior drag force to retard the recrystallization and grain growth process as described by Zenner pinning mechanisms [122].

Figure 5-1 shows that alloy A has predominantly devoid of equiaxed recrystallized grains, while alloys B and C has higher degree of equiaxed grains. It appears that copper seems to be impacting the recrystallization resistance. Previous work has shown that Zr containing 7xxx alloys have exhibited strong recrystallization resistance [77]. However, they have not looked at the effect of alloying elements such as Cu on the recrystallization resistance. The Barker's etching method is good for revealing fully recrystallized grains, however, they

may not be sensitive in the revealing the sub-grain boundaries. To confirm this trend, data from the EBSD method was used. **Figure 5-2** shows that alloy A has higher amount of low angle grain boundary (misorientation < 15^{o}) while the percentage of high-angle grain boundaries (misorientation > 15^{o}) increases for alloy B and C. The low angle grain boundaries represent the sub grains in the unrecrystallized microstructure. The trend in the EBSD data is in line with the optical microscope images after Barkers etch. This means that for a given Zr concentration, the degree of recrystallization increases with an increase in Cu content. As mentioned above, dispersoids are very effective in retarding nucleation and grain growth in aluminum alloys. Based on the current composition range, Al_3Zr is the likely dispersoid type forming for these alloys. According to the Zenner pinning equation, there are two factors, such as volume fraction and size of the dispersoids, affect the ability for dispersoid to retard grain growth. Robson et al. [123] proposed that alloying elements in 7xxx alloys affect Al_3Zr precipitation. The authors found that Mg had the highest impact on the number density of Al_3Zr formation. Increasing the Mg content led to an increase in the number density of Al_3Zr dispersoids. They also observed that the mean radius of the dispersoids did not change significantly with the composition. The pinning pressure, which affects the strength and hardness of the alloy, is directly proportional to the volume fraction of Al_3Zr and inversely proportional to the radius. Since the radius was comparable between the compositions, the pinning effectiveness was mainly determined by the number density of Al_3Zr dispersoids.

During direct chill casting of the 7xxx alloys, Zr tends to segregate at the center of the grain in super saturated solid solution of Al matrix. This is due to the peritectic reaction during solidification and the low diffusivity of the Zr [124] [125]. The number density of Al_3Zr is

affected by presence of other solute elements in the aluminum lattice. C. Sigli [126] used the regular solution model to study the solubility of the metastable zirconium related to L12 type Al_3Zr. They noticed that the interaction parameter was most positive for Zr-Mg and Zr-Li, negative for Zr-Al and close to zero for Zr-Cu. The interaction parameter represents the thermodynamic binding energy between the like and unlike atoms. The positive interaction parameter value resulted in weaking of the Al-Zr bond in the aluminum matrix and this affected the solubility of Zr in the aluminum matrix since Al-Zr bond in FCC lattice are being replaced by Mg and Zn leading to formation of the second phase Al_3Zr. According to this model, Cu does not affect the precipitation unlike Mg. However, during casting, a sufficient amount of the eutectic phases such as AlCuMgZn are formed. With an increase in Cu levels thermodynamically there is more tendency for phase formation. The DSC data in **Figure 5-4** clearly show that as the Cu content in the alloys increases, the area under curve (**Table 5-4**) for the peak in the temperature range of 478^{o}C to 482^{o}C also increases.

Table 5-4: Enthalpy value of the endothermic reactions from the DSC measurements.

Samples	Onset (^{o}C)	Peak (^{o}C)	Endset (^{o}C)	Delta H (J/g)
Alloy A	478.7	480.6	482.9	-0.33
Alloy B	475.3	477	479.5	-7.18
Alloy C	474.9	477.2	480	-8.65
7075	485	490	497	-3.73

This temperature range is associated with the dissolution of the AlCuMgZn eutectic phases [127]. The area under the peak could be directly correlated with the concentration of eutectic phases in the alloys. Therefore, higher eutectic phases after casting could lead to a

lower amount of Mg in the solid solution, which in turn may affect the formation of Al_3Zr leading to higher recrystallization.

The data from this work provide new insight into the relationship between Cu and the recrystallization resistance in Zr-containing alloys. A higher concentration of Cu could lead to a smaller number of Al_3Zr and this affects the recrystallization resistance of the alloys. The number density of Al_3Zr could not be accurately quantified due to its nonuniform distribution in the grain interior. However, the effect of number density can be observed in terms of recrystallization resistance.

5.4.3 Effect of Cu on SCC resistance

In 7xxx alloy series the SCC failures have been attributed to both anodic dissolution and hydrogen-assisted cracking mechanisms [128]. The anodic dissolution have been correlated to the intergranular corrosion [39, 40], while hydrogen-assisted cracking correlated with the trapping sites present in the alloys [41, 42]. For the anodic dissolution mechanism to be dominant, the environmental condition should favor the selective attack of the grain boundaries or adjacent regions anodic to the rest of the microstructure without increasing the critical hydrogen concentration in the trapping sites [129]. In the current study, the SCC testing was carried out in the peroxide-containing solution, so the principal cathodic reaction will be of oxygen reduction rather than hydrogen evolution. The solution containing peroxide is also used in the evaluating the corrosion resistance of wrought alloys as it can selectively attack grain boundary precipitates in wrought heat treatable aluminum alloys [130]. This implies that the testing conditions used in the current work favor anodic dissolution more than hydrogen-assisted cracking mechanism.

In **Figure 5-7**, the strain ratio decreases with an increase in Cu content, which indicates that SCC susceptibility is negatively affected by an increase in Cu content. Previous work in the literature had shown that Cu addition improves SCC resistance due to changes in slip system and altering the dissolution kinetics of the $MgZn_2$ particle [59, 84]. The discrepancy could be due to the usage of different testing methodologies. In the current work, SSRT was used for SCC screening, while majority of the literature data were from the crack growth rate measurements under constant stress. The advantage of SSRT is the reduction in crack incubation period due to the application of raising the load at a constant rate [131]. As a result, SSRT is sensitive to the localized corrosion resistance of the material, as the applied rising load facilitates crack nucleation from defects, such as corroded area. The metallographic cross section images (**Figure 5-8**) after SSRT confirm the crack initiation from the pitting corrosion sites. With the increase in Cu, we have seen that the susceptibility of the alloy to pitting corrosion increases due to the higher number of the Al_7Cu_2Fe particles. Cross-section images (**Figure 5-10**) from the immersion experiments without applied stress have shown similar trend. Therefore, in the presence of the applied slow strain rate, the likelihood of crack nucleation is high in alloys containing higher Cu. In the case of the standard 7075 alloy, the crack appears to be propagating along the grain boundaries. This is due to the susceptibility to intergranular corrosion, as can be seen **Figure 5-10**.

Corrosion morphology is affected by the grain boundary microstructure. The difference in the electrochemical dissolution potentials between the grain interior and the grain boundaries precipitate phases results in intergranular corrosion. The discontinuity of precipitation along the grain boundary or the incorporation of more noble elements to

reduce the difference in dissolution potential could minimize the IGC [132, 133]. From the STEM images (**Figure 5-3**) of the high solute alloys, we can see that the grain boundaries were relatively clean of precipitates and even if they were present, they are discontinuous. This could be due to the presence of higher fraction of unrecrystallized grains in the alloys. Fine Al_3Zr dispersoids pin the subgrain boundaries in unrecrystallized grains and retard the transition to the high angle recrystallized grain boundary (**Figure 5-2**), thus remarkably inhibiting recrystallization (**Figure 5-1**) and stabilizing the deformation recovery microstructure [74]. The low-angle grain sub-boundaries in unrecrytallized microstructures are not energetically favorable for the M-phase precipitation. Since its energy is closer to grain interior and significantly lower than the recrystallized grain boundaries, the concentration of precipitates is lower and more discretely distributed [134]. Alternatively, Al_3Zr have been reported to act as a nucleation site for the M-phase in Zr containing 7xxx alloys [135, 136]. Therefore, a combination of these factors could have minimized precipitation along the grain boundaries. Since 7075 does not contain Al_3Zr dispersoids to form low angle sub-grain boundaries, the precipitates are continuously distributed along the high angle grain boundaries.

SEM images (**Figure 5-9**) of the fractured samples show a difference in morphology between the high solute and the standard 7075 alloy. In case of high-solute alloys, the fracture surface exhibits transgranular fracture due to mechanical overload. However, in case of 7075, we could observe clear sign of the brittle intergranular fracture. This could be attributed to the differences in the corrosion morphology of the alloys.

The results of this study supports the growing body of evidence on the impact of the grain boundary precipitate discontinuity on the IGC and SCC. However, the generalizability of

the results could be limited by the testing environment, as mentioned earlier in this section. However, the present work has demonstrated the high solute 7xxx alloys can be designed to have an improved localized corrosion resistance in peak aged temper under oxidizing environments.

5.5 Conclusion

In this study, the results show that the Cu addition has multifactor effect on the microstructure and corrosion resistance of the high solute 7xxx alloys. Compared to the standard 7075, these high-solute alloys have improved IGC and SCC. An increase in Cu content leads to an increase in the number of Al_7Cu_2Fe particles and this, in turn, increases the pitting susceptibility of the alloys. Similarly, the addition of Cu increases the number of fully recrystallized grains in the alloy, leading to the formation of a high angle grain boundary. Despite this trend, the grain boundary precipitates are largely discontinuous, resulting in no IGC. The presence of stress leads to nucleation of cracks from the pitting corrosion sites and the resulting strain ratios were much higher compared to standard 7075. The testing conditions were conducive to promoting anodic dissolution events, and as a result the impact of the hydrogen-assisted cracking in these alloys remains unknown. By controlling the levels of key alloying elements such as Cu and Zr, we can achieve a microstructure that is resistant to IGC and SCC under oxidizing conditions.

CHAPTER 6: EFFECT OF ZINC TO MAGNEESIUM RATIO ON THE SCC RESISTANCE OF HIGH SOLUTE 7XXX ALLOYS IN HUMID ENVIRONMENT

6.1 Background

In the previous chapter, the effect of alloy composition on stress corrosion cracking (SCC) was studied in the NaCl containing environment. As mentioned in the previous discussion section, the test environment promotes anodic dissolution. A recent safety information bulletin (SIB No: 2018-04) published by the European Aviation Safety Agency (EASA) indicates that a 7xxx high solute composition may be susceptible to cracking in a moist environment. Therefore, the objective of this chapter is to assess the effect of the composition, specifically on the grain boundary features, on the SCC in a humid environment. This work was done in collaboration with Dr. Shawn Yu (Senior Scientist, Novelis inc), who performed the DFT calculations.

6.2 Approach

The SCC tests were carried out in two key environmental conditions, 35°C at 85% RH and at 70^{o}C at 85% RH. Due to the limitations of the environment, the samples were not subjected to slow strain rate tests but instead were subjected to the constant displacement method. Two types of strain conditions were used, namely the uniaxial and four-point bend test and they were based on ASTM standards G49-85 (2019) and G39-99 (2021), respectively. For microstructural characterization, scanning transmission electron microscopy (STEM) and the energy dispersive spectrum (EDS) were used to image and

measure composition of grain boundary features, respectively. DFT calculations were carried out using the Vienna ab initio simulation package (VASP) to determine the segregation energy and embrittlement potency of solute elements in ∑5 high angle aluminum grain boundaries.

6.3 Results

6.3.1 Stress corrosion cracking test in the humid environment

Table 6-1 shows the results of the uniaxial constant displacement test in an environment of 35°C with 85% relative humidity. A significant difference in the time to failure was found between the high-solute alloys and the conventional 7075. Alloy A failed after three days of exposure, while Alloy B failed in less than 10 days. The conventional 7075 alloy did not fail even after seven weeks of exposure.

Table 6-1: Summary test results of samples stressed at 80% yield strength in humid environments.

Samples	**Days to failure**		
	35ºC at 85% RH **Duration: 49 days** **Applied stress: uniaxial**	**70ºC at 85% RH** **Duration: 100 days** **Applied stress: uniaxial**	**70ºC at 85% RH** **Duration: 100 days** **Applied stress: 4 point bend**
Alloy A	Failed, 3 days	Failed, 1 day	Failed, 1 day
Alloy B	Failed, 10 days	Failed, 2 days	Failed, 1 day
7075	Passed	Passed	Passed

Figure 6-1 shows the metallography cross section of the failed samples. We could observe the clear sign of cracking in both high-solute alloys.

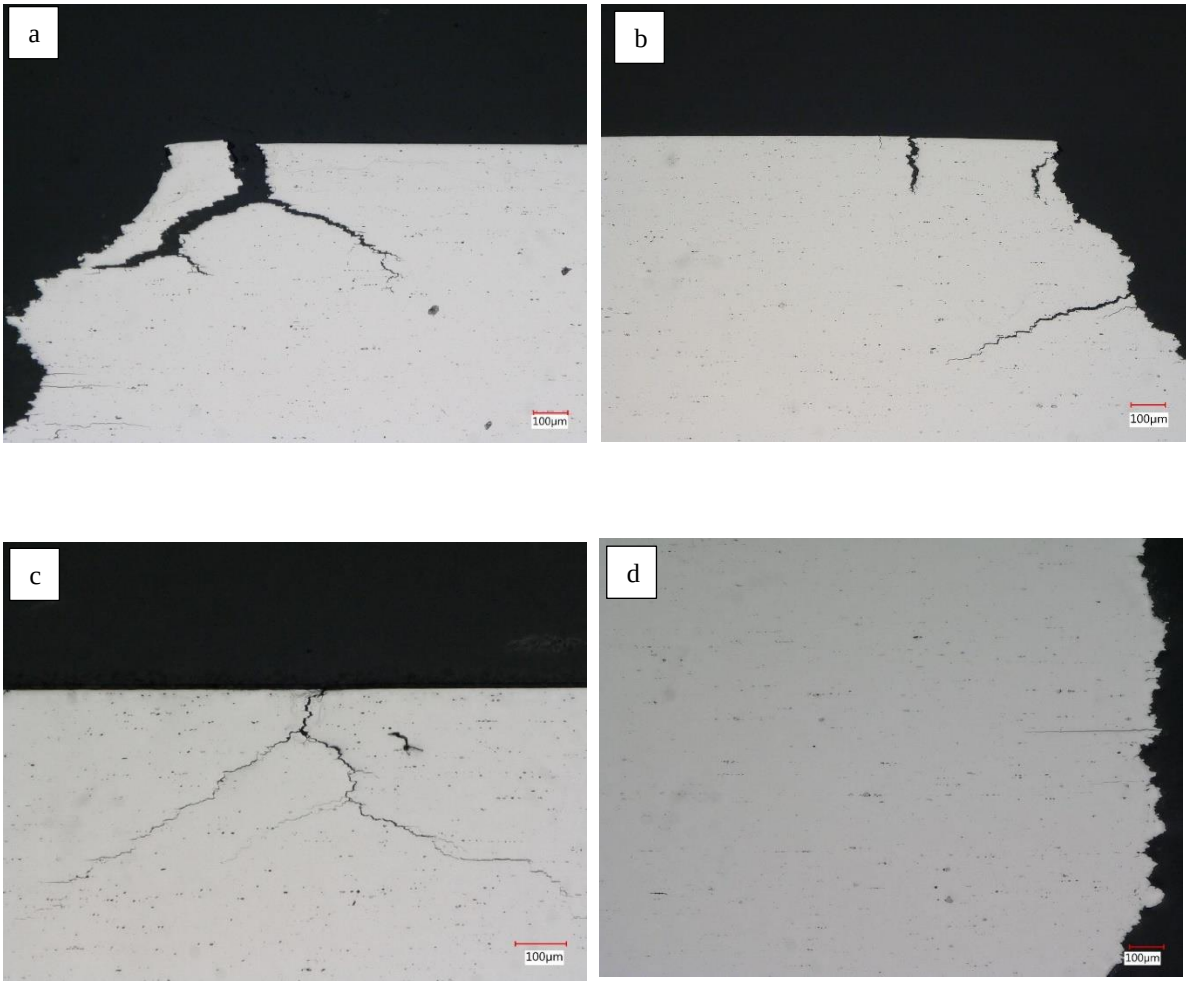

Figure 6-1: Metallography cross section of the fractured samples (a) alloy A (b) alloy B in 35ºC at 85% RH, (c) alloy A (d) alloy B in 70ºC at 85% RH.

Closer to the edge of the fracture, we observed the presence of secondary cracks propagating perpendicular to the applied stress direction. The tortuous path of the cracks appeared to have propagated along the grain boundaries. Crack propagation features looked comparable between the two alloys. Additionally, we also did not observe any sign of localized corrosion attack, such as pitting or intergranular corrosion. **Figure 6-2** shows SEM images of the fractured surface of Alloy A under secondary electron mode and we could observe two distinct fracture morphologies. The first type can be observed at the edge of the fracture surfaces (region a), the cracks were propagating along the grain boundaries and there was little or no deformation on the grain surfaces. Other areas of the samples, such as regions b and c, contained similar morphology. Region b covered an area containing a mixture of coarse and fine grain size, and the faces of the grains looked smooth without any signs of crack arrest markings. In contrast, the grain facets of region c were rough. The second type was observed in region d that had dominant feature containing river patterns or quasi cleavage-like fracture morphology in the grain facets.

In the case of alloy B (**Figure 6-3**), the failed samples exhibited features similar to those of alloy A in terms of intergranular fracture. The region a images taken at the edge of broken samples showed crack propagating along the grain boundaries; however, the facets of the grains showed cleavage-like fracture morphology. In regions b and c, the fracture morphology is of the intergranular type; however, in region d, the fracture surface exhibits a mixture of rough ridges and intergranular features.

Table 6-1 also shows the data from the uniaxial constant displacement testing of the samples at 70°C in 85% relative humidity. Here again both alloys A and B failed after a few days of exposure, but the conventional 7075 alloy passed the test even after 100 days

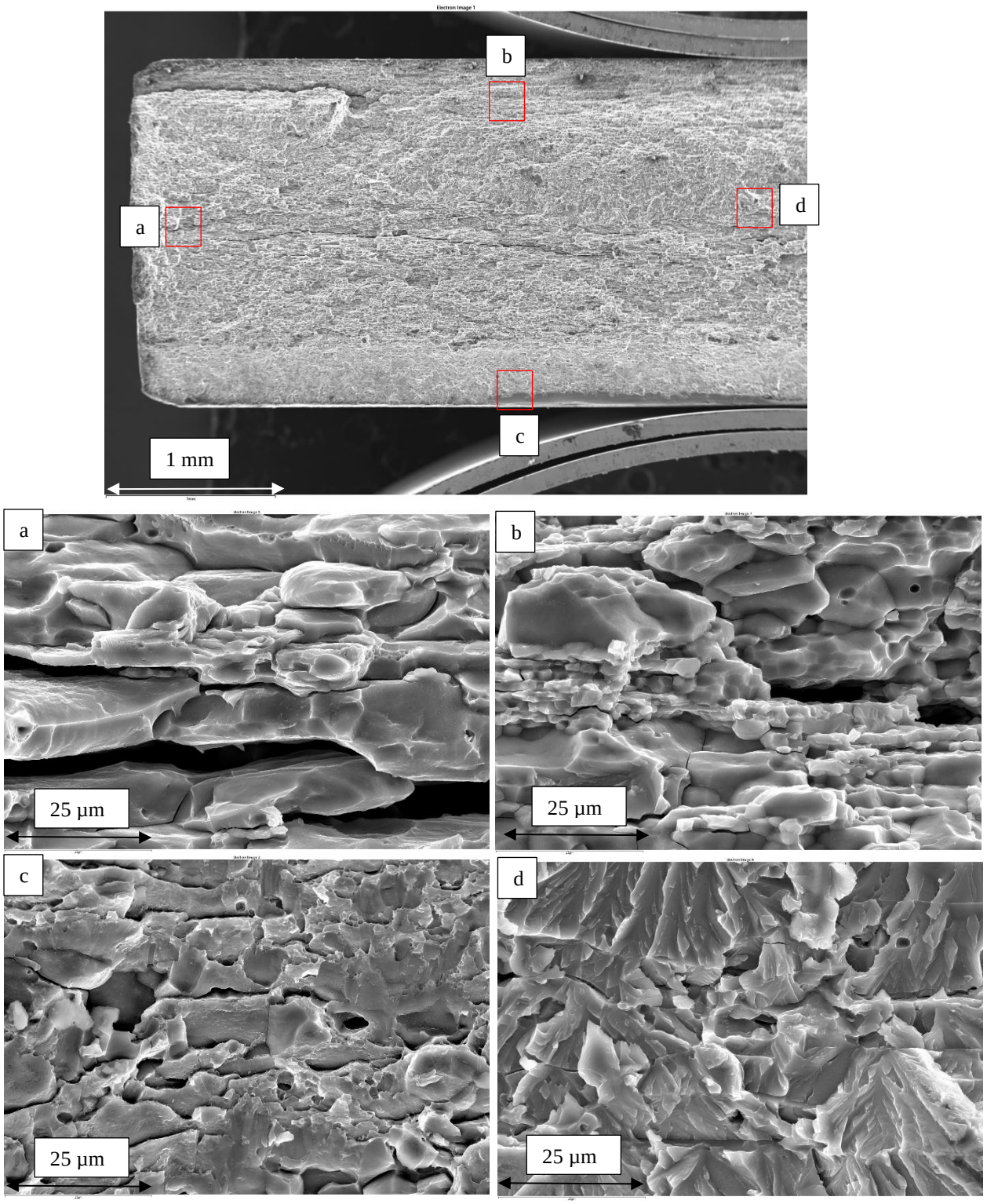

Figure 6-2: SEM images of the fractured surface of alloy A in 35ºC at 85% RH.

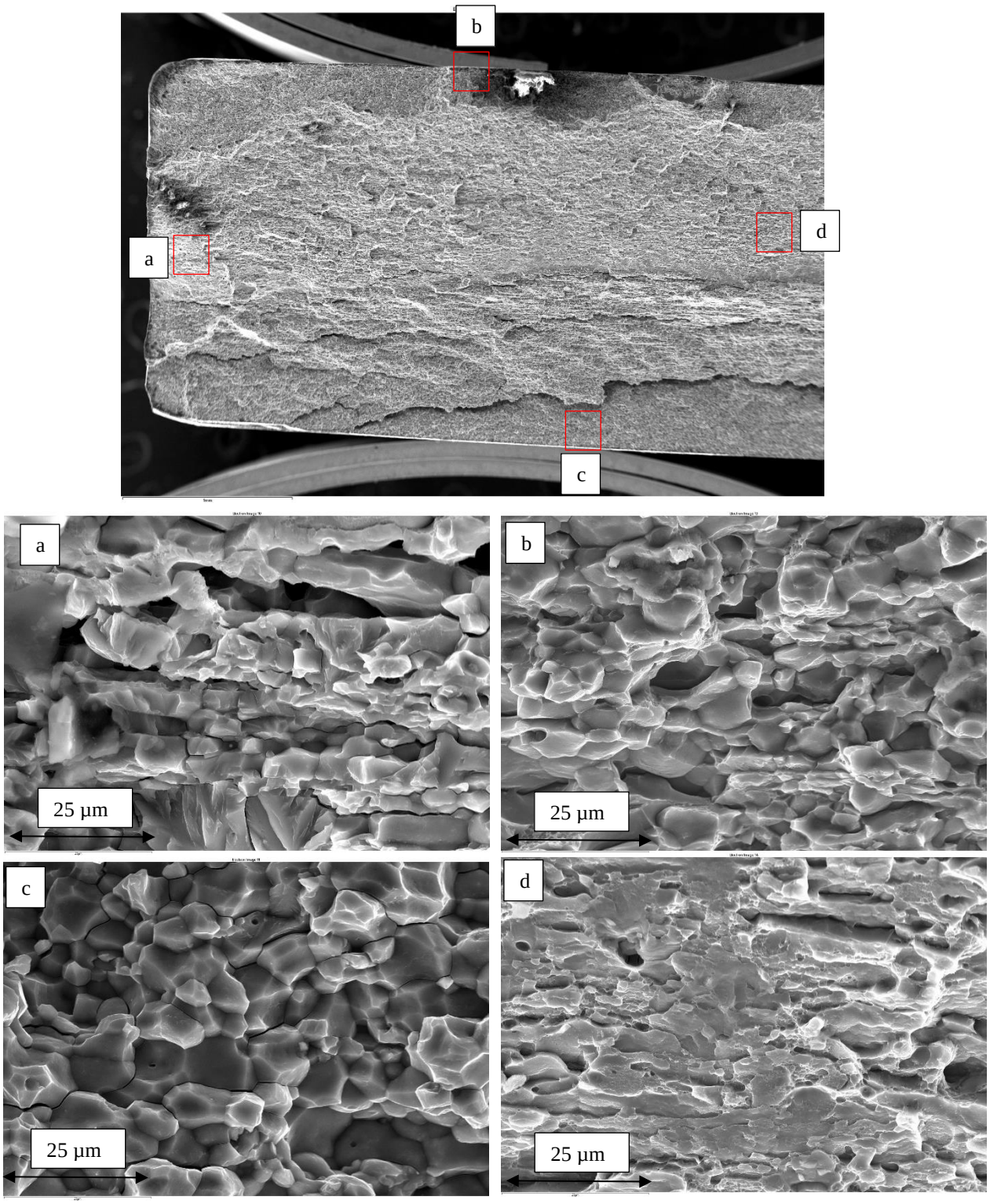

Figure 6-3: SEM images of the fractured surface of alloy B in 35ºC at 85% RH.

of exposure. Increasing the temperature to 70°C reduced the failure time in alloys A and B compared to the testing at 35°C. However, the morphological features of the fractured samples were comparable in both temperatures. **Figure 6-1** shows the cross-section view of the failed samples, and we could observe the presence of cracks near the fractured region. The path of the crack appeared to be intergranular; however, no sign of localized corrosion attack was observed. Similar features were observed in SEM images of the fractured sections. In case of alloy A (**Figure 6-4**), we could observe the crack initiation at the edge of the fractured region a. The area surrounding this crack exhibited a cluster of microvoids or dimple-like features. Regions b and c had similar features in terms of the intergranular brittle fracture, as the facets of the grains were smooth. Region d exhibited a distinct river-like pattern or quasi cleavage fracture, as observed in the 35^{o}C environment. Alloy B showed (**Figure 6-5**) a clear sign of intergranular cracks in the edge of the fracture surface region a and region b. However, the morphology of region c had a mixture of intergranular fracture features with a shallow cluster of voids/dimples like features. Interestingly, the fracture surface in region d had a smooth surface with a shallow ridge.

6.3.2 Effect of applied stress on the SCC performance in humid environment.

In the previous section, the samples were stressed using the uniaxial constant displacement method, and the failure locus was not always in the middle of the gauge section. To minimize the scatter, the samples were subjected to four-point bend testing. **Table 6-1** shows the SCC performance of the samples strained using the four-point bend method. Here again, both alloys A and B failed the test in a manner similar to that of the uniaxial constant displacement samples including the days of failure and the failure locus was always at the middle of the bend samples, where the stress was maximum.

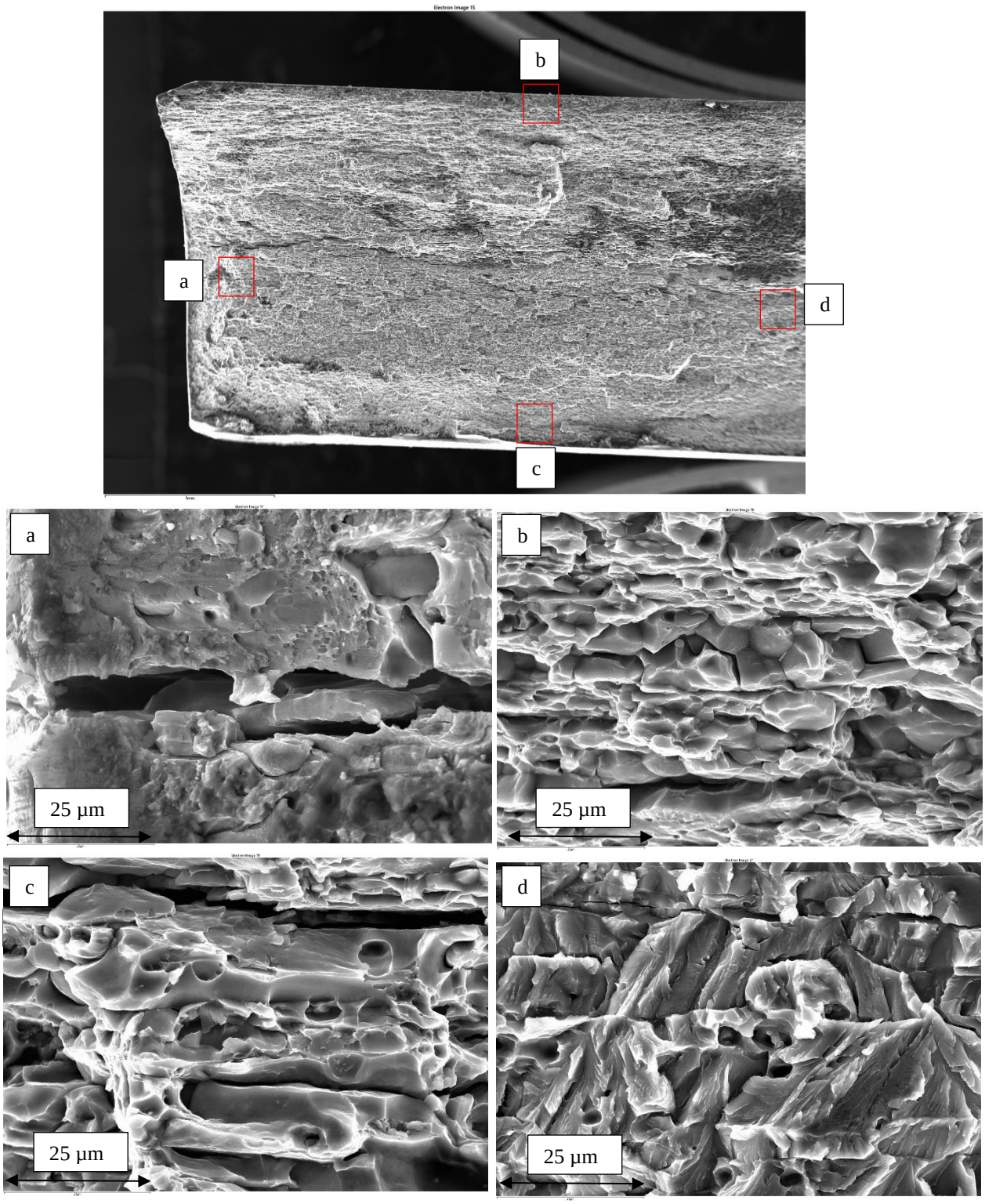

Figure 6-4: SEM images of the fractured surface of alloy A in 70ºC at 85% RH.

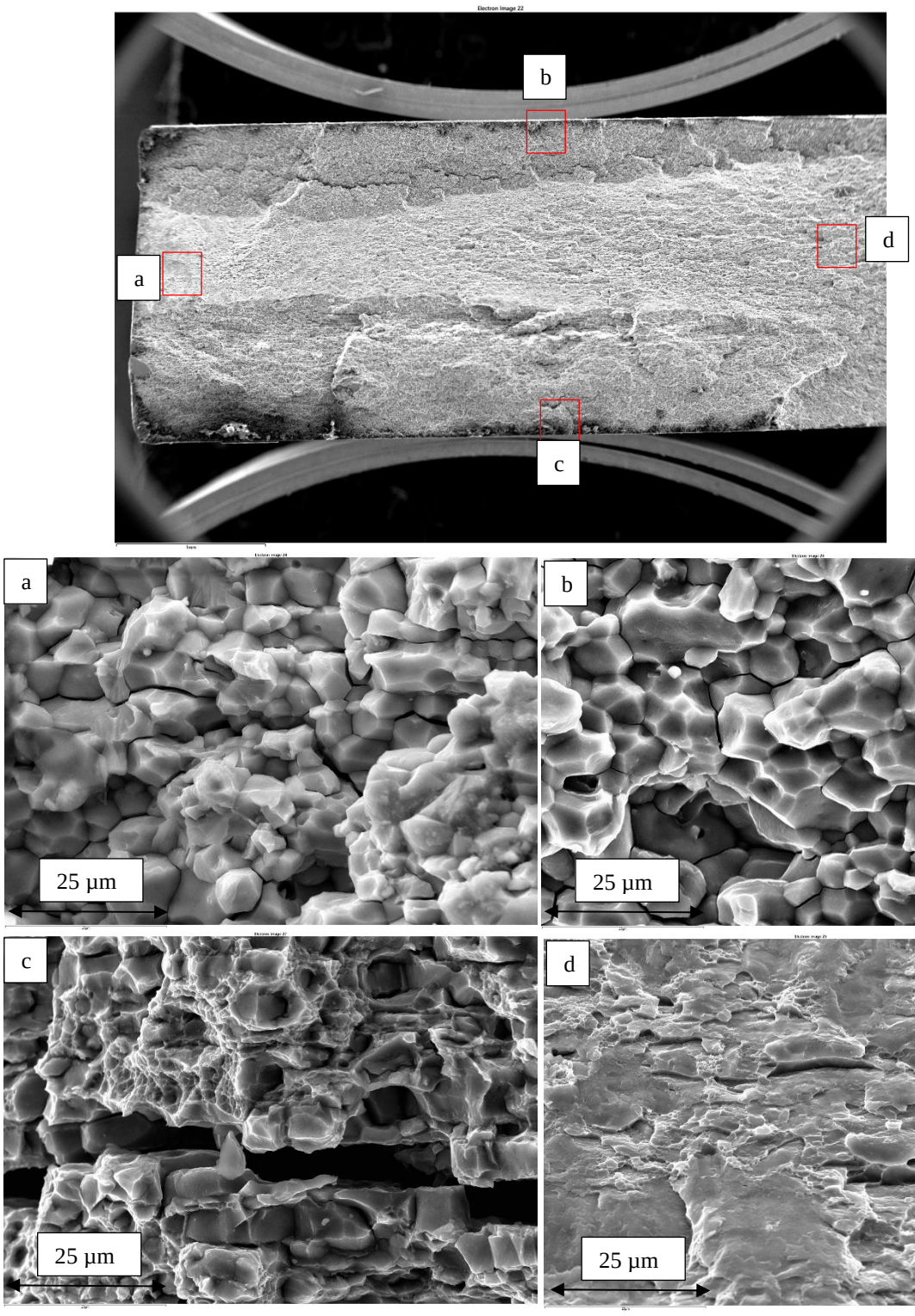

Figure 6-5: SEM images of the fractured surface of alloy B in 70ºC at 85% RH.

The conventional 7075 alloys did not crack after 100 days of exposure. Metallography cross-sectional images (**Figure 6-6**) show a higher degree of cracking in alloys A and B. The cracks in the fractured section ran perpendicular to the stress direction, and the path resembled intergranular cracking. The **Figure 6-7** shows the SEM images of the fractured samples from the four-point bend test. In the case of alloy A, the fracture morphology resembled that of a brittle fracture. The higher magnification image at the edge of the fracture surface clearly showed intergranular cracking. The grain facets were smooth and the fracture was propagating along the grain boundaries. Alloy B also exhibited a similar type of fracture morphology, as in the high-magnification image we could observe a clear sign of crack propagating along the grain boundaries.

To study the effect of the applied stress level on the SCC of the materials in a humid environment, the alloys were exposed to 20% and 50% YS.

Table 6-2: Effect of applied stress level on SCC performance in humid environment.

Samples	**Days to failure in 70°C at 85% RH,**		
	70°C at 85% RH **Duration: 100 days** **Stress level: 20% Yield stress**	**70°C at 85% RH** **Duration: 100 days** **Stress level: 50% Yield stress**	**70°C at 85% RH** **Duration: 100 days** **Stress level: 20% Yield stress**
Alloy A	Passed	Failed, 3 days	Failed, 1 day
Alloy B	1 failed at 64 days	Failed, 5 days	Failed, 1 day
7075	Passed	Passed	Passed

Table 6-2 shows the days of failure of the samples at different stress levels. The conventional 7075 alloy passed the test at 20% and 50% YS stress levels. Interestingly, both alloys A and B continued to exhibit failures at the 50% YS stress level. Alloy A failed after 3 days while alloy B failed after 5 days. **Figure 6-6** shows the metallography cross-section images of the samples after failure. The fracture features were comparable to the 80% YS data. The cracks were propagating in a direction perpendicular to the stress. Similar observations were seen in the SEM images (**Figure 6-7**) of the fracture samples. The fracture surface of alloy A had two types of features in the high-magnification images, the first resembled the intergranular fracture, with cracks propagating along the grain boundaries. The grain facets were smooth similar to the observations in 80% YS samples.

In the second type, we could observe regions that had cleavage – like morphology with very rough ridges that were observed in uniaxial constant displacement fixtures. However, the alloy B exhibited only the intergranular brittle fracture feature.

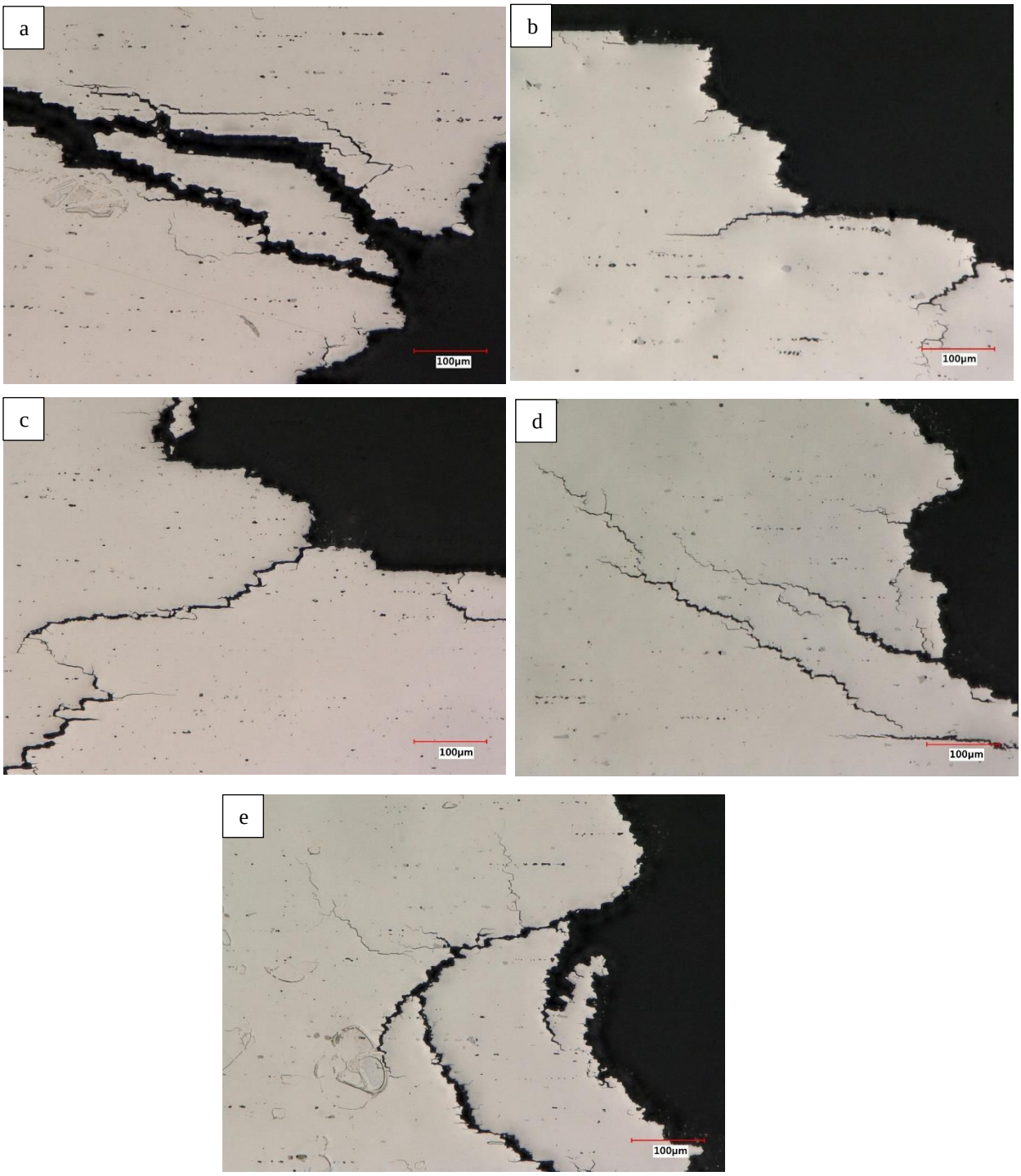

Figure 6-6: Cross section of the fractured samples (a) alloy A, (b) alloy B at 80% YS (c) alloy A (d) alloy B at 50% YS (e) alloy B at 20% YS.

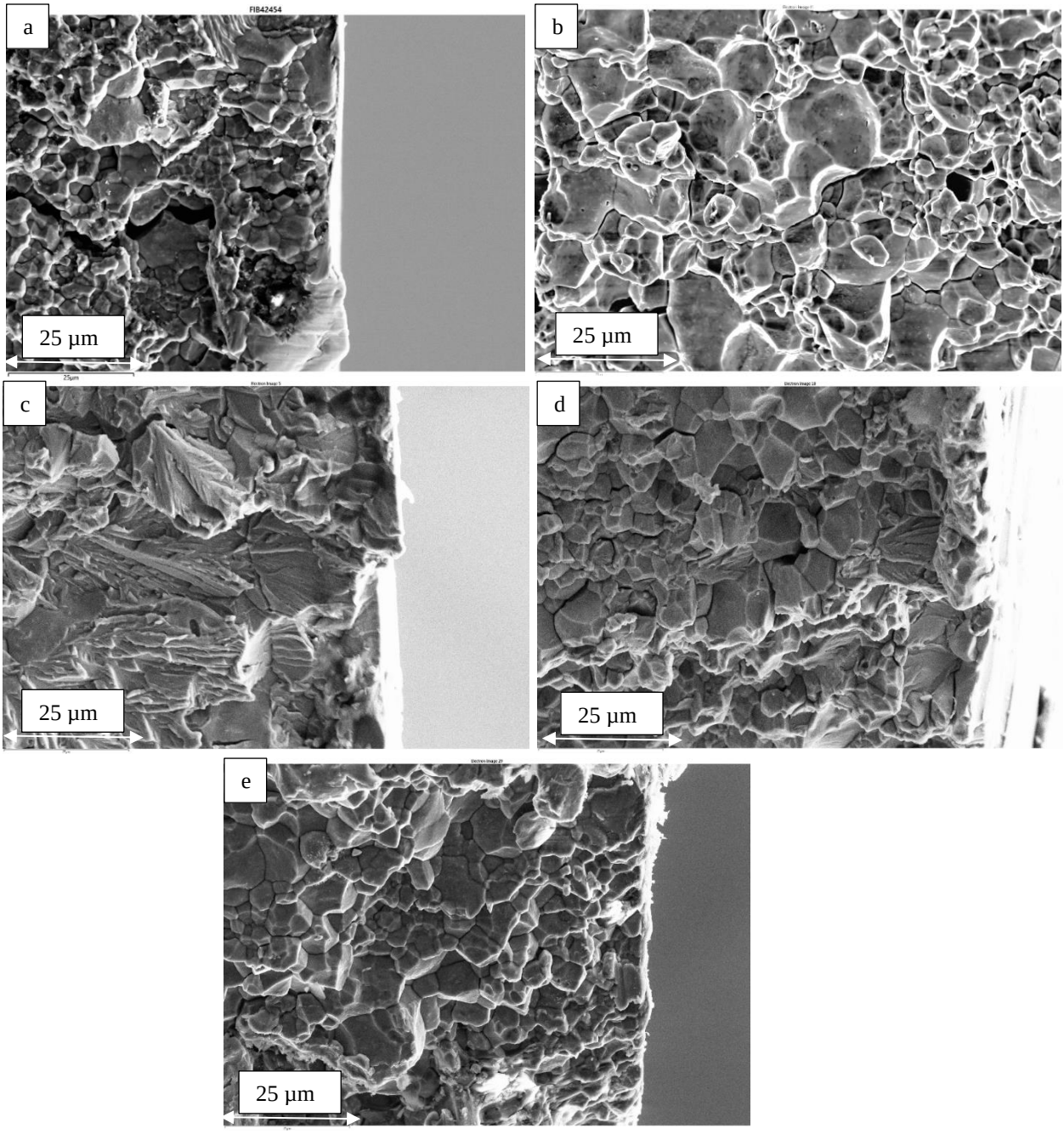

Figure 6-7: SEM images of the fractured samples (a) alloy A, (b) alloy B at 80% YS (c) alloy A (d) alloy B at 50% YS (e) alloy B at 20% YS.

The tests revealed a significant difference in SCC performance at a stress level of 20% YS. Alloy A samples survived 100 days of exposure without a single failure. Alloy B performed similarly at this stress level, except for one sample that failed after 64 days of exposure. **Figure 6-6** and **Figure 6-7** shows the metallography cross section and SEM images of the fractured samples at 20% YS level. Interestingly, the fracture morphology was comparable to 50% YS and 80% YS levels. The cracks were propagating perpendicular to the stress direction in the intergranular path. The high-magnification images of the fractured surface resembled a brittle intergranular fracture with little or no deformation on the facets of the grains. The Alloy B samples that survived the exposure duration did not show the micro-cracks.

To assess the impact of the environment on the mechanical properties of the alloys, we exposed the samples to three different test cycles without applying any applied stress. The **Figure 6-8** shows the summary of the tensile properties such as yield strength and total elongation from the three environment exposure. The yield strength values did not change significantly between pre- and post-exposure in the three different environments. However, a significant difference was found in the total elongation. The

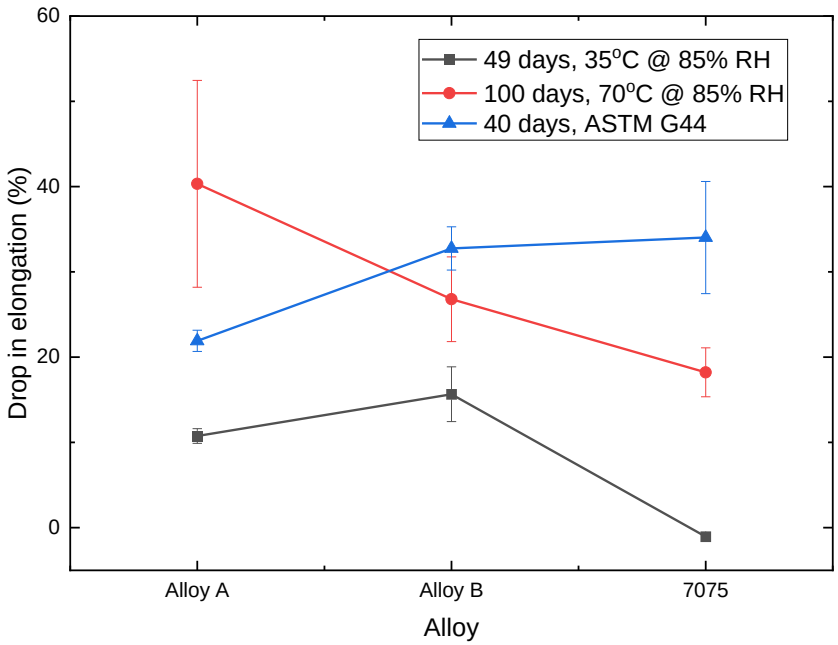

Figure 6-9 highlights the percentage drop in elongation in these environments. The drop in elongation was lowest in 7-week exposure at 35°C at 85% RH. Depending on the alloy composition, the highest drop in elongation varied as function of environment. For example, alloy A showed the highest drop in elongation in 100 days of exposure at 70 ° C, 85% RH conditions, while alloy B showed its highest drop in 40 days of exposure in ASTM G44. Conventional 7075 showed a similar trend to that of alloy B, however, the drop in the elongation percentage was very high in ASTM G44 compared to other variants.

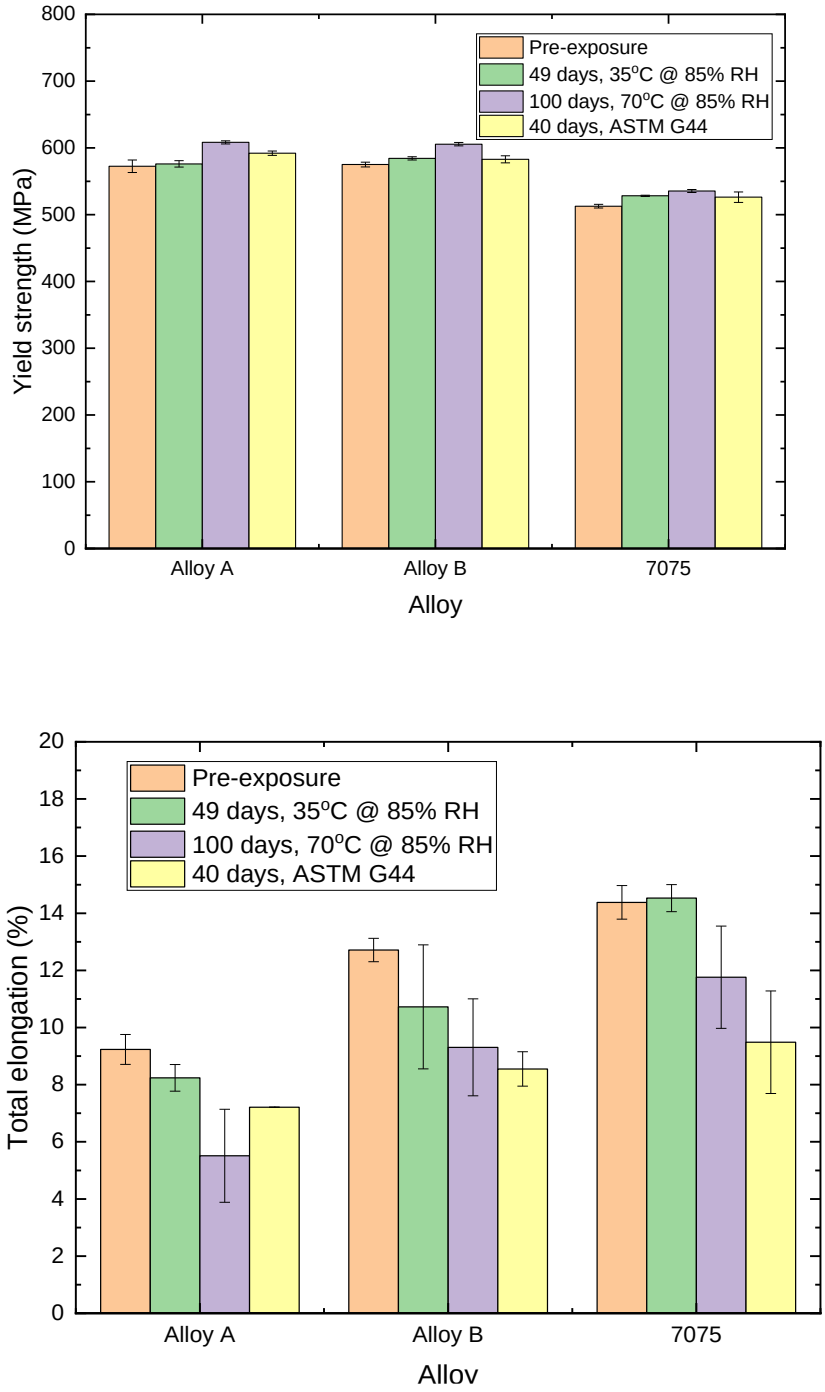

Figure 6-8: Mechanical properties before and after exposure of the alloys in the different corrosion test cycles in absence of any applied stress.

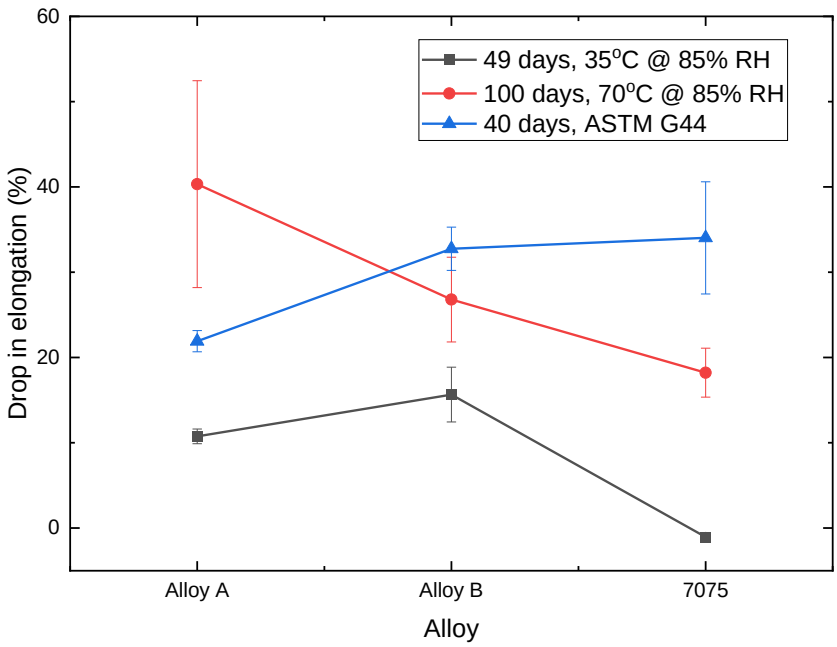

Figure 6-9: Percentage drop in elongation of the samples after exposure to different corrosion test cycles in absence of any applied stress.

Figure 6-10 shows cross-sectional images of the samples under different environmental exposures after tensile testing. After 49 days of exposure in 35°C at 85% RH, there was no widespread localized corrosion attack. However, increasing the temperature to 70 ° C and prolonged exposure at 100 days certainly increased the localized corrosion spots. In alloy A, we could observe crack nucleation from the pitting corrosion sites.

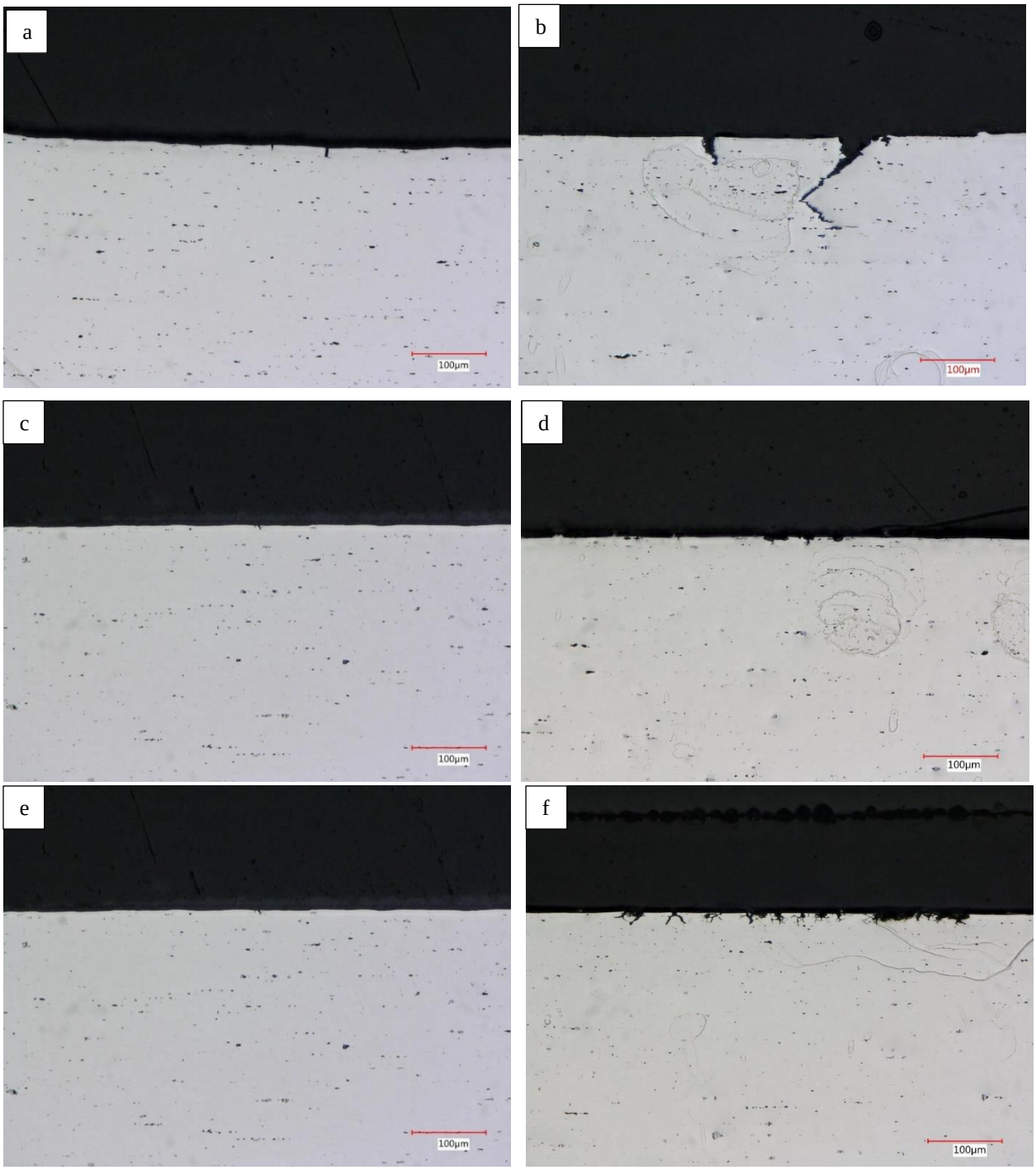

Figure 6-10: Cross section images of the samples after tensile testing in (a) alloy A (b) alloy B (c) 7075 in 7 week exposure in 35ºC at 85% RH (d) alloy A (e) alloy B (vi) 7075 in 100 days exposure in 70ºC at 85% RH.

Alloy B continued to exhibit a pitting-type attack morphology, but the conventional 7075 showed early signs of intergranular corrosion attack. The samples after 40 days of exposure (**Figure 6-11**) in ASTM G44 did not show any significant localized corrosion attack in alloy A. In the case of alloy B and 7075, we could observe continuous microscopic pits with depths less than 10 µm.

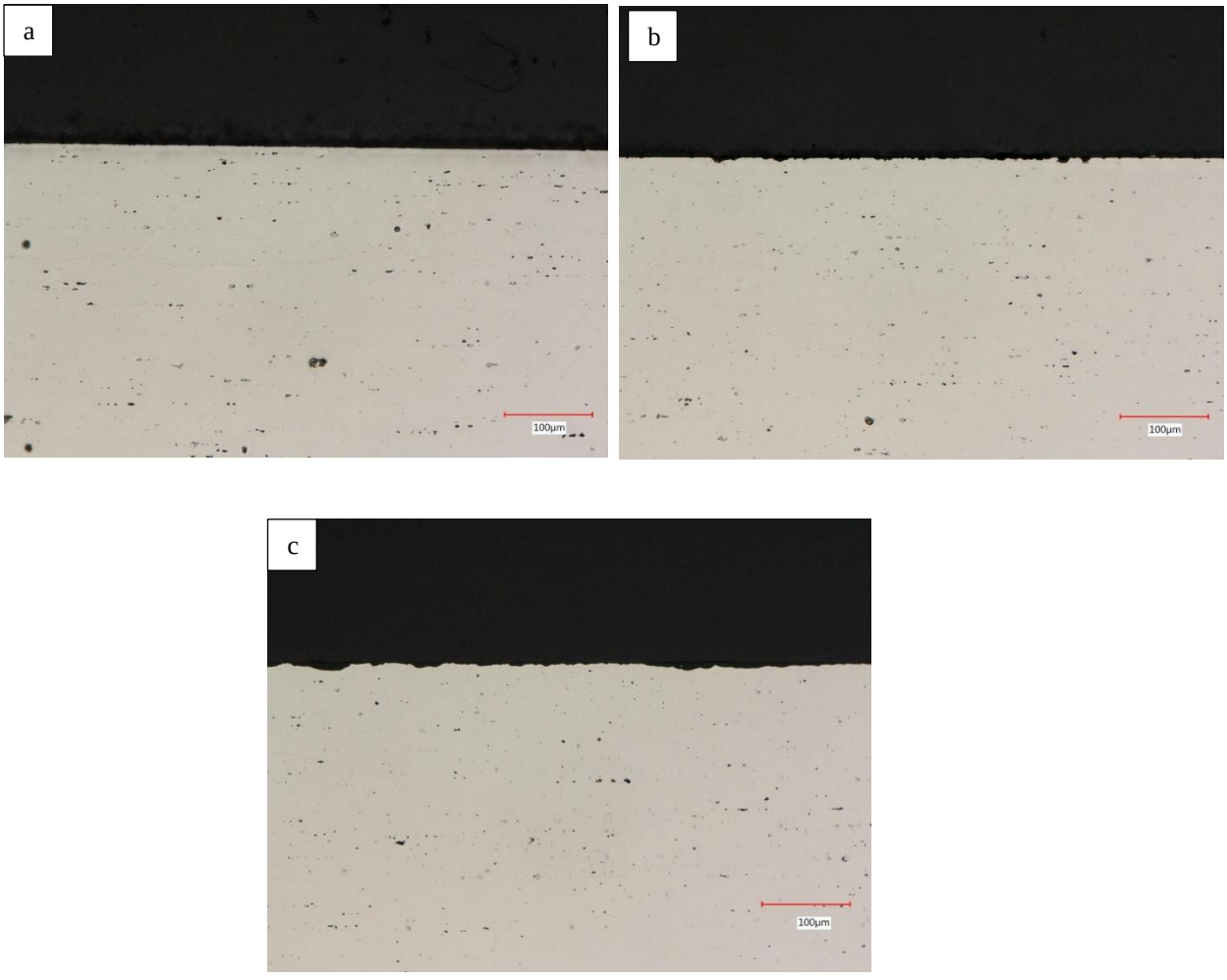

Figure 6-11:Cross section images of the samples after tensile testing (i) alloy A (ii) alloy B (iii) 7075 in 40 days in ASTM G44.

Figure 6-12 shows the fracture surface images after tensile testing for the preexposure samples. The fractured edge of Alloy A exhibited higher density of clustered microvoids/dimple-like ductile fracture features. Even in the middle of the fractured area, we could observe these micro-voids and the presence of rough surfaces on the grain interiors.

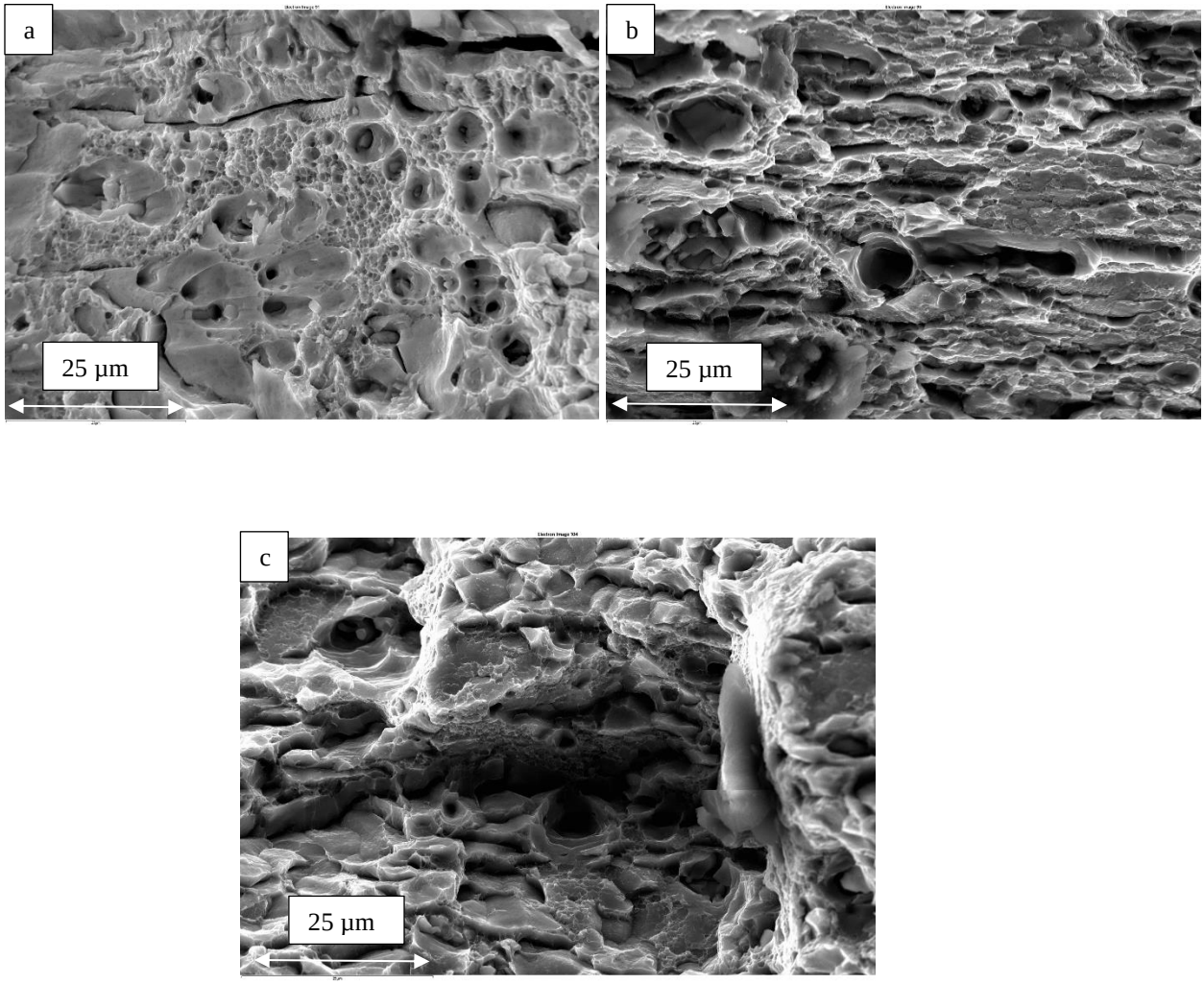

Figure 6-12: SEM images of the fractured pre-exposure samples (a) alloy A (b) alloy B (c) 7075 after tensile test.

In addition to these characteristic features, alloy B also exhibited voids around the intermetallic particles. The conventional 7075 alloy also exhibited these features. In summary, irrespective of the composition, the fracture regions of the pre-exposure samples contained predominantly ductile type of fracture features such as clustered voids/dimple-like features and no sign of brittle fracture features.

The fracture surface of the samples after exposure to 35^{o}C at 85% RH is shown in the **Figure 6-12**. Interestingly, alloy A did not exhibit any significant brittle fracture behavior despite 49 days of exposure. The surface of the fracture edges was still dominated by dimple-like features. Alloy B also exhibited this type of feature, despite both alloys failing the test when 80% YS stress was applied externally. The conventional 7075 alloy also showed dimple-like features and no signs of brittle intergranular fracture.

An increase in temperature (70^{o}C) and duration (100 days) affected the fracture surface morphologies (**Figure 6-13**) of high-solute alloys. Alloy A that had a 40% drop in elongation showed mixed fracture morphology. In the SEM images, we could observe regions of dimple-like features but there was region containing river-like quasi cleavage fracture patterns that were previously observed in stressed samples. Alloy B also exhibited such mixed morphology, similar to that of alloy A. In fact, in alloy B we were able to observe more regions containing river-like ridge patterns after tensile tests. The conventional 7075 alloy continued to exhibit only a dimple-shaped feature and did not show any signs of brittle fracture.

After exposure for 40 days in the G44 testing environment, Alloy A exhibited largely dimple-like (**Figure 6-14**) characteristics throughout the fracture region.

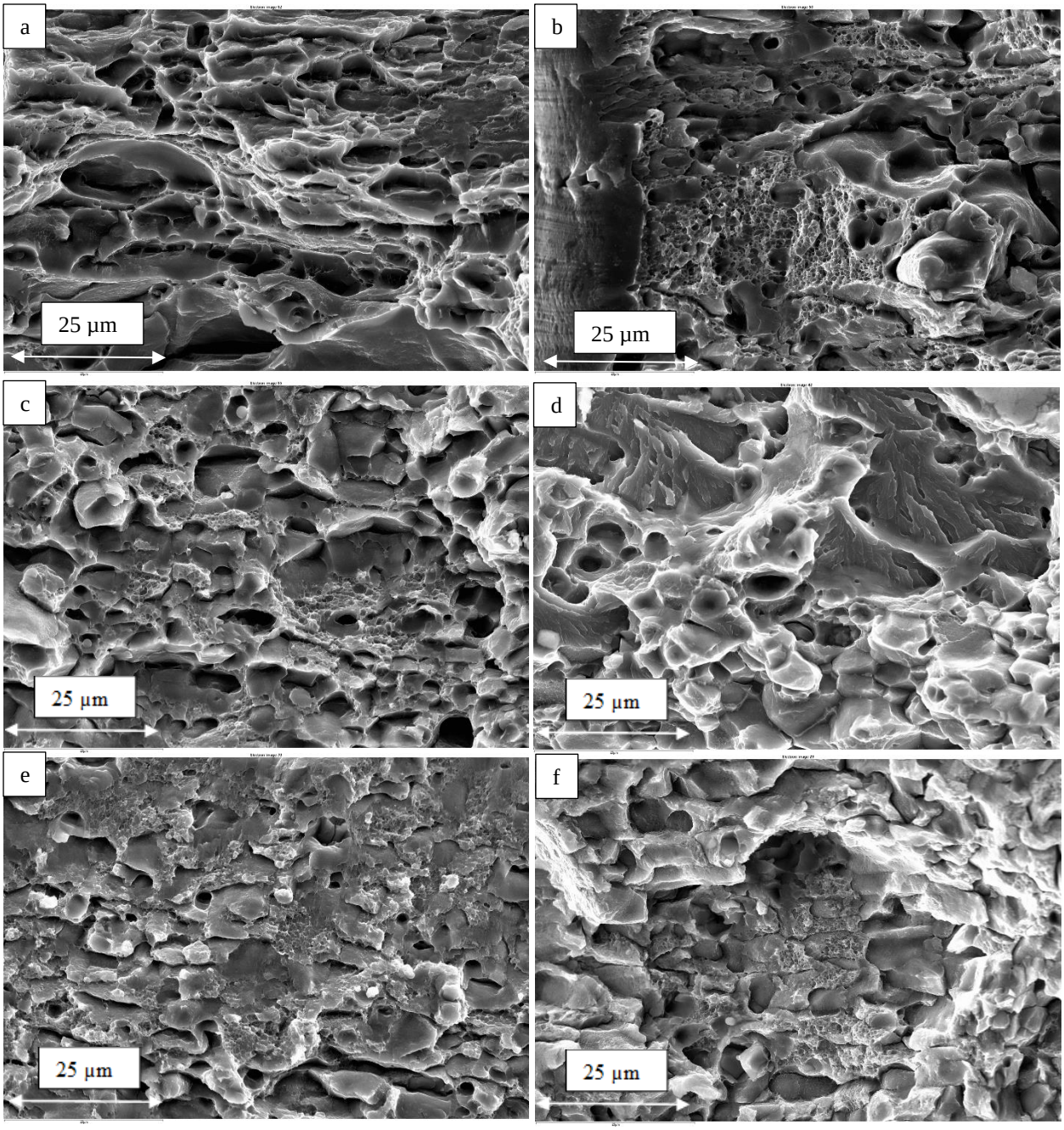

Figure 6-13: Fractured surface images of the samples after tensile testing in (a) alloy A (b) alloy B (c) 7075 in 7 weeks exposure in 35ºC at 85% RH (d) alloy A (e) alloy B (f) 7075 in 100 days exposure in 70ºC at 85% RH.

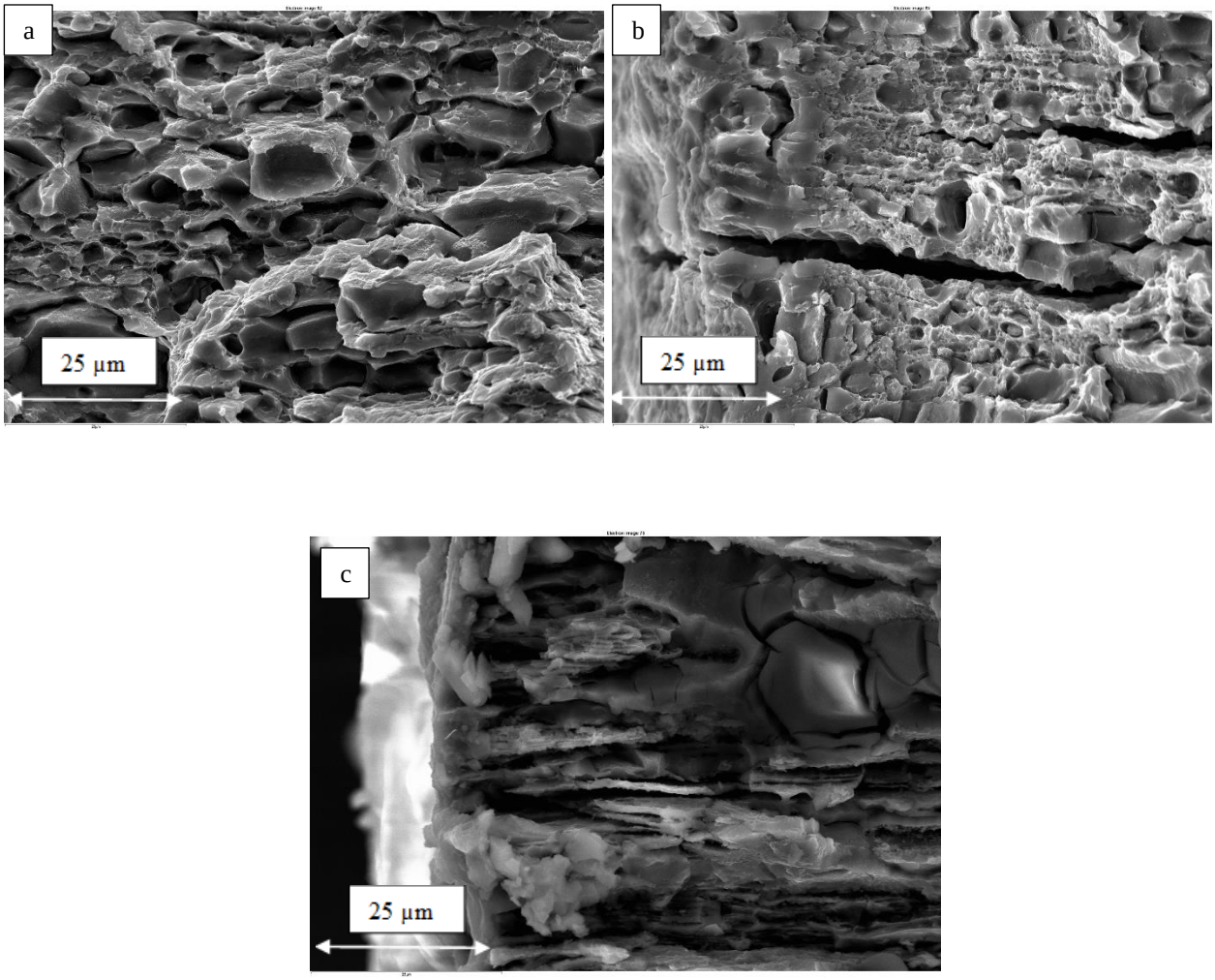

Figure 6-14: Fracture surface of the samples after tensile testing (a) alloy A (b) alloy B (c) 7075 in 40 days in ASTM G44.

There was no clear sign of brittle fracture despite a 20% loss in elongation. Alloy B also exhibited dimple like features, despite the clear evidence of pitting corrosion and crack initiation at the edge of the fracture surface. The conventional 7075 also exhibited a similar type of fracture surface; however, a significant corrosion attack that resembled a mixture of pitting and intergranular corrosion was observed at the edge of the fracture surface.

6.3.3 Microstructure Characterization

In the previous chapter, an extensive microstructure characterization of these three alloys was carried out. The grain boundary microstructural features were specifically chosen for analysis since the fracture surface examination clearly showed that cracks propagated along the grain boundaries. **Figure 6-15** shows the STEM images of the grain boundary for the three alloys, and we could observe the presence of precipitates along the boundary and the adjoining precipitate-free zone (PFZ). In the case of alloy A, the precipitates were not present in all boundaries and they were largely discontinuous in the sections where they were found. Similarly, alloy B also exhibited a discontinuous presence, though they were present in the majority of the grain boundaries. The conventional 7075 alloy showed the continuous presence of fine precipitates.

Table 6-5 shows the EDS composition of the precipitates and the adjoining precipitate-free zone. The precipitates have a higher amount of solute elements such as Mg, Zn, and Cu compared to the precipitate free zone. The scatter in the data was high, particularly in the PFZ because of the beam drifting during the EDS measurements. To confirm the trend in elemental segregation in both features, the equilibrium composition was used for comparative purposes.

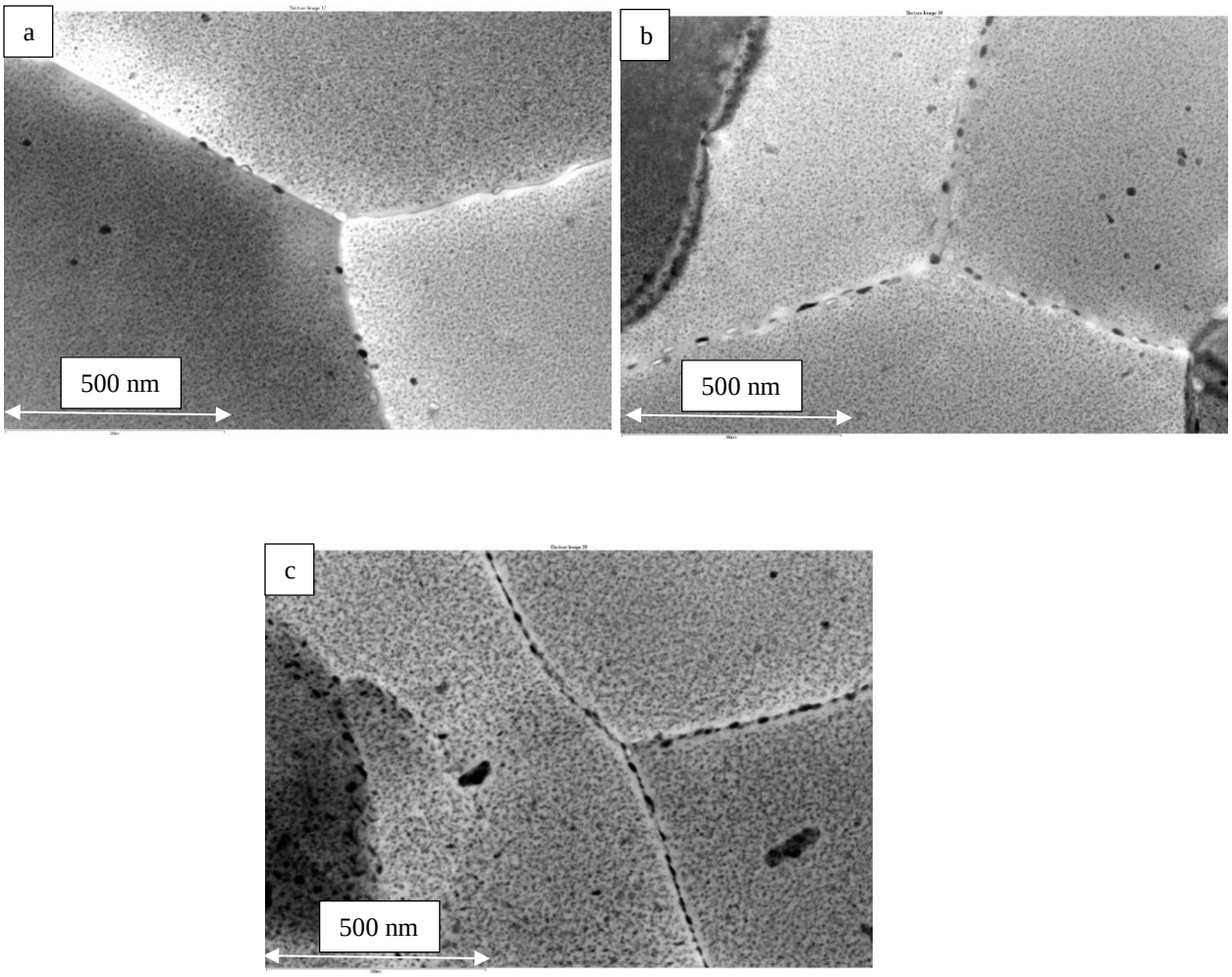

Figure 6-15: STEM - bright field images of the grain boundary microstructure (a) alloy A (b) alloy B (c) 7075.

Table 6-3 contains the equilibrium composition of the grain boundary precipitate and adjoining precipitate-free zone based on JMatpro and Thermo-Calc calculations, respectively. The predicted solute contents were higher than the values measured experimentally from EDS. However, the trend in the Zn/Mg ratio is in a range similar to the equilibrium calculated values for grain boundary precipitates, but PFZ data was not following this trend because of the issues encountered during EDS measurements as mentioned above.

Table 6-3: Composition of grain boundary precipitates (GBP) and adjoining precipitate free zone (PFZ) from JMatpro and ThermoCalc predictions.

Sample	EDS composition PFZ (wt%)				EDS composition GBP (wt%)			
	Zn	Mg	Cu	Zn/Mg	Zn	Mg	Cu	Zn/Mg
7075	0.78	1.48	0.97	0.53	55.4	18.2	15.38	3.04
Alloy A	1.54	0.62	0.18	2.51	75.12	16.62	3.95	4.52
Alloy B	1.46	0.61	0.75	2.41	71.6	16.36	9.14	4.38
Alloy C	1.46	0.63	0.76	2.33	70.18	16.52	9.69	4.25
Alloy D	1.17	0.97	0.56	1.21	72.48	16.5	7.46	4.39
Alloy E	1.11	1.03	0.74	1.07	68.49	16.81	9.82	4.07
Alloy F	0.95	1.24	0.76	0.95	68.46	16.81	9.84	4.07

The **Figure 6-16** shows the correlation between the Zn / Mg ratio (from EDS measurements) in the grain boundary precipitates to days to failure at 70 ° C at 85% RH environment. As the Zn/Mg ratio increases, the days to failure had decreased considerably. In case of 7075, the Zn/Mg ratio was 2.66 and the samples had run out at 100 days of exposure. On the other hand, alloy A had a Zn / Mg ratio of 4.2 and the samples failed within one day of exposure, while alloy B had a Zn / Mg ratio of 4 and the samples failed within two days of exposure. A similar trend (**Figure 6-16**) was observed between the PFZ Zn/Mg ratio (from Thermo-Calc) and days to failure. At a higher Zn / mg ratio, such as

alloy A and B, the samples failed early, and at a lower Zn/mg ratio, the samples survived as in the case of 7075. In order to test whether such a relationship between Zn/Mg ratio exists in 7xxx alloys, the testing matrix was expanded to include values in between these extremes.

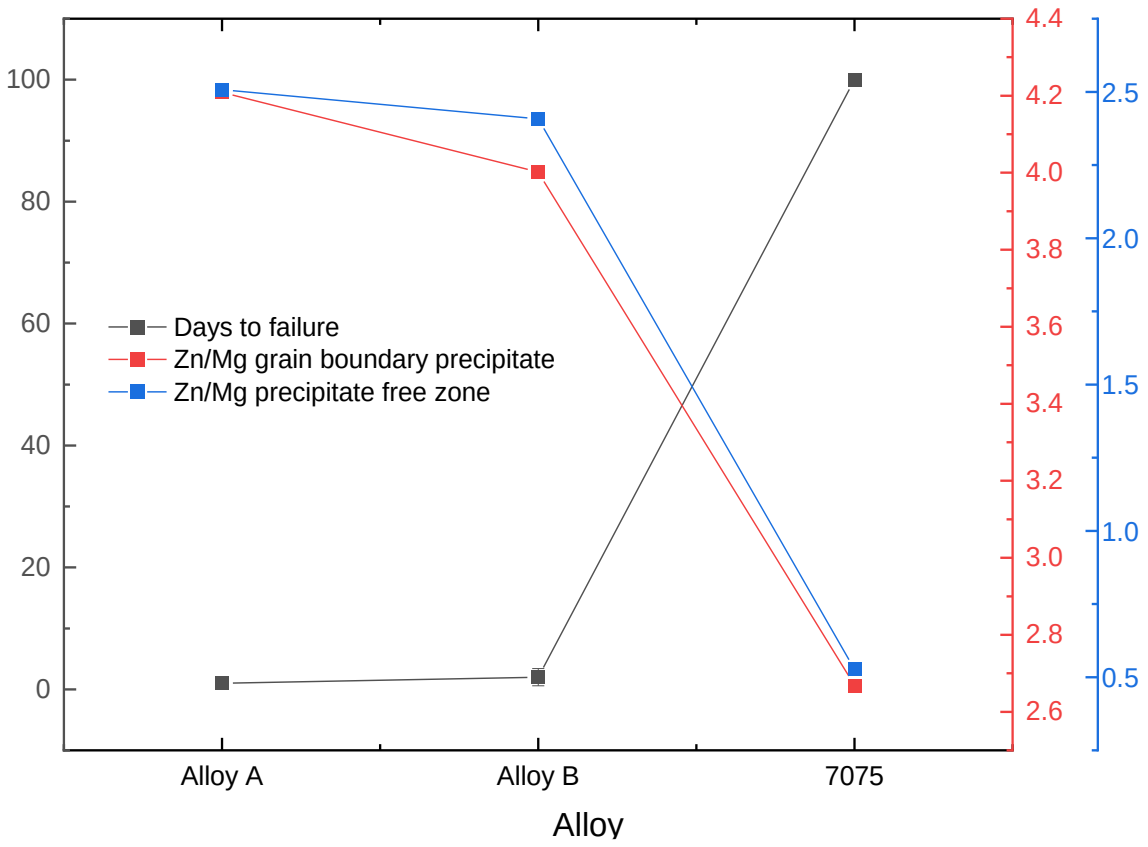

Figure 6-16: Effect of the grain boundary precipitate and adjoining precipitate free zone Zn/Mg ratio on days to failure in 70ºC at 85%RH.

6.3.4 SCC testing of expanded compositions in a humid environment

Table 6-4 shows the composition and bulk ratio of the alloys that were used in this work to validate the correlation.

Table 6-4: Alloy composition (wt%) of the samples and their average corresponding days to failure that were stressed to 80% YS in a four-point bend configuration and exposed to 70 ° C at 85% RH.

Sample	Cr	Cu	Fe	Mg	Mn	Si	Zn	Zr	Zn/Mg ratio	Average days to failure
7075	0.19 - 0.29	1.59 – 1.79	0.17 – 0.28	2.54 – 2.74	0.02 – 0.12	0.04 – 0.14	5.79 – 5.99	0.01 – 0.11	2.28	100*
Alloy A	0.01 – 0.11	0.30 - 0.50	0.16 – 0.26	2.16 – 2.36	0.03 – 0.13	0.08 - 0.18	9.13 – 9.23	0.13 – 0.23	4.23	1
Alloy B	0.03 – 0.13	1.17 - 1.37	0.18 – 0.28	2.18 – 2.38	0.03 – 0.13	0.07 – 0.17	8.82 – 9.02	0.13 – 0.23	4.05	2
Alloy C	0.12 – 0.22	1.23 – 1.43	0.22 – 0.42	2.30 – 2.50	0.05 – 0.15	0.24 – 0.34	9.27 – 9.47	0.12 – 0.22	4.03	12
Alloy D	0.11 – 0.22	0.97 – 1.17	0.22 - 0.42	2.42 – 2.62	0.04 – 0.14	0.32 – 0.42	8.18 – 8.28	0.13 – 0.23	3.38	14
Alloy E	0.11 – 0.22	1.29 – 1.49	0.21 – 0.41	2.51 – 2.71	0.05 – 0.15	0.09 – 0.19	8.12 – 8.32	0.12 – 0.22	3.24	71
Alloy F	0.11 – 0.22	1.28 - 1.48	0.22 – 0.42	2.48 - 2.68	0.05 – 0.15	0.06 – 0.16	6.89 – 7.09	0.13 – 0.23	2.78	75

In this table, we could also observe variations in other alloying elements such as Cu and Si between the alloys. Additionally, this set of compositions also had a higher level of Cr compared to alloy A and B. The table also shows the average days to failure of samples that were stressed to 80% YS in a four-point bend configuration and exposed to 70 ° C at 85% RH. Unlike 7075, these samples exhibited failures during the exposure period; however, there was a noticeable difference in days to failure as a function of the bulk Zn/Mg ratio. Alloys E and F whose Zn/Mg ratio was closer to the 7075 level had higher days (70) to failure. Similarly, alloy C and D Zn/Mg ratios were closer to alloys A and B and subsequently had shorter cycles (15) to failure. **Figure 6-17** shows cross-sectional images of the failed samples in the 70^{o}C at 85% RH environment. All samples clearly exhibited signs of cracking and the crack path appeared to have been propagated along the grain boundaries.

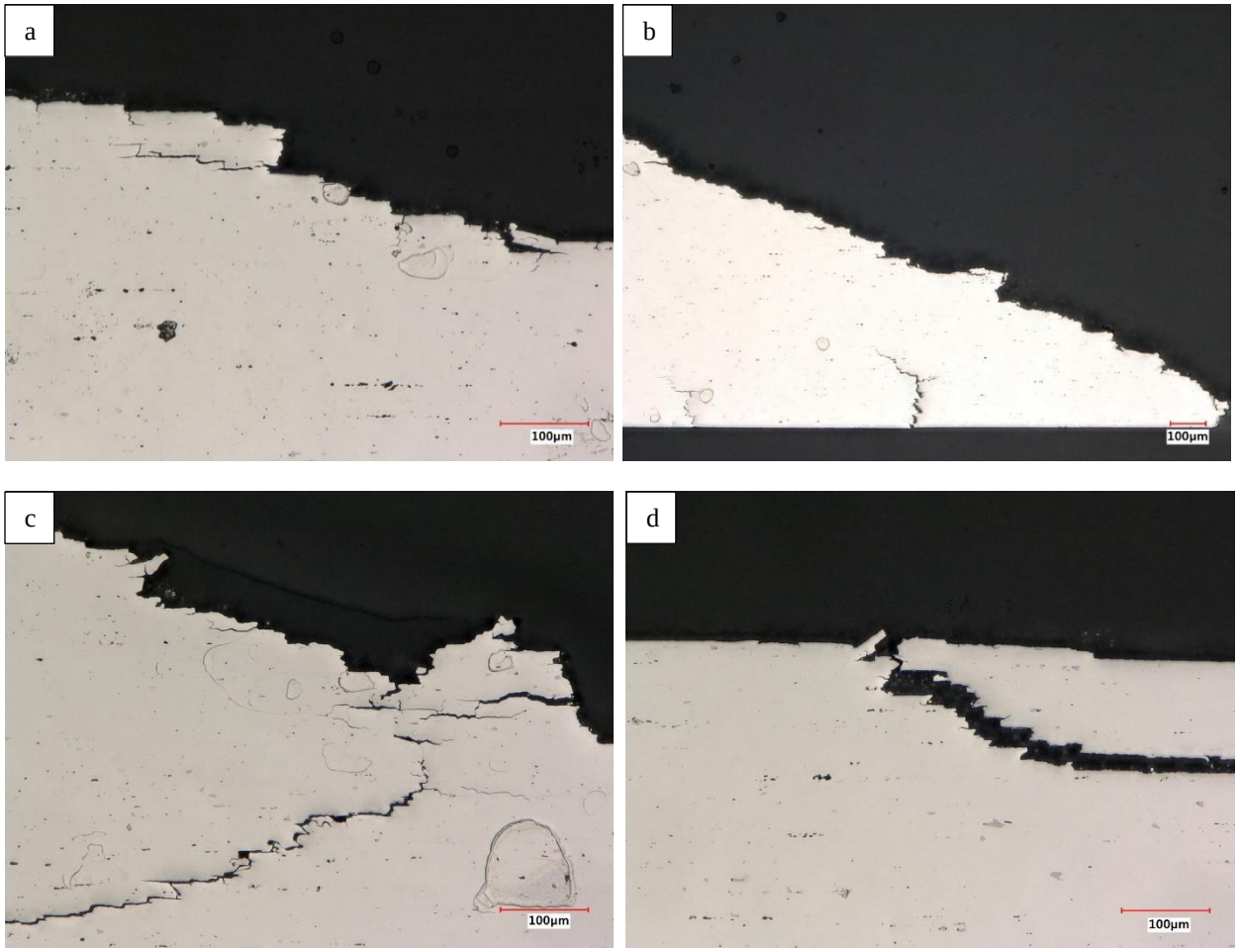

Figure 6-17: Cross section of the failed samples (a) alloy C (b) alloy D (c) alloy E (d) alloy F after exposure in 70ºC at 85% RH.

Interestingly, in any of these alloys, no obvious signs of localized corrosion attack were observed. Similarly, the fracture surface (**Figure 6-18**) of the samples under SEM clearly showed evidence of a brittle fracture with cracks propagating along the grain boundary.

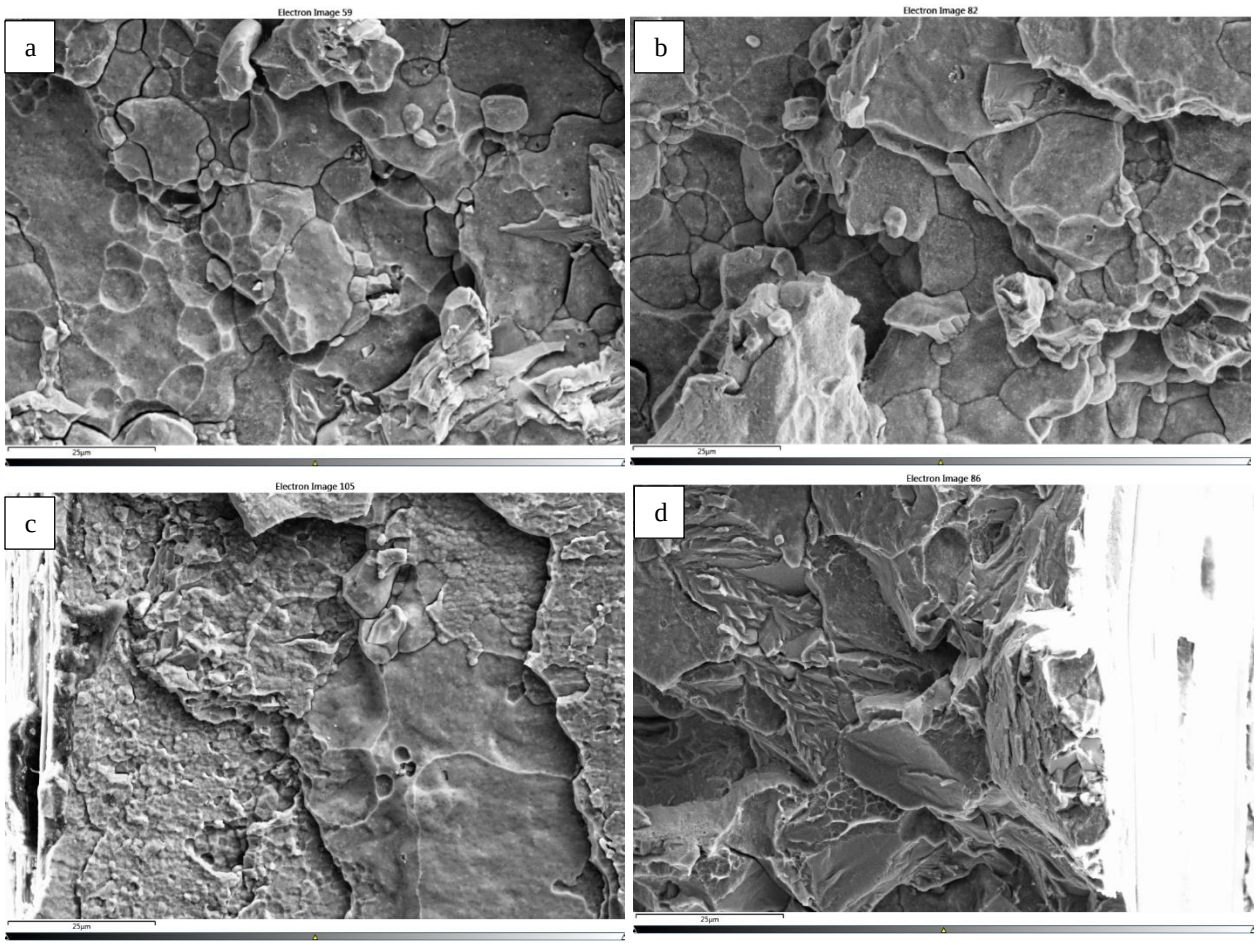

Figure 6-18: SEM images of the fractured samples (a) alloy C (b) alloy D (c) alloy E (d) alloy F after exposure in 70ºC at 85% RH.

The grain boundary features (**Figure 6-19**) were comparable with alloy A and B in terms of discontinuity in grain boundary precipitates.

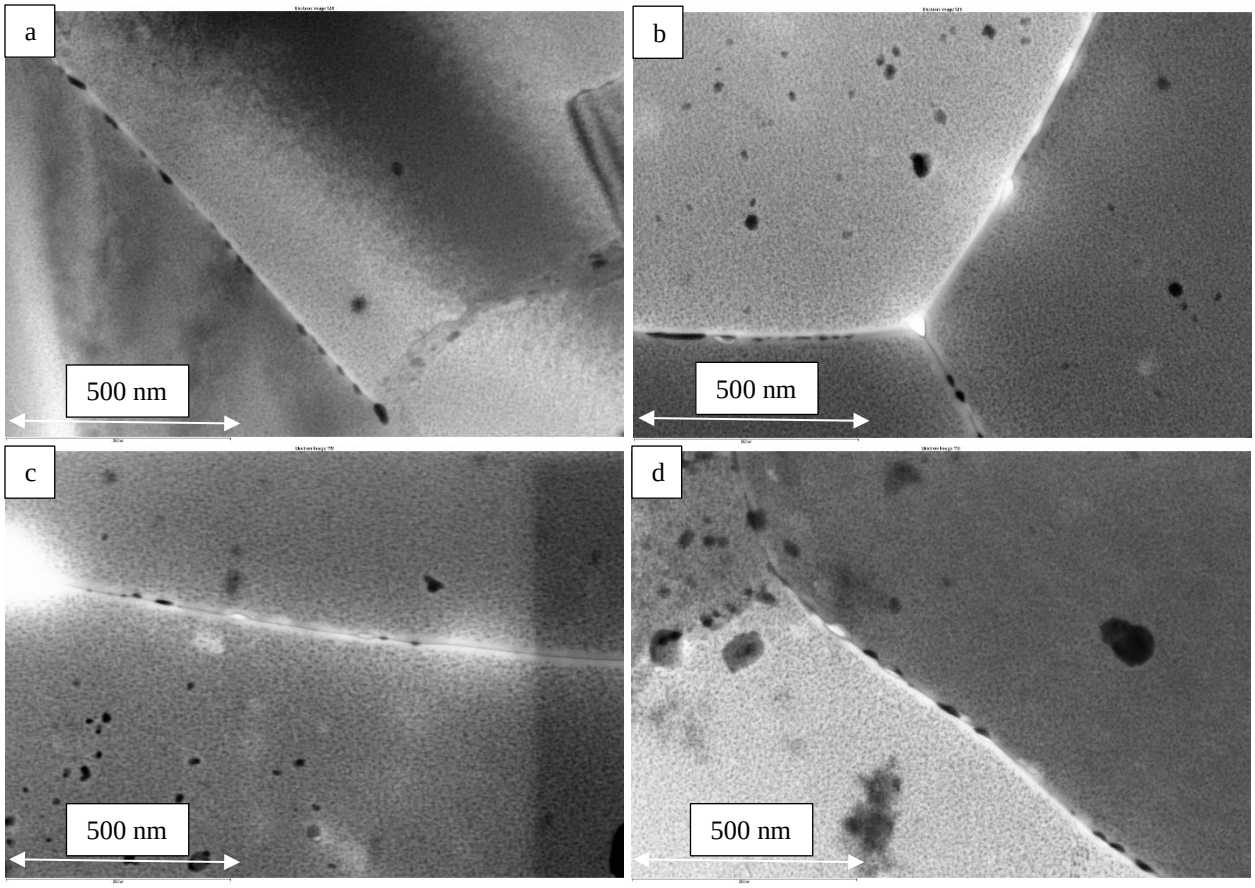

Figure 6-19: STEM - bright field image of grain boundary microstructure features of (a) alloy C (b) alloy D (c) alloy E (d) alloy F.

Table 6-5 shows the EDS composition of the grain boundary precipitate and the adjoining PFZ. As expected, the level of solute concentration in the precipitates was higher compared to that of the PFZ. Similarly, these values were lower than those of the equilibrium composition of the JMatpro and Thermo-Calc data. The **Figure 6-20** shows the correlation between the Zn/Mg ratio of the grain boundary precipitates and the PFZ of days to failure. In both cases, a higher Zn/Mg ratio resulted in the lower cycles to failure.

Table 6-5: Composition of grain boundary precipitates (GBP) and adjoining precipitate free zone (PFZ) from STEM-EDS measurements.

Sample	EDS composition PFZ (wt%)				EDS composition GBP (wt%)			
	Zn	Mg	Cu	Zn/Mg	Zn	Mg	Cu	Zn/Mg
7075	1.85± 2.12	1.37±0.65	3.32±1.63	1.34	20.6 ± 10.1	7.72±2.57	5.59±2.26	2.66
Alloy A	1.83±1.14	2.55±0.95	1.46±0.25	0.71	29.25±6.17	6.95±1.28	1.96±0.83	4.20
Alloy B	1.78±0.86	1.51±0.99	3.65±3.01	1.17	26.49±6.65	6.62±1.49	2.81±0.91	4
Alloy C	3.14 ± 1.5	1.13±0.46	1.48±0.82	2.77	22.6 ± 8.5	6.03±3.2	4.51± 2.3	3.75
Alloy D	3.58±1.31	1.31±0.22	1.41±0.23	2.73	24.75±6.60	6.69±2.16	3.50±1.61	3.69
Alloy E	2.67±0.97	1.26±0.25	4.35±1.3	2.12	18.21±4.04	4.87±0.98	2.80±0.36	3.73
Alloy F	0.96±0.46	0.8±0.14	3.86±0.70	1.2	24.09±5.39	6.86±1.88	4.13±0.84	3.5

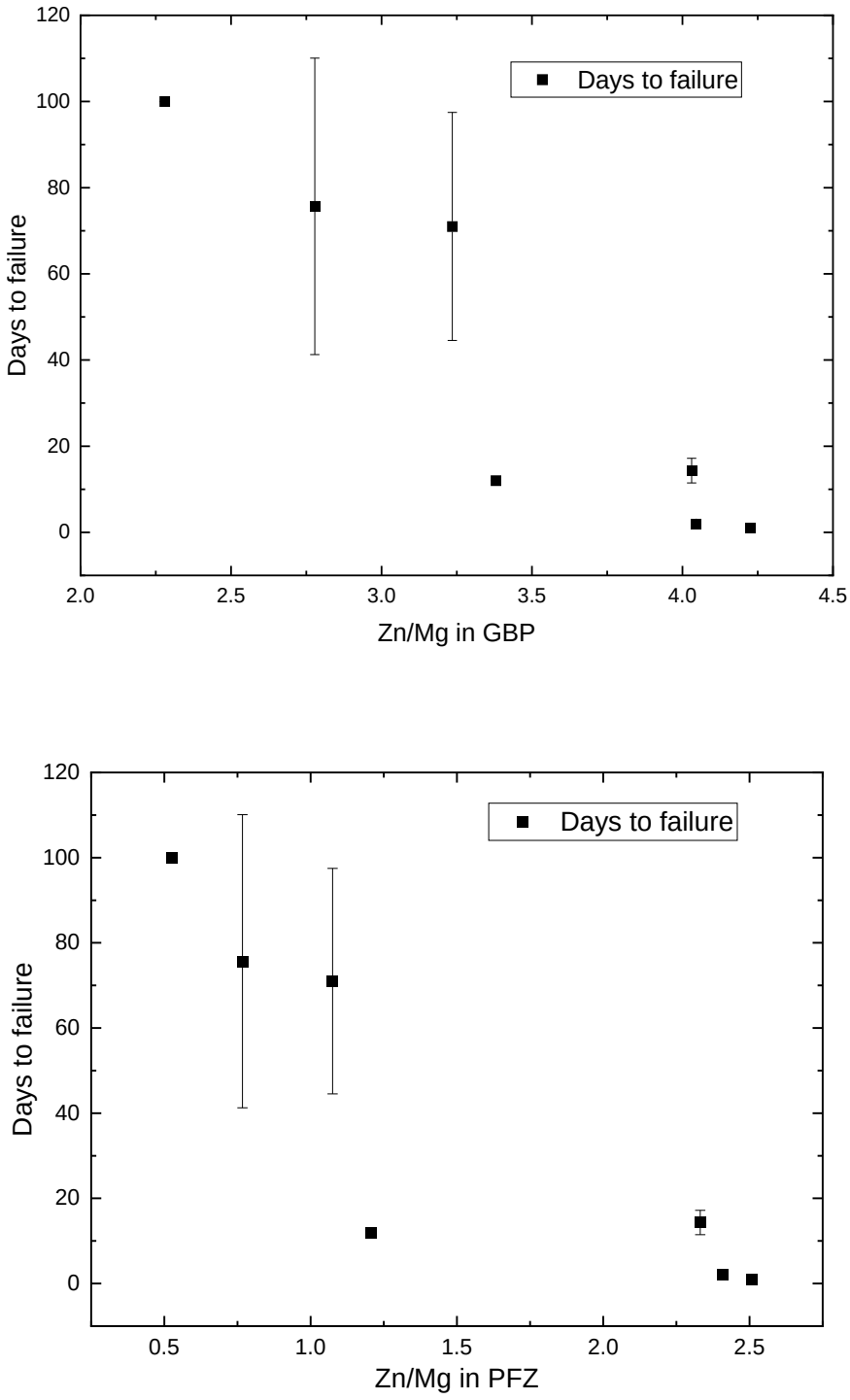

Figure 6-20: Effect of grain boundary features composition (top) precipitate (bottom) adjoining precipitate free zone on the days to failure in 70ºC at 85% RH.

To validate the causation between the correlation, a density functional theory (DFT) simulation was used to assess the embrittlement energy of the grain boundary in the presence of adsorbed hydrogen.

6.3.5 DFT calculation

The DFT first-principles calculations are based on the electronic density, a fundamental property of the system that can be calculated directly from the using the Kohn-Sham equations. These calculations aim to predict the properties of materials and molecules from the fundamental laws of physics, without any experimental input. The Rice-Wang thermodynamic model was used to assess the embrittlement potency. The model suggests that embrittlement potency can be described as the impurity's ability to decrease the "Griffith work" of brittle boundary separation. This ability is directly proportional to the difference in binding energies of the impurity at the grain boundary (GB) and the free surface (FS). If the impurity is more energetically favorable at the GB than at the FS, it can enhance the GB's resistance to brittle intergranular fracture. Conversely, if the impurity is less energetically favorable at the GB than at the FS, it can weaken the GB's resistance to brittle intergranular fracture [137]. **Figure 6-21** shows the schematic of the aluminum supercell used for the DFT calculation of segregation energy and embrittlement potency of solute elements for a $\sum 5$ symmetric high angle grain boundary of {210} [001]. The segregation energy from the DFT calculation of H, Mg and Zn is shown in **Table 6-6**. All the elements had negative value for the grain boundary segregation energy. Mg had the lowest value of -0.38 eV/atom while Zn had -0.13 eV/atom in presence of Mg. Interestingly H had lower segregation energy than Mg with a value of – 0.24 eV/ atom.

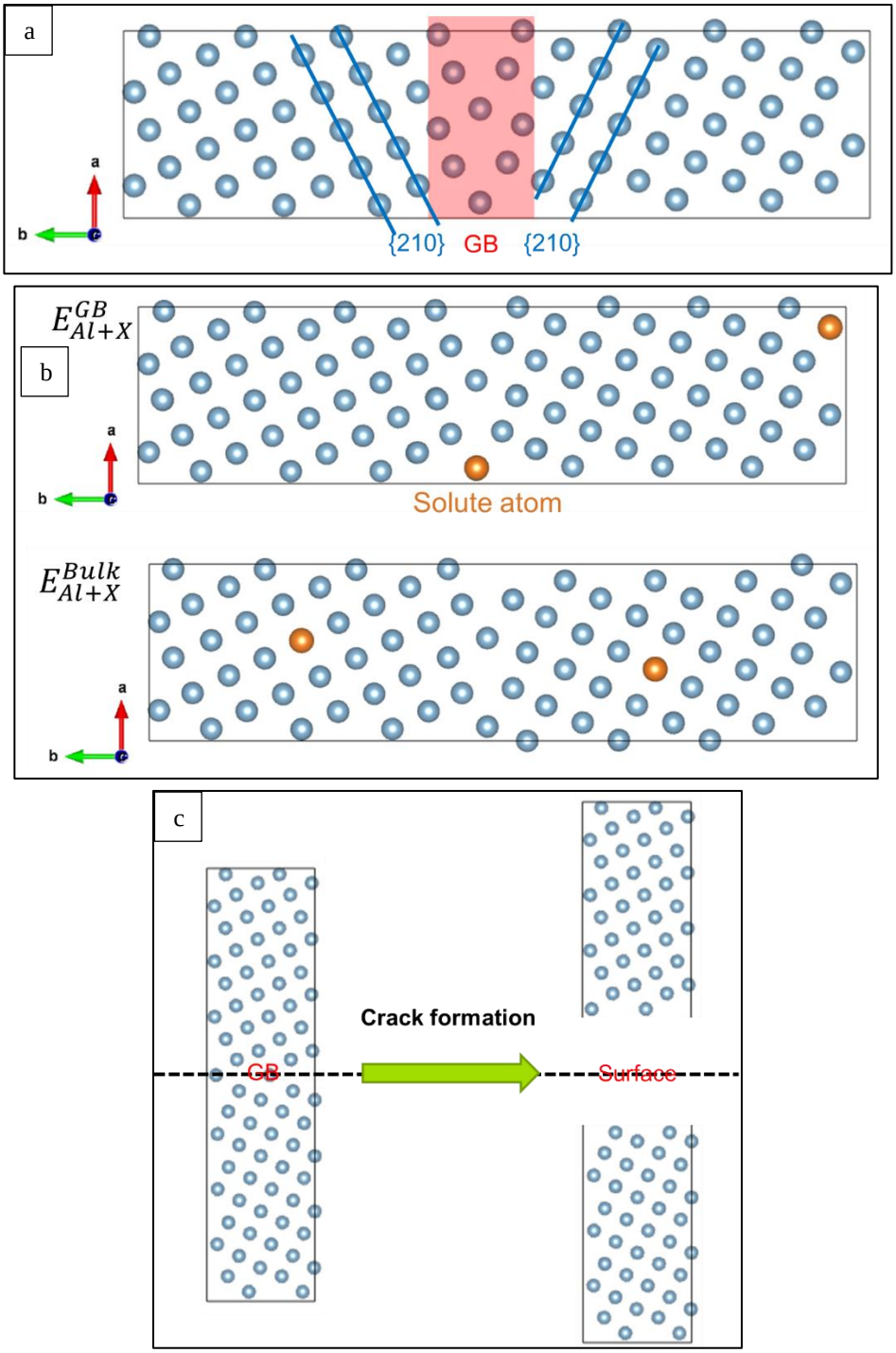

Figure 6-21: Atom positioning for the DFT calculations (a) schematic of ∑5 grain boundary (b) schematic for calculating the E_{Seg}^{GB} segregation energy (c) schematic for calculating E_{Seg}^{FS} the fractured surface energy.

Table 6-6: Segregation energy of key solute elements in ∑5 grain boundary from the DFT calculations.

Element	Segregation energies per atom (eV)
H	-0.24
Mg	-0.37
Zn in presence of Mg	-0.13

Figure 6-22 shows the effect of solute elements on the embrittlement energy aluminum supercell with a ∑5 grain boundary. Al supercell that was devoid of any impurity presence at the grain boundary had embrittlement energy of -471.46 mJ/m^2. Adding solute elements such as Mg to the grain boundary decreased the energy to -493.40 mJ/m^2 and a similar effect was observed (-490 mJ/m^2) in the concurrent presence of Mg and Zn.

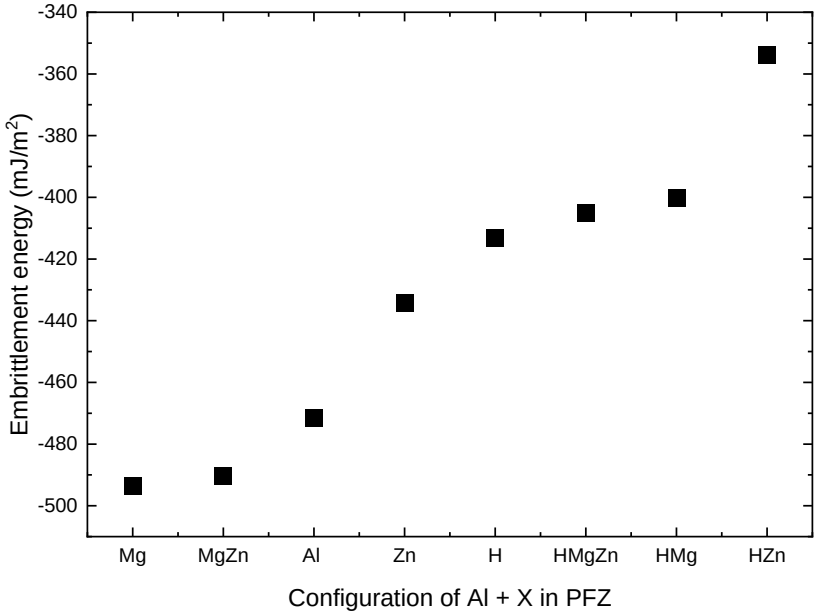

Figure 6-22: Effect of solute element presence on the embrittlement energy of the ∑5 grain boundary precipitate free zone (PFZ).

On the contrary, the presence of Zn atoms alone at the grain boundary increased the embrittlement energy to -434 mJ/m^2. When the H atom was added to the configuration, the

overall embrittlement energy of the supercell was shifted to a more positive value compared to the base configuration without hydrogen. For example, the embrittlement potency of Mg-Zn-H and Zn-H was -404 mJ/m^2 and -353 mJ/m^2 respectively compared to the supercell without hydrogen presence. Extending the DFT calculations to different Zn/Mg ratio, the following relationship is obtained as shown in **Figure 6-23**. The trend is similar to the data obtained in the **Figure 6-20**.

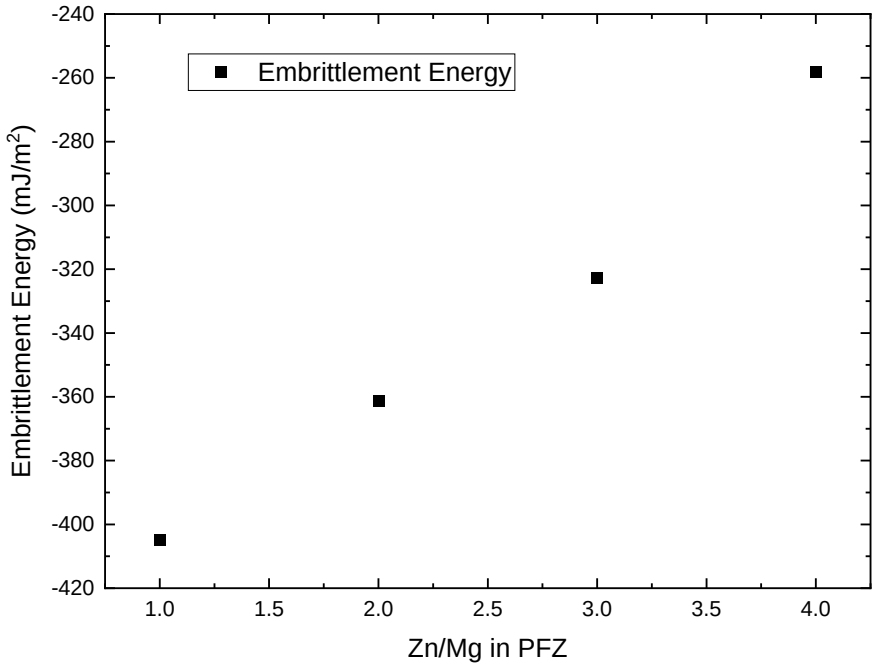

Figure 6-23: Effect of Zn/Mg ratio on the embrittlement energy of the grain boundary in presence of one hydrogen.

6.4 Discussion

The Zn/Mg ratio appears to have a significant impact on the SCC resistance of the 7xxx alloys in humid environments. The alloys that performed very well in the SCC tests in an

oxidizing environment (NaCl + H_2O_2) showed poor resistance to cracking when exposed to relative humidity at 85% RH in the absence of NaCl. High-solute alloys exhibited rapid failure in this environment even when the temperature was maintained at 35 ° C. The cross-sectional analysis of the failed samples clearly showed the presence of intergranular cracks near the fractured region. Similarly, the samples showed a clear sign of brittle fracture under the SEM. For a given composition, the applied stress had a significant impact on the days of failure but did not affect the failure morphology. Microstructure and composition analysis indicated the correlation between the Zn/Mg ratio grain boundary features and days to failure. The DFT calculations clearly showed that an increase in the Zn content in the precipitate-free zone increased the embrittlement potency in the presence of adsorbed hydrogen, thereby increasing the tendency to environmental fracture in a humid environment.

6.4.1 Cracking in the humid environment

The problem of 7xxx alloys cracking in a moist environment is gaining traction due to the release of the EASA SIB 2018-04R2 report. The report particularly highlighted the brittle fracture of the 7xxx alloy plates that had high levels of solute elements such as Zn (> 6 wt%) at 70°C at 85% relative humidity. The most significant part was the complete absence of NaCl in this test environment, and the samples cracked under the influence of moisture alone. Interestingly, under these environmental conditions, legacy low solute 7xxx alloys such as 7075 did not fail. Aluminum typically undergoes oxidation in humid environment conditions, leading to the formation of Al_2O_3, however, the corresponding cathodic reaction in this environment is hydrogen evolution as shown in the following equation [138, 139].

$$2Al\ (S) + (3 + x)H_2O\ (g)\ \rightarrow Al_2O_3 * X(H_2O)(s) + 3H_2\ (g)$$

The humid environment is particularly aggressive because of the formation of the chemisorbed hydrogen $H_{ads}(C)$, which proceeds with a single-electron reduction as shown in the following equation.

$$H_2O + e^- \rightarrow H_{ads}(C) + OH^-$$

Since bare aluminum has high hydrogen fugacity (i.e. effective pressure) and the concentration of dissolved atomic hydrogen near the surface can reach levels of approximately 20,000 parts per million by weight [140]. As a result, material failures are attributed to the hydrogen-induced cracking phenomenon [39, 141, 142]. A signature feature of hydrogen-induced failure in aluminum alloys is loss of ductility in the absence of widespread pitting or intergranular attack [143]. The fracture surface of aluminum alloys shows a unique pattern of hydrogen-assisted cracking, which is characterized by intergranular and quasi-cleavage-like fractures. This is attributed to hydrogen segregation at the grain boundaries, resulting in a brittle fracture along the grain boundary [144, 145]. For SCC to occur, three conditions must be met simultaneously, they are environmental, applied stress, and susceptible material [146]. The following subsections discuss the implication of these aspects for the high solute 7xxx alloy fracture in the moist environment.

6.4.2 Effect of environment

Table 6-1 clearly shows that alloys A and B performed poorly in the humid environment (85% RH) at 35°C and 70°C. However, the conventional 7075 alloy did not fail under these

conditions. The analysis of the fracture surface (**Figure 6-2**, **Figure 6-3**, **Figure 6-4**, **Figure 6-5**) and cross-section images (**Figure 6-1**) clearly showed the dominant presence of brittle intergranular and quasi-cleavage-like morphology in the humid environment. This was a drastic difference in the results compared to the trend observed in the oxidizing environment ASTMD1384 containing 1% H_2O_2 as reported in the previous chapter. Cracks in the oxidizing environment originated from pitting corrosion sites; however, no such features were observed in the failed samples in humid environment. Furthermore, in an oxidizing environment the ductile fracture was found to be the primary mode of failure for high-solute alloys. On the other hand, in a humid environment, the dominant brittle fracture features suggest that the grain boundaries are the weakest point. These differences in performance highlight the significance of environment on the SCC behavior of high- and low-solute 7xxx alloys.

Even in the case of unstressed samples, the environmental effect can be observed. The loss in elongation for alloy A was small in ASTM G44, while conventional 7075 showed a higher percentage of loss in elongation (**Figure 6-9**). Due to the low Cu content, the number of Al_7Cu_2Fe particles was lower, leading to better pitting resistance, while conventional 7075 had higher pitting sensitivity due to the higher number of Al_7Cu_2Fe particles. This could have affected the final elongation values. However, when exposed to 70°C at 85% RH, alloy A exhibited more drop in elongation than 7075, despite no signs of extensive pitting. A greater proportion of intergranular fracture characteristics were observed in samples of alloys A and B that were exposed to humid environments, compared to samples from the preexposure set and the ASTM G44. Previous studies have also documented that the corrosion of 7xxx alloys in NaCl-containing environments is caused by the selective

dissolution of $MgZn_2$ precipitates or dissolution of matrix around Al_7Cu_2Fe particles [43, 113, 147]. The corrosion morphology observed in the humid environment is consistent with a previous study by Knight et al. [132], which demonstrated that only hydrated oxide was present on the surface and that there was no significant pitting or localized corrosion attack.

The change in SCC performance may be mainly attributed to differences in the cathodic reactions required to support the corresponding anodic activity. In oxidizing environments, the main cathodic reaction is the oxygen reduction reaction, and hydrogen evolution occurs only at very high potentials [148-150]. As mentioned above, the cathodic reaction in a moist environment is hydrogen evolution because of water reduction. This suggests that the mechanism of SCC varies depending on the environment. When the environment contains Cl^- and is oxidizing, the SCC failure is governed by anodic dissolution of grain boundary precipitates or pitting corrosion around intermetallic particles. However, in a humid environment, the failure mode may be dictated by chemisorbed hydrogen resulting from the cathodic reduction of water. The differences in performance between 7075 and high-solute alloys can be attributed to microstructural features that facilitate hydrogen trapping along grain boundaries.

6.4.3 Effect of stress

The application of external stress certainly accelerated the failure of high-solute alloys in the humid environment. The fracture surface (**Figure 6-7**) was dominated by the presence of brittle fracture features such as quasi-cleavage and intergranular fracture. The morphology was comparable to that of the unstressed samples (**Figure 6-13**), but the key

difference was in the amount of brittle fracture features. The most interesting results were the failure of the high solute alloys at 35°C at 85% RH and no evidence of signature crack arresting marks was observed in SEM (**Figure 6-2**, **Figure 6-3**). This suggests that the crack velocity was very high under test conditions. The results are in line with the observations reported by Holroyd et al. [151]. In their work, they reported cracking of 7xxx alloys in the temperature range from 10^{o}C to 80^{o}C at different relative humidity. They attributed the cracking to the formation of AlH_3 at grain boundaries.

What is noteworthy is that the unstrained specimens, when exposed to this humid environment, only experienced a 10% reduction in elongation after being exposed for a period of seven weeks. These results from **Figure 6-9** imply that the applied stress played an important role in accelerating the failure of the samples. This acceleration of failure could be due to the accumulation of hydrogen in the high-stress region. It has been postulated that during mode I loading, the hydrogen tend to accumulate in a region of triaxial stress located before the tip of the crack, making the material in this region very brittle [152, 153].

Even at elevated temperature (70°C), the high-solute alloys A and B lost 40% of elongation after 100 days of exposure in the absence of stress. However, in the presence of stress, the samples failed after a few days of exposure. The days to failure at 70°C were shorter than the days to failure at exposure to 35°C. The observations are in line with the finding of Scully et al. [154]. They reported that hydrogen-assisted cracking should follow Arrhenius kinetics, and as a result, the crack velocity would increase exponentially with an increase in temperature. These results clearly highlight the importance of stress and temperature to fractures in a humid environment.

The findings also imply that there exists an applied stress threshold, equivalent to 20% of the yield strength, below which a fracture does not occur, and no micro cracks were observed on the surface. This could imply that the rate-controlling stage could be the initiation of the crack. Considering the gauge thickness of only 2mm, the crack propagation rate would be quite rapid for this type of cross-sectional geometry. The findings and analyses were consistent with the study by Fransciso et al. [155] that showed that the time to failure of 7449 increased significantly as the applied stress decreased from 80% to 50% of the yield stress. In particular, the samples did not show any indication of cracking at 28% of the yield stress.

Holroyd et al. [151] formulated their hypothesis based on the research of Ciaraldi et al. [156] who reported the presence of AlH_3 on the fracture surface of Al-5.6Zn-2.6 Mg after conducting slow strain rate tests. However, if AlH_3 was indeed forming on the grain boundaries, then all 7xxx alloys would have failed under these exposure conditions. Nevertheless, the conventional 7075 alloy managed to pass the testing. In the same manner, the high- and low-solute alloys were subjected to identical loading conditions, indicating that the diffusion of hydrogen under tensile stress between interstitial spaces should not alter, unless there exist microstructural trapping sites that are more energetically favorable. Furthermore, the characteristics of the intergranular fracture suggest that the microstructure of the material plays a crucial role under the influence of stress.

6.4.4 Effect of microstructure of material

In the previous chapter, the microstructures of alloys A and B were reported to differ from that of conventional 7075. Due to varying levels of recrystallized grains, a higher amount of low angle grain boundaries were observed in high-solute alloys compared to the 7075. The low-angle grain boundaries not only affects precipitation discontinuity but they also reported to provide higher resistance to crack propagation [157, 158]. The presence of grain boundary and grain boundary precipitates causes dislocations to pile up at high angle grain boundaries, creating difficulty in gliding across these boundaries, ultimately resulting in the nucleation of intergranular cracks at these high angle grain boundaries [159, 160]. As observed in the preceding section, the primary controlling factor in a humid environment seems to be the rate of crack initiation. Furthermore, the high crack velocity suggests that the misorientation angle of grain boundaries has minimal impact on the fracture resistance of high solute alloys in such conditions. These results are in line with observations of Schwarzenböck et al. [161] where they observed more planar cracks in new generation of high solute 7xxx alloys in a humid environment that had higher level of unrecrytallized grain boundaries. This suggests that enhancing the low angle grain boundary content of high-solute alloys might not necessarily enhance their SCC resistance in a humid environment.

Another key difference observed between the high-solute alloy and the conventional 7075 alloy was the discontinuity of the precipitate at the grain boundaries (**Figure 6-15** and **Figure 6-19**). In an oxidizing Cl^- containing environment, the precipitates are selectively attacked, affecting the intergranular corrosion resistance. In the case of the 7075 alloy, the continuous presence of precipitates along the grain boundary made the alloy highly susceptible to intergranular corrosion and subsequently to intergranular SCC in the

presence of stress. However, in a humid environment, the primary reaction is the surface oxidation of aluminum to Al_2O_3, and due to lack of Cl^- ions the grain boundary precipitates were intact, as the cross-sectional images did not show any significant attack at the grain boundary. On the other hand, the high-solute alloys that showed superior resistance to grain boundary corrosion in a Cl^- environment experienced brittle intergranular fracture in a Cl^- free humid environment. The cross-sectional images of the high-solute alloys did not show any sign of localized grain boundary attack in a humid environment. This implies that the continuity of grain boundary precipitates does not play a role in SCC mechanisms in a humid environment.

The other category of microstructural features that could affect the SCC performance in humid environments are the energetically favorable traps of hydrogen. In aluminum alloys, the common traps are dispersoids, strengthening precipitates, and grain boundaries. The high solute alloys A and B contain Zr, and as a result Al_3Zr is the main dispersoid, while in conventional 7075 contains Cr and as a results Al_3Cr is the principle dispersoids. Recently, Safyari et al. [162] work using the silver microprinting method showed that Al_3Zr dispersoids traps hydrogen. The elastic interaction between the coherency strain and hydrogen was suggested as the reason for the accumulation of hydrogen in the Al_3Zr dispersoids. It was noted that Cr-containing dispersoids did not trap hydrogen as effectively as Al_3Zr dispersoids. Similar observations were confirmed by first-principles calculations on the trapping of H by L12-Al_3Zr particles by Liu et al. [163]. DFT calculations showed that the hydrogen spontaneously adsorbs onto the surface of L12-Al_3Zr (111), with the most stable adsorption site determined as the FCC hollow site. These results suggest that the Al_3Zr would act as a good hydrogen trapping site and thereby improving the SCC

resistance in a moist environment. However, the present findings indicate that the high-solute alloys A and B containing Al_3Zr had a brittle intergranular fracture, while the conventional 7075 alloy passed the test. This suggests that the grain boundary characteristics in high-solute alloys could still determine the failure mode despite the presence of Al_3Zr in the matrix. Recently Al_7Cu_2Fe has been reported to trap hydrogen and thereby reducing the effect of hydrogen partitioning from $MgZn_2$ resulting in higher SCC resistance [164]. This effect was not observed in this work, since alloy B had a higher percentage of Al_7Cu_2Fe than alloy A due to the difference in the Cu level, but both failed in the humid environment. The discrepancy could be due to insufficient hydrogen diffusion inside the Al_7Cu_2Fe particles and at the interface between the aluminum matrix and the particles.

SCC resistance could be impacted by two main grain boundary features, namely, the composition of the grain boundary precipitates and the adjoining PFZ. Tsuru et al. [165] used first-principles calculations and found that most of the interstitial sites within the $MgZn_2$ crystal were not suitable as trap sites. However, the trap sites located at the interface between $MgZn_2$ and Al were more stable than other potential trap sites. Furthermore, the study highlighted that hydrogen atoms tend to be trapped around Mg rather than Zn. However, the EDS analysis from the present work (**Table 6-5**) revealed that the Zn level of the grain boundary precipitate increases with an increase in the bulk Zn content. This could result in weaker trapping, making the causation of the observed correlation unlikely. The STEM images also showed that the precipitates at the grain boundaries were coarser and largely discontinuous. In the case of alloy A, because of the higher fraction of the low angle grain boundaries, they were fairly clean. These observations further strengthen the

argument that the grain boundary precipitates may not play a direct role in humid environment SCC.

As seen in the **Figure 6-20**, the composition of the precipitate-free zone had a strong impact on the SCC resistance in humid environment. With an increase in the Zn/Mg ratio, the time to failure decreased significantly. Gruhl et al. [166] work was the first to show the effect of Zn content on the SCC resistance of 7xxx series alloys. They reported that the higher Zn concentration in the solid solution decreases the time of failure for a given value of applied stress. It was hypothesized that a reciprocal electronic effect occurs between foreign atoms and hydrogen ions, whereby elements with a valence lower than the matrix attract hydrogen atoms while elements with higher valence repel them. Schwarzenböck et al. [161] also observed such a correlation between the bulk Zn content and the SCC resistance in humid environment. They suggested that a higher Zn content in the near-surface matrix or M phase may potentially lead to a reduction in passivation and an increase in the permeability of the oxide layer, leading to a higher rate of hydrogen ingress at the surface. This may have an impact on the crack initiation stage and also contribute to the provision of hydrogen necessary for crack growth. However, the influence of hydrogen ingress on the initiation or propagation was not explored in this study. In the current work, using DFT calculations, the connection between the adsorbed hydrogen and the susceptibility of high-solute alloys to grain boundary cracking are clearly established.

6.4.5 Hydrogen enhanced de-cohesion

Hydrogen-Enhanced decohesion (HEDE) mechanism entails a decrease in the electron charge density between the metal atoms located in the vicinity of the crack tip, where hydrogen builds up through stress-assisted diffusion. This leads to a weakening of the bonds between adjacent metal atoms and eventually results in their tensile separation [167]. The presence of adsorbed hydrogen at specific sites such as grain boundaries could result in decohesion, and, additionally, bond weakening may also occur due to segregation of metalloid impurities or solute alloying elements, together with hydrogen [168, 169]. A featureless fracture surface (crack arresting marks) is a signature of the decohesion mechanism [170].

To determine the effect of decohesion, the concept of embrittlement potency from the Rice and Wang model was used in the DFT calculations [171]. The model explains the intergranular embrittlement mechanism as a competition between plastic crack blunting and brittle boundary separation. The term "embrittlement potency" refers to the alteration in adhesion energy at grain boundaries caused by segregant species [172]. As per the Rice-Wang model, its magnitude is determined by this alteration given by the following equation.

$$E_{Seg}^{Crack} = E_{Seg+X}^{GB} - E_{Seg}^{FS}$$

$$E_{Seg+X}^{GB} = E_{Al+X}^{GB} - E_{Al+X}^{Bulk}$$

Where E_{Seg}^{Crack} is the embrittlement potency, E_{Seg+X}^{GB} is segregation energy of solute species X, E_{Seg}^{FS} is the free surface energy, E_{Al+X}^{GB} is the total energy of the system with a GB and X

atom in a site along the GB, E_{Al+X}^{Bulk} is the total energy of the system with a GB and X atom in a bulk site. When the E_{Seg}^{GB} is negative, then the species will segregate at grain boundary. The DFT calculation showed that the segregation energy per atom of Zn species in presence of Mg at the grain boundary was -0.13 eV. This indicates that Zn will preferentially segregate at the grain boundary. The grain boundary concentration of the segregated species is related to the bulk concentration by the McLean equation [173].

$$\frac{C_{GB}}{1 - C_{GB}} = C_{Bulk} \exp\left(-\frac{E_{Al+Zn}^{GB}}{RT}\right)$$

where C_{GB} and C_{Bulk} are the Zn concentrations in the GB and bulk, respectively, E_{Al+Zn}^{GB} is the total energy of the system with a GB and Zn atom in a site along the GB, T is the absolute temperature, and R is the universal gas constant. This equation indicates that the Zn concentration of grain boundary will increase with increasing bulk concentration. This relationship in the equation is mirrored by the data (**Table 6-5 and Table 6-3**) obtained from both the STEM EDS and ThermoCalc predictions.

The DFT calculations showed (**Figure 6-22**) that even in absence of adsorbed hydrogen, Mg appears to have strengthened the grain boundaries while Zn weakens the grain boundaries of Al. The strengthening of the grain boundary is reported as a result of the charge transfer mechanism arising from the electronegativity difference between Mg (1.31) and Al (1.61). The segregation of Mg towards the Al grain boundary results in a transfer of charge from the Mg atom to the Al atoms, resulting in an increase in charge density between the Mg and Al atoms and subsequent bond formation that is a mixture of ionic and metallic character [172]. This, in turn, enhances the bonding between Al atoms along

the grain boundary and consequently increases its strength. The reason for the embrittling impact of Zn is due to a decrease in the bonding charge density along the Zn-Al bonds, which causes these bonds to weaken compared to the Al-Al bonds as reported by Zhang et al. [137].

The embrittlement potency is increased further with the presence of adsorbed H atoms, as shown in the **Figure 6-22** especially Mg-H. This could be due to the higher electronegativity of adsorbed H that stabilizes the Al-H bond and resulting in weakening of the Al-Al bond in the grain boundary. Alternatively, Wilson et al. [174] proposed that the introduction of H significantly hinders the development of ligament structures that act as links across the vacuum structures, and the crystals remain in their face-centered cubic structure throughout the experiment. Zhao et al. [175] in Al-Mg-Zn alloys, reported that when Mg is present, the powerful driving force for hydrogen to segregate towards a free surface rather than a potential interstitial site at grain boundaries favors intergranular decohesion and drives the system towards crack initiation. However, the **Figure 6-22** shows that Zn-H had higher embrittlement potency than Mg-H and Zn-Mg-H, which suggests that with the increase in the Zn/Mg ratio in PFZ (**Figure 6-23**), the embrittlement potency of the grain boundary will increase further resulting in HEDE in humid environment.

6.5 Conclusions

The testing environment affected the SCC resistance of the high solute 7xxx alloys. At 85% relative humidity, the high-solute alloys that were stressed to 80% yield stress failed after a few days of exposure while conventional 7075 survived the test. Fracture surface examination confirmed the brittle fracture features such as cleavage-like morphology and the crack propagated along the grain boundary. Under humid conditions, surface oxidation was the anodic reaction, and no sign of localized pitting or IGC was observed in high-solute alloys. An increase in the temperature of the testing environment and the level of applied stress accelerated the time to failure of the high solute alloys. There was a correlation between the Zn/Mg ratio of the precipitate free zone and the time to failure. DFT calculations were used to identify the causation behind the correlation and validate the experimental observations. The results implied that the hydrogen-enhanced decohesion (HEDE) was the operating mechanism under these tested conditions.

CHAPTER 7: EFFECT OF JOINING METHODS ON THE IGC AND SCC RESISTANCE OF 7075 TO 5182 DISSIMILAR JOINT.

7.1 Background

This work aims to characterize and understand the link between the microstructure and the corrosion performance of commonly used joining methods such as resistance spot welding and self-pierce riveting in the automotive industry.

7.2 Approach

2.8 mm thick 7075-T6 and 1.5 mm thick 5182-O were subjected to resistance spot welding (RSW) using the proprietary Novelis joining sequence, while self-piercing rivet (SPR) joints were made at Bollhoff. After joining, the samples were subjected to heat treatment at 180° C for 20 min to simulate the paint bake cycle in automotive production. The joint samples were characterized using EBSD, SEM, EDS, and microhardness testing. The samples were subjected to a wide range of electrochemical tests, including polarization, zero resistance ammetery, and scanning vibrating electrode technique. To assess the impact of localized electrochemical reactions on the longevity of the joints, the samples were exposed to short (ASTM G110), medium (ASTM G85-A2), and long-term (cyclic corrosion and stress humidity test) accelerated corrosion tests.

7.3 Results

7.3.1 Microstructure Characterization

The typical composition of the alloy used in this work is shown in **Table 7-1.** There was a distinct difference in the compositions between the alloys specifically for elements such as of Zn, Mg, Cu, and Si. The primary alloying element in 5182 was Mg (4 wt%), while 7075 contained a lower amount of Mg (2.35%) but it had significantly higher amounts of Cu, Zn, and Si.

Table 7-1: Typical composition of the alloys used in this work.

Alloy	Composition in wt%						
	Cr	**Cu**	**Fe**	**Mg**	**Mn**	**Si**	**Zn**
7075	0.19 – 0.29	1.59 – 1.79	0.17 – 0.27	2.54 – 2.74	0.03 – 0.13	0.04 – 0.14	5.79 – 5.99
5182	0.1 - 0.3	0.05 – 0.25	0.23 – 0.33	4.5 – 4.7	0.33 – 0.43	0.06 – 0.16	0.25 – 0.45

Figure 7-1 shows the plane and cross-section view of the RSW and SPR joints. The plane view images showed no signs of defects in the joints. There was no sign of hot cracking or material transfer in the RSW, while both the button section and region adjoining the rivet were largely free of cracks as well. However, the cross-sectional images clearly showed the presence of defects such as small cracks and pores I n the fusion area of the RSW joint. These defects were restricted to the center of the weld and did not extend into the faying surfaces. The cross-section images of the SPR did not reveal any imperfections, and the joining materials conformed to the rivet and button section geometry.

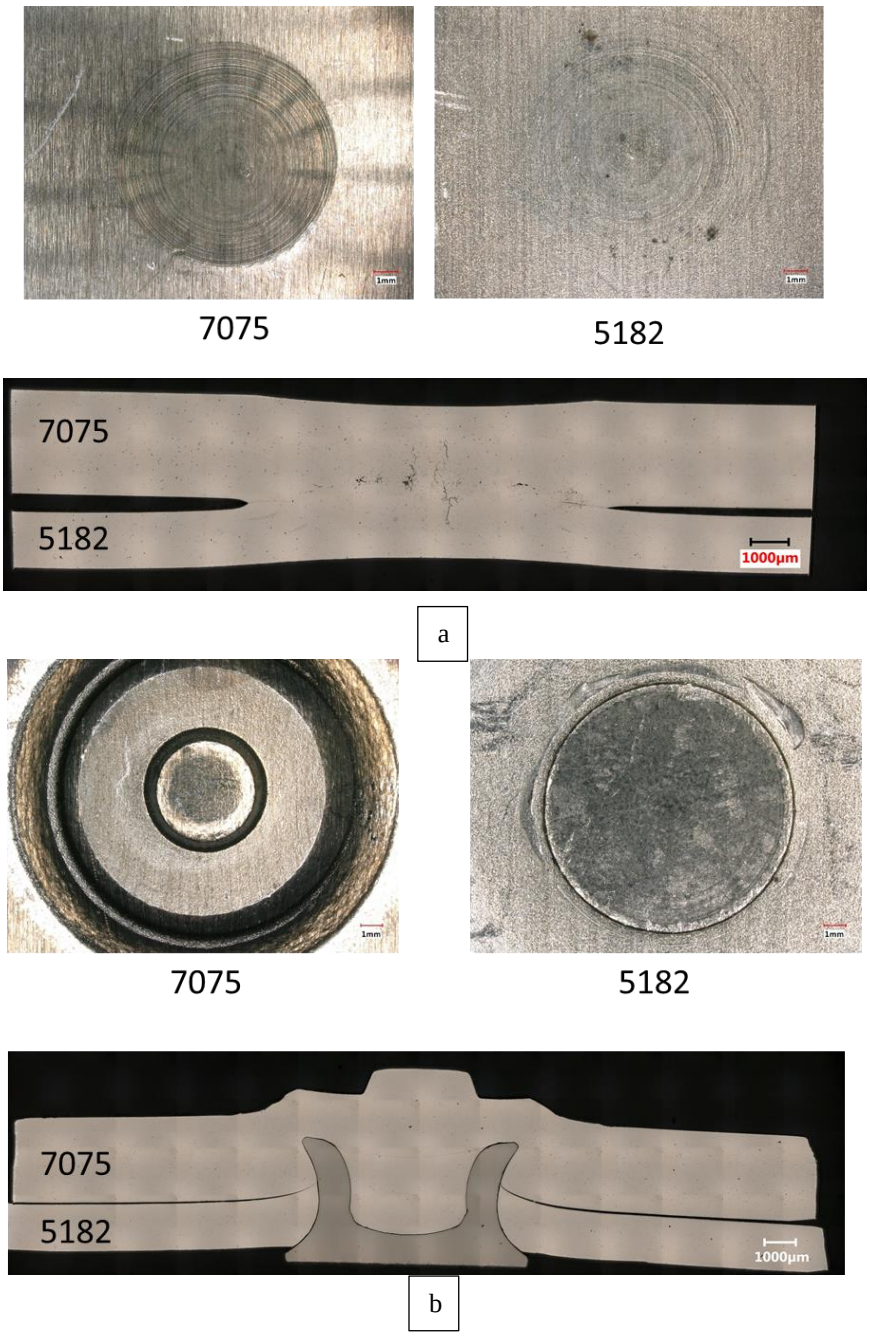

Figure 7-1: Optical plane and cross-section view images of (a) RSW and (b) SPR joints.

Figure 7-2 and **Figure 7-3** show the data from the EBSD analysis of the joint sections to reveal the grain structure. From the Euler maps, we could observe that 7075 and 5182 base metal had fully recrystallized grains with elongated and equiaxed shapes respectively.

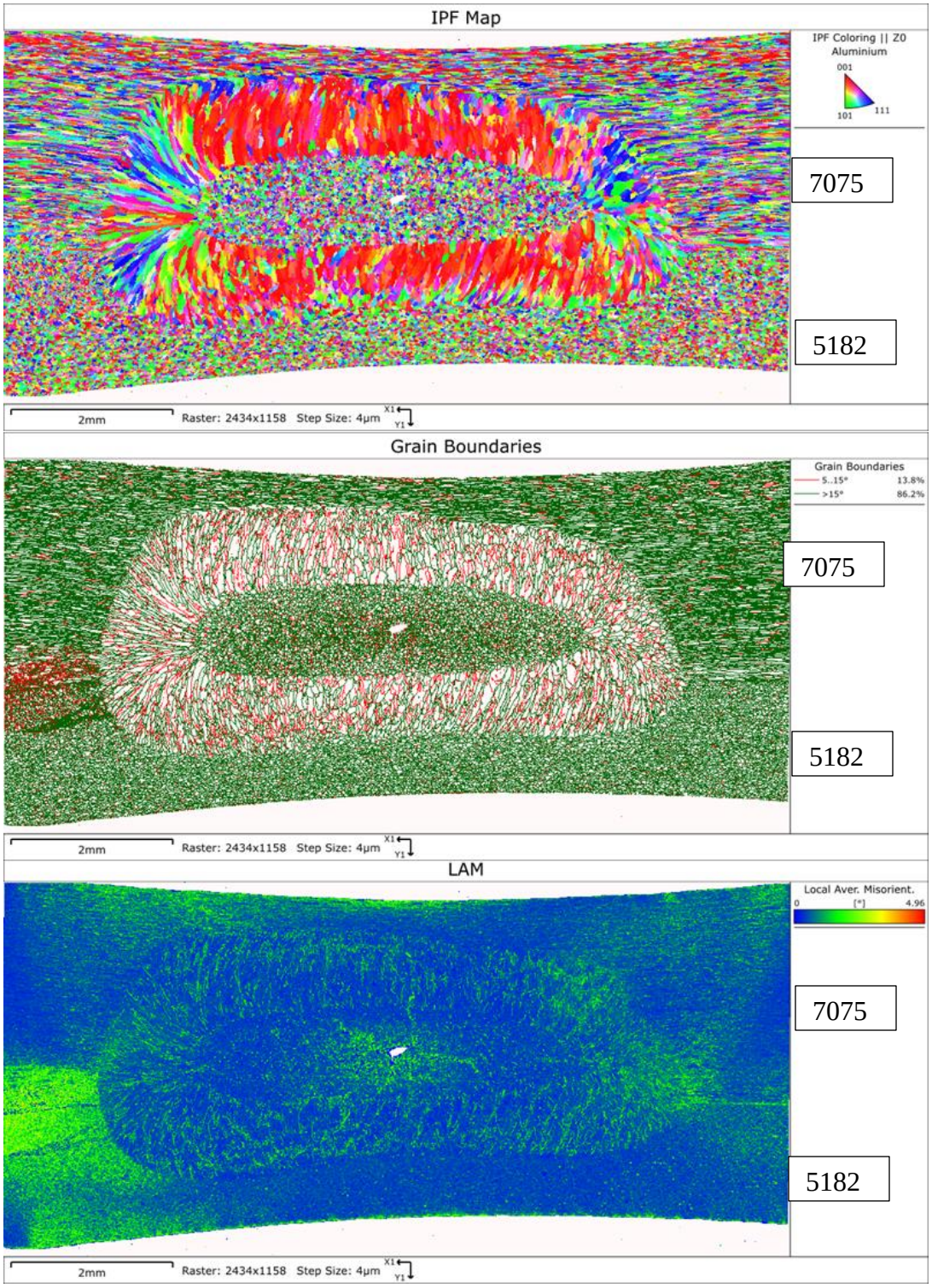

Figure 7-2: EBSD data of the RSW joint (Top) inverse pole figure map (middle) grain boundary mis-orientation map (bottom) local average mis-orientation map

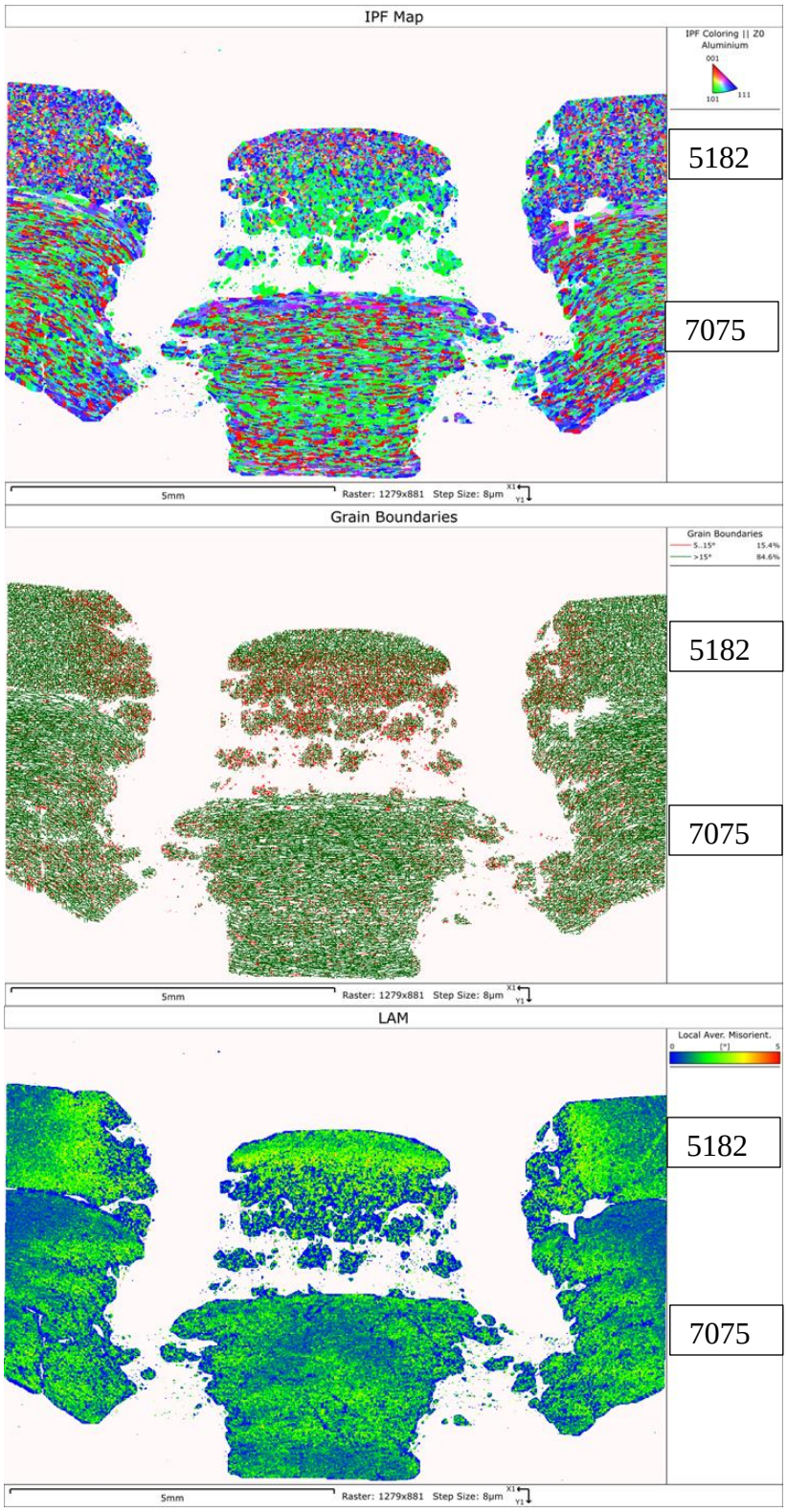

Figure 7-3: EBSD analysis of SPR joints (Top) inverse plane figure (middle) grain boundary misorientation map (bottom) local average misorientation map.

The center of the RSW section (fusion region) was also fully recrystallized but the size of the grains was smaller than the base material. We could also observe the presence of cracks in the fusion zone. The region between the base metal and the fusion zone contained columnar regions with elongated grain shapes. The heat-affected zone did not show any change in grain size for both alloys. The welding process also affected the misorientation angle and we could observe that the columnar region predominantly contained the low-angle grain boundaries (misorientation < 15^{o}). The fusion zone also contained a high level of low-angle grain boundaries, however, the heat-affected zone of 7075 and 5182 did not show a dramatic difference in the misorientation angle distribution. The local strain variations were represented by the local average misorientation map. This is a pixel-based measurement that calculates the average misorientation between a point on the 3x3 measurement grid and its neighbors. We could see that the heat-affected zone predominantly contained high levels of the local strains. This was the case in both 7075 and 5182; however, the strain distribution was observed in deeper areas only in the case of 7075. A high density of residual strain was also recorded in the columnar and base metal interface region. In addition, the fusion zone also contained residual strain, but it was restricted to the center region.

Unlike RSW joints, the SPR method did not result in any gradient grain size (**Figure 7-3**). 5182 flowed nicely into the rivet area, and the shape of the grains just under the rivet did not change significantly. However, the shape of the grains adjacent to the rivet was elongated along the direction of penetration in both 7075 and 5182. The overall indexing rate was poor in this region and at the interface of the 5182 - 7075 section under the rivet.

In the button section of the joints, 7075 grains elongated along the direction of the deformation.

A higher density of the low-angle grain boundaries was observed in 5182 in the regions below and adjacent to the steel rivet. Although low angle boundaries were observed in 7075, the extent and distribution were not concentrated at the specific location, such as the button section. The local distribution of the strain was much higher in SPR compared to that in RSW. A higher degree of localized strains was observed in the sections under and adjacent to the rivet in the case of the 5182, while 7075 exhibited severe strain localization in the button section.

The EBSD data only show the grain orientation, however, to get information on the precipitate morphology, SEM images were taken in back scattered (BSE) mode.

Figure 7-4 clearly shows that a fusion welding process such as RSW had a clear effect on the precipitation kinetics of the faying surfaces. Under current magnification, the grain boundary precipitation was not observed in the base materials. As we move toward the center of the weld section, we could observe distinct grain boundary precipitates. The heat-affected zone of 7075 and 5182 looked very different. The grain boundary precipitates were continuous in 7075; adjoining the grain boundary region we could observe a distinct region that was devoid of any precipitates. The grain interior had a higher density of coarse precipitates compared to the base material.

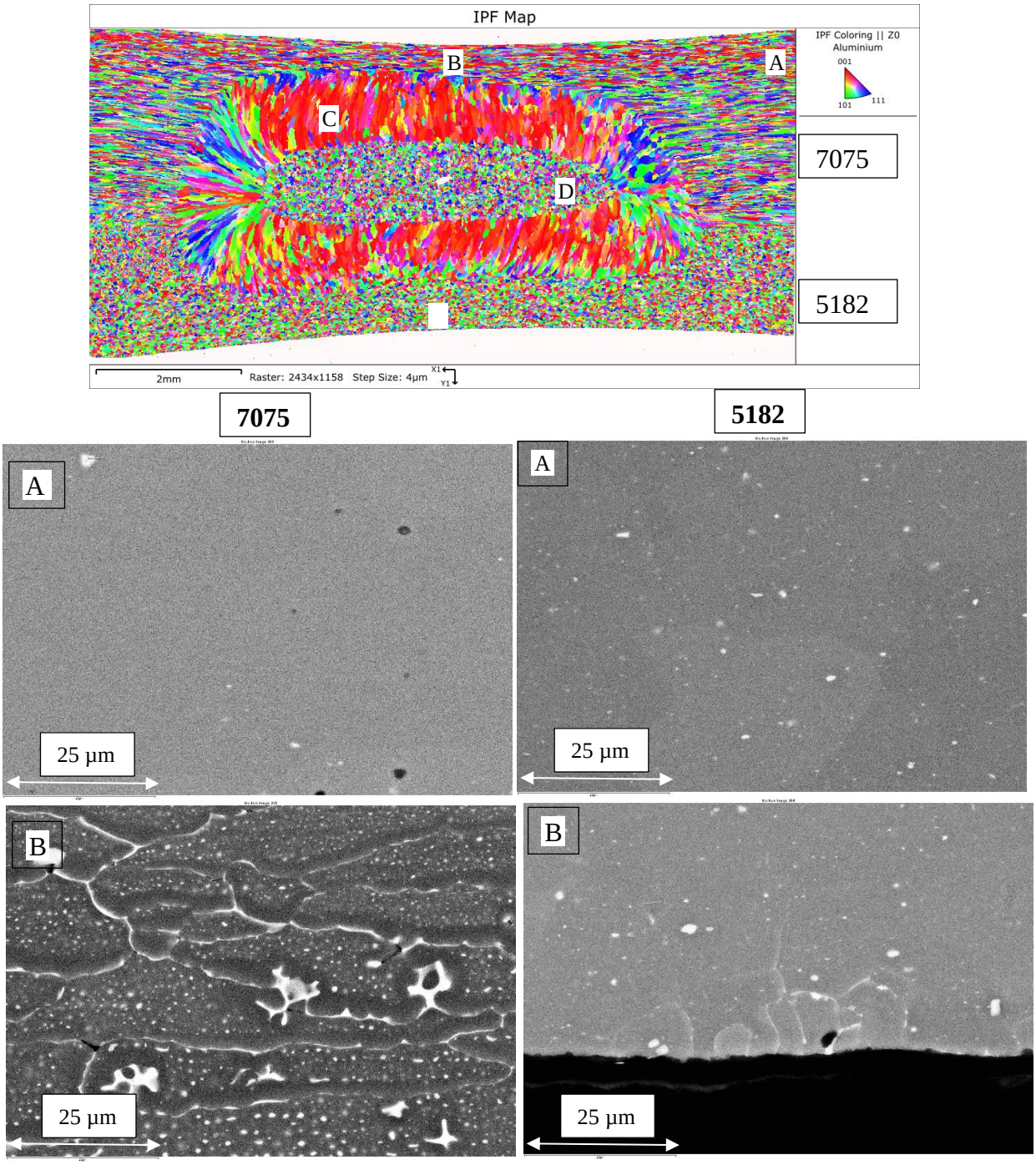

Figure 7-4: SEM - backscattered images of RSW cross section at (A) base metal (B) heat affected zone (c) columnar region (D) fusion region.

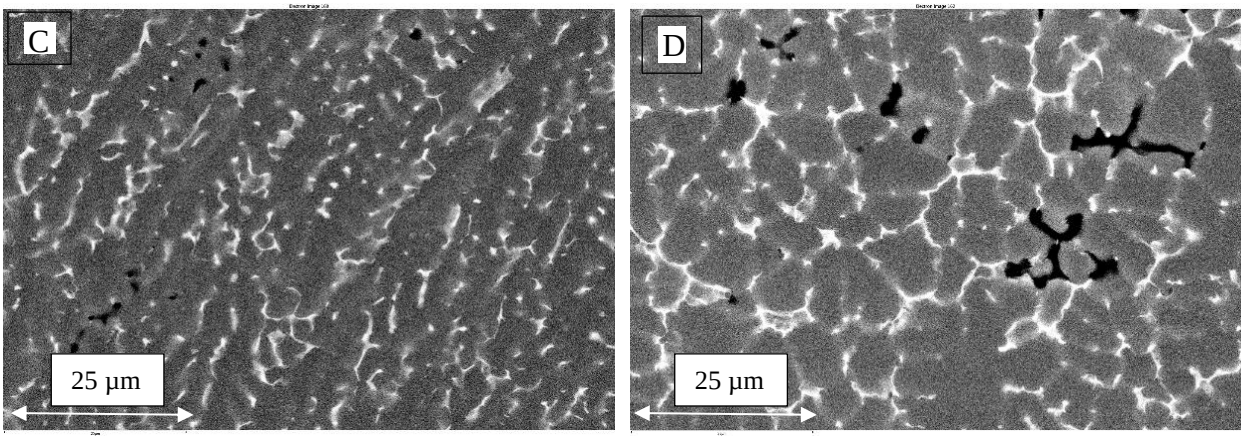

Figure 7-4 continued: SEM - backscattered images of RSW cross section at (A) base metal (B) heat affected zone (c) columnar region (D) fusion region.

In **Figure 7-5** we can see that the precipitates in the grain boundaries had higher levels of Zn and Mg compared to the adjoining precipitate-free region. The 5182 heat-affected zone was not as dramatic as 7075 but we could still observe the continuous grain boundary precipitation.

Although there was an increase (**Figure 7-6**) in the Mg level of the precipitates at the grain boundary, they weren't as significant as in the 7075 section. Similarly, the 7075 had a distinct columnar region microstructure compared to the fusion zone.

Figure 7-4 shows that the continuous coverage of the precipitates along the grain boundary and the grain interior is free of any particles. We could also observe that the grain boundary precipitates were smaller in size compared to the fusion zone. The columnar regions also had pores-like regions that were devoid of any precipitates. However, the fusion zone contained more of these defects. SPR samples did not show any signs of precipitate coarsening and defects.

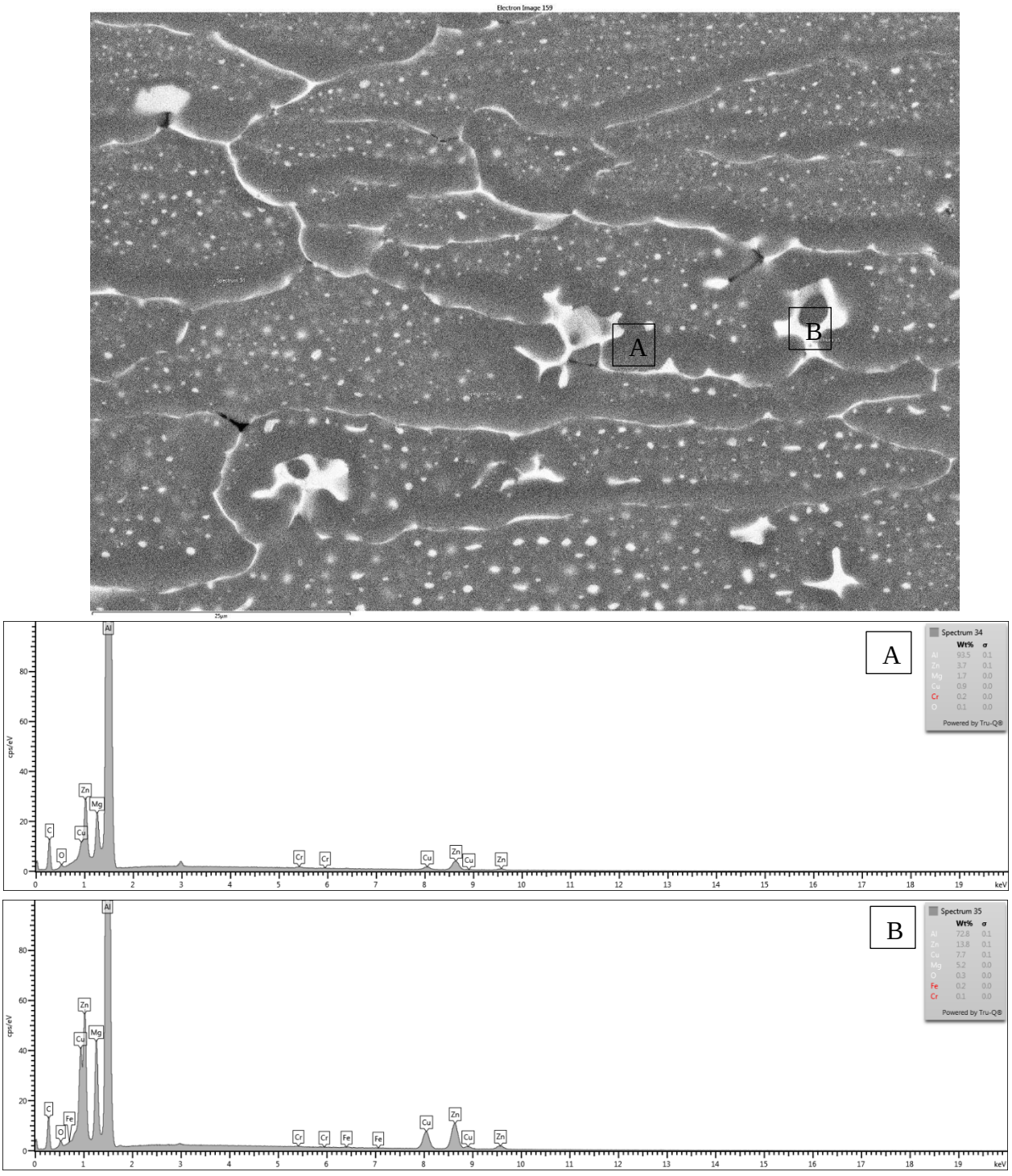

Figure 7-5: Heat affected zone of 7075 in RSW joint SEM-BSE image (Top) EDS spectrum of precipitate free zone (middle) and precipitate in grain boundary (bottom).

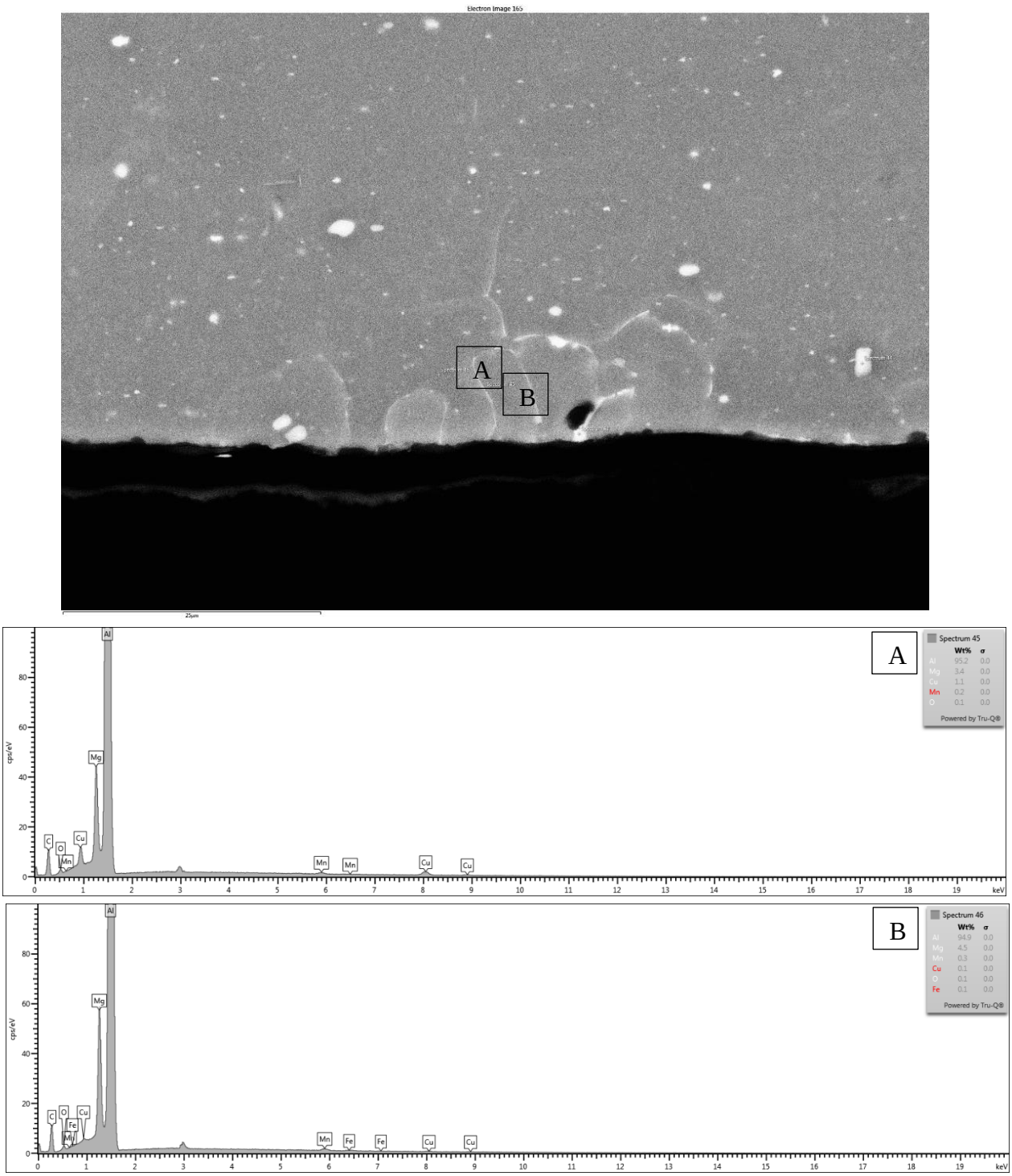

Figure 7-6: Heat affected zone of 5182 in RSW joint SEM-BSE image (Top) EDS spectrum of precipitate free zone (middle) and precipitate in grain boundary (bottom).

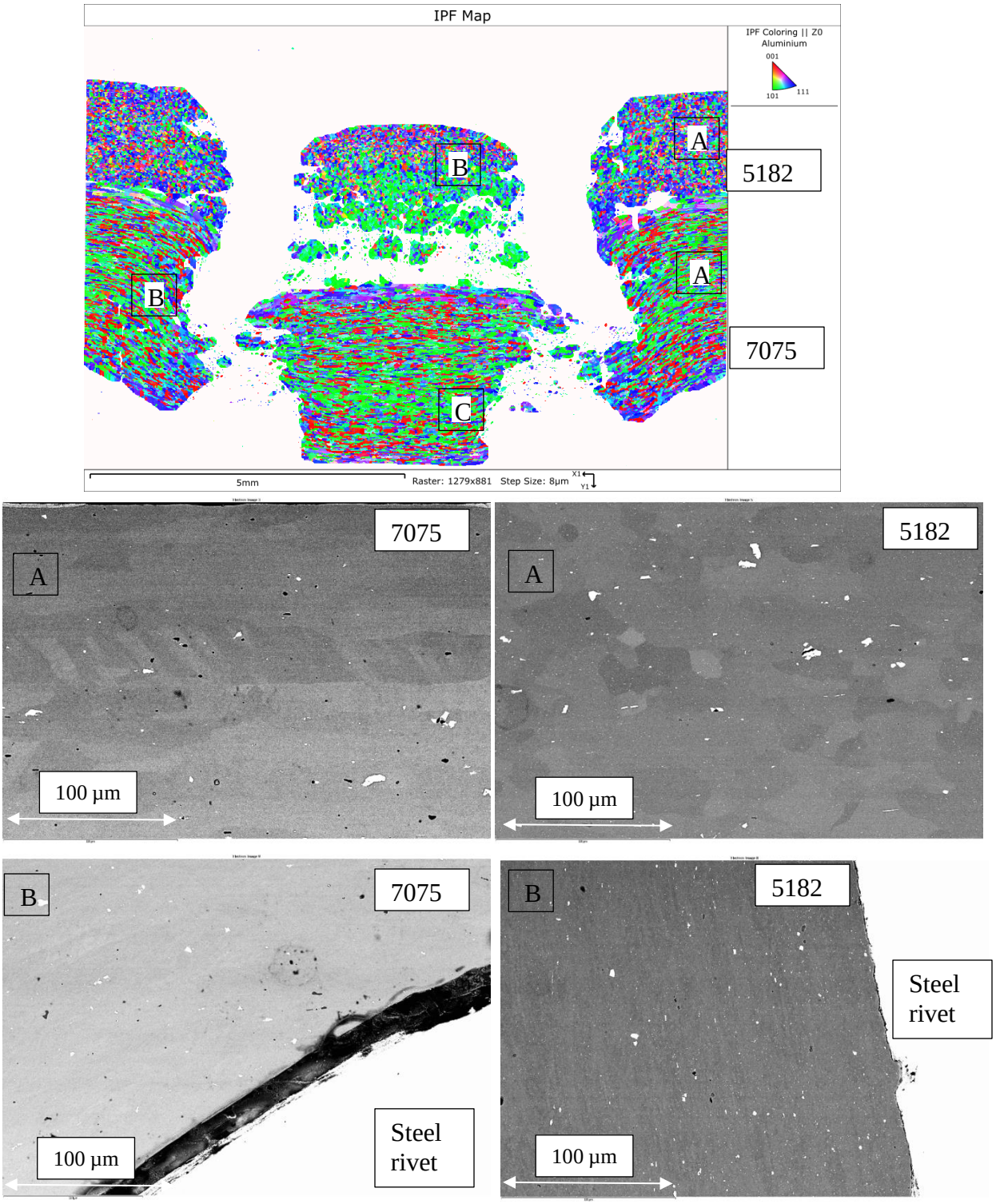

Figure 7-7: SEM - backscattered images of SPR cross section at (A) base metal (B) rivet region (c) button section.

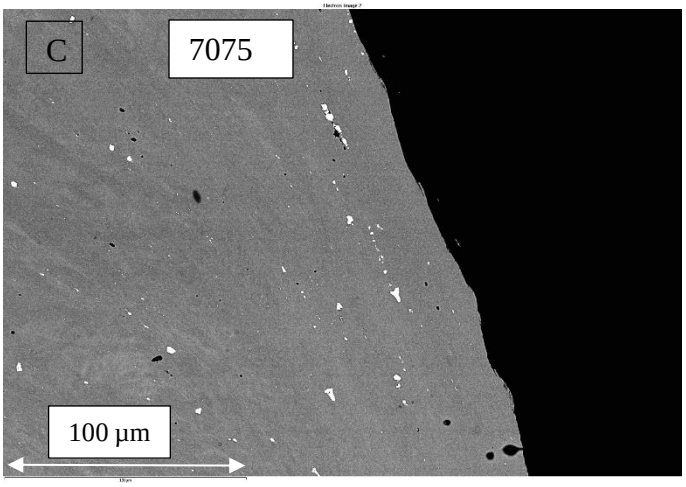

Figure 7-7 continued: SEM - backscattered images of SPR cross section at (A) base metal (B) rivet region (c) button section.

Figure 7-7 shows the SEM BSE images of the SPR joint taken at different spots. With the channeling contrast, we could observe recrystallized grains of different geometry in 7075 (elongated) and 5182 (equiaxed) sections. In the region near the rivet, we could observe the grains stretched along the deformation direction. Similarly, in the button section, we could observe the elongated grains as well.

The mechanical properties of the joints were assessed using the micro-hardness and tensile test. **Figure 7-8** and **Figure 7-9** show the distinct difference between the micro-hardness between the RSW and SPR joints. The base metal hardness values of 7075-T6 and 5182-O temper were 190 HV, and 77 HV respectively. To highlight the hardness variation across different regions, the profile was extracted from the hardness map. In the case of the RSW, the line profile AB corresponds to the hardness variation of the 7075 heat affected zone and compared to the base metal the hardness of heat affected zone decreased by 10%.

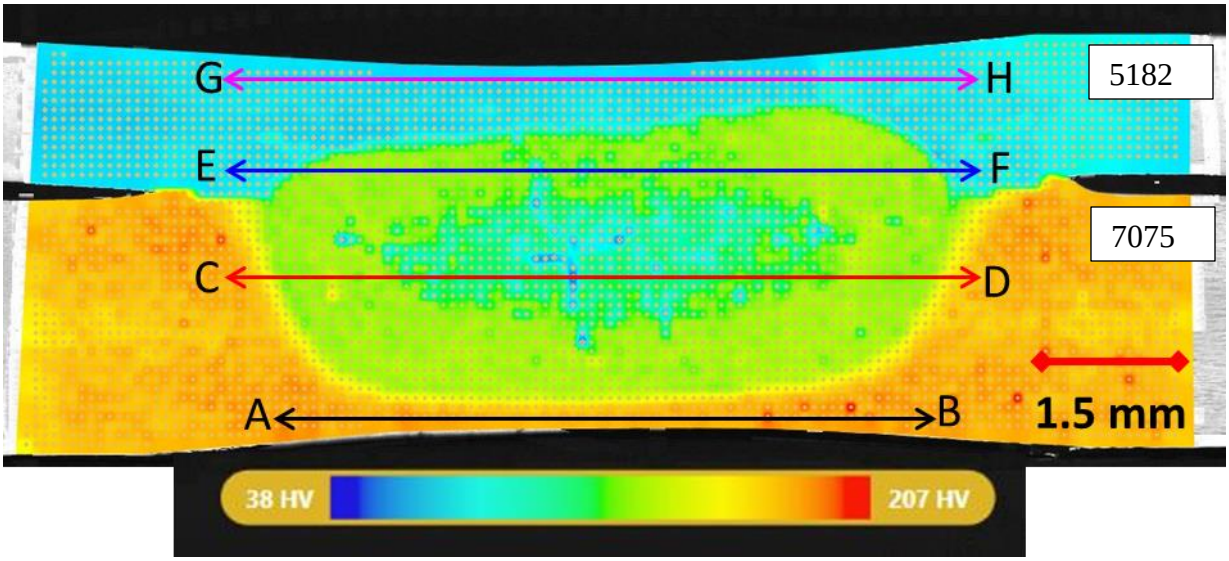

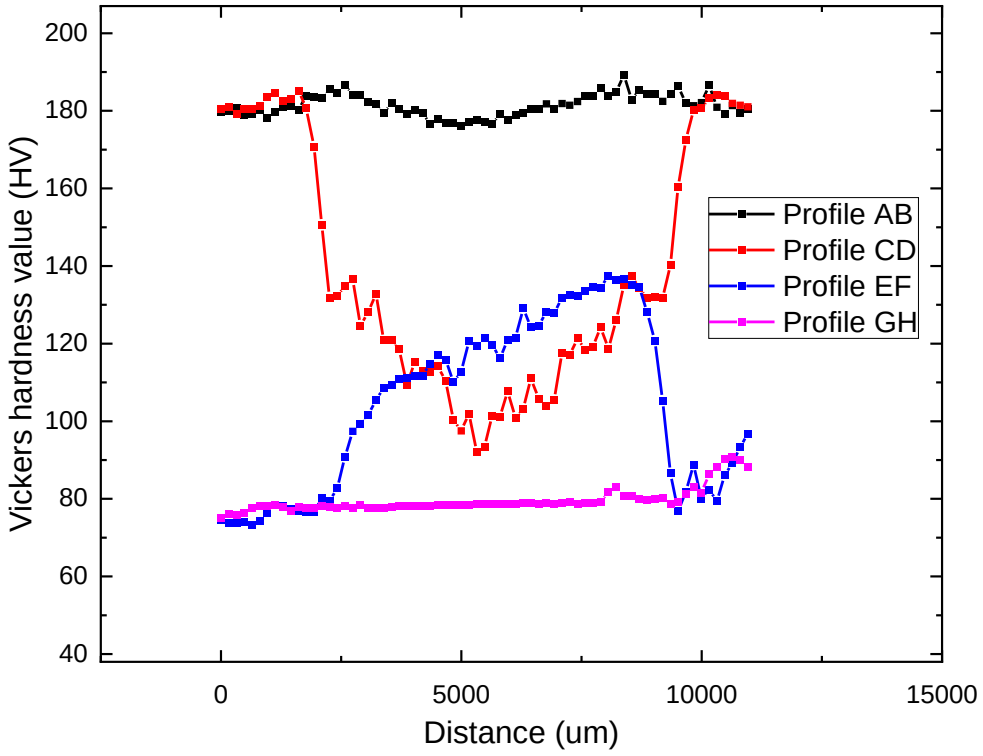

Figure 7-8: Microhardness of RSW joint (top) line profile at specific region (bottom).

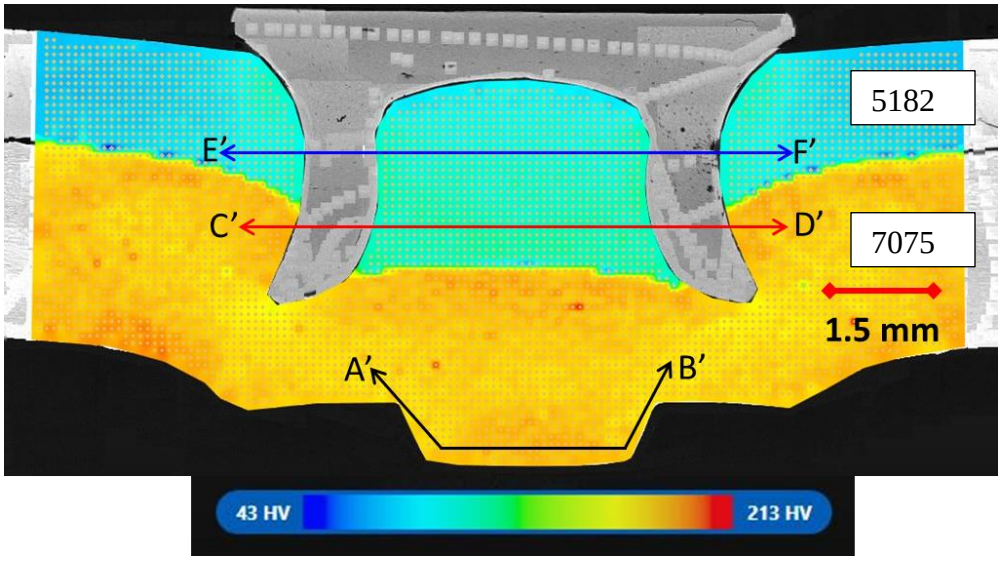

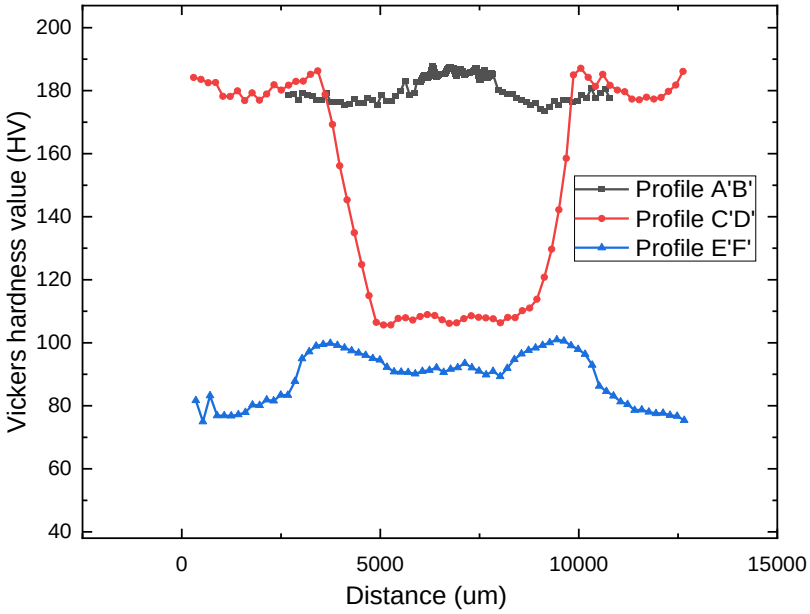

Figure 7-9: Microhardness of SPR joint (top) line profile at specific region (bottom).

However, no such change in hardness was observed in case of the heat affected zone of 5182, as shown in the line profile GH. The columnar and fusion region hardness profile for 7075 was represented by line CD, and we could observe up to 25% drop (140 HV) and 47% drop (100 HV) in hardness value for columnar and fusion region compared to the base metal. Interestingly, the profile (EF) across 5182 columnar region shows an increase in hardness value of 120 HV (55% increase) compared to the base metal.

In case of SPR (**Figure 7-9**), the profile A'B' corresponds to the button section of 7075 and we could observe a slight increase in the hardness value compared to the base metal. Hardness across the joint section interface was depicted by profile C'D', the section containing a high hardness (180 HV) value corresponded to 7075 while the valley section corresponded to 5182 with a hardness value of 100 HV. This value was higher than the 5182 base metal and line profile E'F' highlights this variation.

The strength of the joints was evaluated by the uniaxial tensile test (**Table 7-2)** and we could observe that the strength of the RSW joints was higher than the SPR joints by 30%. We could also notice that the RSW joints had a higher level of scatter compared to SPR joints. The locus of the failure (**Figure 7-10**) for the RSW was along the joint interface. In the case of the SPR joint, the 5182-material adjoining the rivet underwent significant deformation leading to joint failure.

Table 7-2: Maximum strength of the joints from tensile testing.

Sample	Joint strength (N)
RSW	5781 ± 289
SPR	4428 ± 53

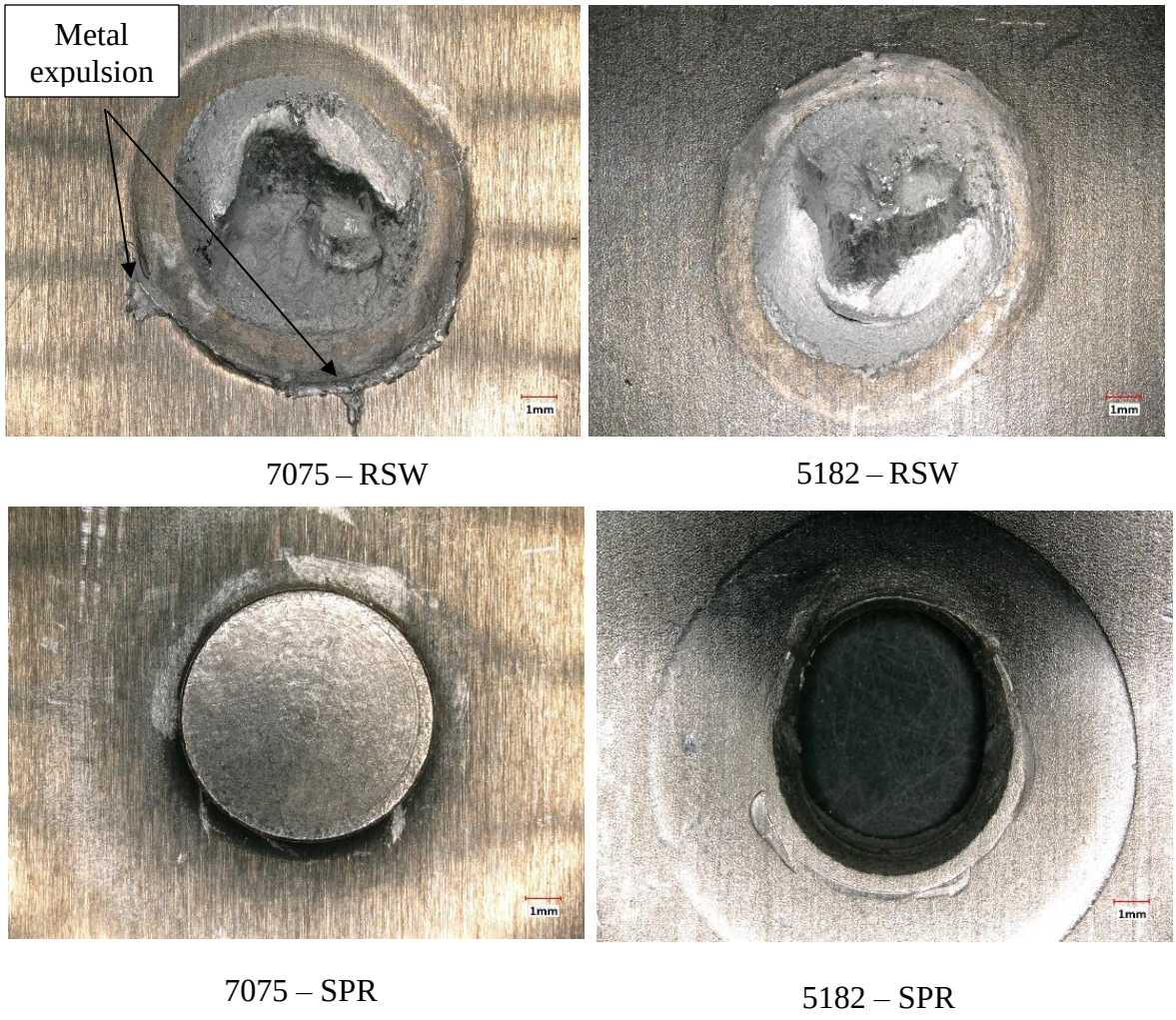

Figure 7-10: Macro images of the joint fracture surface after tensile testing.

7.3.2 Corrosion Testing of joints

Polarization experiments were carried out to assess the impact of the joining method on the corrosion behavior. The experiments were carried out in flat cell at three distinct region. The base metal section pertains to the surface of the sheet that has not undergone any joining method, while the RSW section pertains to the heat-affected zone of the joint. On the other hand, the SPR section corresponds to the button and the steel rivet region of 7075

and 5182, respectively. The 7075 base metal had E_{corr} of -550 mV_{SCE}, while the RSW and SPR sections of 7075 had slightly active E_{corr} of -588 mV_{SCE}. During the anodic sweep (**Figure 7-11**), of the 7075-base metal section, the current initially increased and reached a limiting value at -470 mV_{SCE}. A further increase in potential reached an inflection point beyond which the current increased dramatically. However, both RSW and SPR sections did not exhibit this type of behavior; instead, any increase in potential beyond E_{corr} the current increased logarithmically. The cathodic polarization profile (**Figure 7-12**) profile of the 7075 joint sections looked similar. They exhibited limiting current values over the potential range -700mV_{SCE} to -1200mV_{SCE}, further increase in the potential resulted in sharp increase in current. The 5182 base metal had E_{corr} of -780mV_{SCE} which was more active than the 7075 base metal and their respective joint variants. The anodic polarization behavior (**Figure 7-11**) was similar to that of the 7075 base metal in terms of shape and features. The RSW section of the 5182 had a more positive E_{corr} than the base metal and did not exhibit the passivation breakdown behavior. The current increased logarithmically as the potential was swept in the positive direction. The SPR section of the 5182 joint exhibited similar polarization behavior, but the E_{corr} value was most negative, -1.02 mV_{SCE}. The most striking observation here was the three orders of magnitude increase in dissolution current. Cathodic polarization (**Figure 7-12**) of 5182 sample showed a measurable change in the current value in the region -900mV_{SCE} to -1200mV_{SCE}. The base metal had the lowest current density in this region, followed by the RSW and SPR. In all cases, the shape remained consistent and at high overpotentials, the current values were in a similar order of magnitude.

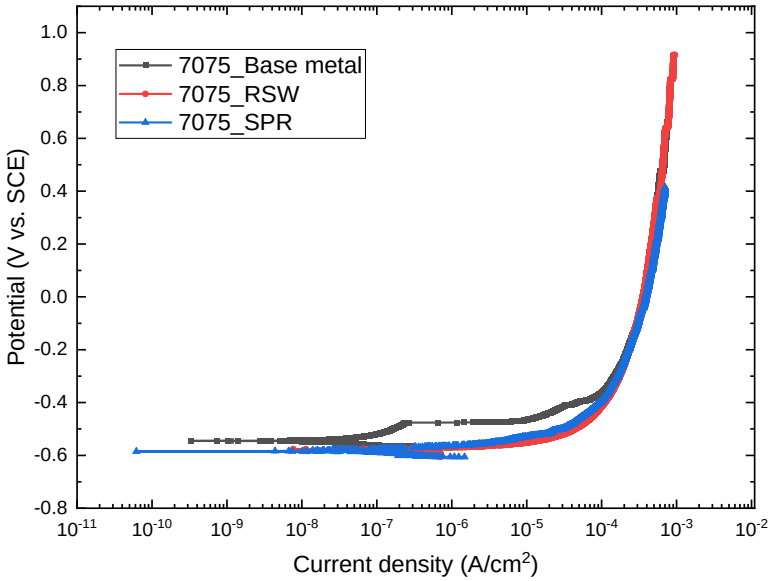

Figure 7-11: Anodic polarization plots of different region of 7075 (Top) and 5182 (bottom) joint section in ASTM D1384 solution.

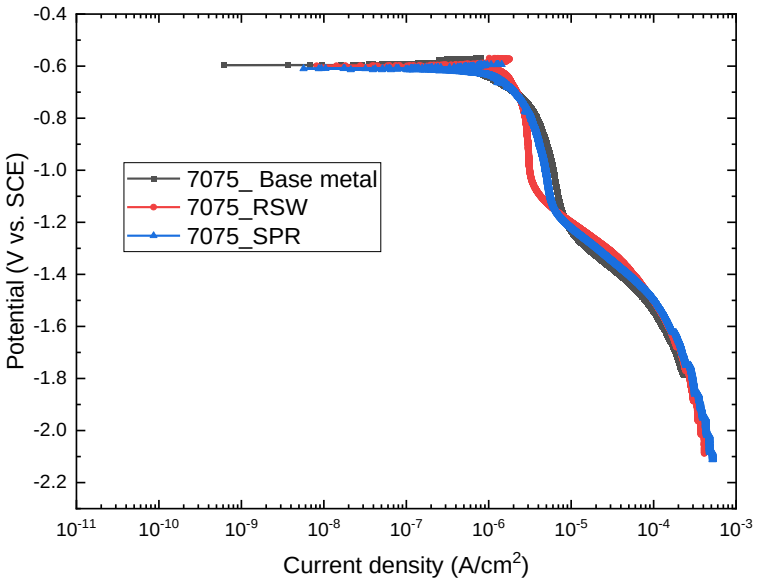

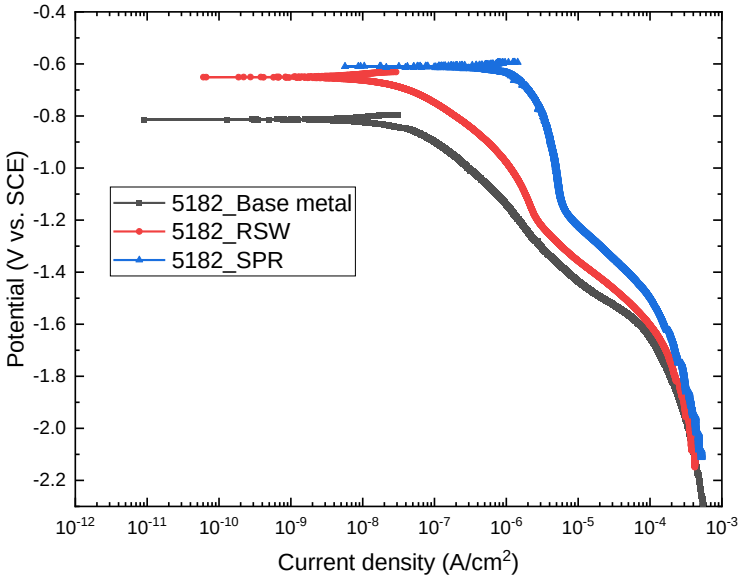

Figure 7-12: Cathodic polarization of different region of 7075 (Top) and 5182 (bottom) joint section in ASTM D1384 solution.

The electrochemical coupling of dissimilar joints was evaluated by zero resistance ammetery (ZRA). **Figure 7-13** shows the galvanic current transients for the different joint couple as a function of time in 3.5% NaCl containing 10% H_2O_2. The current transients of the base metal couple started at -2 µA/cm^2 followed by a peak at +10 µA/cm^2 and finally reached a steady state value of -100 nA/cm^2. The transients for the RSW joints started with a positive value of +100 µA/cm^2 and steadily decreased before stabilizing at +40 nA/cm^2. Interestingly, there were also major differences in the current profile of the SPR joints. The transients started with a very negative value of -300 µA/cm^2 and progressively increased and settled at +100 µA/cm^2.

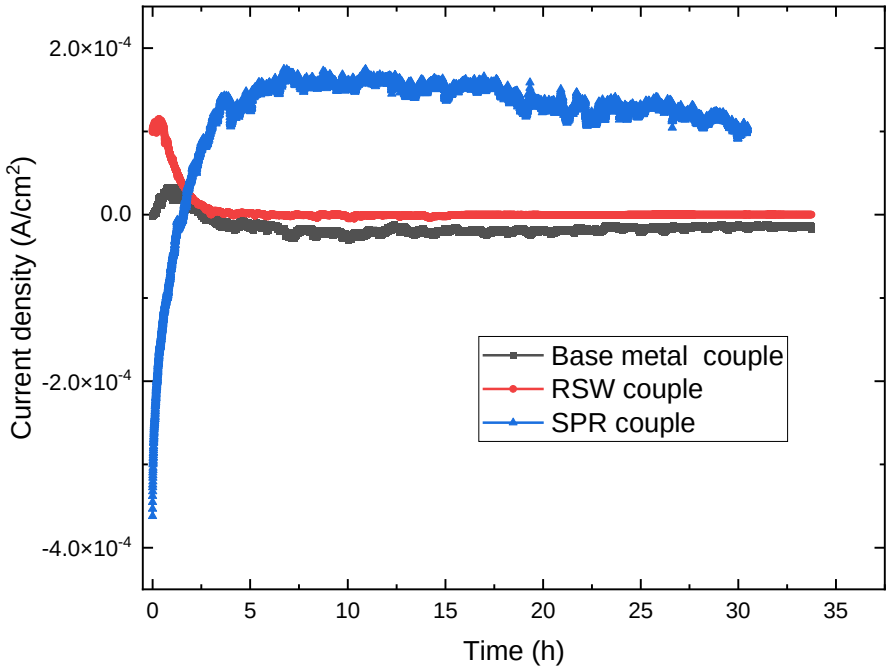

Figure 7-13: Galvanic current transients of joint 7075 and 5182 couple under different configurations.

The SVET measurements provided an overview of the corrosion activity at the local level. In the case of the RSW joints (**Figure 7-14**), the maximum anodic current was measured in the center of the fusion zone during the initial period of immersion.

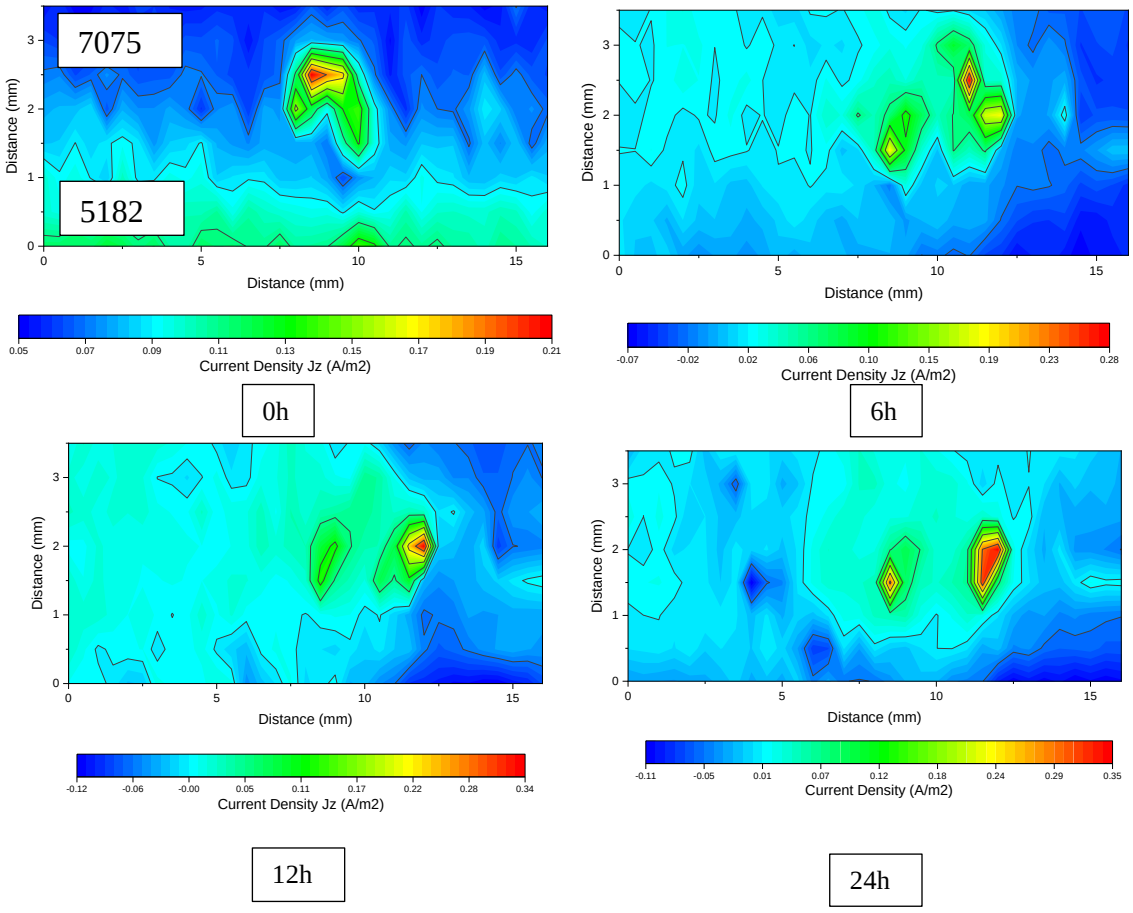

Figure 7-14: SVET current density maps of RSW joint after 0, 6, 12 and 24h of immersion in 0.5 wt% NaCl.

What stands out in this figure was the absence of the cathodic regions in the scanned area, as the recorded current was only positive in value. After six hours of exposure, the activity remained in the fusion zone, but we could observe the emergence of a clearly defined cathodic activity region. The activity in the fusion zone was caused by two distinct corrosion events. Even after 24 h of exposure, the peak current density did not change

significantly. Surprisingly, both the heat affected zone and columnar region did not exhibit any distinct characteristics during the testing period.

The SPR section showed (**Figure 7-15**) strong cathodic activity at the center of the joint during the initial immersion period.

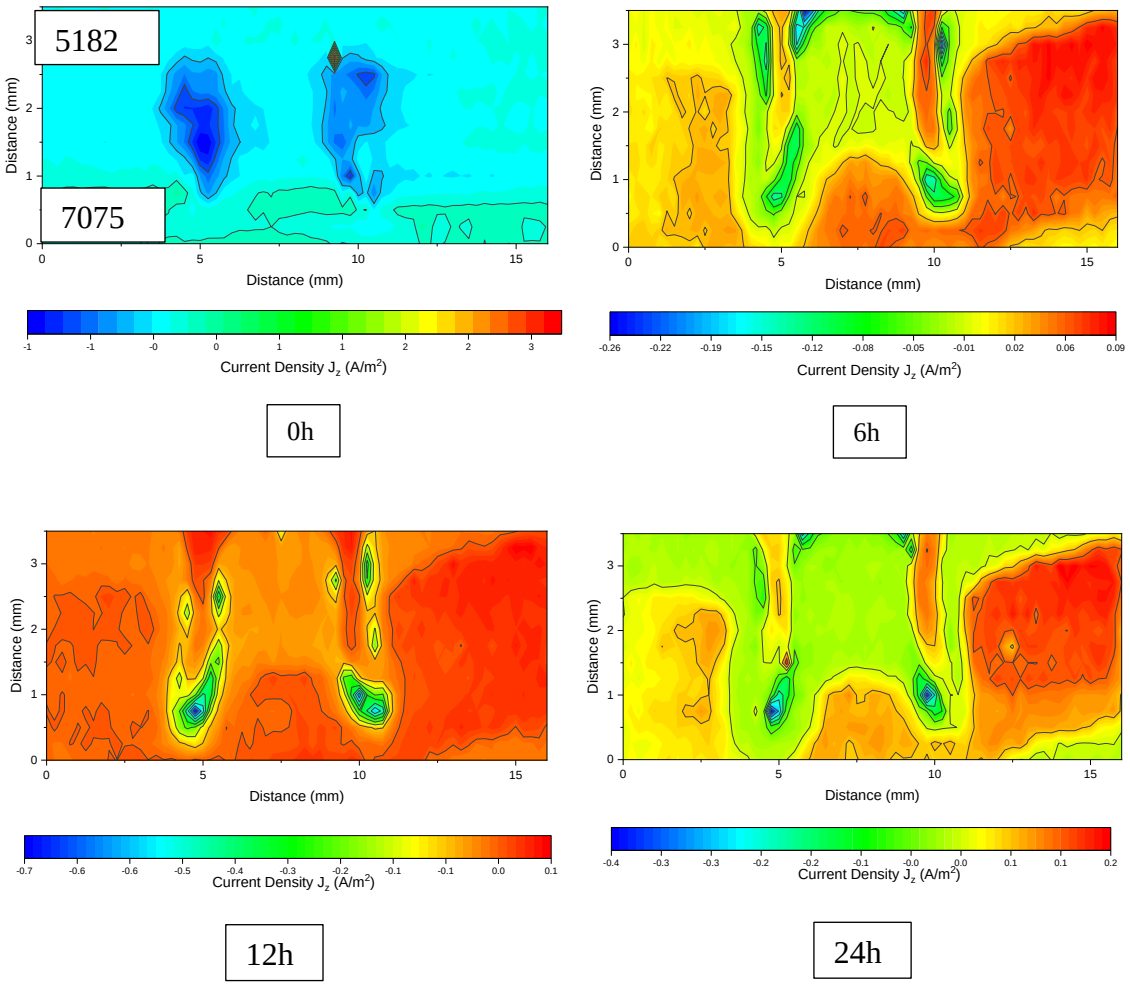

Figure 7-15: SVET current density maps of SPR joint after 0, 6, 12 and 24h of immersion in 0.5 wt% NaCl.

The measured peak anodic current value was almost 10 times higher than the RSW joint for the same exposure period. This peak anodic activity was observed in the 5182 section right next to the steel rivet, but nonetheless, anodic activity was still observed across the 7075 section as well. With the increase in exposure time, cathodic activity was still observed near the steel rivet, but the anodic activity was fluctuating between the adjoining 5182 and 7075 sections. The peak anodic current decreased dramatically after six hours of exposure, and it remained in a similar range for the rest of the exposure period. To quantitatively describe the corrosion activity of the joint cross-section, further analysis was conducted as described below.

First SVET data was separated into two maps, the anodic map, wherein all positive current densities were summed and all current densities in cathodic region are taken as zero. Similarly, in a cathodic map, anodic regions are taken as zero and cathodic regions are marked by negative current densities [176]. **Figure 7-16** shows the total anodic and cathodic current density measured in the SPR and RSW joints in 0.5wt% NaCl solution over the course of 24 h. The anodic current density in RSW was higher compared to that in the SPR section during the initial period of immersion. Interestingly, during the course exposure period, the total current decreased and reached the plateau value 4 A/m^2. Although the current density of the SPR sample started off with a lower value than that of RSW, during the 24h exposure period it continued to increase and ended with an almost two times higher than RSW samples. The cathodic current density profile of the RSW was similar to that of the anodic current density counterpart at a longer exposure time. The trend in cathodic current was particularly surprising in the case of SPR considering that the anodic current transients continued to increase while the cathodic counterpart have started to stabilize.

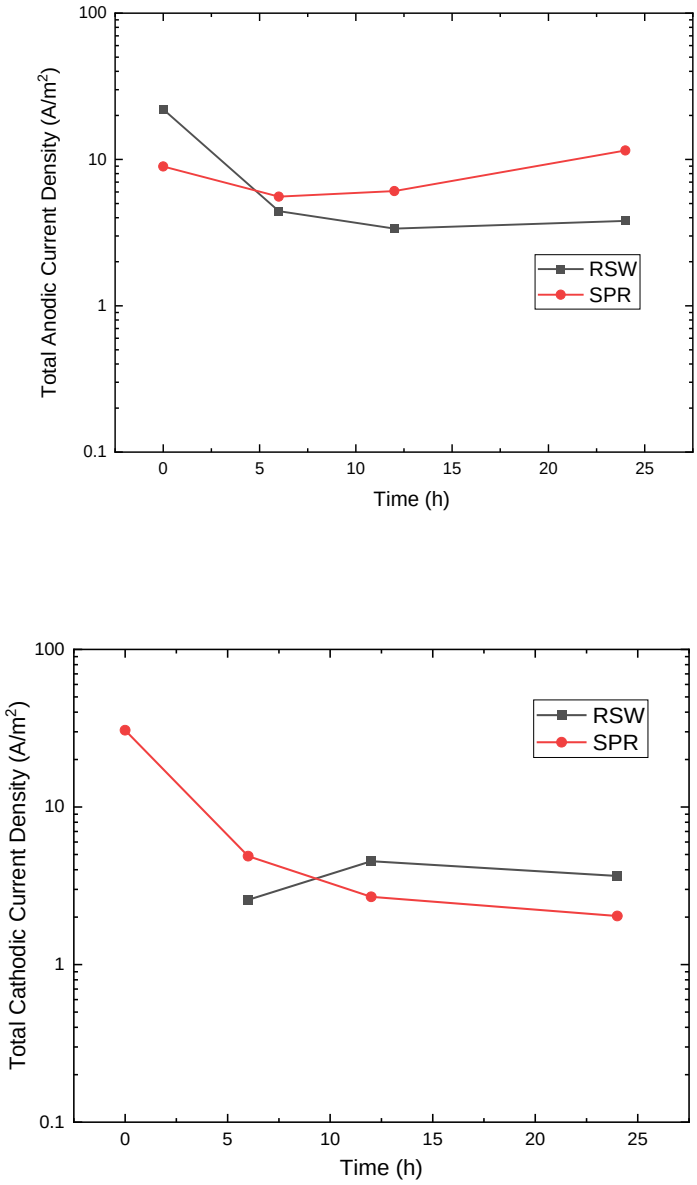

Figure 7-16: Total anodic (top) and cathodic (bottom) densities from the SVET map in 0.5 wt% NaCl.

To determine the morphology of the corrosion attack, ASTM G110 testing was carried out. From the low magnification images (**Figure 7-17**), we could observe that the 7075 section of the RSW joint contained a higher number of corrosion sites compared to the 5182 section. A significant difference in the severity of the corrosion attack was found between

heat affected zone and the base metal of 7075. The former region underwent extensive attack, while the latter remained relatively intact.

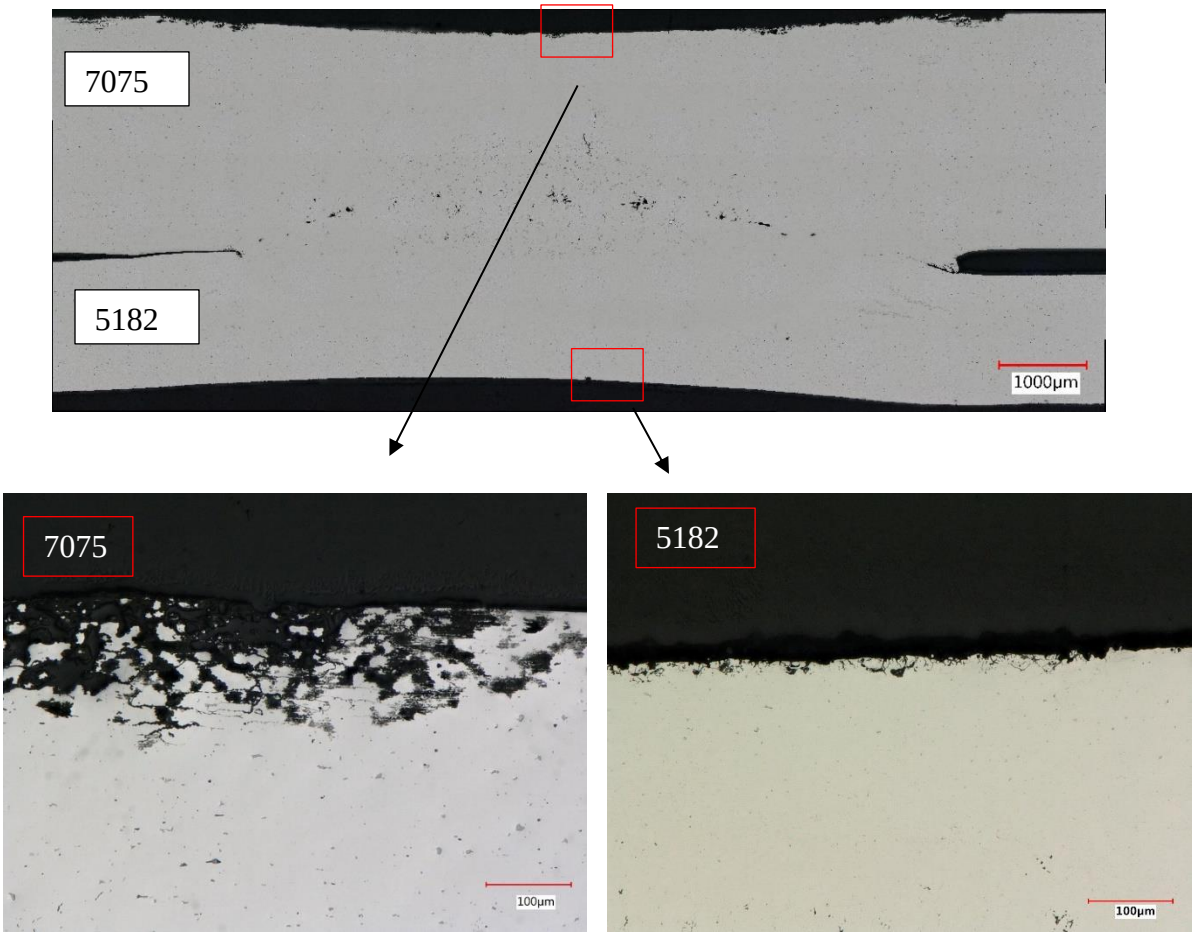

Figure 7-17: Cross of the RSW joint after 24h exposure in ASTM G110.

In the high magnification images, the corroded area had a mixture of pitting corrosion and selective attack of the grain boundaries in the 7075 section. The maximum attack depth was 200 µm. In case of 5182, only a few spots of corrosion attack can be observed in general. Here again, the attack region was mainly restricted to the heat-affected zone

compared to base metal. The attack depth was less than 10 µm, almost 20 times lower than that for the 7075 heat affected zone.

Figure 7-18 shows the SEM images of the 7075 section of the RSW joint to highlight the morphology of the corrosion attack in the heat affected zone. At low magnification, we could observe the corrosion attack propagated in the intergranular mode. Similarly, the high magnification images clearly showed the presence of the continuous precipitates along the grain boundaries. The single most striking observation to emerge from the analysis was the absence of precipitates in the corrosion product.

Unlike RSW, the SPR samples (**Figure 7-19**) did not undergo this degree of corrosion attack. The attack morphology was mostly pitting except in the button section, where 7075 resembled the exfoliation attack morphology. The section near the steel rivet and the 5182 interface did not have any significant corrosion attack.

To assess the effect of residual stress from the joining process on corrosion performance, the samples were exposed to the ASTM G85-A2 cyclic corrosion test over a period of 28 days. **Figure 7-20** shows the residual strength data for the joint samples before and after exposure. After 28 days of exposure, both the SPR and RSW joints showed a decrease in strength values. In the case of RSW joints, the drop was about 8% to 5329 N, while in the case of SPR the drop was 10% to 3996 N. No significant differences were found between the performance of the RSW and SPR joints. From the cross-section images, we could see that 7075 sections underwent significant corrosion attack compared to the 5182 sections irrespective of the joining methods. However, there was a clear difference in attack depth and mode of the 7075 between the joints.

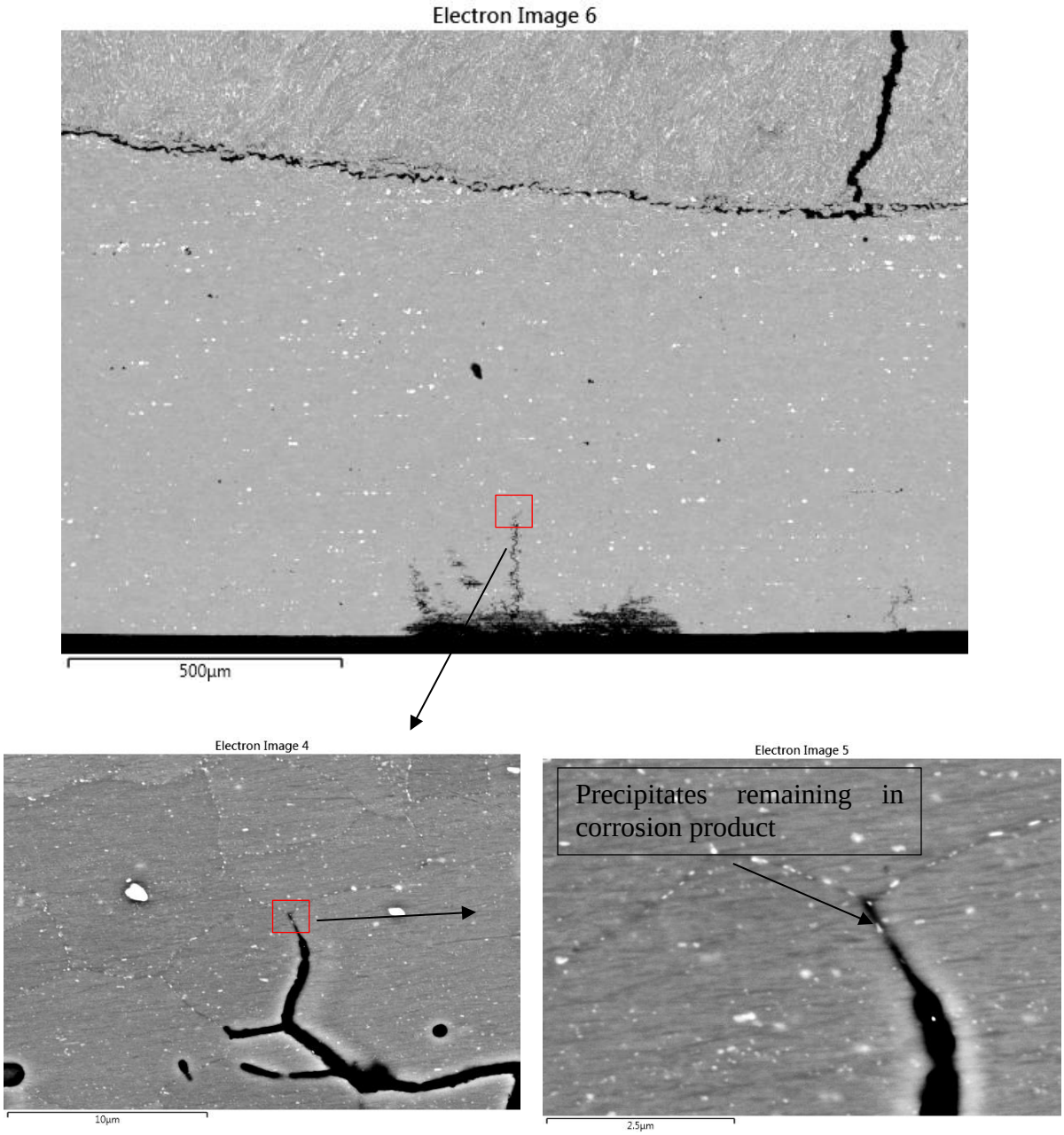

Figure 7-18: SEM-BSE images of the 7075 sections of the RSW joint after 24h immersion in ASTM G110.

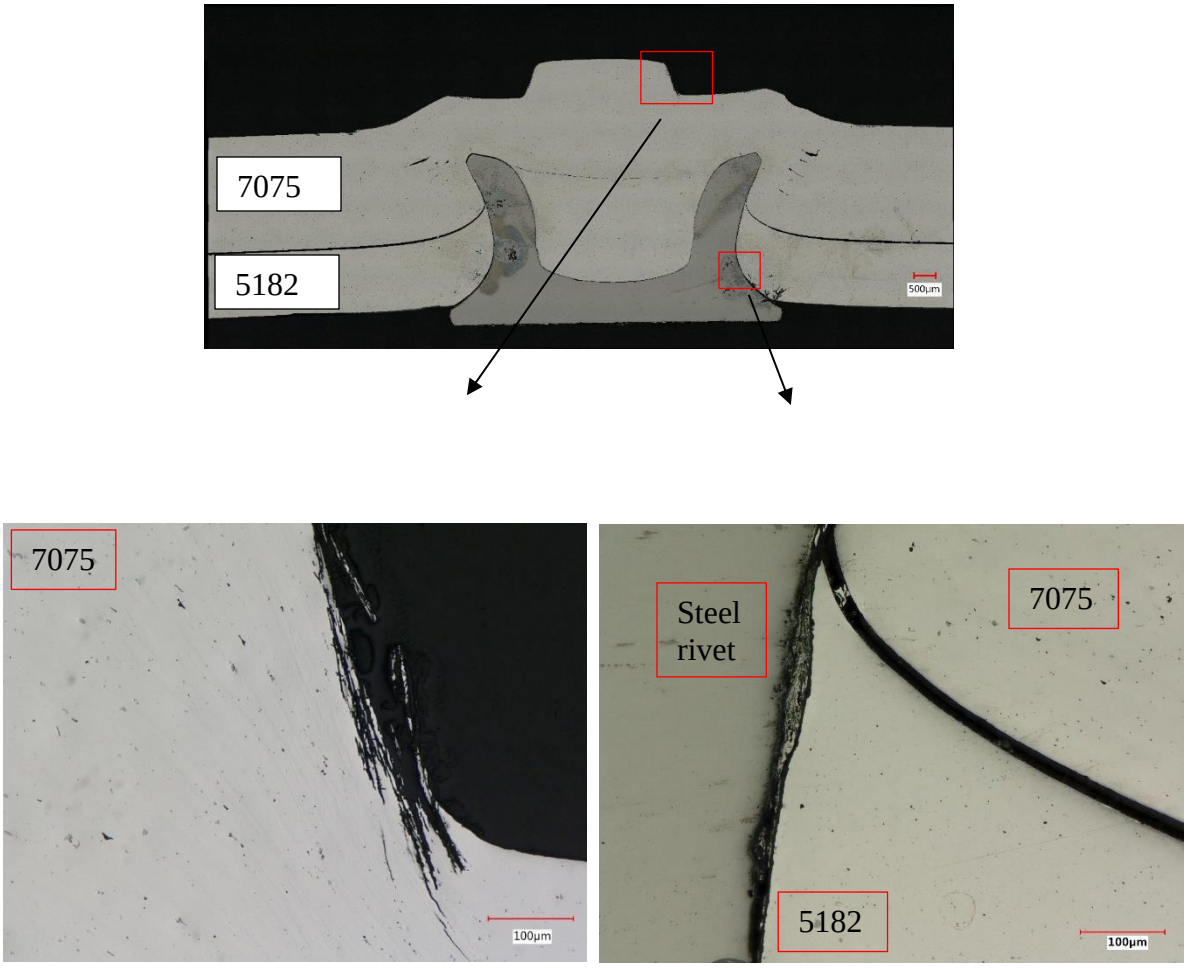

Figure 7-19: Cross section of SPR joint after 24h immersion in ASTM G110.

To illustrate, the SEM images (**Figure 7-21**) of the 7075 sections were taken after exposure. In the RSW joint, the attack occurred in the heat affected zone and the corrosion front propagated along the grain boundaries. On the other hand, in the SPR joints, the 7075 attack was restricted to the button section of the joint. The SEM images showed that the corrosion attack was microstructural pitting happening around the coarse particles.

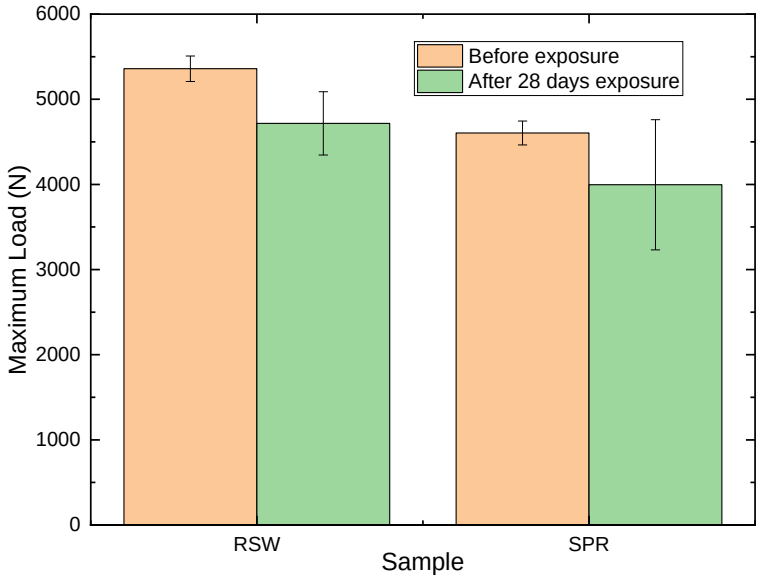

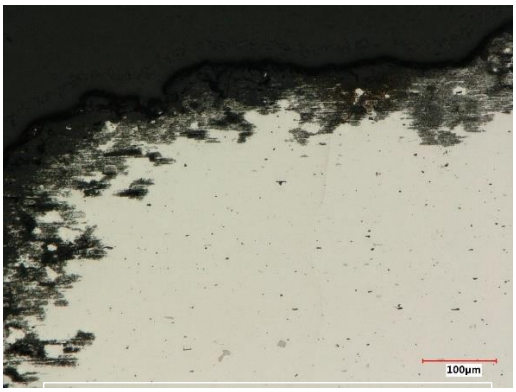

7075 – RSW – heat-affected zone

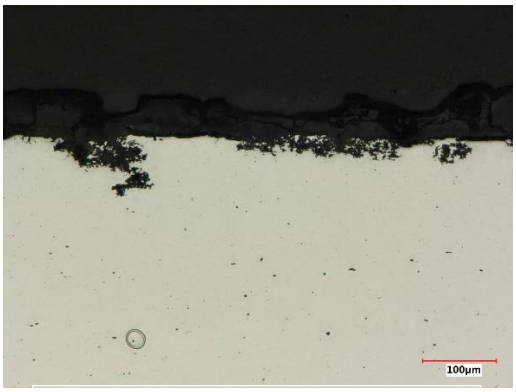

5182 – RSW – heat-affected zone

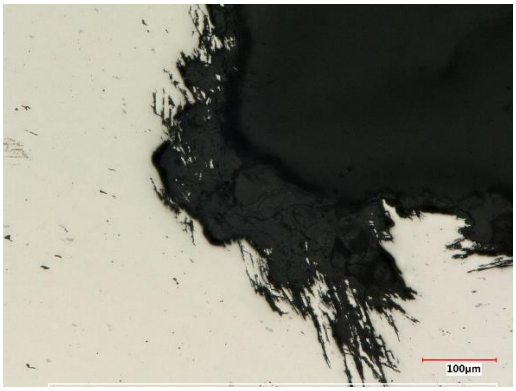

7075 – SPR – button section

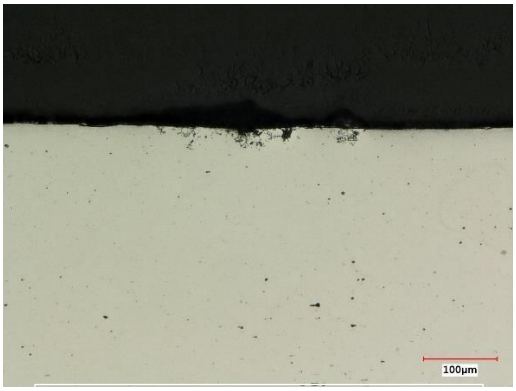

5182 – SPR – near rivet

Figure 7-20: Results from 28 day exposure in ASTM G85-A2 testing without applied stress. Residual joint strength (top), cross section of RSW (middle) and SPR (bottom) joints.

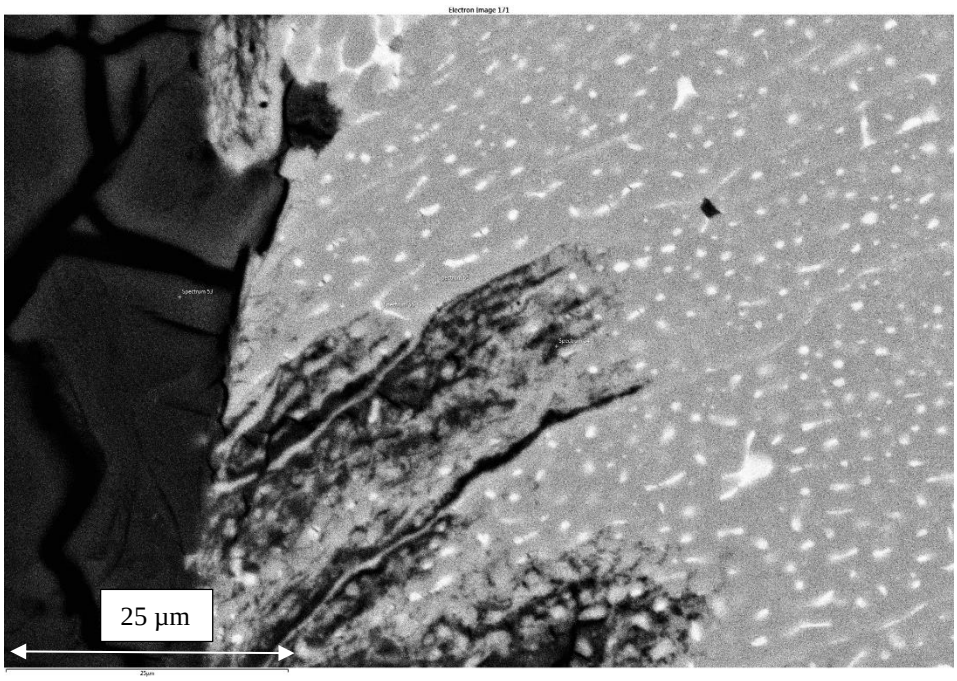

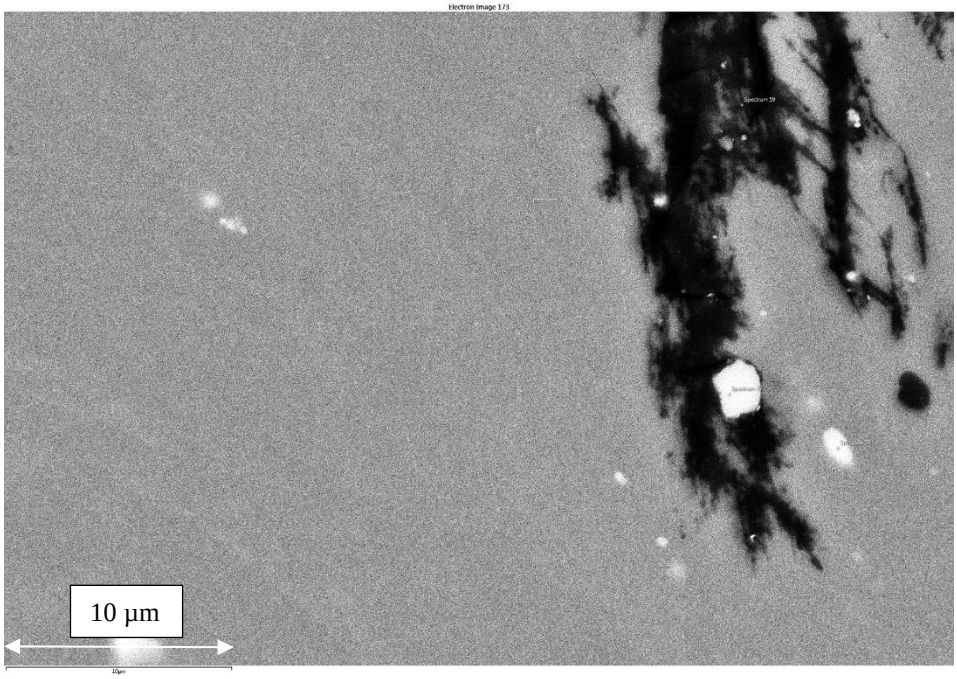

Figure 7-21: SEM-BSE images of the 7075 sample in RSW heat affected zone (top) and SPR button section (bottom) after 28-days exposure in ASTM G85-A2.

Figure 7-22 shows the fracture morphology of the joints before and after exposure to ASTM G85-A2. The RSW preexposure sample failure locus (**Figure 7-10**) was along the weld region between the faying surfaces. The failure mode did not change after 28 days of exposure as it was still occurring along the weld region.

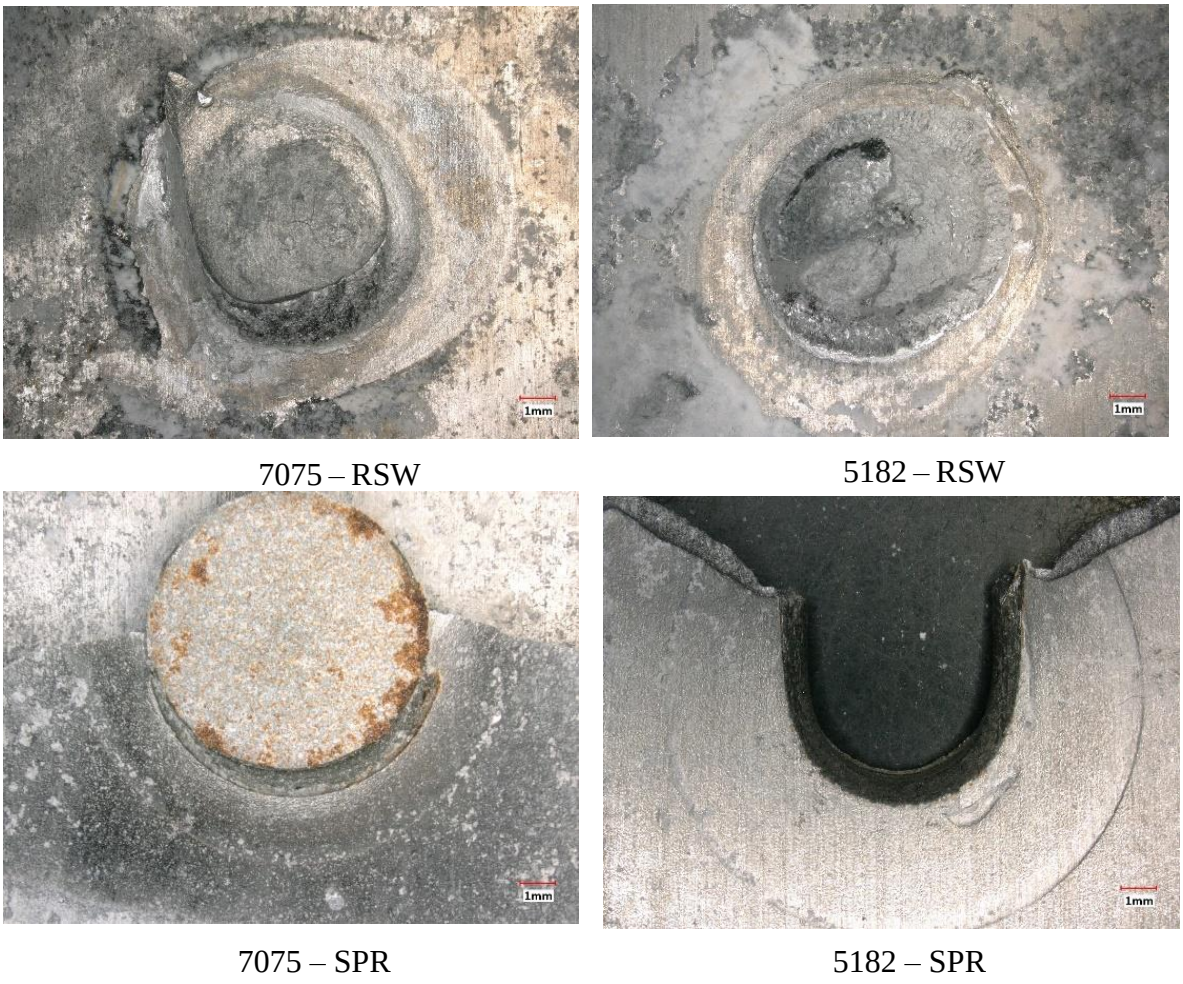

7075 – RSW 5182 – RSW

7075 – SPR 5182 – SPR

Figure 7-22: Macro images of the joint fracture surface after 28 days ASTM G85-A2 test followed by tensile test.

SPR samples exhibited similar fracture behavior as the pre-exposure samples since the 5182 around the rivet region deformed significantly. The breakup of the metal after exposure was due to the excessive mechanical force that was applied to remove 5182. The most striking result that emerged from this work was that the applied stress, 50% of joints peak strength, did not affect the joint corrosion performance. **Figure 7-23** shows the residual strength of the joints before and after corrosion exposure. The cross-section images indicated early signs of the IGC attack in the heat-affected zone of 7075. However, no such corrosion attack was observed in the 5182 section. Similarly, there was no sign of any primary or secondary cracks in the cross-section images. The fracture locus (**Figure 7-24**) after tensile testing was comparable with preexposure as both exhibited interfacial failure in RSW and deformation of the 5182 section around the rivet in SPR. Even with the applied stress, the residual strength of the joint did not decrease after 100 days of exposure. The RSW joints exhibited only a 7% decrease in strength, while the SPR samples did not show any measurable drop in strength. Similarly, macro-images also showed that there was no significant accumulation of the corrosion product after the exposure period. **Figure 7-25** shows the residual strength of the joints after 100 days of exposure in a humid environment and applied stress did not affect the final strength of the joints.

7.4 Discussion

The mode of joining clearly affected the final microstructure of the 7075 to 5182 couple. The fusion welding process resulted in a gradient microstructure with microscale defects. However, the mechanical interlocking methods resulted in a deformed microstructure closer to the rivet areas. Differences in microstructure had an impact on corrosion properties.

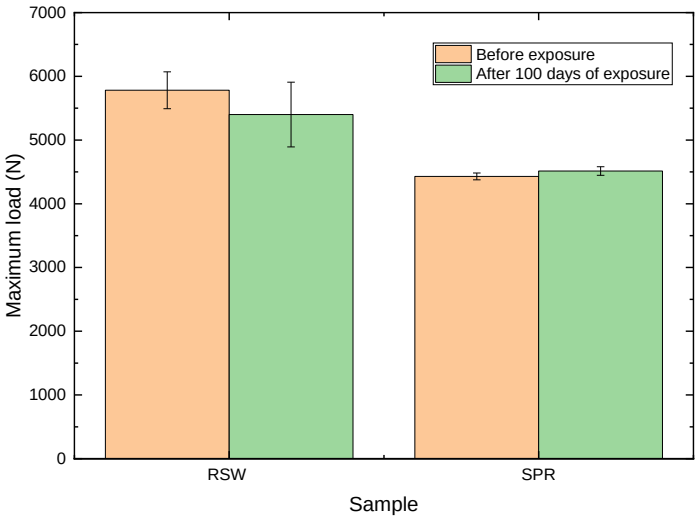

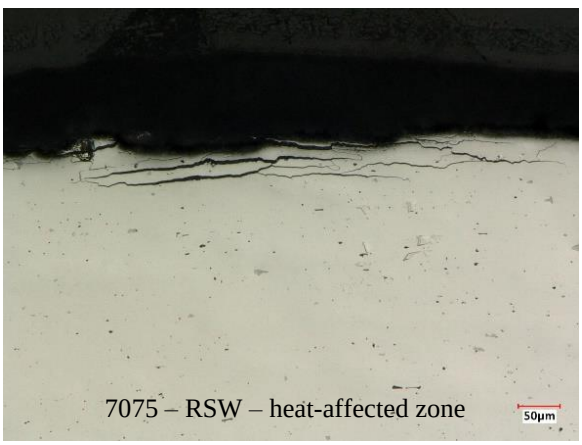

7075 – RSW – heat-affected zone

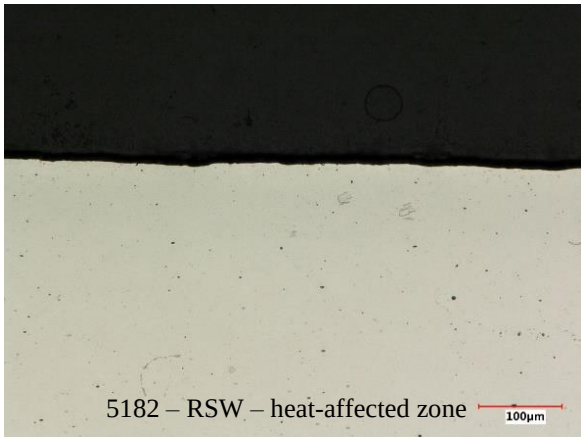

5182 – RSW – heat-affected zone

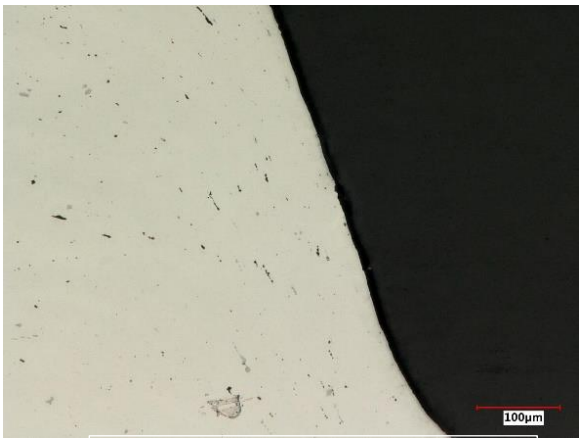

7075 – SPR – button section

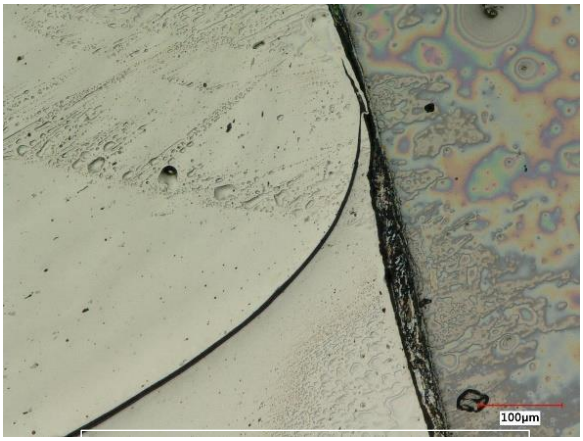

5182 – SPR – near rivet

Figure 7-23: Results from 100 day exposure in cyclic corrosion test cycle with applied stress. Residual joint strength (top), cross section of RSW (middle) and SPR (bottom) joints.

7075 – RSW

5182 – RSW

7075 – SPR

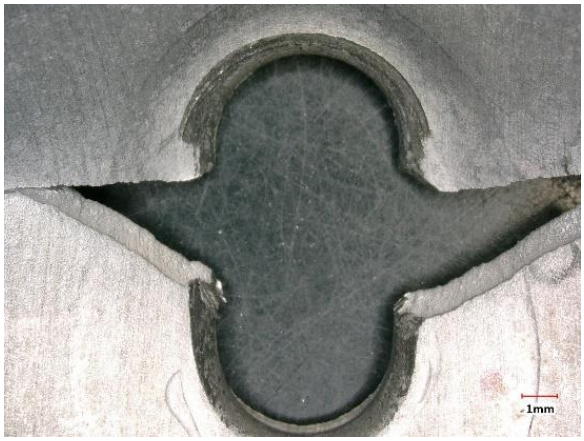

5182 – SPR

Figure 7-24: Macro images of the joint fracture surface after 100 days in cyclic corrosion test with applied stress followed by tensile test.

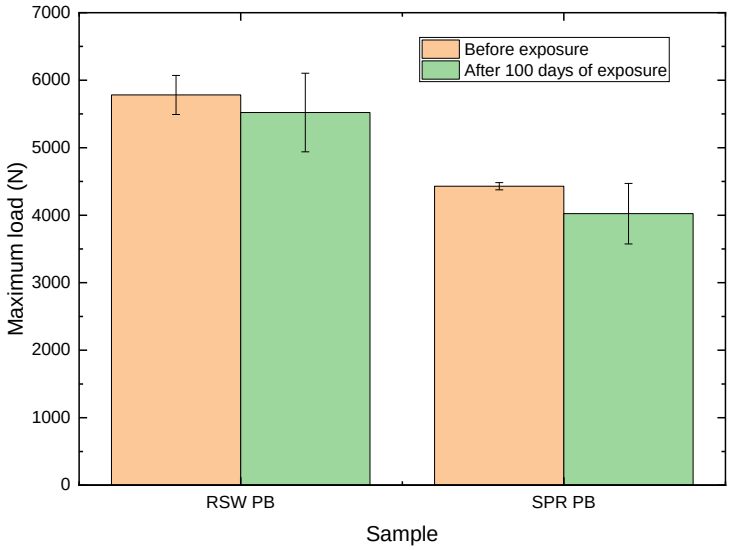

Figure 7-25: Residual strength of the joints before and after 100 days exposure in humid environment with applied stress.

The galvanic couple between the base metal 7075 and 5182 had a different trend in the ZRA data compared to RSW and SPR joint couple. The SVET data highlighted that the fusion zone of the RSW was more active than the heat affected and the base metal. Similarly, the region adjacent to the steel rivet was most active in the SPR joints. Short-term accelerated testing showed that the 7075 alloy underwent IGC in heat affected zone of RSW while the button section of the SPR joint underwent microstructural pitting. The long-term accelerated corrosion and SCC testing did not have any negative impact due to the joining methods.

7.4.1 Microstructural Changes

One of the artifacts of the fusion welding process, such as RSW, is a formation of the gradient microstructure due to the temperature gradient associated with the welding process [177]. The extent of the gradient microstructure depends on the welding parameters and alloy composition [178, 179]. In addition to microstructure variation, fusion welding

processes are known to generate defects. In **Figure 7-1** the plane view images of the joints did not show any visible defects or material transfer from the welding electrode. However, in the cross-section images, we could observe two types of defects, namely pores and cracks in the fusion region.

Pores in the fusion weld are due to the various phenomenon such as shrinkage strain, expulsion and degassing of gaseous hydrogen during weld pool solidification, [180]. In the case of RSW of 7075, the pores are more likely due to expulsion or hydrogen rejection. The ejection of molten metal at the interface of the faying surface due to excessive heat input is called expulsion. This is attributed to the narrow plastic and the large freezing range due to the high solute content. Even the application of forging force/electrode pressure, may not be enough to seal the expanding molten nugget/fusion zone being ejected from the weld region. The macro-images (**Figure 7-10**) of the samples after the tensile tests showed signs of expulsion in 7075 but 5182 did not show such features. Similar results were obtained in the weld schedule development by Dobosy et al [181] for the 1mm thick 7075-T6.

Hydrogen degassing is another potential reason for the formation of pore in the weld pool of the RSW joints. During the heating cycle hydrogen from the moisture trapped in the oxide layer gets dissolved in the interface of the faying surfaces as the nugget is forming. However, as the molten weld pool begins to solidify, hydrogen comes out of the solution in the form of gas bubbles that get trapped resulting in porosity. Several authors [182, 183] [81] have reported pore formation solely to hydrogen not only in RSW but also in other fabrication methods, such as the selective laser melting process, as they did not observe any evidence of expulsion. Based on the experimental evidence (**Figure 7-10**) and

literature data, we attribute the pores to the combination of hydrogen and expulsion mechanisms.

The second type of defect observed in the fusion regions is the cracks. These cracks are associated with rapid solidification of the weld nugget. They are generally perpendicular to the faying surfaces and are caused due to the non-uniform stress and strain fields during welding sequence. During the heating stage, under the combined action of the applied electrode force and heat input, the center of the welding area is under compressive stress. Due to rapid cooling of the weld region, the stress state changes to tensile, the contraction rate that translates to stress magnitude is highest along the direction parallel to the faying surfaces. The high solute level of 7075 could have exacerbated the cracking. These results are in line with those of Li et al. [184] who reported hot cracking in the nuggets of 6061 to 7075 consistently across all the welding parameters. However, the degree of cracking in the present work is not as extensive reported in the literature. This may be the result of differences in welding schedule, as the one used in this work allows control cooling to minimize thermal stress, and the addition of forging force facilitate the closing of some of these defects. These results imply that weld defects cannot be completely eliminated, and this could explain the higher scatter in the joint strength of RSW (**Table 7-2**). These findings might not be representative of all types of 7075 welding combinations.

The SPR joints (**Figure 7-1**) were free of microscopic defects such as cracks and pores. This could be due to a couple of factors. The first is the absence of any heat input or generation during the process of joining, and the second could be due to the stack configuration. The softer 5182 on the top provides an easy access of the rivet into the material during the piercing stage and enabling flow of the 7075 in the button section.

These findings confirm those of an earlier study by Kim et al. [185] on SPR of 7075 and 5052. These results need to be interpreted with caution, because the design and geometry of the rivet and die play a vital role in achieving defect-free SPR joints of 7075 in T6 temper.

Figure 7-2 shows the gradient grain structure of the RSW joints. The base metal is the reference region that is not affected by the thermo mechanical process during the welding sequence. The solution heat treatment and annealing process have resulted in fully recrystallized grains in 7075 and 5182 respectively. The fusion zone of the weld contains grain with smallest size, this is due to the rapid cooling of the molten metal at the end of the welding sequence. The adjacent columnar region had an elongated grain structure, and this indicates that the region has experienced significant grain growth compared to the base metal. Theoretical work in the literature [186] had predicted the temperature to 450° C, which is higher than the typical recrystallization temperature of aluminum. Since the grains in these regions are already recrystallized, this high temperature facilitates the grain growth. The ratio of the temperature gradient (G) and growth rate (R) have been reported to determine the area ratio of the fusion zone to the columnar region. The present results indicate that the welding conditions occurred at mid G/R value, due to lower area ratio fusion zone to columnar region [187]. The heat affected zone closer to the weld electrode has not shown any changes in the grain size, and this could be due to the low heat input and contact with the water-cooled electrode tip. The results are in line with the data in the literature [188], where the RSW microstructure had a gradient grain structure regardless of the faying alloy chemistry.

The RSW process appears to have affected the grain boundary misorientation angle of the columnar and fusion zone. As shown in **Figure 7-2**, the density of the low angle grain boundaries was higher in the columnar zone; this could be due to the dynamic recovery mechanism. The high stacking fault energy of aluminum and its alloys typically favors dynamic recovery during hot deformation [189]. The plastic deformation of the applied forging force and high temperature during welding could have facilitated the motion of the dislocation leading to formation of a large number of subgrains with low-angle intergranular boundaries. In the fusion zone, the phenomenon of continuous recrystallization could have led to the formation of equiaxed and high angle grain boundaries as a result of rapid solidification of the melt pool. Similar results of the misorientation angle were obtained in the fusion and columnar zones in other joining methods such as ultrasonic spot welding [190], friction stir spot welding [48], friction stir processing [191] of 7xxx series aluminum alloys.

The welding process has also resulted in the formation of residual strain in joint sections. LAM maps could qualitatively indicate the deformation-induced local orientation gradients within grains, they have a unique linear correlation with the true plastic strain and can be an appropriate parameter for evaluating local plastic deformation [192]. The high strain areas in heat affected zone of the 7075 and 5182 could be attributed to the applied forging force during the welding sequence. Similarly, the reason for the high strain at the interface of the columnar region and the base metal adjoining the faying surfaces could be due to the warpage from thermal stress due to thickness difference between the 7075 and 5182. These results are in line with data from the literature in which higher residual stresses are observed after spot welding of aluminum [193-195]. Similarly, the work on 6061-T6 spot welded

joints showed that residual stresses, measured by the neutron diffraction method, are highest in the center of the fusion zone and decrease as we move away from this region [196]. Although the results need to be interpreted with care because the residual strain measured here is qualitative, however the data from present work clearly highlight the localized strain variation. The data from these literatures also indicate that the residual stress could be as the high as yield stress of material in the localized region and so they might be sufficient to initiate corrosion cracking.

The presence of low-angle grain boundaries is generally considered beneficial for higher IGC resistance. However, the high temperature and the subsequent nonequilibrium cooling process have huge impact on the precipitation of the solute elements along the grain boundaries, negating the influence of the misorientation angle. Similarly, these unique microstructural features are observed in the weld interior, but the corrosion attack generally begins from the heat affected zone that already has an unfavorable precipitate microstructure on the grain boundaries.

Figure 7-4 shows that in addition to the changes in grain size there is clear difference in the presence of second phase particles in the weld region. Although fully recrystallized, the fusion zone resembles as cast microstructure [197, 198]. The grain boundaries of this area are decorated with a high level of solute elements. The composition of these phases is closer to $Mg(Zn,Cu,Al)_2$ and AlMgCuZn types [199]. The grain interior appears to be free of any precipitation despite the addition of the paint bake temperature simulation. This could be due to either the fine precipitates not visible under the SEM or lack of the solute elements in the matrix to initiate precipitation, since there is heavy solute elements segregation on the grain boundaries. The fusion zone experiences the highest temperature

(up to 600 ° C) during the welding sequence [186]. Under these conditions, both 7075 and 5182 undergoes melting and once welding current is stopped, the rapid cooling in these regions freezes the microstructure in the as-cast state. The columnar region contains a similar type of feature, including the solute segregation in the grain boundaries. This indicates that in addition to the grain growth, the higher temperature was able to redissolve the precipitates in the matrix and leading to solute segregation during the slower quench. Interestingly, the results reveal that the heat affected zone, which did not show any changes in the EBSD analysis, had a distinct microstructure compared to the base metal region. The temperature in this region could reach up to 300° C, accelerated the coarsening of the matrix precipitates (**Figure 7-5** and **Figure 7-6**) in the grain interior and while the grain boundaries have the continuous presence of the precipitates. The composition of the grain boundary precipitates is equivalent to $Mg(CuZnAl)_2$ phase [199].

The SPR joints did not show any of these microstructural characteristics. The channeling contrast SEM images **Figure 7-7** agree well with the EBSD data (**Figure 7-3**) confirming that the deformations near the rivet and button region resulted in a change in grain shape but not in precipitate size, continuity etc. The strain localization for 5182 is concentrated mainly under the rivet head and along the side walls of the rivet. The 5182 sheet was joined in the fully annealed O-temper state and the strain localization could be due to strain hardening. In case of 7075, the strain localization was observed in the button region specifically at die interface. These localization phenomena could affect the hardness of the material locally.

In both joint types, the hardness of the base metal (**Figure 7-8** and **Figure 7-9**) are comparable and this indicates that the region did not undergo major changes in the

microstructure. 7075 is a heat treatable class of aluminum alloys, and the strengthening comes from the precipitation hardening mechanism. Any changes in microhardness could be directly correlated with changes in strengthening precipitate size and distribution of the strengthening precipitate. The hardness of the heat affected zone is lower than that of the base metal. From the SEM (**Figure 7-4**) images we could observe that the microstructure had coarsened the precipitates and these changes could have impacted the hardness value in this region. The columnar region had a lower hardness than the heat-affected zone but higher than the fusion zone. SEM images for the columnar region showed the presence of solute segregation along the grain boundary, but the interior is relatively free of precipitates. With the data from the hardness measurements, we could attribute the presence of coarsened precipitates in the grain interior, and due to the magnification limitation, we are not able to observe the remaining particles. The fusion zone was the softest region of the weld due to several compounding effects. The typical cast microstructure of the nugget, with interconnected eutectics formed during post-weld solidification, might not support as much load as the base metal [200].

On the other hand, 5182 is a non-heat treatable aluminum alloy and its strength mainly from the solid solution strengthening or strain hardening, depending on the application temper [201]. As mentioned previously, 5182 used in this work were in fully annealed O-temper. The heat-affected zone did not show any dramatic change despite the presence of residual strain, as indicated by the EBSD LAM maps (**Figure 7-3**). SEM images confirmed the presence of grain boundary precipitates but the lack of change in hardness indicates that the Mg content in the solid solution did not change dramatically in the heat-affected zone. The columnar section in the 5182 not only had a microstructure similar to that of the

7075 but also the same mechanical properties. This confirms the formation of a metallurgical bond at the interface of the joint section. Similar observations have been reported in the RSW of 5052-O to 6014-T4, where the columnar and fusion zone had similar mechanical properties in the 5052 and 6014 sections [202].

In case of the variation in the hardness of the SPR joint (**Figure 7-9**), the softest region corresponds to the 5182 section and the hardness drops from 180 HV to 107 HV as we profile across the joint. Since there were no major microstructural changes, the difference in variation is mainly due to the base material. Interestingly, there are a couple of sections, where the accumulated plastic strain from the joining process affects the hardness value. In the profile A'B' we can observe the effect of strain hardening on the bottom button section of the 7075, the region corresponding to the high strain accumulation in LAM maps (**Figure 7-3**) has higher hardness relative to the base material. Similar variation could be observed in 5182 section in the profile E'F'. These results confirm that the mechanical joining process still leads to minor variations in the microstructure leading to strain accumulation and a corresponding change in the mechanical properties. These results are in line with those obtained by Moraes et al. [203] work on the SPR joining of aluminum alloy 6082-T4 to as cast magnesium alloy AM 60B, where they observed a significant accumulation of plastic deformation that led to an increase in aluminum sheet hardness near the button section. The location of the fracture (**Figure 7-10**) during the uniaxial test is consistent with the hardness map. The RSW joint failed along the interface (fusion zone) and the SPR joints failed around the 5182 hole, since both had lowest hardness in the joint section.

7.4.2 Impact on Corrosion Performance

The microstructure changes observed in the previous section not only affect the mechanical properties but also impact corrosion performance as well. Gradient microstructure changes and the residual stress are prime sources not only initiating corrosion but also for enabling stress corrosion cracking (SCC) failure under certain conditions. The polarization plot in **Figure 7-11** clearly demonstrates the impact of the joining process on the electrochemical properties. The 7075 base metal samples exhibit distinct passivation breakdown behavior; however, both heat affected zone of the RSW section and button section of the SPR exhibits active dissolution. The reason for this behavior could be associated with the localized change in microstructure and strain accumulation, respectively. In case of RSW, the heat affected zone contains coarsened precipitates (**Figure 7-5**), and this indicates that the level of the solute such as Mg, Cu in the matrix had decreased in this region. This in turn decreased the breakdown potential, leading to active dissolution [204]. However, the button section of the SPR did not show any sign of particle coarsening but the EBSD LAM map (**Figure 7-3**) clearly showed the presence of residual stress. The accumulation of residual stress has been shown to decrease the pitting potential due to changes in passivation behavior [205, 206]. Interestingly, these results are not in line with those of the authors who found that residual stresses improved corrosion behavior in 7075 and other aluminum alloys [207-209]. In these studies, the stress measured in the samples was compressive in nature. However, the microstructure in the button section clearly shows features related to deformation due to tensile stress. The cathodic polarization (**Figure 7-12**) did not show any changes, indicating that the anodic reactions are responsible for the observed changes. These results imply that both the mechanical joining and the fusion welding sequence could clearly affect the localized corrosion resistance of the 7075.

5182 also exhibited a similar type of shift in the anodic polarization behavior (**Figure 7-11**). The heat-affected section of RSW exhibited active dissolution while the base metal exhibited passivation behavior because of the shifting of free corrosion potential in the noble direction. Even in cathodic polarization (**Figure 7-12**), there is a marked increase in the oxygen reduction limiting current compared to the base metal. This behavior could be attributed to the presence of Cu particles that were transferred from the welding electrode [210, 211]. The other potential reason could be sensitization of the heat affects zone. The SEM images of this section (**Figure 7-6**) showed precipitation of AlMg particles along the grain boundary, indicating signs of sensitization and it has been documented in the literature that sensitized 5xxx alloys results in reduced pitting potential [212] [213]. The rivet section of the 5182 SPR joint exhibited active dissolution and a significant increase in the oxygen reduction current density. The changes are mainly related to the presence of the steel rivet rather than 5182 as the latter covers 50% of the exposed area. The electrochemical behavior of the individual section has highlighted the impact of the joining process. During in service conditions, this localized behavior could impact the overall galvanic corrosion resistance of the joints.

Figure 7-13 shows the signature galvanic corrosion transients for the different couple. In the base metal configuration, the current flow was negative for the 7075-T6. This implies that the 5182 is more active and acts as an anode in this couple. The initial increase in the current transients in positive direction indicates that the 7075 surface is more active than 5182. This could be due to the presence of deformed layers near the surface (NSM) layers. The current later decreases to reach a plateau negative current. This indicates that when the active layers in 7075 had been consumed and the high Mg content of 5182 could make it

more active. The RSW couple galvanic current is opposite to the base metal and this indicates that the welding schedule has modified the electrochemical activity. The large positive current value could be an indication of the shift in composition of the NSM layers and particularly making the 7075-T6 surface is more active than 5182. Over the period of immersion, the current decreases and reaches steady state positive value of 100 nA/cm^2, indicating that the changes are significant only on the surface. The SPR transients are by far the most interesting trend. The initial deep negative value indicates a stronger galvanic couple between the steel rivet and 7075. The subsequent increase in the current value could be due to the dissolution of the Zn-Sn-Al protection layer of the steel rivets [214]. The transition from negative to positive current indicates the shift in electrochemical activity. This could be due to the coupling of the steel. The present results imply that even though the RSW has a significant change in microstructure, the resulting macro galvanic coupling is much weaker than the SPR joints.

SVET data provide an overview of the localized corrosion activity of the joint cross section arising from the galvanic effect. The joint corrosion activity of RSW (**Figure 7-14**) was mainly restricted to the center of the fusion zone, this could be due to the presence of coarse solute rich phases. As seen in the SEM images (**Figure 7-4**), this region resembles an as-cast microstructure with severe segregation solute phases such as Mg, Zn etc. The phases are anodic to the matrix and, as a result, undergo dissolution when exposed to saline solution [215, 216]. The adjoining columnar region also contains similar phases, but the phases in the fusion zone are coarser, resulting in higher measurable activity during SVET scans. Similarly, the data do not show significant activity in the heat-affected zones of 5182 and 7075. This could be due to the particle size effect as mentioned above. The SEM

images (**Figure 7-5** and **Figure 7-6**) of the heat affected zones showed signs of particle coarsening but the size was still smaller compared to the fusion zone; therefore restricting the scan size to the heat affected zone could shed more light on corrosion activity.

The trend in the SVET data from the SPR joint (**Figure 7-15**) is quite similar to the RSW joint. Key electrochemical activity was restricted to the center of the joint section. However, the driving force behind the activity is the galvanic coupling with the steel rivet. The SEM images (**Figure 7-7**) did not show any significant changes in microstructure in terms of precipitate size or distribution. The microstructure of the base metal alloy is retained in the joint, but the addition of the cathodic steel rivet increase the drive for galvanic coupling. The macro galvanic corrosion transients in **Figure 7-13** shows that the 7075 was cathodic during the initial period of immersion, however, the SVET data show that the steel rivet was cathodic in nature. This discrepancy could be due to the removal of the sacrificial Zn coating during cross-sectional sample preparation.

Figure 7-16 shows the total anodic and cathodic current measured over the exposure period. In the case of RSW the anodic current stabilizes and reaches a steady value, while the SPR anodic current continues to increase during the exposure period. Most of this anodic activity was occurring at several millimeters away from the joint (**Figure 7-15**). This behavior could be related to the throwing power of the steel rivet. Due to the large cathodic active area, it can support the anodic activity that is far away from the rivet region. This implies that galvanic coupling due to the RSW is short-range, while SPR can sustain corrosion at larger distances. These results need to be interpreted with caution, because the current values measured in SVET are highly localized and do not directly equate to high overall mass loss of the joints [94].

The morphology of the corrosion attack is influenced by the local microstructure as shown in **Figure 7-17**. The heat affected zone of 7075 and 5182 exhibited an intergranular corrosion attack, while the base metal exhibited only pitting type of corrosion. This could be directly related to the continuous presence of precipitates along the grain boundaries as seen in the SEM images (**Figure 7-18**). The strengthening precipitates are too fine to be observed in conventional SEM, so techniques such as TEM or STEM is used. However, in the heat affected zone, the precipitates are not only coarsened in the matrix but also in the boundaries because of the temperature gradient during welding. The composition of these precipitates measured by EDS confirmed that they are anodic to the matrix. Although the columnar and fusion zone contained coarser particles of similar composition type, due to the cross-section of view of the samples, it was not immediately clear on the extent of corrosion attack in the fusion zone. However, the gap adjacent to the interface of the joint did not show any accumulation of the corrosion product; this could mean that the lap joint configuration did not provide easy access for the NaCl solution to reach the center of the joint during exposure. The corrosion morphology of the heat-affected zone is consistent with prior literature data [217]. Recent data reported by Navaser et al. [218] showed pitting corrosion in the heat affected zone, but these differences in results may be due to the usage friction stir processing, where the thermal gradient in the heat affected zone could be smaller.

The corrosion morphology of SPR joints is similar to their respective base metals. The mechanical joining methods did not result in any change in precipitate size or continuity. Similarly, the gap adjacent to the joint did not indicate any accumulation of the corrosion product, implying that the crevice corrosion may not have happened in the current stack

configuration. These results from current work suggest that the under the lap joint configuration, the corrosion attack was limited to the outer surfaces and there was no significant corrosion activity occurred at the interface of the faying surfaces.

Interesting results were observed during accelerated corrosion testing of joints using ASTM standard and automotive original equipment manufacturer (OEM) test methods. In ASTM G85-A2, both the SPR and RSW joints did not show a significant decrease in residual joint strength (**Figure 7-20**), although the corrosion morphology of the joints (**Figure 7-21**) was comparable to the 24h exposure in the ASTM G110 test solution. Furthermore, as shown in **Figure 7-22**, the fracture mode of the joints did not change after exposure. A similar trend was observed in the samples where 50% joint strength was applied as external load. Even after 100 days of exposure to the OEM cyclic corrosion test cycle, stress corrosion cracking was not observed (**Figure 7-23**). When the testing environment was switched to hot (70^{o} C) and humid (85% relative humidity) conditions, no sign of premature failure was observed. For the failure of SCC to occur three key conditions such as susceptible microstructure, suitable environment, and sufficient residual/applied stress level are needed simultaneously [129, 219, 220]. SEM images of the corroded samples clearly shown that microstructure in the heat-affected zone is clearly susceptible to IGC. Such a morphology is observed in the accelerated test environments such as ASTM G85-A2, despite this SCC was not observed. These results suggest that both residual and applied stress conditions are not strong enough to trigger SCC. For in-service conditions, 50% applied load is highly unlikely and most of the times the structures are designed to ensure absence of any applied load in the joint sections. The test results in a humid environment also indicate that the hydrogen effect of surface oxidation does not

have an impact on the performance of the joints. These findings might not be representative of all the testing environments; however, the results of this study underline that despite a susceptible microstructure, the SCC failure is not observed in tested environments.

7.5 Conclusions

The results from the present work confirm that automotive joining methods such as RSW and SPR have an impact on the localized microstructure. The RSW results in the formation of a gradient microstructure in the weld area. The fusion and columnar zone exhibit severe solute segregation on the grain boundaries, in addition to changes in the grain sizes. The residual stresses were also observed in the weld section, particularly in the interface of base metal and columnar region. SPR, on the other hand, did not exhibit such stark microstructure changes, however, widespread residual stress was observed near rivet and button section. These changes in the microstructure had an impact on localized corrosion performance such as pitting and galvanic transients. However, this did not impact during the long term accelerated corrosion testing of the joints. This implies that the 7075 to 5182 joints could be used in the medium corrosion severity environment in automotive applications.

CHAPTER 8: CONCLUSIONS AND FUTURE WORK

8.1 Overview

The objective of this work was to understand the effect of alloy composition, processing sequence, and joining methods on the grain boundary microstructure and its subsequent effect on structural forms of corrosion (IGC, SCC) in the 7xxx class of sheet gauge alloys. Due to the complex grain boundary microstructure and corrosion property relationship, an efficient research scheme was needed to minimize or isolate the secondary effects.

The research scheme was designed in such a manner that when one of the variables of interest was changed, the rest of the processing parameters were kept constant. For example, in Chapter 4, the upstream processing conditions such as composition, homogenization, and hot rolling were kept constant; only the cold rolling schedule was changed to obtain samples of the different grain size. The solutionizing and ageing steps were also kept constant. The same methodology was applied to Chapters 5 and 6, apart from changes to the alloy composition the rest of downstream processing conditions were kept constant. The other unique aspect of this work was the predominant use of materials from an actual industrial plant production process to ensure consistency in the quality and the test material being representative of the real application.

The study revealed that the three factors (processing, composition, joining) uniquely influenced the size, continuity, and composition of the grain boundary precipitates and adjoining precipitate-free zone, which in turn affected the IGC and SCC performance of the materials. The results from this work showed that the grain boundary features that

control the corrosion mechanism vary uniquely, depending on the environment. The key findings and implications for designing corrosion-resistant alloys are summarized below.

8.2 Effect of grain size on the IGC and SCC resistance of 7075 alloy

8.2.1 Summary

1. The decrease in the percentage of cold rolling reduction and increase in recovery anneal temperature led to an increase in grain size of the materials.
2. The grain size increase affected the grain boundary precipitates size and continuity. Large grains had coarser and discontinuous grain boundary precipitates, while smaller grains had finer and continuous grain boundary precipitates. This in turn affected IGC and SCC performance.
3. When exposed the NaCl containing oxidizing environment, the discontinuous precipitation in the coarse grain material resulted in pitting corrosion, while the continuous precipitation in small grain materials resulted in IGC.
4. Under the influence of the external stress, the crack initiated and propagated along the corroded grain boundary leading to intergranular stress corrosion cracking in small grain materials.
5. The correlation between the grain boundary precipitate size and the maximum crack depth was also established.
6. SCC mechanism in oxidizing NaCl containing environment was found to be due to the anodic dissolution mechanism.

8.2.2 Implications

By engineering the grain size, the IGC resistance of the 7075 alloy can be improved. The methods used in this work can be applied on an industrial scale. The coarser grain size also provides larger window for the hot forming process.

8.3 Effect of copper on the SCC resistance of high solute zirconium containing 7xxx alloys

8.3.1 Summary

1. The addition of Cu to high-solute Zr-containing alloys impacted the formation of Al_7Cu_2Fe particles and Al_3Zr dispersoids.
2. Higher Cu led to the formation of more Al_7Cu_2Fe particles during alloy casting. This decreased the resistance to pitting in the oxidizing environment due to a stronger galvanic coupling with the matrix.
3. Higher Cu led to the formation of more eutectic AlMgCuZn phases and, in turn, decreased the number density of Al_3Zr. This had resulted in lower recrystallization resistance and formation of high-angle grain boundaries.
4. Despite these changes, high-solute alloys exhibited only pitting corrosion morphology, while the conventional 7075 exhibited IGC in oxidizing environment due to discontinuity of precipitates along the grain boundary.
5. In presence of applied stress, the cracks nucleated from the pitting corrosion sites of high solute alloys resulting in higher strain ratio values than for the 7075 alloy. The SCC mechanism was attributed to the anodic dissolution mechanism.

8.3.2 Implications

By controlling the levels of key alloying elements, such as Cu and Zr, we can achieve a microstructure that is resistant to IGC and SCC under oxidizing conditions.

8.4 Effect of Zn/Mg ratio on the SCC resistance of high solute 7xxx alloys in humid environment

8.4.1 Summary

1. High-solute alloys that showed superior resistance to IGC and SCC in oxidizing Cl^- containing environments performed poorly in humid environments. However, the 7075 was resistant to SCC under these conditions.
2. The applied stress played a major role in accelerating the failure of the high-solute alloys in humid environment. When the applied stress was about 20% yield stress, the samples survived the test duration.
3. STEM-EDS measurements showed that the Zn / Mg ratio of the PFZ played vital role in determining the SCC resistance of the 7xxx alloys in humid environment.
4. The DFT calculations validated the correlation. The concurrent presence of Zn-H resulted in greater embrittlement of the grain boundary.
5. The results indicate that hydrogen-enhanced decohesion to be the operating mechanism in humid environment.

8.4.2 Implications

Engineering 7xxx alloys with a low Zn/Mg ratio can improve stress corrosion cracking (SCC) resistance in specific humid environmental applications. Alternatively, a reduction in the operating stress levels could improve the durability of the alloys.

8.5 Effect of joining methods on the IGC and SCC resistance of 7075 to 5182 dissimilar joint.

8.5.1 Summary

1. The RSW and SPR methods resulted in gradient microstructure in the joint area. Furthermore, the joining methods resulted in residual stress that led to plastic strain generation.
2. The heat-affected zone in the RSW joint increased the susceptibility to the IGC. SVET data showed that the solute segregation in the fusion zone made the region very active to corrosion transients.
3. SPR joints did not show any IGC; however, the SVET data showed that the steel rivet could sustain corrosion current for features at larger distances.
4. Galvanic corrosion experiments showed that the SPR couple had higher current flow compared to RSW joint couple.
5. Despite these susceptible microstructures, the dissimilar joints did not fail during the long-term accelerated corrosion tests.

8.5.2 Implications

The 7075-5182 dissimilar joints can be used in areas of medium corrosion severity of automotive applications.

8.6 Future work

The present work provided an understanding of the impact of the key alloy design factors on the IGC and SCC resistance of 7xxx alloys. Further studies are needed to gain deeper insights of the grain boundary microstructure on the corrosion performance.

1. Identify the grain boundary precipitate size threshold at which the corrosion morphology changes from intergranular corrosion (IGC) to pitting. This will help metallurgists design appropriate processes to achieve the required grain size and subsequent IGC resistance.
2. Explore the effect of composition on accelerated aging conditions. Current research was carried out in the peak age (T6) temper, which typically requires 24 hours of heat treatment. However, due to cost and logistical constraints, Original Equipment Manufacturers (OEMs) prefer shorter aging cycles. Therefore, it is necessary to investigate the impact of composition on these accelerated aging tempers.
3. Determine an alternative to Zr for the formation of Al3X-type dispersoids to inhibit recrystallization in high Cu alloys.
4. Use statistical physics-based random solid solution models to determine Zn atom positions relative to Mg for calculating the embrittlement energy for different Zn/Mg ratios.

5. Evaluate the susceptibility of joints to stress corrosion cracking (SCC) under other loading modes, such as the bending moment, to simulate joints in parts with complex geometry.

CHAPTER 9: APPENDIX A – POTENTIAL CONTROL SSRT EXPERIMENTS

9.1 Background

The objective of this work is to evaluate the effect of the applied potential on the slow strain rate testing performance of 7075 alloys in the T6 and T73 temper. This study was carried out as a method development for evaluating the dominant corrosion mechanisms.

9.2 Experimental

The samples were solutionized at 480^{o}C for 5 min followed by quenching in water at the rate of 350^{o}C/s. The samples were subsequently aged to T6 and T73 tempers. Electrochemical polarization experiments were carried out in 3.5% NaCl solution with saturated calomel (SCE) as a reference electrode and graphite rod as a counter electrode. A scan rate of 10 mV/min was used. For SSRT experiments, the samples were machined to a dog bone geometry and subjected to a strain rate of 2×10^{-6} s^{-1} in air and 3.5 wt% NaCl environment. Anodic and cathodic potentials were applied during SSRT testing in a NaCl environment based on the polarization data. The fractured samples were subjected to the metllography cross section and examination of the fracture surface to determined the cracking mode. To determine the changes in the microstructure of the grain boundary, the samples were subjected to STEM imaging.

9.3 Results and Discussions

9.3.1 Electrochemical Polarization

Figure 9-1 shows the anodic and cathodic polarization of the T6 and T73 samples in the NaCl solution. The free corrosion potential (E_{corr}) for both tempers was around -720 mV_{SCE}. During anodic polarization, both tempers did not show any sign of passivation. With an increase in potential from the free corrosion potential, the current increased rapidly. This behavior is called active dissolution. At high overpotentials, the current reached a limiting state and this behavior is due to the mass transport limitations. The current values were the same for both tempers, and this indicates that the general corrosion behavior is comparable between the tempers. In the cathodic polarization, we could observe a limiting current region between the -800 mV_{SCE} to -1200 mV_{SCE} and this is associated with the oxygen reduction region and at higher overpotentials the current increased rapidly due to hydrogen evolution.

9.3.2 Slow strain rate test

The SSRT was carried out in air and in 3.5 wt% NaCl as shown in **Figure 9-2**. The stress to failure between the air and simple 3.5wt% NaCl environment were comparable in both T6 and T73 tempers. However, the applied potential has a significant effect on the bending force to failure. With a small anodic overpotential of +50mV of the free corrosion potential, the T6 temper exhibits a significant drop in mechanical properties. The samples did not even reach the yield strength value. The deep cathodic polarization to -1600 mV_{SCE} resulted in a drop in elongation but it was not as significant as the -670mV_{SCE} polarization.

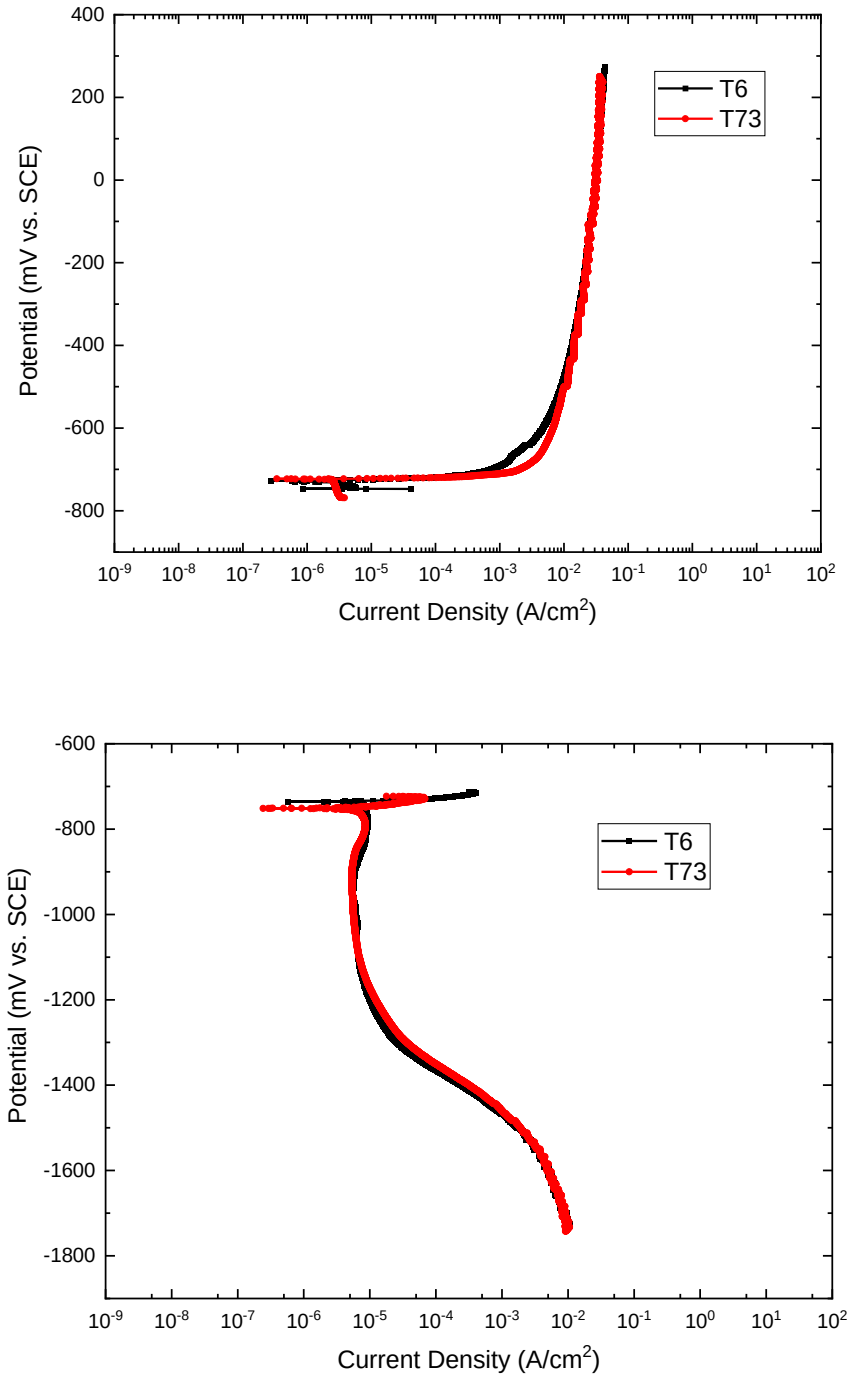

Figure 9-1: Electrochemical anodic (above) and cathodic (below) polarization of T6 and T73 temper in 3.5% NaCl.

From the polarization plot, it can be seen that at -670mV$_{SCE}$, the sample experiences only active dissolution, the recorded current was around +1 mA/cm^2. From the cathodic polarization plot, it can be seen that at -1600 mV$_{SCE}$, the hydrogen evolution appears to be the main reaction and the measured current was around -3mA/cm^2. Despite an increase in the applied current by three times, the drop in elongation was less compared to the anodic polarization.

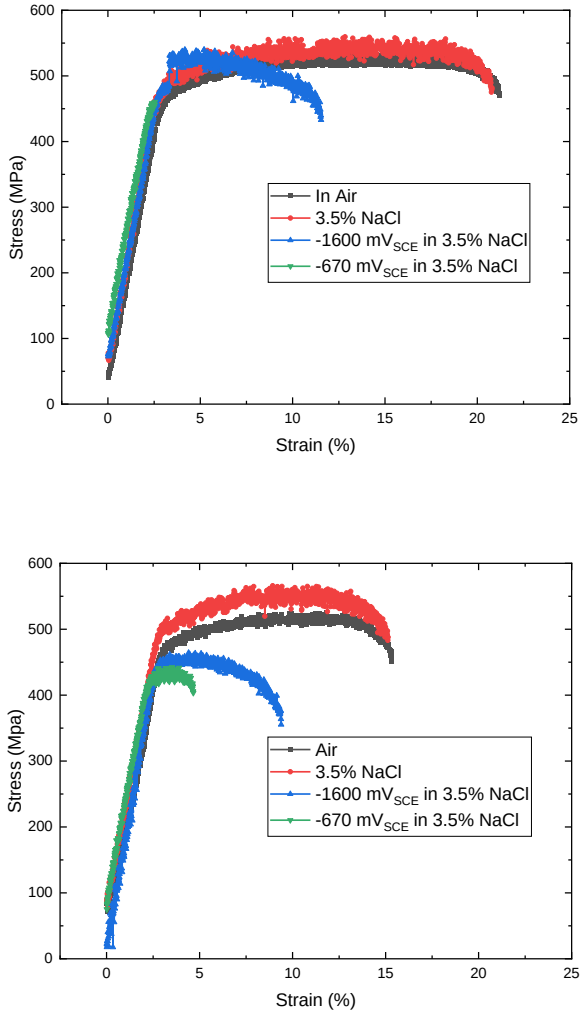

Figure 9-2: Effect of applied potential on SSRT of T6 (above) and T73 (below) in 3.5wt% NaCl.

Similarly, the magnitude of the anodic overpotential was much smaller compared to the applied cathodic overpotential. A similar trend was observed in the T73 temper, the key difference being that the drop in elongation was comparable to T6. **Figure 9-3** shows the effect of applied potential on the strain ratio of the samples in a 3.5% NaCl environment.

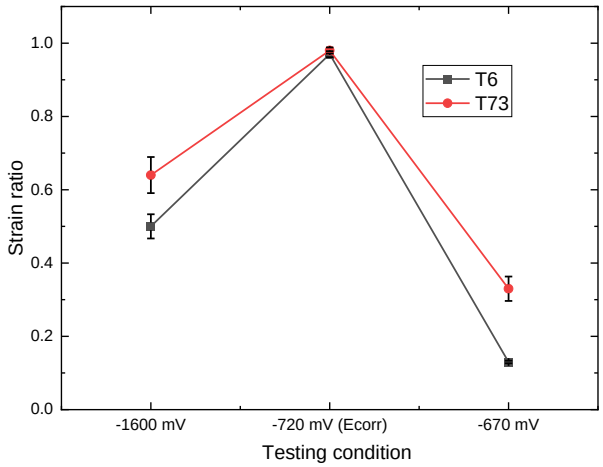

Figure 9-3: Effect of applied potential on the strain ratio in 3.5 wt% NaCl

At the free corrosion potential, the strain ratio was close to 1, which indicates that both tempers are resistant to SCC. However, when -670mV$_{SCE}$ was applied, the strain ratio decreased to 0.13 and 0.33 in T6 and T73 tempers, respectively. This indicates that both materials appear to be susceptible to SCC, with T6 being the most significant. At high cathodic overpotentials, the strain ratio drops to 0.5 and 0.64 in the cases of T6 and T73 tempers, respectively. This indicates that anodic dissolution could be the dominant mechanism due to the significant drop in the strain ratio for small anodic overpotentials.

9.3.3 Fracture Surface Examining

Figure 9-4 shows the side view of the fracture surface under an optical microscope. We could observe that the presence of corrosion sites was largely observed in the applied

potential samples compared to samples fractured under the E_{corr}. The degree of attack was consistently higher in the T6 samples compared to T73. The samples fractured under the anodic overpotential resulted in a higher degree of localized attack compared to the samples polarized at -1600mV_{SCE}. Under the cathodic overpotential, hemispherical pits were largely observed. This could be due to local alkalinization due to the H2 on the samples surface. The surface morphology also resembled that of the features etched in NaOH solution.

Figure 9-5 shows the images of the fracture surface under the SEM. The samples fractured in E_{corr} show ductile dominant features such as the presence of microvoids. The characteristics were consistent with the higher strain ratio values. The T6 samples that were fractured under anodic polarization showed evidence of brittle intergranular fracture features; however, the T73 samples under anodic polarization continued to exhibit dominant ductile features. Under cathodic polarization both T6 and T73 samples continued to exhibit ductile dominant features. This could be due to the higher strain ratio values, indicating that the samples have undergone plastic deformation prior to failure.

9.3.4 Unstressed samples

To determine the corrosion morphology of the samples, potentiostatic polarization was carried out in 3.5% NaCl over a period of 24h in the two overpotentials as shown in **Figure 9-6**. The current values measured during the cathodic over potentials were higher compared to those of the anodic polarization. The figure also shows the metallography cross section of the samples after 24 h of polarization. It could be seen that the depth of attack in T6 after anodic polarization was higher compared to that of the T73 samples.

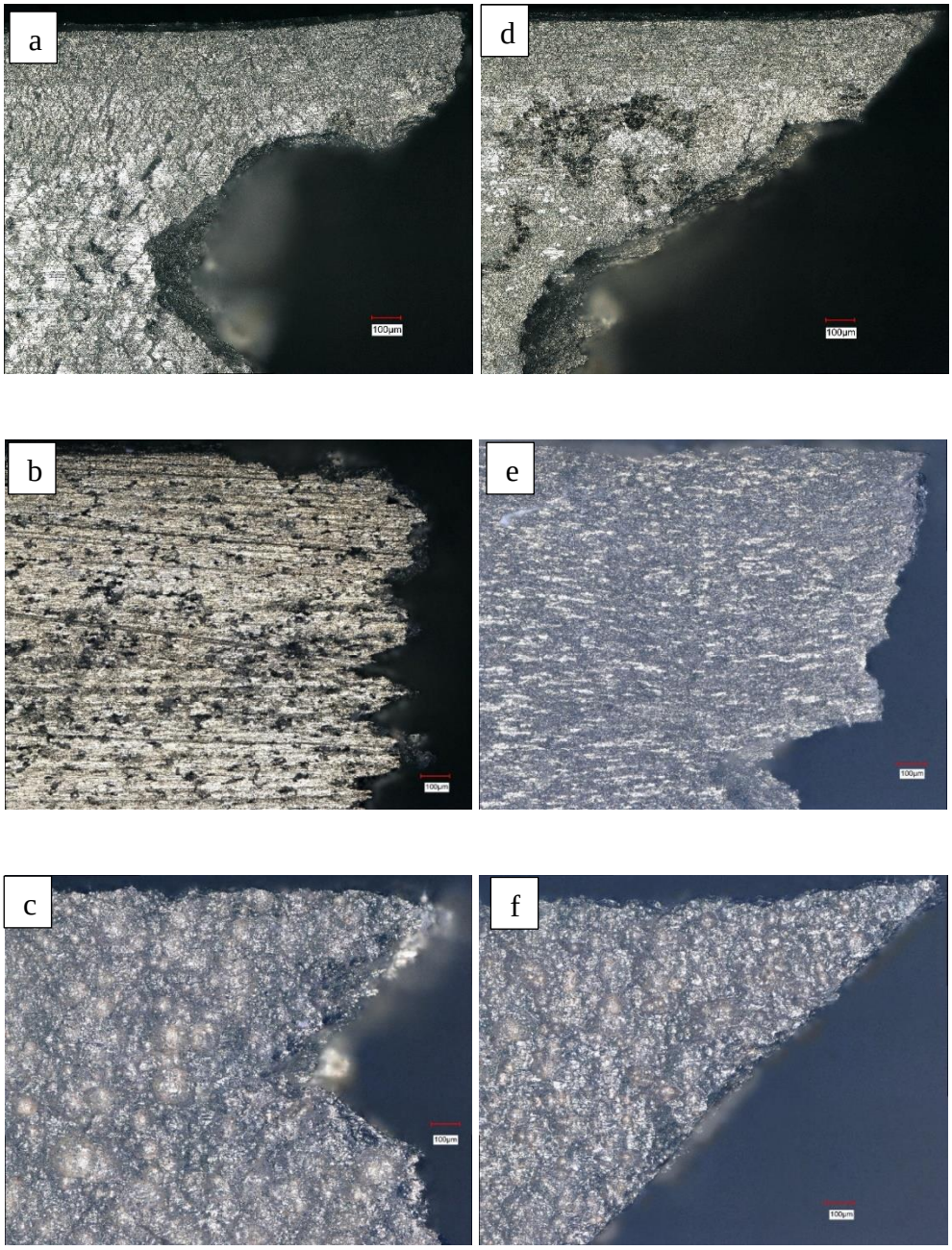

Figure 9-4: Optical microscope images of the fractured T6 (a,b,c) and T73 (d,e,f) after SSRT in 3.5wt% NaCl. Images a, d corresponds to E_{corr}, b, d corresponds to -670mV$_{SCE}$ and c, f corresponds to -1600mV$_{SCE}$.

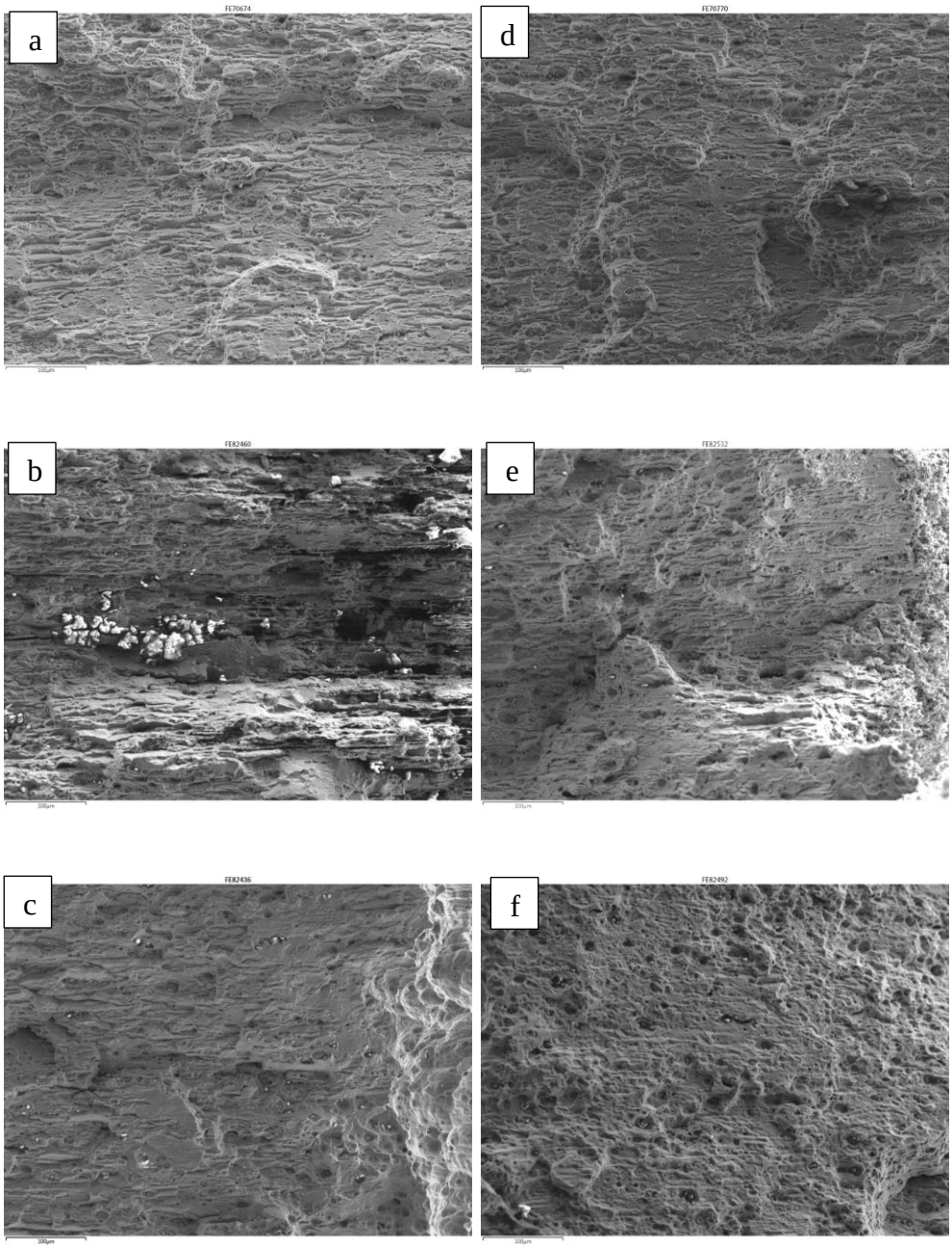

Figure 9-5: SEM fractured surface of T6 (a,b,c) and T73 (d,e,f) after SSRT in 3.5wt% NaCl. Images a, d corresponds to E_{corr}, b, d corresponds to -670mV$_{SCE}$ and c, f corresponds to -1600mV$_{SCE}$.

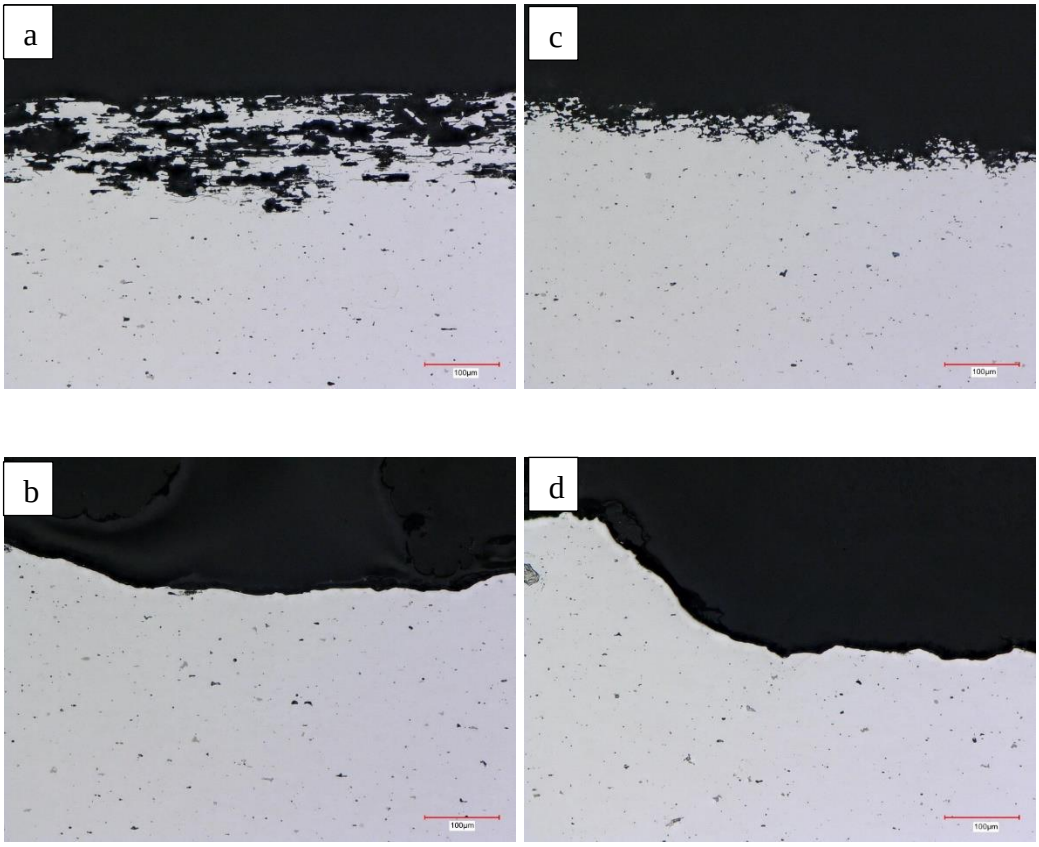

Figure 9-6: Metallography cross section of T6 (a, b) and T73 (c, d) after 24h exposure in potentiostatic polarization. Images a, c corresponds to -670 mV_{SCE} and b, d corresponds to -1600 mV_{SCE}.

More importantly, the intergranular corrosion attack was dominant in the T6 temper. Under the cathodic polarization, no sign of localized attack was observed, instead, severe metal loss was seen. This could be due to local alkalinization due to the evolution of hydrogen.

9.3.5 Scanning transmission electron microscopy

Figure 9-7 shows bright field STEM images of the T6 and T73 temper samples. As expected, the size of the precipitates were smaller in matrix of the T6 compared to the T73. However, the difference could be observed along the grain boundaries as well.

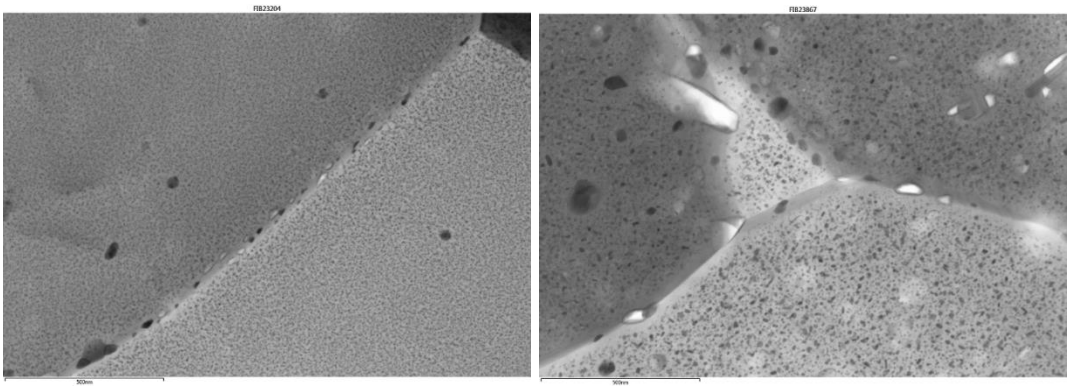

Figure 9-7: STEM bright field images of grain boundaries of T6 (left) and T73 (right).

The precipitates at the grain boundary were small and continuous in T6 samples, while they were coarse and discontinuous in T73. This could be the reason behind the selective attack of the grain boundary during the anodic polarization, resulting in a large drop in the strain ratio.

9.4 Summary

Under open circuit potential, the strain ratio of T6 and T73 was close to 1, indicating the samples are not susceptible to SCC in 3.5wt% NaCl. However, the application of a +50mV overpotential significantly decreased the strain ratio values. The drop in strain ratio was consistently higher in T6 compared to T73. The cross section under the potentiostatic polarization clearly showed that the selective attack of the grain boundaries was evident in T6. STEM images also showed that the precipitates were small and continuous in the grain boundary of T6 compared to T73.

CHAPTER 10: APPENDIX B METHODS FOR EVALUATING THE PRESENCE OF TRAPPED HYDROGEN IN 7XXX ALLOYS

10.1 Background

The objective of this work is to evaluate methods for determining trapped hydrogen in aluminum alloys.

10.2 Fusion extraction method

In this method, aluminum samples are heated in a controlled environment to liberate the trapped hydrogen. For this work, the LECO RHEN602 was used, and the method is based on ASTM E2792. The measurements were outsourced to Element Lab in Chicago. To determine the hydrogen content, 7075 samples were exposed to ASTM D1384 test solution containing hydrogen peroxide for a period of 5 and 24 hours. The unexposed sample was used as a blank reference. **Figure 10-1** shows the results from the first round of testing, and, compared to the blank samples, the hydrogen content in the exposed samples was higher. Similarly, with an increase in exposure time, the amount of trapped hydrogen increased. Since the results were promising, a second batch of samples was sent to analysis. In this set, the samples were exposed to 70 ° C at 85% RH for 100 days (**Figure 10-2**). Although, compared to the unexposed samples, the hydrogen content after 100 days of exposure was higher, the difference net hydrogen difference between 7075 and high solute alloy A was very small. As we have seen in Chapter 6, these high solute alloys exhibited nearly 40% drop in elongation for this exposure period compared to the unexposed surface.

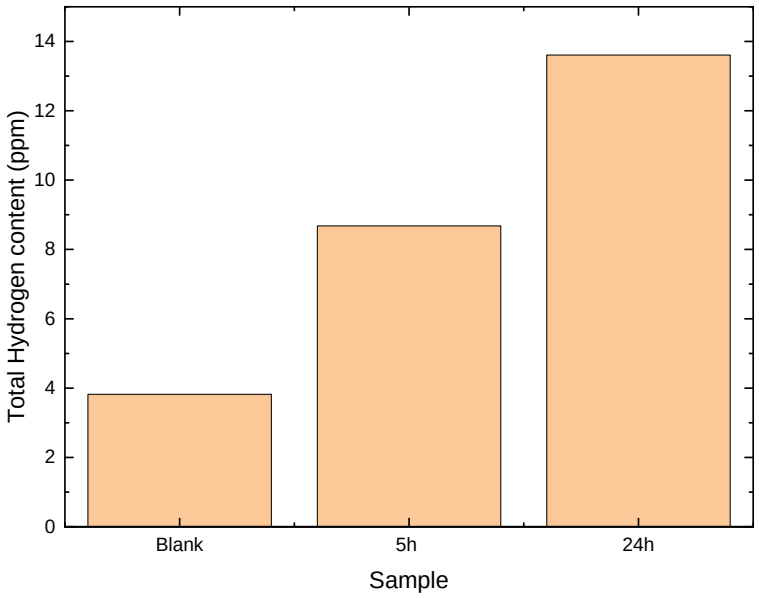

Figure 10-1: Measured hydrogen concentration as function of exposure time in ASTM D1384 containing 1% H_2O_2

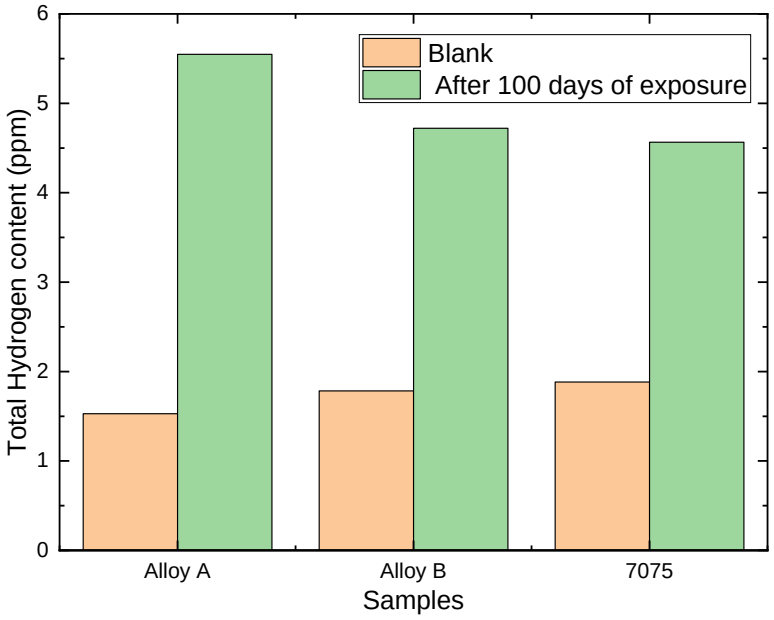

Figure 10-2: Effect of exposure duration on hydrogen content in 70°C at 85% RH environment.

10.3 Hydrogen Permeation Method

In this method, a Devanathan cell is used where one side of the sample is generated during a cathodic reaction on the surface, and after the hydrogen is diffusing through the metal, it is oxidized on the other side of the cell chamber. The surface of the samples exposed to the oxidizing chamber is coated with a thin layer of Pd. Current transients are measured on the oxidizing side, and when hydrogen reaches the surface, the measured current increases. By analyzing the plot, the diffusivity and concentration of the trapping site can be obtained. The schematic of the set-up and associated calculations are shown in **Figure 10-3**.

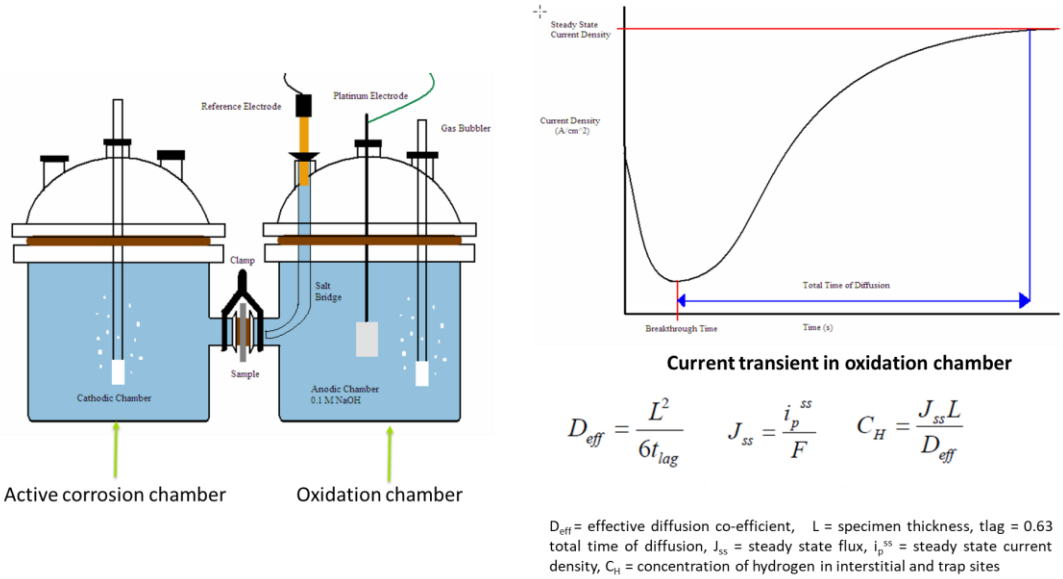

Figure 10-3: Schematic of hydrogen permeation set up and associated current transient equations for calculating diffusivity and concentration of trapping sites.

The conditions used for measuring the hydrogen diffusivity are shown in the **Table 10-1**. However, in all these cases, reliable results could not be achieved because of the instability of the Pd layer in the oxidizing solutions.

Table 10-1: Experimental conditions obtained from literature [221-223]

Sputtered layer	Cathodic cell	Anodic cell
Pd (40 nm thickness) one side (Anodic)	3.5% NaCl, applied current is -10 mA/cm^2	0.001M $K_2Cr_2O_7$, applied potential is +100mV vs SCE
Pd (40 nm thickness) one side (Anodic)	0.01M NaOH at E_{corr}	Phosphate buffer solution pH 7, at Ecorr
Ni (200 nm thickness) Two side	0.1M NaOH, applied current is -3mA/cm^2	0.1M NaOH, applied potential is 100 mV vs. HgO/Hg

The **Figure 10-4** shows the optical microscope images of the anodic side after the permeation experiments. The localized attack could be clearly seen under three conditions. Pd is inert to the oxidizing solutions, but it continues to exhibit attack in both the phosphate buffer and $K_2Cr_2O_7$ solution. Simiarly, Ni is very stable in NaOH solution, but selective grain boundary attack could be observed. It appears that the sputtered deposited thin films are not uniform and as a result, reliable results could not be deduced from these experiments.

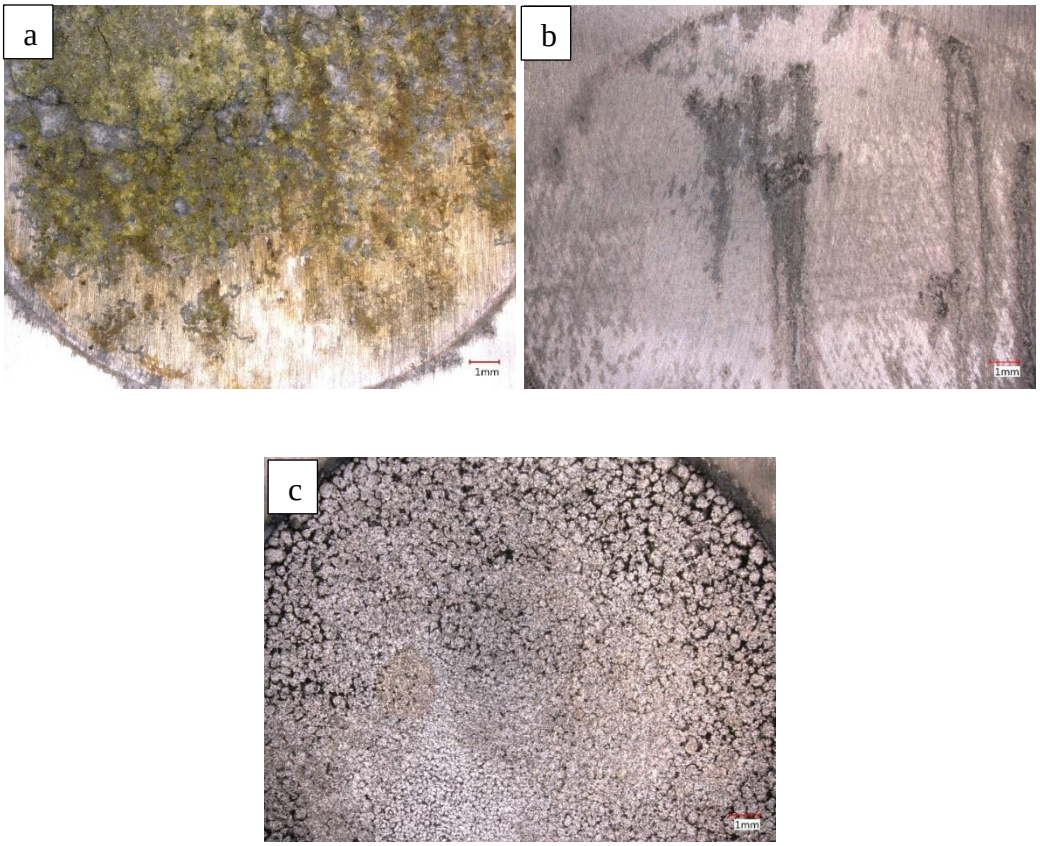

Figure 10-4: Optical microscope images of the anodic side of (a) Pd in $K_2Cr_2O_7$ (b) Pd in phosphate buffer solution (c) Ni in NaOH solution after the permeation experiments.

10.4 Summary

In the literature, three conditions were identified to carry out permeation experiments to determine the diffusivity and trapping site concentrations. However, reliable data could not be obtained under any of the conditions due to the deposited breakdown of the sputtered layer.

REFERENCES

[1] M. Takahashi, Sheet steel technology for the last 100 years: progress in sheet steels in hand with the automotive industry, isij international, 55 (2015) 79-88.

[2] R. Heuss, N. Müller, S.A. Sintern Wv, A. Tschiesner, Lightweight, heavy impact. McKinsey & Company, in, 2012.

[3] S.J. Andersen, C.D. Marioara, J. Friis, S. Wenner, R. Holmestad, Precipitates in aluminium alloys, Advances in Physics: X, 3 (2018) 1479984.

[4] J.R. Davis, Corrosion of aluminum and aluminum alloys, Asm International, 1999.

[5] T.P. Hovorun, K.V. Berladir, V. Pererva, S. Rudenko, A. Martynov, Modern materials for automotive industry, (2017).

[6] B. Smith, S. Adela, M. Shashank, F. Terni, Technology Roadmaps: Intelligent Mobility Technology, Materials and Manufacturing Processes, and Light Duty Vehicle Propulsion, Ann Arbor, MI: Center for Automotive Research, (2017).

[7] M. Ghosh, A. Ghosh, A. Roy, Renewable and sustainable materials in automotive industry, Encyclopedia of Renewable and Sustainable Materials 2020, (2020) 162-179.

[8] J. Galán, L. Samek, P. Verleysen, K. Verbeken, Y. Houbaert, Advanced high strength steels for automotive industry, Revista de metalurgia, 48 (2012) 118.

[9] B. Engl, T. Heller, R. Kawalla, Status and potential of materials development as reflected in steels for the automotive industry, in: Forum technische Mitteilungen ThyssenKrupp, Thyssen Krupp, 1999, pp. 20-25.

[10] W.C. Philips, Technische Mitteilungen ThyssenKrupp 4(1999) 6.

[11] S. Keeler, M. Kimchi, Advanced high strength steels Application Guidelines, version 5, world auto steel, World Steel Association, Brussels, (2014).

[12] I. Gutiérrez-Urrutia, D. Raabe, Multistage strain hardening through dislocation substructure and twinning in a high strength and ductile weight-reduced Fe–Mn–Al–C steel, Acta Materialia, 60 (2012) 5791-5802.

[13] T. Hilditch, T. De Souza, P. Hodgson, Properties and automotive applications of advanced high-strength steels (AHSS), in: Welding and joining of advanced high strength steels (AHSS), Elsevier, 2015, pp. 9-28.

[14] L. Baker, S. Daniel, J. Parker, Metallurgy and processing of ultralow carbon bake hardening steels, Materials Science and Technology, 18 (2002) 355-368.

[15] J.R. Fekete, D.C. Strugala, Z. Yao, Advanced sheet steels for automotive applications, JOM, 44 (1992) 17-21.

[16] J. Patel, C. Klinkenberg, K. Hulka, Hot rolled HSLA strip steels for automotive and construction applications, in: Proc. Int. Symposium Niobium 2001, 2001, pp. 647-674.

[17] C.C. Tasan, M. Diehl, D. Yan, M. Bechtold, F. Roters, L. Schemmann, C. Zheng, N. Peranio, D. Ponge, M. Koyama, An overview of dual-phase steels: advances in microstructure-oriented processing and micromechanically guided design, Annual Review of Materials Research, 45 (2015) 391-431.

[18] H. Ghassemi-Armaki, R. Maaß, S. Bhat, S. Sriram, J. Greer, K. Kumar, Deformation response of ferrite and martensite in a dual-phase steel, Acta Materialia, 62 (2014) 197-211.

[19] H. Yi, Review on δ-transformation-induced plasticity (TRIP) steels with low density: the concept and current progress, Jom, 66 (2014) 1759-1769.

[20] P. Mallick, Advanced materials for automotive applications: An overview, Advanced materials in automotive engineering, (2012) 5-27.

[21] M. Ren, P. Lu, X. Liu, M. Hossain, Y. Fang, T. Hanaoka, B. O'Gallachoir, J. Glynn, H. Dai, Decarbonizing China's iron and steel industry from the supply and demand sides for carbon neutrality, Applied Energy, 298 (2021) 117209.

[22] A.I. Taub, Automotive materials: technology trends and challenges in the 21st century, MRS bulletin, 31 (2006) 336-343.

[23] J. Hirsch, Recent development in aluminium for automotive applications, Transactions of Nonferrous Metals Society of China, 24 (2014) 1995-2002.

[24] J. Hirsch, Automotive trends in aluminium-The European perspective, in: Materials Forum, Citeseer, 2004, pp. 15-23.

[25] A. Heinz, A. Haszler, C. Keidel, S. Moldenhauer, R. Benedictus, W. Miller, Recent development in aluminium alloys for aerospace applications, Materials Science and Engineering: A, 280 (2000) 102-107.

[26] A. Mayyas, A. Qattawi, M. Omar, D. Shan, Design for sustainability in automotive industry: A comprehensive review, Renewable and sustainable energy reviews, 16 (2012) 1845-1862.

[27] T.A. BASER, U. Elif, V. AKINCI, New Trends in Aluminum Die Casting Alloys for Automotive Applications, The Eurasia Proceedings of Science Technology Engineering and Mathematics, 21 (2022) 79-87.

[28] J.R. Kissell, R.L. Ferry, Aluminum structures: a guide to their specifications and design, John Wiley & Sons, 2002.

[29] N. Hashimoto, Application of Aluminum extrusions to automotive parts, KOBELCO Technology Review, 35 (2017) 69-75.

[30] W.D. Callister Jr, D.G. Rethwisch, Fundamentals of materials science and engineering: an integrated approach, John Wiley & Sons, 2020.

[31] J. Benedyk, Aluminum alloys for lightweight automotive structures, in: Materials, design and manufacturing for lightweight vehicles, Elsevier, 2010, pp. 79-113.

[32] W. Miller, L. Zhuang, J. Bottema, A.J. Wittebrood, P. De Smet, A. Haszler, A. Vieregge, Recent development in aluminium alloys for the automotive industry, Materials Science and Engineering: A, 280 (2000) 37-49.

[33] G. Sha, A. Cerezo, Early-stage precipitation in Al–Zn–Mg–Cu alloy (7050), Acta Materialia, 52 (2004) 4503-4516.

[34] A.S.M.H.T.S.C. Exposition, N.B. Dahotre, A. International, Heat Treating and Surface Engineering: Proceedings of the 22nd Heat Treating Society Conference and the 2nd International Surface Engineering Congress : 15-17 September, 2003, Indianapolis, Indiana, USA, ASM International, 2003.

[35] F. Viana, A. Pinto, H. Santos, A. Lopes, Retrogression and re-ageing of 7075 aluminium alloy: microstructural characterization, Journal of Materials Processing Technology, 92 (1999) 54-59.

[36] S.P. Knight, N. Birbilis, B.C. Muddle, A.R. Trueman, S.P. Lynch, Correlations between intergranular stress corrosion cracking, grain-boundary microchemistry, and grain-boundary electrochemistry for Al–Zn–Mg–Cu alloys, Corrosion Science, 52 (2010) 4073-4080.

[37] X. Zhao, Exfoliation corrosion kinetics of high strength aluminum alloys, in, The Ohio State University, 2006.

[38] M. Bobby Kannan, P. Bala Srinivasan, V.S. Raja, 8 - Stress corrosion cracking (SCC) of aluminium alloys, in: V.S. Raja, T. Shoji (Eds.) Stress Corrosion Cracking, Woodhead Publishing, 2011, pp. 307-340.

[39] T. Burleigh, The postulated mechanisms for stress corrosion cracking of aluminum alloys: A review of the literature 1980-1989, Corrosion, 47 (1991) 89-98.

[40] M. Bobby-Kannan, V. Raja, R. Raman, A. Mukhopadhyay, Influence of multistep aging on the stress corrosion cracking behavior of aluminum alloy 7010, Corrosion, 59 (2003).

[41] V. Raja, Hydrogen embrittlement susceptibility of over aged 7010 Al-alloy, Journal of materials science, 41 (2006) 5495-5499.

[42] E. Charitidou, G. Papapolymerou, G. Haidemenopoulos, N. Hasiotis, V. Bontozoglou, Characterization of trapped hydrogen in exfoliation corroded aluminium alloy 2024, Scripta Materialia, 41 (1999) 1327-1332.

[43] D. Najjar, T. Magnin, T. Warner, Influence of critical surface defects and localized competition between anodic dissolution and hydrogen effects during stress corrosion cracking of a 7050 aluminium alloy, Materials Science and Engineering: A, 238 (1997) 293-302.

[44] W. Gruhl, THE STRESS CORROSION BEHAVIOUR OF HIGH STRENGTH ALZNMG ALLOYS, (1978).

[45] R.K. Gupta, A. Deschamps, M.K. Cavanaugh, S.P. Lynch, N. Birbilis, Relating the early evolution of microstructure with the electrochemical response and mechanical performance of a Cu-rich and Cu-lean 7xxx aluminum alloy, Journal of The Electrochemical Society, 159 (2012) C492-C502.

[46] B. Sarkar, M. Marek, E. Starke, The effect of copper content and heat treatment on the stress corrosion characteristics of Ai-6Zn-2Mg-X Cu alloys, Metallurgical Transactions A, 12 (1981) 1939-1943.

[47] D. Spinella, Common Joining Methods Used in Aluminium Structures, in, 2013.

[48] J.-Q. Su, T. Nelson, R. Mishra, M. Mahoney, Microstructural investigation of friction stir welded 7050-T651 aluminium, Acta materialia, 51 (2003) 713-729.

[49] V. Fiore, L. Calabrese, E. Proverbio, R. Passari, A. Valenza, Salt spray fog ageing of hybrid composite/metal rivet joints for automotive applications, Composites Part B: Engineering, 108 (2017) 65-74.

[50] R.R. Ambriz, D. Jaramillo, Mechanical behavior of precipitation hardened aluminum alloys welds, Light Metal Alloys Applications, (2014) 35-59.

[51] N.R. Harrison, S.G. Luckey, Hot stamping of a B-pillar outer from high strength aluminum sheet AA7075, SAE International Journal of Materials and Manufacturing, 7 (2014) 567-573.

[52] K.D. Ralston, N. Birbilis, Effect of Grain Size on Corrosion: A Review, CORROSION, 66 (2010) 075005-075005-075013.

[53] E. Sikora, X.J. Wei, B.A. Shaw, Corrosion Behavior of Nanocrystalline Bulk Al-Mg-Based Alloys, CORROSION, 60 (2004) 387-398.

[54] T. Tsai, T. Chuang, Role of grain size on the stress corrosion cracking of 7475 aluminum alloys, Materials Science and Engineering: A, 225 (1997) 135-144.

[55] L. Christodoulou, H.M. Flower, Hydrogen embrittlement and trapping in Al6%・Zn-3%・Mg, Acta Metallurgica, 28 (1980) 481-487.

[56] W. Tian, S. Li, J. Liu, M. Yu, Y. Du, Preparation of bimodal grain size 7075 aviation aluminum alloys and their corrosion properties, Chinese Journal of Aeronautics, 30 (2017) 1777-1788.

[57] K.G. Krishna, K. Sivaprasad, T.S. Narayanan, K.H. Kumar, Localized corrosion of an ultrafine grained Al–4Zn–2Mg alloy produced by cryorolling, Corrosion Science, 60 (2012) 82-89.

[58] Y.-g. Liao, X.-q. Han, M.-x. Zeng, M. Jin, Influence of Cu on microstructure and tensile properties of 7XXX series aluminum alloy, Materials & Design, 66 (2015) 581-586.

[59] T. Marlaud, A. Deschamps, F. Bley, W. Lefebvre, B. Baroux, Influence of alloy composition and heat treatment on precipitate composition in Al–Zn–Mg–Cu alloys, Acta Materialia, 58 (2010) 248-260.

[60] R.G. Kamat, D.J. Chakrabarti, R.R. Mohanty, R.V. Kulkarni, D.E. Bendzinski, J. Timm, High strength 7xxx aluminum alloys and methods of making the same, in, Google Patents, 2017.

[61] C. Wu, R.G. Kamat, Y. Wang, S.R. Wagstaff, R.R. Mohanty, R.V. Kulkarni, D.E. Bendzinski, Y. Yuan, Aluminum alloy products having selectively recrystallized microstructure and methods of making, in, Google Patents, 2019.

[62] T. Ramgopal, P. Schmutz, G. Frankel, Electrochemical behavior of thin film analogs of Mg (Zn, Cu, Al) 2, Journal of The Electrochemical Society, 148 (2001) B348-B356.

[63] D. Xu, N. Birbilis, P. Rometsch, Effect of S-phase dissolution on the corrosion and stress corrosion cracking of an as-rolled Al-Zn-Mg-Cu alloy, Corrosion, The Journal of Science and Engineering, 68 (2012) 035001-035001-035001-035010.

[64] S.-S. Wang, I.-W. Huang, L. Yang, J.-T. Jiang, J.-F. Chen, S.-L. Dai, D.N. Seidman, G. Frankel, L. Zhen, Effect of Cu content and aging conditions on pitting corrosion damage of 7xxx series aluminum alloys, Journal of The Electrochemical Society, 162 (2015) C150-C160.

[65] Q. Meng, G. Frankel, Effect of Cu content on corrosion behavior of 7xxx series aluminum alloys, Journal of The Electrochemical Society, 151 (2004) B271-B283.

[66] N.H. Holroyd, G. Scamans, Stress corrosion cracking in Al-Zn-Mg-Cu aluminum alloys in saline environments, Metallurgical and Materials Transactions A, 44 (2013) 1230-1253.

[67] S. Wang, B. Luo, Z. Bai, C. He, S. Tan, G. Jiang, Effect of Zn/Mg ratios on microstructure and stress corrosion cracking of 7005 alloy, Materials, 12 (2019) 285.

[68] X.-z. Wu, D.-h. Xiao, Z.-m. Zhu, X.-x. Li, K.-h. Chen, Effects of Cu/Mg ratio on microstructure and properties of AA7085 alloys, Transactions of Nonferrous Metals Society of China, 24 (2014) 2054-2060.

[69] G.E. Totten, D.S. MacKenzie, Handbook of Aluminum: Volume 2: Alloy Production and Materials Manufacturing, CRC press, 2003.

[70] T. Minoda, H. Yoshida, Effect of grain boundary characteristics on intergranular corrosion resistance of 6061 aluminum alloy extrusion, Metallurgical and Materials Transactions A, 33 (2002) 2891-2898.

[71] Z. Jia, G. Hu, B. Forbord, J.K. Solberg, Effect of homogenization and alloying elements on recrystallization resistance of Al–Zr–Mn alloys, Materials science and engineering: A, 444 (2007) 284-290.

[72] A.R. Eivani, S. Valipour, H. Ahmed, J. Zhou, J. Duszczyk, Effect of the Size Distribution of Nanoscale Dispersed Particles on the Zener Drag Pressure, Metallurgical and Materials Transactions A, 42 (2011) 1109-1116.

[73] K. Chen, H.-C. Fang, Z. Zhang, X. Chen, G. Liu, Effect of of Yb, Cr and Zr additions on recrystallization and corrosion resistance of Al–Zn–Mg–Cu alloys, Materials Science and Engineering: A, 497 (2008) 426-431.

[74] H. Fang, K. Chen, X. Chen, H. Chao, G. Peng, Effect of Cr, Yb and Zr additions on localized corrosion of Al–Zn–Mg–Cu alloy, Corrosion Science, 51 (2009) 2872-2877.

[75] H. Fang, H. Chao, K. Chen, Effect of recrystallization on intergranular fracture and corrosion of Al–Zn–Mg–Cu–Zr alloy, Journal of Alloys and Compounds, 622 (2015) 166-173.

[76] A. G34-01, Standard Test Method for Exfoliation Corrosion Susceptibility in 2XXX and 7XXX Series Aluminum Alloys (EXCO Test), American Society for Testing and Materials: West Conshohocken, PA, USA, (2013).

[77] S. Chen, K. Chen, P. Dong, S. Ye, L. Huang, Effect of recrystallization and heat treatment on strength and SCC of an Al–Zn–Mg–Cu alloy, Journal of alloys and compounds, 581 (2013) 705-709.

[78] M.B. Kannan, V. Raja, A. Mukhopadhyay, P. Schmuki, Environmentally assisted cracking behavior of peak-aged 7010 aluminum alloy containing scandium, Metallurgical and Materials Transactions A, 36 (2005) 3257-3262.

[79] S.-n. Wu, B. Ghaffari, E. Hetrick, M. Li, Z.-h. Jia, Q. Liu, Microstructure characterization and quasi-static failure behavior of resistance spot welds of AA6111-T4 aluminum alloy, Transactions of Nonferrous Metals Society of China, 24 (2014) 3879-3885.

[80] S.M. Manladan, F. Yusof, S. Ramesh, M. Fadzil, Z. Luo, S. Ao, A review on resistance spot welding of aluminum alloys, The International Journal of Advanced Manufacturing Technology, 90 (2017) 605-634.

[81] F. Hayat, Effect of aging treatment on the microstructure and mechanical properties of the similar and dissimilar 6061-T6/7075-T651 RSW joints, Materials Science and Engineering: A, 556 (2012) 834-843.

[82] S. Wu, B. Ghaffari, E. Hetrick, M. Li, Q. Liu, Z. Jia, Thermo-mechanically affected zone in AA6111 resistance spot welds, Journal of Materials Processing Technology, 249 (2017) 463-470.

[83] S. Maddela, B.E. Carlson, Corrosion Characterization of Resistance Spot-Welded Aluminum and Steel Couple, Journal of Manufacturing Science and Engineering, 141 (2019).

[84] S. Knight, N. Birbilis, B. Muddle, A. Trueman, S. Lynch, Correlations between intergranular stress corrosion cracking, grain-boundary microchemistry, and grain-boundary electrochemistry for Al–Zn–Mg–Cu alloys, Corrosion Science, 52 (2010) 4073-4080.

[85] N. Birbilis, M.K. Cavanaugh, R.G. Buchheit, Electrochemical behavior and localized corrosion associated with Al7Cu2Fe particles in aluminum alloy 7075-T651, Corrosion Science, 48 (2006) 4202-4215.

[86] S. Brauser, L.-A. Pepke, G. Weber, M. Rethmeier, Deformation behaviour of spot-welded high strength steels for automotive applications, Materials Science and Engineering: A, 527 (2010) 7099-7108.

[87] D.B. Williams, C.B. Carter, D.B. Williams, C.B. Carter, The transmission electron microscope, Springer, 1996.

[88] J.I. Goldstein, D.E. Newbury, J.R. Michael, N.W. Ritchie, J.H.J. Scott, D.C. Joy, Scanning electron microscopy and X-ray microanalysis, Springer, 2017.

[89] L. Marks, http://www.numis.northwestern.edu/360/STEM.pdf, in, 2022.

[90] A.J. Schwartz, M. Kumar, B.L. Adams, D.P. Field, Electron backscatter diffraction in materials science, Springer, 2009.

[91] S.I. Wright, M.M. Nowell, D.P. Field, A review of strain analysis using electron backscatter diffraction, Microscopy and microanalysis, 17 (2011) 316-329.

[92] R.N. Parkins, Slow strain rate testing-25 years experience, ASTM Special Technical Publication, 1210 (1993) 7-7.

[93] K.B. Deshpande, Experimental investigation of galvanic corrosion: Comparison between SVET and immersion techniques, Corrosion Science, 52 (2010) 2819-2826.

[94] A. Bastos, M. Quevedo, O. Karavai, M. Ferreira, On the application of the scanning vibrating electrode technique (SVET) to corrosion research, Journal of The Electrochemical Society, 164 (2017) C973.

[95] A.S.f. Testing, Materials–ASTM, ASTM G85: standard practice for modified salt spray (fog) testing, in, ASTM West Conshohocken, 2011.

[96] A. G44-99, Standard practice for exposure of metals and alloys by alternate immersion in neutral 3.5% sodium chloride solution, (2003).

[97] H. Zheng, X.-G. Li, R. Tran, C. Chen, M. Horton, D. Winston, K.A. Persson, S.P. Ong, Grain boundary properties of elemental metals, Acta Materialia, 186 (2020) 40-49.

[98] R. Tran, Z. Xu, B. Radhakrishnan, D. Winston, W. Sun, K.A. Persson, S.P. Ong, Surface energies of elemental crystals, Scientific data, 3 (2016) 1-13.

[99] E. Nes, J.A. Wert, Modeling of recrystallization in alloys with a bimodal particle size distribution, Scripta metallurgica, 18 (1984) 1433-1438.

[100] J.F. Humphreys, Nucleation in recrystallization, in: Materials Science Forum, Trans Tech Publ, 2004, pp. 107-116.

[101] J. Bi, Z. Lei, Y. Chen, X. Chen, Z. Tian, J. Liang, X. Zhang, X. Qin, Microstructure and mechanical properties of a novel Sc and Zr modified 7075 aluminum alloy prepared by selective laser melting, Materials Science and Engineering: A, 768 (2019) 138478.

[102] J. Leng, B. Ren, Y. Dong, H. Wu, Grain Refinement and Strengthening Mechanism Analysis of an Ultrahigh Strength Sc (Er)–Zr–7075 Aluminum Alloy, Physics of Metals and Metallography, 122 (2021) 1597-1604.

[103] S. Papadopoulou, A. Kontopoulou, E. Gavalas, S. Papaefthymiou, The Effects of Reduction and Thermal Treatment on the Recrystallization and Crystallographic Texture Evolution of 5182 Aluminum Alloy, Metals, 10 (2020) 1380.

[104] Y. Saito, Monte Carlo simulation of grain boundary precipitation, Materials Science and Engineering: A, 223 (1997) 125-133.

[105] R. Zhang, R. Gupta, C. Davies, A. Hodge, M. Tort, K. Xia, N. Birbilis, The influence of grain size and grain orientation on sensitization in AA5083, Corrosion, 72 (2016) 160-168.

[106] S.P. Knight, Stress corrosion cracking of Al-Zn-Mg-Cu alloys: effects of heat-treatment, environment, and alloy composition, in, Monash University, 2008.

[107] R. Goswami, S. Lynch, N.H. Holroyd, S.P. Knight, R.L. Holtz, Evolution of grain boundary precipitates in Al 7075 upon aging and correlation with stress corrosion cracking behavior, Metallurgical and Materials Transactions A, 44 (2013) 1268-1278.

[108] J.-F. Li, Z.-w. Peng, C.-X. Li, Z.-Q. Jia, W.-j. Chen, Z.-Q. Zheng, Mechanical properties, corrosion behaviors and microstructures of 7075 aluminium alloy with various aging treatments, Transactions of Nonferrous Metals Society of China, 18 (2008) 755-762.

[109] F. Andreatta, H. Terryn, J. De Wit, Corrosion behaviour of different tempers of AA7075 aluminium alloy, Electrochimica acta, 49 (2004) 2851-2862.

[110] T. Ramgopal, P.I. Gouma, G.S. Frankel, Role of Grain-Boundary Precipitates and Solute-Depleted Zone on the Intergranular Corrosion of Aluminum Alloy 7150, CORROSION, 58 (2002) 687-697.

[111] R.P. Wei, C.-M. Liao, M. Gao, A transmission electron microscopy study of constituent-particle-induced corrosion in 7075-T6 and 2024-T3 aluminum alloys, Metallurgical and Materials Transactions A, 29 (1998) 1153-1160.

[112] R. Buchheit, A compilation of corrosion potentials reported for intermetallic phases in aluminum alloys, Journal of the Electrochemical Society, 142 (1995) 3994.

[113] N. Birbilis, R.G. Buchheit, Electrochemical characteristics of intermetallic phases in aluminum alloys: an experimental survey and discussion, Journal of the Electrochemical Society, 152 (2005) B140.

[114] L. Yuan, M. Guo, K. Yu, J. Zhang, L. Zhuang, Multi-scale iron-rich phases induce fine microstructures in Al-Zn-Mg-Cu-Fe alloys, Philosophical Magazine, 101 (2021) 1417-1442.

[115] S.-S. Wang, I.-W. Huang, L. Yang, J.-T. Jiang, J.-F. Chen, S.-L. Dai, D.N. Seidman, G. Frankel, L. Zhen, Effect of Cu content and aging conditions on pitting corrosion damage of 7xxx series aluminum alloys, Journal of The Electrochemical Society, 162 (2015) C150.

[116] N. Qiao, X.K. Liu, X.Q. Jiang, Z.Q. Chen, C.M. Li, H.M. Che, Effect of Cu on the Microstructure of 5052 Aluminum Alloy, in: Advanced Materials Research, Trans Tech Publ, 2015, pp. 200-204.

[117] Z. Szklarska-Smialowska, Pitting corrosion of aluminum, Corrosion science, 41 (1999) 1743-1767.

[118] I. Muller, J. Galvele, Pitting potential of high purity binary aluminium alloys—I. Al・Cu alloys. Pitting and intergranular corrosion, Corrosion Science, 17 (1977) 179-193.

[119] Q. Meng, G. Frankel, Effect of Cu content on corrosion behavior of 7xxx series aluminum alloys, Journal of the Electrochemical Society, 151 (2004) B271.

[120] R.K. Gupta, A. Deschamps, M.K. Cavanaugh, S.P. Lynch, N. Birbilis, Relating the early evolution of microstructure with the electrochemical response and mechanical performance of a Cu-rich and Cu-lean 7xxx aluminum alloy, Journal of The Electrochemical Society, 159 (2012) C492.

[121] C. Liu, Y. Bi, R. Benedictus, Modelling Al3Zr precipitation in an AA7050 alloy, in: Nie JF, Morton AJ, and Muddle B C. Proceedings of the 9th International Conference on Aluminium Alloys, Australia: Institute of Materials Engineering Australasia Ltd, 2004.

[122] A. Eivani, S. Valipour, H. Ahmed, J. Zhou, J. Duszczyk, Effect of the size distribution of nanoscale dispersed particles on the Zener drag pressure, Metallurgical and Materials Transactions A, 42 (2011) 1109-1116.

[123] J. Robson, P. Prangnell, Modelling Al3Zr dispersoid precipitation in multicomponent aluminium alloys, Materials Science and Engineering: A, 352 (2003) 240-250.

[124] A. Mikhaylovskaya, A. Mochugovskiy, V. Levchenko, N.Y. Tabachkova, W. Mufalo, V. Portnoy, Precipitation behavior of L12 Al3Zr phase in Al-Mg-Zr alloy, Materials Characterization, 139 (2018) 30-37.

[125] B. Morere, R. Shahani, C. Maurice, J. Driver, The influence of Al3Zr dispersoids on the recrystallization of hot-deformed AA 7010 alloys, Metallurgical and Materials Transactions A, 32 (2001) 625-632.

[126] C. Sigli, Zirconium solubility in aluminum alloys, in: Materials Forum, 2004, pp. 1353-1358.

[127] N. Nayan, S. Narayana Murty, M. Mittal, P. Sinha, Optimization of homogenizing mode for aluminum alloy AA7075 using calorimetric and microstructural studies, Metal Science and Heat Treatment, 51 (2009) 330-337.

[128] M. Puiggali, A. Zielinski, J. Olive, E. Renauld, D. Desjardins, M. Cid, Effect of microstructure on stress corrosion cracking of an Al-Zn-Mg-Cu alloy, Corrosion Science, 40 (1998) 805-819.

[129] M.B. Kannan, P.B. Srinivasan, V. Raja, Stress corrosion cracking (SCC) of aluminium alloys, in: Stress corrosion cracking, Elsevier, 2011, pp. 307-340.

[130] A. G110-92, Standard practice for evaluating intergranular corrosion resistance of heat treatable aluminum alloys by immersion in sodium chloride+ hydrogen peroxide solution, (2003).

[131] E.L. Hibner, Improved SSR test for lot acceptance criterion, ASTM SPECIAL TECHNICAL PUBLICATION, 1210 (1993) 290-290.

[132] S. Knight, K. Pohl, N. Holroyd, N. Birbilis, P. Rometsch, B. Muddle, R. Goswami, S. Lynch, Some effects of alloy composition on stress corrosion cracking in Al–Zn–Mg–Cu alloys, Corrosion Science, 98 (2015) 50-62.

[133] W. Huo, J. Hu, H. Cao, Y. Du, W. Zhang, Y. Zhang, Simultaneously enhanced mechanical strength and inter-granular corrosion resistance in high strength 7075 Al alloy, Journal of Alloys and Compounds, 781 (2019) 680-688.

[134] A. Lervik, S. Wenner, O. Lunder, C.D. Marioara, R. Holmestad, Grain boundary structures and their correlation with intergranular corrosion in an extruded Al-Mg-Si-Cu alloy, Materials Characterization, 170 (2020) 110695.

[135] Y. Zhang, C. Bettles, P.A. Rometsch, Effect of recrystallisation on Al3Zr dispersoid behaviour in thick plates of aluminium alloy AA7150, Journal of Materials Science, 49 (2014) 1709-1715.

[136] H.-y. Li, J.-j. Liu, W.-c. Yu, Z. Hui, D.-w. Li, Microstructure evolution of Al–Zn–Mg–Cu alloy during non-linear cooling process, Transactions of Nonferrous Metals Society of China, 26 (2016) 1191-1200.

[137] S. Zhang, O.Y. Kontsevoi, A.J. Freeman, G.B. Olson, First principles investigation of zinc-induced embrittlement in an aluminum grain boundary, Acta Materialia, 59 (2011) 6155-6167.

[138] R. Ricker, D. Duquette, The role of hydrogen in corrosion fatigue of high purity Al-Zn-Mg exposed to water vapor, Metallurgical Transactions A, 19 (1988) 1775-1783.

[139] J. Scully, G. Young Jr, S. Smith, Hydrogen embrittlement of aluminum and aluminum-based alloys, in: Gaseous hydrogen embrittlement of materials in energy technologies, Elsevier, 2012, pp. 707-768.

[140] G.A. Young, J.R. Scully, Hydrogen production, absorption and transport during environment assisted cracking of an Al-Zn-Mg-(Cu) alloy in humid air, in: International conference on hydrogen effects on material behavior and corrosion deformation interactions, 2002, pp. 22-26.

[141] H. Yamada, M. Tsurudome, N. Miura, K. Horikawa, N. Ogasawara, Ductility loss of 7075 aluminum alloys affected by interaction of hydrogen, fatigue deformation, and strain rate, Materials Science and Engineering: A, 642 (2015) 194-203.

[142] M. Moshtaghi, M. Safyari, T. Hojo, Effect of solution treatment temperature on grain boundary composition and environmental hydrogen embrittlement of an Al–Zn–Mg–Cu alloy, Vacuum, 184 (2021) 109937.

[143] S. Kumar, T. Namboodhiri, Precipitation hardening and hydrogen embrittlement of aluminum alloy AA7020, Bulletin of Materials Science, 34 (2011) 311-321.

[144] J. Albrecht, A. Thompson, I. Bernstein, The role of microstructure in hydrogen-assisted fracture of 7075 aluminum, Metallurgical Transactions A, 10 (1979) 1759-1766.

[145] N. Takano, Hydrogen diffusion and embrittlement in 7075 aluminum alloy, Materials Science and Engineering: A, 483 (2008) 336-339.

[146] R.C. NEWMAN, R. Procter, Stress corrosion cracking: 1965–1990, British Corrosion Journal, 25 (1990) 259-270.

[147] R. Goswami, S. Lynch, N.H. Holroyd, S.P. Knight, R.L. Holtz, Evolution of grain boundary precipitates in Al 7075 upon aging and correlation with stress corrosion cracking behavior, Metallurgical and Materials Transactions A, 44 (2013) 1268-1278.

[148] A. Singh, Y. Lin, W. Liu, S. Yu, J. Pan, C. Ren, D. Kuanhai, Plant derived cationic dye as an effective corrosion inhibitor for 7075 aluminum alloy in 3.5% NaCl solution, Journal of Industrial and Engineering Chemistry, 20 (2014) 4276-4285.

[149] D. Arnott, N. Ryan, B. Hinton, B. Sexton, A. Hughes, Auger and XPS studies of cerium corrosion inhibition on 7075 aluminum alloy, Applications of Surface Science, 22 (1985) 236-251.

[150] I.-W. Huang, B.L. Hurley, F. Yang, R.G. Buchheit, Dependence on temperature, pH, and Cl− in the uniform corrosion of aluminum alloys 2024-T3, 6061-T6, and 7075-T6, Electrochimica Acta, 199 (2016) 242-253.

[151] N.H. Holroyd, G. Scamans, Crack propagation during sustained-load cracking of Al-Zn-Mg-Cu aluminum alloys exposed to moist air or distilled water, Metallurgical and Materials Transactions A, 42 (2011) 3979-3998.

[152] A. Thompson, I. Bernstein, Effect of hydrogen on behavior of materials, in, Metallurgical Society of AIME, New York, 1976.

[153] S. Liang, Y. Zhu, M. Huang, L. Zhao, Z. Li, Key role of interaction between dislocations and hydrogen-vacancy complexes in hydrogen embrittlement of aluminum: discrete dislocation plasticity analysis, Modelling and Simulation in Materials Science and Engineering, 29 (2021) 065003.

[154] G.A. Young, J.R. Scully, The effects of test temperature, temper, and alloyed copper on the hydrogen-controlled crack growth rate of an Al-Zn-Mg-(Cu) alloy, Metallurgical and Materials Transactions A, 33 (2002) 1167-1181.

[155] U. De Francisco, N.O. Larrosa, M.J. Peel, Hydrogen environmentally assisted cracking during static loading of AA7075 and AA7449, Materials Science and Engineering: A, 772 (2020) 138662.

[156] S. Ciaraldi, J. Nelson, R. Yeske, E. Pugh, Hydrogen effects in metals, Warrendale, USA, TMS-AIME, (1981) 437.

[157] W. Xu, Y. Xin, B. Zhang, X. Li, Stress corrosion cracking resistant nanostructured Al-Mg alloy with low angle grain boundaries, Acta Materialia, 225 (2022) 117607.

[158] C. Meng, D. Zhang, L. Zhuang, J. Zhang, Correlations between stress corrosion cracking, grain boundary precipitates and Zn content of Al–Mg–Zn alloys, Journal of Alloys and Compounds, 655 (2016) 178-187.

[159] N. Deshpande, A. Gokhale, D. Denzer, J. Liu, Relationship between fracture toughness, fracture path, and microstructure of 7050 aluminum alloy: Part I. Quantitative characterization, Metallurgical and materials transactions A, 29 (1998) 1191-1201.

[160] Y. Lang, Y. Cai, H. Cui, J. Zhang, Effect of strain-induced precipitation on the low angle grain boundary in AA7050 aluminum alloy, Materials & Design, 32 (2011) 4241-4246.

[161] E. Schwarzenböck, E. Ollivier, A. Garner, A. Cassell, T. Hack, Z. Barrett, C. Engel, T.L. Burnett, N.H. Holroyd, J.D. Robson, Environmental cracking performance of new generation thick plate 7000-T7x series alloys in humid air, Corrosion Science, 171 (2020) 108701.

[162] M. Safyari, M. Moshtaghi, T. Hojo, E. Akiyama, Mechanisms of hydrogen embrittlement in high-strength aluminum alloys containing coherent or incoherent dispersoids, Corrosion Science, 194 (2022) 109895.

[163] Y. Liu, X. Zhang, Z.-B. Xiao, Y. Huang, Hydrogen adsorption on L12-Al3X (X= Zr, Sc) surface and its diffusion in the bulk: A first-principles study, Vacuum, 182 (2020) 109680.

[164] H. Fujihara, K. Shimizu, H. Toda, A. Takeuchi, M. Uesugi, Suppression of Hydrogen Embrittlement due to Local Partitioning of Hydrogen to Dispersed Intermetallic Compound Particles in Al–Zn–Mg–Cu Alloys, Materials Transactions, 63 (2022) 1406-1415.

[165] T. Tsuru, M. Yamaguchi, K. Ebihara, M. Itakura, Y. Shiihara, K. Matsuda, H. Toda, First-principles study of hydrogen segregation at the MgZn2 precipitate in Al-Mg-Zn alloys, Computational Materials Science, 148 (2018) 301-306.

[166] W. Gruhl, Stress corrosion cracking of high strength aluminium alloys, International Journal of Materials Research, 75 (1984) 819-826.

[167] I. Milne, R.O. Ritchie, B.L. Karihaloo, Comprehensive structural integrity: Cyclic loading and fatigue, Elsevier, 2003.

[168] K. Yoshino, C. McMahon, The cooperative relation between temper embrittlement and hydrogen embrittlement in a high strength steel, Metallurgical and Materials Transactions B, 5 (1974) 363-370.

[169] R. Messmer, C. Briant, The role of chemical bonding in grain boundary embrittlement, Acta Metallurgica, 30 (1982) 457-467.

[170] S. Lynch, Hydrogen embrittlement phenomena and mechanisms, Corrosion reviews, 30 (2012) 105-123.

[171] J.R. Rice, J.-S. Wang, Embrittlement of interfaces by solute segregation, Materials Science and Engineering: A, 107 (1989) 23-40.

[172] S. Zhang, O.Y. Kontsevoi, A.J. Freeman, G.B. Olson, Cohesion enhancing effect of magnesium in aluminum grain boundary: A first-principles determination, Applied Physics Letters, 100 (2012) 231904.

[173] D. McLean, A. Maradudin, Grain boundaries in metals, Physics Today, 11 (1958) 35.

[174] B.T. Wilson, J.D. Robson, C.P. Race, Modelling Hydrogen Embrittlement using Density Functional Theory: A theoretical approach to understanding environmentally assisted cracking in 7xxx series aluminium alloys, in: MATEC Web of Conferences, EDP Sciences, 2020, pp. 04006.

[175] H. Zhao, P. Chakraborty, D. Ponge, T. Hickel, B. Sun, C.-H. Wu, B. Gault, D. Raabe, Hydrogen trapping and embrittlement in high-strength Al alloys, Nature, 602 (2022) 437-441.

[176] B. Kannan, C. Glover, H. McMurray, G. Williams, J. Scully, Performance of a magnesium-rich primer on pretreated AA2024-T351 in full immersion: a galvanic throwing power investigation using a scanning vibrating electrode technique, Journal of The Electrochemical Society, 165 (2018) C27.

[177] J.C. Lippold, Welding metallurgy and weldability, John Wiley & Sons, 2014.

[178] G. Çam, G. İpekoğlu, Recent developments in joining of aluminum alloys, The International Journal of Advanced Manufacturing Technology, 91 (2017) 1851-1866.

[179] N. Williams, J. Parker, Review of resistance spot welding of steel sheets Part 1 Modelling and control of weld nugget formation, International materials reviews, 49 (2004) 45-75.

[180] A. Handbook, Welding, brazing and soldering, in, ASM international Materials Park, 1993.

[181] Á. Dobosy, M. Gáspár, I. Török, Resistance Spot Welding of 7075 Aluminium Alloy, in: Vehicle and Automotive Engineering 2: Proceedings of the 2nd VAE2018, Miskolc, Hungary, Springer, 2018, pp. 679-693.

[182] S. Sun, P. Liu, J. Hu, C. Hong, X. Qiao, S. Liu, R. Zhang, C. Wu, Effect of solid solution plus double aging on microstructural characterization of 7075 Al alloys fabricated by selective laser melting (SLM), Optics & Laser Technology, 114 (2019) 158-163.

[183] S. Wu, C. Yu, W. Zhang, Y. Fu, L. Helfen, Porosity induced fatigue damage of laser welded 7075-T6 joints investigated via synchrotron X-ray microtomography, Science and Technology of Welding and Joining, 20 (2015) 11-19.

[184] H. Li, W. Yan, Z. Li, B. Mariusz, J. Senkara, Y. Zhang, Numerical and experimental study of the hot cracking phenomena in 6061/7075 dissimilar aluminum alloy resistance spot welding, Journal of Manufacturing Processes, 77 (2022) 794-808.

[185] D.-W. Kim, J. Xu, W. Li, D. Blake, Force characteristics of self-piercing riveting, Proceedings of the Institution of Mechanical Engineers, Part B: Journal of Engineering Manufacture, 220 (2006) 1259-1266.

[186] R.S. Florea, Experiments and simulation for 6061-T6 aluminum alloy resistance spot welded lap joints, in, Mississippi State University, 2012.

[187] P. Bamberg, G. Gintrowski, Z. Liang, A. Schiebahn, U. Reisgen, N. Precoma, C. Geffers, Development of a new approach to resistance spot weld AW-7075 aluminum alloys for structural applications: an experimental study – Part 1, Journal of Materials Research and Technology, 15 (2021) 5569-5581.

[188] S. Turnage, K. Darling, M. Rajagopalan, W. Whittington, M. Tschopp, P. Peralta, K. Solanki, Influence of variable processing conditions on the quasi-static and dynamic behaviors of resistance spot welded aluminum 6061-T6 sheets, Materials Science and Engineering: A, 724 (2018) 509-517.

[189] F.J. Humphreys, M. Hatherly, Recrystallization and related annealing phenomena, elsevier, 2012.

[190] S. Mohammed, Y. Jaya, A. Albedah, X. Jiang, D. Li, D. Chen, Ultrasonic spot welding of a clad 7075 aluminum alloy: Strength and fatigue life, International Journal of Fatigue, 141 (2020) 105869.

[191] J.-Q. Su, T.W. Nelson, C.J. Sterling, Microstructure evolution during FSW/FSP of high strength aluminum alloys, Materials Science and Engineering: A, 405 (2005) 277-286.

[192] A.G. Kalashami, C. DiGiovanni, M. Razmpoosh, F. Goodwin, N. Zhou, The role of internal oxides on the liquid metal embrittlement cracking during resistance spot welding of the dual phase steel, Metallurgical and Materials Transactions A, 51 (2020) 2180-2191.

[193] S. Hassanifard, M. Zehsaz, K. Tohgo, The effects of electrode force on the mechanical behaviour of resistance spot-welded 5083-O aluminium alloy joints, Strain, 47 (2011) e196-e204.

[194] D. Afshari, M. Sedighi, M. Karimi, Z. Barsoum, On residual stresses in resistance spot-welded aluminum alloy 6061-T6: experimental and numerical analysis, Journal of materials engineering and performance, 22 (2013) 3612-3619.

[195] I.R. Nodeh, S. Serajzadeh, A.H. Kokabi, Simulation of welding residual stresses in resistance spot welding, FE modeling and X-ray verification, Journal of materials processing technology, 205 (2008) 60-69.

[196] R. Florea, C. Hubbard, K. Solanki, D. Bammann, W. Whittington, E. Marin, Quantifying residual stresses in resistance spot welding of 6061-T6 aluminum alloy sheets via neutron diffraction measurements, Journal of Materials Processing Technology, 212 (2012) 2358-2370.

[197] Z. Zhao, J. Cui, J. Dong, B. Zhang, Effect of low-frequency magnetic field on microstructures and macrosegregation of horizontal direct chill casting 7075 aluminum alloy, Journal of Materials Processing Technology, 182 (2007) 185-190.

[198] R. Nadella, D. Eskin, L. Katgerman, Role of grain refining in hot cracking and macrosegregation in direct chill cast AA 7075 billets, Materials Science and Technology, 23 (2007) 1327-1335.

[199] S. Park, W. Kim, Difference in the hot compressive behavior and processing maps between the as-cast and homogenized Al-Zn-Mg-Cu (7075) alloys, Journal of Materials Science & Technology, 32 (2016) 660-670.

[200] S.-n. Wu, B. Ghaffari, E. Hetrick, L. Mei, Z.-h. Jia, L. Qing, Microstructure characterization and quasi-static failure behavior of resistance spot welds of AA6111-T4 aluminum alloy, Transactions of Nonferrous Metals Society of China, 24 (2014) 3879-3885.

[201] Ø. Ryen, B. Holmedal, O. Nijs, E. Nes, E. Sjölander, H.-E. Ekström, Strengthening mechanisms in solid solution aluminum alloys, Metallurgical and Materials Transactions A, 37 (2006) 1999-2006.

[202] T. Lee, Resistance spot weldability of heat-treatable and non-heat-treatable dissimilar aluminium alloys, Science and Technology of Welding and Joining, 25 (2020) 543-548.

[203] J.F. Moraes, J. Jordon, X. Su, L.N. Brewer, B.J. Fay, J. Bunn, L. Sochalski-Kolbus, M. Barkey, Residual stresses and plastic deformation in self-pierce riveting of dissimilar aluminum-to-magnesium alloys, SAE International Journal of Materials and Manufacturing, 11 (2018) 139-150.

[204] Y. Birol, F. Birol, B. Yuksel, O. Duygulu, Corrosion behaviour of twin belt cast EN AW 7075 alloy, Materials and Corrosion, 64 (2013) 881-889.

[205] J.-f. Li, Z.-q. Zheng, Corrosion and Potentiostatic Polarization of an Al-Cu-Li Alloy Under Tensile Stress, in: ICAA13 Pittsburgh: Proceedings of the 13th International Conference on Aluminum Alloys, Springer, 2016, pp. 443-450.

[206] T. Cui, D. Liu, P.a. Shi, J. Liu, Y. Yi, H. Zhou, Effect of stress and galvanic factors on the corrosion behave of aluminum alloy, Journal of Wuhan University of Technology-Mater. Sci. Ed., 33 (2018) 688-696.

[207] Y. Yang, W. Zhou, Z. Tong, L. Chen, X. Yang, E.A. Larson, X. Ren, Electrochemical corrosion behavior of 5083 aluminum alloy subjected to laser shock peening, Journal of materials engineering and performance, 28 (2019) 6081-6091.

[208] O. Hatamleh, P.M. Singh, H. Garmestani, Corrosion susceptibility of peened friction stir welded 7075 aluminum alloy joints, Corrosion Science, 51 (2009) 135-143.

[209] S. Žagar, J. Grum, Evaluation of the residual stresses and corrosion resistance of shot-peened 7075 aluminium alloy under different states, International Journal of Materials and Product Technology, 53 (2016) 335-348.

[210] S. Dong, G. Kelkar, Y. Zhou, Electrode sticking during micro-resistance welding of thin metal sheets, IEEE transactions on electronics packaging manufacturing, 25 (2002) 355-361.

[211] I. Lum, S. Fukumoto, E. Biro, D. Boomer, Y. Zhou, Electrode pitting in resistance spot welding of aluminum alloy 5182, Metallurgical and Materials Transactions A, 35 (2004) 217-226.

[212] R. Jones, D. Baer, M. Danielson, J. Vetrano, Role of Mg in the stress corrosion cracking of an Al-Mg alloy, Metallurgical and Materials Transactions A, 32 (2001) 1699-1711.

[213] R. Zhang, S.P. Knight, R.L. Holtz, R. Goswami, C.H.J. Davies, N. Birbilis, A survey of sensitization in 5xxx series aluminum alloys, Corrosion, 72 (2016) 144-159.

[214] M.A. Karim, T.-E. Jeong, W. Noh, K.-Y. Park, D.-H. Kam, C. Kim, D.-G. Nam, H. Jung, Y.-D. Park, Joint quality of self-piercing riveting (SPR) and mechanical behavior under the frictional effect of various rivet coatings, Journal of Manufacturing Processes, 58 (2020) 466-477.

[215] A.I. Ikeuba, B. Zhang, J. Wang, E.-H. Han, W. Ke, P.C. Okafor, SVET and SIET study of galvanic corrosion of Al/MgZn2 in aqueous solutions at different pH, Journal of the Electrochemical Society, 165 (2018) C180.

[216] J. Han, K. Ogle, Dealloying of MgZn2 intermetallic in slightly alkaline chloride electrolyte and its significance in corrosion resistance, Journal of The Electrochemical Society, 164 (2017) C952.

[217] C.A. Widener, D.A. Burford, B. Kumar, J. Talia, B. Tweedy, Evaluation of post-weld heat treatments to restore the corrosion resistance of friction stir welded aluminum alloy 7075-T73 vs. 7075-T6, in: Materials science forum, Trans Tech Publ, 2007, pp. 3781-3788.

[218] M. Navaser, M. Atapour, Effect of friction stir processing on pitting corrosion and intergranular attack of 7075 aluminum alloy, Journal of Materials Science & Technology, 33 (2017) 155-165.

[219] N. Holroyd, A. Vasudevan, L. Christodoulou, Stress corrosion of high-strength aluminum alloys, Treatise on Materials Science and Technology, 31 (2012) 463.

[220] G. Scamans, N. Birbilis, R. Buchheit, Corrosion of aluminum and its alloys, in: Shreir's Corrosion, Elsevier, 2010, pp. 1974-2010.

[221] M.J. Danielson, Use of the Devanathan–Stachurski cell to measure hydrogen permeation in aluminum alloys, Corrosion Science, 44 (2002) 829-840.

[222] S. Adhikari, J. Ai, K.R. Hebert, K. Ho, C. Wang, Hydrogen in aluminum during alkaline corrosion, Electrochimica acta, 55 (2010) 5326-5331.

[223] C.-b. Zheng, B.-h. Yan, K. Zhang, G. Yi, Electrochemical investigation on the hydrogen permeation behavior of 7075-T6 Al alloy and its influence on stress corrosion cracking, International Journal of Minerals, Metallurgy, and Materials, 22 (2015) 729-737.